



# Impact of preclinical PET scanner characteristics on the overall image quality

Kajal Aggarwal

## ► To cite this version:

Kajal Aggarwal. Impact of preclinical PET scanner characteristics on the overall image quality. Human health and pathology. Université de Strasbourg, 2019. English. NNT : 2019STRAE028 . tel-02490686

**HAL Id: tel-02490686**

**<https://theses.hal.science/tel-02490686>**

Submitted on 25 Feb 2020

**HAL** is a multi-disciplinary open access archive for the deposit and dissemination of scientific research documents, whether they are published or not. The documents may come from teaching and research institutions in France or abroad, or from public or private research centers.

L'archive ouverte pluridisciplinaire **HAL**, est destinée au dépôt et à la diffusion de documents scientifiques de niveau recherche, publiés ou non, émanant des établissements d'enseignement et de recherche français ou étrangers, des laboratoires publics ou privés.

*ÉCOLE DOCTORALE Physique et Chimie-Physique (ED182)*

IPHC/UMR 7178

**THÈSE** présentée par:

**Kajal AGGARWAL**

soutenue le : 14 octobre 2019

pour obtenir le grade de : **Docteur de l'université de Strasbourg**

Discipline/Spécialité : **Physique/Imagerie Moléculaire**

**Impact of preclinical PET scanner  
characteristics on the overall image quality**

**THÈSE dirigée par :**

**[Dr. BRASSE David]**

Directeur de recherche, IPHC, Strasbourg

**RAPPORTEURS :**

**[Dr. JAN Sébastien]**

Ingénieur, CEA, Orsay

**[Dr. Marie-Laure Gallin-Martel]**

Chargé de recherche, LPSC Grenoble

**EXAMINATEUR :**

**[Pr. LAQUERRIERE Patrice]**

Professeur des Universités, UNISTRA, Strasbourg



*“Your time is limited, so don’t waste it living someone else’s life.”*

Steve Jobs

To my parents  
To bhaiya, bhabhi & Duggu  
To Ankit



# Acknowledgements

I would, first of all, extend my gratitude to Dr. Sébastien Jan and Dr. Marie-Laure Gallin-Martel for accepting to review this thesis and Prof. Dr. Patrice Laquerriere for agreeing to be part of the jury.

Special thank goes to Dr. David Brasse, my thesis supervisor, for his excellent support, advice and for introducing me to the field of medical physics. I would like to thank him for the sometimes difficult but always productive, discussions about this work and for giving me the freedom and strength to explore new ideas. It has been an honour to work with him throughout these years.

Furthermore, I am very grateful to Dr. Frédéric Boisson for all his time to discuss the concepts of PET imaging. My sincere thanks is also going to Dr. Virgile Bekaert for all his help with coding and data analysis. Without his support and encouragement, it would not be possible to achieve the results. I would also like to thank Jean-Michel Gallone. He was always there for all the administrative and technical help. I would also like to thank Dr. Thibaut Merlin (IBRBS, Brest, France) from CASToR software development team, for all his guidance, suggestions and help regarding the CASToR software.

I thank the whole DRHIM department at IPHC. A special thanks goes to Yusuf, Truong, Alexandre and Florian for making the work environment so much fun and interesting. Not to forget, I have really enjoyed my conversations and the tea culture with my tea team (Christian, Rachid and Xiaochao).

Finally, I would like to thank all my friends (Suvi, Swapneel and Sambhit) for all the fun conversation and to Mishu for all the help with grammar corrections. As always, I am forever grateful to my parents and brother for their unconditional love, support and inspiration. I am also grateful to my parents-in-law for their encouragement. And last, but not the least, I would like to thank Ankit (my husband) for all the motivation and for always believing in me. I could not have done it without you all.



# Contents

<b>Introduction</b>	<b>19</b>
<b>1 Basics of PET imaging</b>	<b>23</b>
1.1 Introduction	23
1.2 Physical process	24
1.2.1 Positron decay	24
1.2.2 Annihilation	25
1.2.3 Positron range	26
1.2.4 Photon noncolinearity	27
1.2.5 Types of coincidence events	28
1.3 511 keV gamma photon detectors for PET imaging	28
1.3.1 Interaction of 511 keV gamma photon with matter	29
1.3.2 Scintillation process and detectors	31
1.3.3 Photodetectors	33
1.4 Data acquisition and Image reconstruction	38
1.4.1 Image reconstruction	39
1.5 Figure of Merits	42
1.5.1 Detection efficiency ( $\eta$ )	42
1.5.2 Spatial resolution	43
1.6 Conclusion	45
<b>2 Small animal imaging via PET</b>	<b>47</b>
2.1 Introduction	47
2.2 Background of small animal PET imaging	48
2.3 Challenges in designing small animal PET scanner	49
2.4 Currently available preclinical PET scanners	51
2.5 Summary	52
<b>3 Scanner geometries</b>	<b>53</b>
3.1 Introduction	53
3.2 Fixed parameters for defining scanner geometries	54
3.2.1 Scintillator crystal	54
3.2.2 Scanner diameter	54
3.2.3 Scanner axial coverage	55
3.2.4 Photo-detector	55
3.2.5 Photo-detector readout	56
3.2.6 Number of PET head modules	56
3.3 Variable parameters for defining scanner geometries	57
3.3.1 Crystal size	58
3.3.2 Crystal depth	58



3.4	Scanners geometries . . . . .	59
3.4.1	Scanner A: 2D detection technique . . . . .	60
3.4.2	Scanner B: 2D detection technique + binary sampling . . . . .	63
3.4.3	Scanner C: 2D detection technique + continuous sampling . . . . .	65
3.4.4	Scanner D: 3D detection technique . . . . .	68
3.4.5	IRIS PET Scanner . . . . .	70
3.5	Summary . . . . .	71
<b>4</b>	<b>Simulation and Image reconstruction process</b>	<b>73</b>
4.1	Introduction . . . . .	73
4.2	Monte Carlo (MC) simulations . . . . .	74
4.3	GATE simulation software . . . . .	75
4.3.1	Defining PET scanner geometry . . . . .	75
4.3.2	Source, Phantom and underlying physics processes . . . . .	76
4.3.3	Digitizer . . . . .	76
4.4	Data acquisition approach: Customized . . . . .	78
4.4.1	Introduction . . . . .	78
4.4.2	Validation of the simulated model . . . . .	79
4.5	Image reconstruction process . . . . .	80
4.5.1	System Matrix (A) . . . . .	81
4.5.2	MC generated SM elements ( $a_{ij}$ ) . . . . .	81
4.5.3	Analytical computation of SM elements ( $a_{ij}$ ) . . . . .	83
4.6	CASToR: image reconstruction platform . . . . .	85
4.6.1	Main features . . . . .	85
4.7	CASToR's image reconstruction process . . . . .	86
4.7.1	Identification of geometrical information of the scanner geometry . . . . .	86
4.7.2	Conversion of LM data to the CASToR data file format . . . . .	88
4.7.3	Sensitivity profile generation . . . . .	88
4.7.4	Image reconstruction process . . . . .	89
4.7.5	Summary . . . . .	90
4.8	NEMA NU 4 Standards . . . . .	90
4.9	Conclusion . . . . .	91
<b>5</b>	<b>Performance measurement of the proposed geometries</b>	<b>93</b>
5.1	Introduction . . . . .	93
5.2	Characterization of SM generated using MC simulations . . . . .	94
5.3	Estimation of spatial resolution . . . . .	97
5.3.1	Simulation method . . . . .	98
5.3.2	Data processing and analysis . . . . .	98
5.3.3	Results and discussion . . . . .	99
5.4	Estimation of detection efficiency . . . . .	100
5.4.1	Simulation approach . . . . .	102
5.4.2	Data process and analysis . . . . .	102
5.4.3	Results . . . . .	103
5.5	Estimation of image quality . . . . .	104
5.5.1	Simulation approach . . . . .	104
5.5.2	Data process and analysis . . . . .	104
5.5.3	Results . . . . .	106
5.6	Conclusion . . . . .	111

<b>6</b>	<b>Normalization</b>	<b>113</b>
6.1	Introduction . . . . .	113
6.2	Normalization process . . . . .	114
6.2.1	Standard technique for normalization . . . . .	114
6.3	Analytical approach of normalization . . . . .	115
6.4	Component based normalization approach . . . . .	117
6.4.1	Normalization using MC simulations . . . . .	119
6.5	Comparison with and without normalization correction . . . . .	123
6.5.1	Qualitative comparison . . . . .	123
6.5.2	Quantitative comparison . . . . .	124
6.6	Conclusion . . . . .	125
<b>7</b>	<b>Concluding Remarks and Perspectives</b>	<b>127</b>
	<b>Perspectives</b>	<b>127</b>
<b>A</b>	<b>Gate simulation macros</b>	<b>135</b>
A.1	Scanner A . . . . .	135
A.2	Scanner B . . . . .	137
A.3	Scanner C . . . . .	139
A.4	Scanner D . . . . .	141
<b>B</b>	<b>CASToR generated geometry files</b>	<b>145</b>
B.1	Scanner A . . . . .	145
B.2	Scanner B . . . . .	146
B.3	Scanner C . . . . .	146
B.4	Scanner D . . . . .	147



# List of Figures

1	Comparison of some commercially available scanners (Clairvivo by SHIMADZU, Flex triumph X-PET by Gamma Medica-Ideas, Inveon DPET by Siemens Medical Solutions, rPET-1 by Sedecal, S.A., having a spatial resolution of 2.16 mm, 2.0 mm, 1.6 mm, 1.5 mm respectively at the cFOV) as a function of recovery coefficient estimated following NEMA NU-4 2008 standards . . . . .	20
2	Different commercially available and prototype research PET scanners . . . . .	21
1.1	Glucose and FDG molecule . . . . .	24
1.2	Metabolic trapping of fluorodeoxyglucose (FDG) in the cell. (Reprinted from [Rudd 10]) . . . . .	24
1.3	PET scan showing a small metastasis in the liver, just above the kidney. (Reprinted from [Fine 12]) . . . . .	25
1.4	Positron emission spectrum for F-18 radionuclide. (Reprinted from [Jan 05a]) . . . . .	25
1.5	Positron emission followed by positron scatter in the surrounding medium and subsequent positron-electron annihilation producing two 511 keV gamma photons emitted at 180°. (Adapted from [Phelps 06]) . . . . .	26
1.6	Left: Distribution of positron annihilation sites in water for positrons emitted from F-18 at the center (0,0) of a 2D histogram; Right: Profile through the distribution shown on left, measuring FWHM and FWTM (Full Width at Tenth Maximum) of the distribution. (Reprinted from [Levin 99]) . . . . .	27
1.7	Photon noncolinearity process resulting in emission of two gamma photons (one in blue and the other in green line) emitted at an angle other than 180°. Green line represents two gamma photons emitted at 180° and dotted line represents the LOR as detected by the PET scanner due to noncolinearity. (Adapted from [Phelps 06]) . . . . .	28
1.8	Types of coincidence events detected by PET scanner: A. True coincidence event, B. Scattered coincidence event, C. Random coincidence event, D. Multiple coincidence event. (Reprinted from [Phelps 06]) . . . . .	29
1.9	Different configurations of PET detectors. a) rotating ring configuration; b) detectors arranged in a circular ring; c) detectors arranged in a polygonal ring configuration (Reprinted from [Humm 03]) . . . . .	29
1.10	Types of interaction of 511 keV gamma photons; B. Photoelectric absorption (generating a photoelectron); C. Rayleigh scattering (elastic collision with a bound outer shell electron); D. Compton scattering (Inelastic collision resulting in a scattered photon and recoiled electron) (Reprinted from [O’Hea 15]) . . . . .	30
1.11	Illustration of energy bands and activated acceptor site (energy states in band gap) in a doped inorganic scintillator. (Reprinted from [Knoll 10]) . . . . .	32
1.12	A schematic representation of scintillator detector. (Reprinted from [Phelps 06]) . . . . .	33
1.13	A schematic representation of PET detector, consisting of a scintillator crystal coupled to PMT. An incoming photon deposits its energy in the scintillator, generating low energy (optical photons) shown in red color, which further strikes at the surface of photocathode, liberating a primary electron, that falls on a dynode and generates secondary electrons (Reprinted from [Commons 03]) . . . . .	34

1.14	Schematic representation of a scintillator block segmented into an 8x8 array, coupled to PMT block detector. (Reprinted from [Phelps 06]) . . . . .	35
1.15	Image obtained as a result of flood irradiating the front surface of a block detector with 511 keV photons (Reprinted from [Phelps 06]) . . . . .	35
1.16	Cross-section of dynode structure of a multi-anode PMT and one of the associated electron trajectories (adapted from Hamatsu, 2006) . . . . .	36
1.17	On the left, a reverse bias pn junction, with a depletion region. When a light photon is incident on the depletion region, it produces an electron hole pair, which are drifted apart due to the electric field. On the right a plot showing variation of Gain (M) as a function of applied reverse bias voltage $V_{BIAS}$ . It shows three regions first, where $M = 1$ ; second where M varies linearly with $V_{BIAS}$ and third where M is infinite. . . . .	37
1.18	Parallel combination of several micro-cells. Each micro-cell represents a series combination of a APD (designed to operate in GM mode) and a quenching resistance $R_Q$ . A and K represents anode and cathode respectively. . . . .	38
1.19	The line integral of parallel LORs for a given radioactivity distribution $f(x,y)$ . The line integral of all parallel LORs denotes a projection profile $p(s, \phi)$ ; s being the radial distance and $\phi$ being the given projection angle . . . . .	39
1.20	The 2D line integral for a given 3D radioactivity distribution $f(x,y,z)$ for a given azimuthal angle $\phi$ and co-polar angle $\theta$ . (Reprinted from [Bendriem 13]) . . . . .	40
1.21	Illustration of discretize image space and a LOR joining the detector pair. A system of equation ( $FA = P$ ) is setup to describe the scanner geometry and physics. Each element $F_j$ and $P_i$ of matrix $F$ and $P$ respectively represents the voxel value and the projection measurement. Elements $A_{ij}$ of matrix $A$ represents the SM elements. . . . .	40
1.22	Basic flow chart for iterative image reconstruction process. (Reprinted from [Zeng 10]) . . . . .	41
1.23	Modules showing monolithic (left) and pixelated (right) crystal configurations (Adapted from [González 13]) . . . . .	44
2.1	Models of human and rat brain shown for size comparison. The human brain measures approximately 105 mm from top to bottom while the rat brain measures approximately 10 mm across the same scale. (Adapted from [Myers 02]) . . . . .	49
2.2	Comparative study of PET images of mice having comparable size xenograft tumors; a) orientation of the mouse during the imaging process; b) image acquired via clinical PET scanner; c) image acquired via preclinical PET scanner (Reprinted from [Kiessling 11]) . . . . .	49
2.3	Comparison of pixelated crystal matrices coupled to a detector surface. The crystal matrix on the left consists of crystals with larger crystal sizes as compared to the crystals of crystal matrix present on right side. . . . .	50
3.1	Impact of scanner diameter 'D' (mm) at the cFOV on (left) detection efficiency via solid angle ( $\Omega$ ), calculated as $\Omega = 4 \sin[\tan^{-1}(A/D)]$ where A denotes the axial length of the scanner ( $= 100$ mm); (right) Spatial resolution (mm) via photon noncolinearity calculated as $\Delta_c = 0.0022D$ . . . . .	55
3.2	Schematic illustration (left) and the image (right) of the photodetector modules used for designing scanner geometries; Top row: a 13 mm x 13 mm MPPC module consisting of 4 x 4 array of 3mm x 3mm channel; Bottom row: a 52 mm x 52 mm multianode PMT module consisting of 16 x 16 channels [Hamamatsu 16] . . . . .	56
3.3	Transverse cross section of PET scanner geometries consisting of 4, 6, 8, 10, 12 modules respectively. . . . .	57
3.4	Left (a): A circular scanner geometry showing parallax error for a LOR passing at a radial distance from the cFOV; Right (b): An octagonal scanner geometry, causing gamma photons to be incident at oblique angles even at the cFOV, resulting degraded spatial resolution at the cFOV. (Reprinted from [Ito 11]) . . . . .	57

3.5	Spatial resolution (mm) estimated at the cFOV for a scanner as a function of crystal size (d) using the equation $R_{sys} = k((d/2)^2 + R_{range}^2 + R_{180^\circ}^2)^{\frac{1}{2}}$ . Where k, the constant to reconstruction is taken to be equal to 1, $R_{range}$ , the factor representing the positron range is taken to be 0.1 mm, $R_{180^\circ}$ , the factor representing the positron range is taken to be equal to $0.0022 \times diameter$ (for diameter = 60 mm) . . . . .	58
3.6	Coincidence detection efficiency ( $\epsilon^2$ ) as a function of crystal depth (x), where $\epsilon = 1 - e^{-\mu x}$ . . . . .	59
3.7	Left: Illustration of a circular geometry scanner, where D, d and x represent the scanner diameter, crystal size and crystal depth respectively. Due to the inability of determining the DOI, $d'$ ( $d' = d\cos\theta + x\sin\theta$ ) represent the apparent width of the crystal (Reprinted from [Cherry 12]). Right: Analytically calculated spatial resolution ( $d'/2$ ) for a source kept at different radial positions and for different crystal depths varying from 5 mm to 10 mm (represented via different colours). . . . .	59
3.8	2D illustration of a module of scanner A. The optical photons (red lines) generated in a crystal is spread by the light guide (white) over several channels of the photodetector array (red) . . . . .	60
3.9	Packing fraction (active area/total area) as a function of crystal size (mm) . . . . .	61
3.10	Photograph of the (Left) LYSO crystal matrix where each crystal is having a size of 0.98 mm x 0.98 mm; (Right) MPPC photodetector array consisting of 2 x 4 modules each having a size of 13 mm x 13 mm. Each MPPC consists in 4 x 4 pixels of 3 x 3 mm with a pitch of 3.2 mm . . . . .	61
3.11	Top: Illustration of two axial modules, each consisting of a crystal matrix (23 x 48 crystals) and a photodetectors array (2 x 4); Bottom: Transverse arrangement of radially elongated crystal matrices for scanner A generated via GATE MC simulation platform. . . . .	62
3.12	Illustration of 2 layer of crystal matrix (in different shades of blue colour) radially coupled to each other with a relative offset of half the crystal size in both the directions. . . . .	63
3.13	The flood histogram pattern for dual layer crystal PET scanner, showing the flood positions corresponding to crystals belonging to different crystals. (Adapted from [Ito 11]) . . . . .	64
3.14	Transverse arrangement of crystals for scanner B generated via GATE MC simulation tool. The scanner consist of two crystal matrices (layer shown in blue - crystal matrix layer from scanner A consisting of 23 x 48 crystals; layer shown in red - second crystal matrix consisting of 22 x 47 crystals) . . . . .	65
3.15	Left: A module consisting of axially elongated crystal matrix readout at both the ends; Right: Illustration of the transverse view of scanner C presenting 5 modules (consist of 8 modules) . . . . .	66
3.16	Transverse arrangement of crystals for scanner C generated via GATE MC simulation platform. Crystals are axially (z- direction) elongated and are arranged in a matrix of 16 x 24 x 1 to form a module. The image presents only one ring consisting of 8 modules. The complete scanner C consists in 5 such rings . . . . .	67
3.17	Illustration of arrangement five axial modules, each consisting of 24 x 16 crystals. The axial arrangement of modules is consist of dead spaces ( = 2.6 mm) due to the presence of photodetectors . . . . .	68
3.18	Schematic illustration of monolithic scintillator crystal coupled to a multianode PMT. (Reprinted from [Ito 11]) . . . . .	69
3.19	Arrangement of crystals of scanner D generated via GATE MC simulation tool. Crystals are arranged in a square geometry and the size of each crystal is 50 mm x 50 mm x 8 mm. The image presents two rings, each consisting of 4 modules. . . . .	69
3.20	Left: Arrangement of crystals in IRIS PET scanner generated via GATE MC simulation platform. Crystals are radially elongated and 27 x 26 crystal makes a module. The image presents two rings, each consisting of 8 modules. Right: image of the IRIS PET scanner installed at our facility . . . . .	70

4.1	Digitizer module consisting of a series of signal processing units to process hits into a single. (Reprinted from [Loudos 07]) . . . . .	77
4.2	Graph showing the comparison of detection efficiency curve obtained for a point source placed at different axial positions along the radial center of the scanner. The blue curve presents the detection efficiency values obtained via MC simulations and the red curve represents the real acquisition values. . . . .	80
4.3	Illustration of pixel driven (left) and ray driven (right) projectors. The mapping is shown only for a detector module of the detector pair. . . . .	84
4.4	Illustration of a three dimensional voxel grid along one axis. The SM elements $a_{ij}$ for $i^{th}$ LOR and $j^{th}$ voxel is computed as the length of the intersection between the $i^{th}$ LOR and $j^{th}$ voxel (Reprinted from [Turbell 01]) . . . . .	84
4.5	Illustration of distance driven projection process (Reprinted from [Manjeshwar 06]) . . . . .	85
4.6	Illustration of different nested levels of PET scanner geometry as read by CASToR. The figure presents a cylindrical PET system consisting of 2 layers and each layer contains 28 rsectors. Each rsector is composed of modules (2 in the transverse direction and 3 in the axial). Each module further contains 2 submodules in the transverse direction and each submodule contains pixelated crystal matrix. Layer 1, (having larger radius) contains a 8 x 8 crystal matrix and layer 0 (with smaller radius) contains a 10 x 10 crystal matrix ) presenting Rsectors, Modules, Submodules, Crystals and Layers. (Reprinted from [Merlin 18]) . . . . .	87
4.7	Command line interface for step 1 illustrating the required input files and commands. CASToR requires input macro file as used in GATE and the output file name in which CASToR's readable format of scanner geometry will be stored . . . . .	87
4.8	Command line interface for step 2 illustrating the required input files and commands. For this step CASToR requires an input data file of root format as given by GATE, the name of the geometry file as generated in step 1, a name to store CASToR readable format output data file, input geometry file as also provided in step 1. The other required parameters are optional and are not used in this thesis . . . . .	88
4.9	Illustration of: (a) an example of the sensitivity profile generated by CASToR; (b) the notation concerning the planes of imaging . . . . .	89
5.1	Characterization of SM generated by performing MC simulations for IRIS PET scanner and for four designed scanners on the basis of non-zero elements. . . . .	96
5.2	Illustration of different radial positions where the source is simulated to estimate the scanner spatial resolution. (NEMA NU-4) . . . . .	98
5.3	Radial spatial resolution (mm) estimated via MC simulations for a point source placed at the cFOV as a function of number of iterations of MLEM algorithm for all the four scanner geometries and also for the IRIS PET scanner . . . . .	99
5.4	Comparison of spatial resolution (mm) in all three direction estimated for all the scanner geometries with a point source placed at several radial distances i.e., 5 mm, 10 mm and 15 mm from the cFOV . . . . .	101
5.5	Illustration of IQP geometry consisting of three parts: (1) Body, consisting of a large fillable cylindrical chamber at the top and a solid part at the bottom; (2) Top cover, supporting two cold regions; (3) Bottom cover, to cover the bottom part of the body (Reprinted from NEMA NU-4 2008). Complete IQP is shown at the bottom as used to estimate the quality of reconstructed image in terms of RC and uniformity (Reprinted from [Anizan 12]) . . . . .	105
5.6	IRIS PET: IQP reconstructed images showing the transverse plane consisting of 5 hot rods and the axial plane showing all three parts of the IQP phantom via pre-computed SM elements (left side) and via CASToR (right side) . . . . .	106

5.7	Scanner A: IQP reconstructed images showing the transverse plane consisting of 5 hot rods and the axial plane showing all three parts of the IQP phantom via pre-computed SM elements (left side) and via CASToR (right side) . . . . .	107
5.8	Scanner B: IQP reconstructed images showing the transverse plane consisting of 5 hot rods and the axial plane showing all three parts of the IQP phantom via pre-computed SM elements (left side) and via CASToR (right side) . . . . .	107
5.9	Scanner C: IQP reconstructed image showing the transverse plane consisting of 5 hot rods and the axial plane showing all three parts of the IQP phantom using CASToR . . . . .	108
5.10	Scanner D: IQP reconstructed image showing the transverse plane consisting of 5 hot rods and the axial plane showing all three parts of the IQP phantom using CASToR . . . . .	108
5.11	Graphs presenting RC values estimated as a function of number of iterations for the images reconstructed using pre-computed SM via MC simulations (left) and for the images reconstructed with CASToR using distance driven projector to compute SM elements on-the-fly (right) for IRIS PET (top row), Scanner A (center row) and for Scanner B (bottom row). . . . .	109
5.12	Graphs presenting RC values estimated as a function of number of iterations for the images reconstructed using CASToR using distance driven projector to compute SM elements on-the-fly for Scanner C (left) and for Scanner D (right) . . . . .	110
5.13	Comparison of RC values estimated from IQP reconstructed images for IRIS PET scanner (blue) and for Scanner A (red) as a function of hot rod diameter . . . . .	111
6.1	Illustration of an octagonal preclinical PET scanner geometry (as used for Scanner A). Two LORs joining crystal pairs (a,b) and (c,d) are drawn. The detection efficiency of the LOR joining crystal (a,b) is less as compared to the LOR joining the crystal pair (c,d). . . . .	115
6.2	Illustration of two crystal pairs (a,b) and (a',b'). The red dotted lines represent the mapping performed by distance driven projector, joining all the surfaces of one crystal center to another. The black line joining the centers, at the surface facing the cFOV, of the two crystals represents the LOR and the dotted line presents the extrapolation of LOR inside the crystal. . . . .	116
6.3	IQP image reconstructed using CASToR for Scanner A for GATE simulated data. Normalization coefficients calculated by analytical approach discussed in section 6.3 are Incorporated in CASToR for the reconstruction process. . . . .	117
6.4	Illustration of two crystal pairs (a,b) and (a',b'). The black line represents the LOR joining the two crystals along with the extrapolation of LOR inside the crystals. The red dotted line are some examples of other LORs joining the same crystal pair. . . . .	117
6.5	The graph presents number of detected coincidence events as a function of ring index (blue curve) for Scanner A. Red line represents the normalized detected events after applying axial block profile correction factor. . . . .	120
6.6	Block profile correction $b_u^{ax}$ factors for IRIS PET scanner; Left: the number of detected coincidence events as a function of ring index. Right: the axial block profile factors as a function of ring index. . . . .	120
6.7	Transverse geometrical factor $g_{uv}^{tr}$ as a function of radial distance from the cFOV estimated for Scanner A. . . . .	121
6.8	IQP images reconstructed using CASToR for Scanner A for GATE simulated data without (left) and with (right) analytical corrections implemented for crystal interference effect. The IQP reconstructed image on the left shows white lines in the uniform region of the phantom which is corrected in the reconstructed image on the right side. . . . .	122



6.9	Illustration of a crystal pair where red dotted lines represent the mapping performed by the distance driven projector in CASToR, joining all four side surfaces of the two crystals from the center of a crystal (i.e., half the crystal length) to the center of another. Blue dotted lines are an example of random selection of starting and end point of the projector. . . . .	122
6.10	Comparison of the radial profile of the uniform region of the IQP reconstructed using CASToR without normalization factors (left) and with normalization factors (right) estimated following component based normalization model. . . . .	123
6.11	Comparison of the line profile passing through the center of figure 6.10. Red curve presents the line profile for the radial profile of the uniform region of IQP without incorporating normalization factors. The blue curve presents the same for the image reconstruction process incorporating the normalization factors. . . . .	124
6.12	Comparison of axial profile of GATE simulated IQP reconstructed using CASToR without (left) and with (right) incorporating the normalization factors. . . . .	124
7.1	Comparison of studied scanners with other commercial and research prototype scanners in terms of spatial resolution and detection efficiency. . . . .	129
7.2	Comparison of the radial profile of the uniform region of the IQP reconstructed using CASToR without and with normalization factors. . . . .	131
B.1	Représentation des performances de systèmes TEP en termes de résolution spatiale, efficacité de détection et coefficients de recouvrement. . . . .	167
B.2	Illustration de la disposition cristalline des quatre géométries du scanner (Scanner A, Scanner B, Scanner C et Scanner D) étudiées dans cette thèse, générée à l'aide du logiciel de simulation GATE. . . . .	169
B.3	Gauche: Disposition des cristaux dans le scanner IRIS générée via la plate-forme de simulation GATE MC. Les cristaux sont radialement allongés et le cristal de 27 x 26 en fait un module. L'image présente deux anneaux composés chacun de 8 modules. Droite: image du scanner IRIS installé dans nos locaux . . . . .	169
B.4	Comparaison des scanners étudiés avec d'autres scanners prototypes commerciaux et de recherche en termes de résolution spatiale et d'efficacité de détection. . . . .	174
B.5	Comparaison du profil radial de la région uniforme du IQP reconstruit en utilisant CASToR sans et avec des facteurs de normalisation. . . . .	177

# Nomenclature

<i>CT</i>	Computed Tomography
<i>APD</i>	Avalanche Photo Detector
<i>CASToR</i>	Customizable and Advanced Software for Tomographic Reconstruction
<i>cFOV</i>	center Field Of View
<i>DOI</i>	Depth Of Interaction
<i>EGS</i>	Electron Gamma Shower
<i>FDG</i>	Fluoro-2-deoxy-D-glucose
<i>fMRI</i>	functional Magnetic Resonance Imaging
<i>FOV</i>	Field Of View
<i>FWHM</i>	Full Width at Half Maximum
<i>FWTM</i>	Full Width at Tenth Maximum
<i>GATE</i>	Geant4 Application for Tomographic Emission
<i>GPS</i>	General Particle Source
<i>IQP</i>	Image Quality Phantom
<i>LM</i>	List Mode
<i>LOR</i>	Line Of Response
<i>LSO : Ce</i>	Cerium doped lutetium oxyorthosilicate
<i>LYSO : Ce</i>	cerium doped lutetium yttrium orthosilicate
<i>MC</i>	Monte Carlo
<i>MCNP</i>	Monte Carlo N-Particle
<i>MFP</i>	Mean Free Path
<i>MLEM</i>	Maximum Likelihood Expectation Maximization
<i>MNN</i>	Mean Nearest Neighbour
<i>MPI</i>	Message Passing Interface
<i>MPPC</i>	Multi Pixel Photon Counter

*MRE* Mean Relative Error

*MRI* Magnetic Resonance Imaging

*NEMA* National Electrical Manufacturers Association

*Open – MP* Open Multi-Processing

*PDF* Probability Distribution Function

*PET* Positron Emission Tomography

*PMMA* Poly Methyl Meth Acrylate

*PMT* PhotoMultiplier Tube

*PSF* Point Spread Function

*PVE* Partial Volume Effect

*RC* Recovery Coefficient

*ROI* Region Of Interest

*SCD* Symmetric Charge Divison

*SD* Sensitive Detector

*SiPM* Silicon PhotoMultiplier

*SM* System Matrix

*SNR* Signal-To-Noise Ratio

*US* Ultra Sound

*VOI* Volume Of Interest

# Introduction

In-vivo imaging has emerged as a powerful tool in therapeutic research and drug discovery. Being non-invasive in nature, it enables us to study and quantify the structure and functionality of different tissues of the living body in normal and diseased conditions. In-vivo imaging techniques can be broadly categorized into anatomical and functional imaging techniques. Anatomy refers to the internal structure of the subject, whereas functional refers to the biochemical processes happening inside the subject. X-ray imaging, Computed Tomography (CT), Ultra Sound (US), Magnetic Resonance Imaging (MRI) are some techniques that provide anatomical information whereas, scintigraphy, functional MRI (fMRI) and nuclear imaging techniques provide the functional information. Behaviour and functionality of living cells differ under diseased situation. For example, cancer cells multiply at a faster rate and are more active as compared to normal cells, or dementia affected brain cells consume less energy and eventually die at a faster rate. As disease progresses, altered behaviour of the cells affect the anatomy of the body. For example, cancer cells aggregate into a mass of cells or in Alzheimer, the brain cells that consume less energy die, causing the brain volume to shrink. These significant changes can be imaged using anatomical imaging techniques. However, functional imaging techniques enable us to visualize the altered behaviour of the cells in the early stages of the disease, even before the anatomy changes. Thus, diagnosis and therapy can be done at the initial stages of the disease.

Positron Emission Tomography (PET) is one of the nuclear imaging techniques, used in the field of oncology, cardiology and neurology as a functional imaging modality. This technique requires biomolecules labeled only with positron emitting radionuclides and an imaging device. FDG, a glucose analogue, is the most commonly used biologically active molecule for early tumor detection. During the last three decades, advancement of PET modality and the development of animal models of human disease have lead to the development of PET technology dedicated to animals. The motivation was to study the animal models, non-destructively, to be able to understand the behaviour of a disease and the response to therapy, in its natural biological state. Initially, all the animal dedicated PET scanners were developed for non human primates for neuroscience and cardiology research purposes. To perform the study on non human primates, the size of the observed region were quite similar to the one investigated for patient. In this context, an improvement of spatial resolution was not crucial. Later, during mid 1980s, mice became the suitable choice for modelling human diseases, because of their faster reproduction cycles, shorter lifespan, similarity with human genes, advancement of molecular biological technology etc. The rat has also become a favourable animal model for neurological research due to its bigger brain size as compared to the mouse. However, considering mice and rats as imaging subject, has driven the necessity to design scanners with improved performance. This is so that we can visualize clearly and quantify accurately the tracer uptake in individual organs and in substructures of small animals (rats and mice).

The first and basic challenge of small animal PET technology comes from the size difference between humans and small animals like rats and mice. In order to perform the same research both in humans and mouse, the human and the small animal scanners should have the same ratio of volumetric spatial resolution to the volume of the scanned object. Thus, the small animal scanners require an improvement in spatial resolution. Another important challenge arises due to the fact that the Signal-To-Noise

(SNR) level depends on the number of detected counts per volumetric resolution element. Due to the improved spatial resolution, the voxel size decreases significantly thereby reducing the number of signals from a voxel. Higher the detected counts, higher the SNR value, thus improvement in detection efficiency plays an important role. Furthermore, in order to maintain the natural biological state of small animals, lesser scales of radioactivity is injected in them compared to in humans. However, lower injected radioactivity results in less event statistics and directly impacts the SNR.

By the mid of 1990s, several research groups started developing small animal PET scanners. This lead to the development of several commercial and research prototype systems. In order to identify the critical organs or target areas in small animals, one of the main objective of the research groups is to develop scanners with high spatial resolution. In 2008, NEMA published a guideline to compare the performance of different preclinical PET scanners following a common set of standards. The performance parameters reported are spatial resolution, detection efficiency, count rate measurement (i.e., scatter fraction, noise equivalent count rate), reconstructed image quality via Recovery Coefficient (RC) and uniformity. RC value, i.e., the ratio of observed to true activity in a reconstructed image, is reported to characterize the scanner spatial resolution.

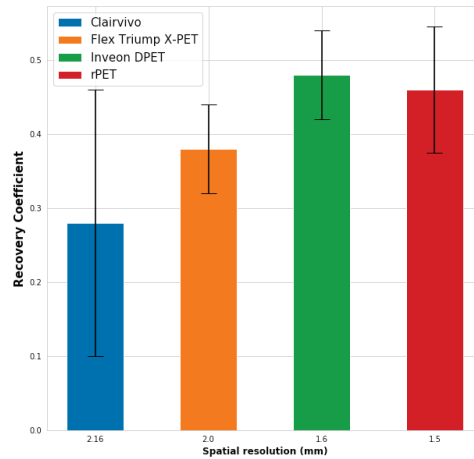


Figure 1 – Comparison of some commercially available scanners (Clairvivo by SHIMADZU, Flex triumph X-PET by Gamma Medica-Ideas, Inveon DPET by Siemens Medical Solutions, rPET-1 by Sedecal, S.A., having a spatial resolution of 2.16 mm, 2.0 mm, 1.6 mm, 1.5 mm respectively at the cFOV) as a function of recovery coefficient estimated following NEMA NU-4 2008 standards

Figure 1 presents a comparison of the RC value of some commercial preclinical PET scanners following NEMA standards. Scanners are arranged from left to right with improving spatial resolution. It is expected that as the spatial resolution improves, the RC value should increase. It can be observed that improving spatial resolution from 2.16 mm to 1.5 mm, the RC value improves as expected. However, the error associated with estimation of RC values is relatively high, consequently making it difficult to correctly quantify the improvement in the RC values.

The error is mainly due to SNR value which further depends on the scanner detection efficiency, reconstruction procedures, scanner geometry etc,. If the amount of improvement in RC value is not greater than the error in its estimation then we cannot correctly quantify the improvement in RC value due to the improvement in spatial resolution. Thus it should be noted that improving spatial resolution alone can compromise other parameters such as detection efficiency and does not result in an improved image quality.

Figure 2 presents a graph showing various commercial and prototype research scanners as a function of their detection efficiency and spatial resolution. It can be observed that as the spatial resolution improves to sub-millimeter level, the detection efficiency is being compromised. Scanners like Quad-Hidac, Prototype scanner by Yamamoto et al have even reached a spatial resolution less than and close to 1 mm with their detection efficiency going down close to 1%.

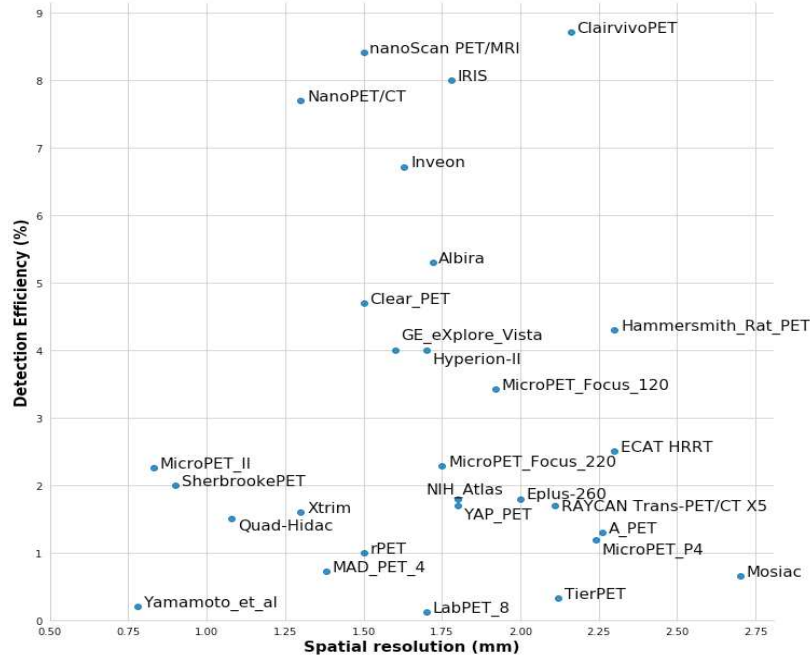


Figure 2 – Different commercially available and prototype research PET scanners

The motivation of this thesis work comes from the above two observations (figure 1 and figure 2). In this thesis one of the major objectives is to study the impact of scanner geometry and its performance parameters such as spatial resolution and detection efficiency on the overall reconstructed image quality. In order to study the impact of scanner geometry, we simulate four scanners developed on the basis of different geometrical approaches. The difference in geometrical approach comes from employing pixelated crystal matrix (enables 2D detection of gamma interaction), stacks of pixelated crystal matrix (enables acquiring information higher than 2D detection) and continuous crystal slab (enables 3D detection). The four scanner geometries are selected on the basis of previous research work performed in our lab. The image quality is characterized in terms of RC value, the error associated with its estimation and uniformity. Our work is mainly based on Monte-Carlo (MC) simulations using the GATE platform. The data are generated following the protocol proposed by the NEMA NU-4 2008 standards. The images are reconstructed using the CASToR platform. CASToR is an open source image reconstruction software. MLEM algorithm is used in the scope of my thesis work to reconstruct all the images. CASToR software makes use of analytical projectors to perform the image reconstruction. Second objective of this thesis is to compare the reconstruction process and the reconstructed image quality when the System Matrix (SM) elements are computed via MC simulations (and are stored on the disk to reconstruct images) and when the elements are computed on-the-fly with the help of projectors (as computed in CASToR).

The thesis manuscript is composed of six chapters. The introduction to all the chapters is as given below:

1. **Chapter 1: Basics of PET imaging:** It provides an introduction to the basic concepts of PET imaging such as the physical processes (positron decay, annihilation etc.,) involved, the emission and detection of gamma photons, the gamma detectors, data acquisition approach and image reconstruction process. Figure of merits (spatial resolution and detection efficiency) are also discussed to characterize the PET scanner performance.
2. **Chapter 2: Small animal imaging PET scanners:** In this chapter, we provide a short introduction to small animal imaging. Some of the major challenges in the field of preclinical PET imaging are also discussed. We also provide examples of commercially available and research prototype preclinical PET scanners.
3. **Chapter 3: Scanner geometries:** In this chapter, we discuss four different scanner geometries studied in this thesis. All the details such as scanners axial Field-Of-View (FOV), transaxial FOV, crystal material, crystal size, photodetectors etc are discussed.
4. **Chapter 4: Simulation and Image reconstruction approaches:** This chapter introduces the general methodology we used to investigate the impact of scanner properties on image quality. We mainly describe the MC simulation, reconstruction platform and our data analysis approach. We also highlight the requirement for normalization corrections and different techniques to perform the normalization process.
5. **Chapter 5: Performance measurement of the scanners:** This chapter presents all the MC simulations performed in the thesis following the standard approach as given in NEMA NU-4 2008 standards. The estimated values of spatial resolution and detection efficiency for all the four scanners and for the state-of-art IRIS PET scanner are reported. We also report the impact of scanners performance on the overall image quality using the Image Quality Phantom (IQP). A comparison is also studied for images reconstructed using MLEM algorithm, where SM elements are computed using two different approaches.
6. **Chapter 6: Normalization:** In this chapter, we highlight the normalization procedure and the role of this correction on the overall image quality. We discuss the different possible normalization approaches to handle the variation in LOR detection efficiency in the field of view. We also report the impact of normalization correction factors on the reconstructed image quality.

# Chapter 1

## Basics of PET imaging

### Contents

<b>1.1</b>	<b>Introduction</b>	<b>23</b>
<b>1.2</b>	<b>Physical process</b>	<b>24</b>
1.2.1	Positron decay	24
1.2.2	Annihilation	25
1.2.3	Positron range	26
1.2.4	Photon noncolinearity	27
1.2.5	Types of coincidence events	28
<b>1.3</b>	<b>511 keV gamma photon detectors for PET imaging</b>	<b>28</b>
1.3.1	Interaction of 511 keV gamma photon with matter	29
1.3.2	Scintillation process and detectors	31
1.3.3	Photodetectors	33
<b>1.4</b>	<b>Data acquisition and Image reconstruction</b>	<b>38</b>
1.4.1	Image reconstruction	39
<b>1.5</b>	<b>Figure of Merits</b>	<b>42</b>
1.5.1	Detection efficiency ( $\eta$ )	42
1.5.2	Spatial resolution	43
<b>1.6</b>	<b>Conclusion</b>	<b>45</b>

### 1.1 Introduction

Positron Emission Tomography (PET) is mainly based on the principle of radionuclide imaging. It makes use of positron emission process as a probe for certain disease situations (such as cancer [Rohren 04, Hoh 93, Conti 91]) or biochemical processes [Nader 06] occurring inside the living subject. The pharmaceuticals used for PET imaging are labeled with positron emitting radioisotopes that decay via positron emission (section 1.2.1). There are several positron emitting radioisotopes that have been used for PET imaging. Carbon-11 ( $^{11}\text{C}$ ), Nitrogen-13 ( $^{13}\text{N}$ ), Oxygen-15 ( $^{15}\text{O}$ ), Fluorine-18 ( $^{18}\text{F}$ ), Potassium-38 ( $^{38}\text{K}$ ), Copper-62 ( $^{62}\text{Cu}$ ), Copper-64 ( $^{64}\text{Cu}$ ), Zirconium-89 ( $^{89}\text{Zr}$ ) etc., are some examples of positron emitting radioisotopes. With a half-life of approximately two hours (109.7 minutes),  $^{18}\text{F}$  has been the main radioisotope used in pharmaceutical radio labeling these last decades.

Benefiting from the suitable properties of  $^{18}\text{F}$  [Le Bars 06, Jacobson 14], 2-[ $^{18}\text{F}$ ] fluoro-2-deoxy-D-glucose (FDG) has been proven to be significant in the initial diagnosis [Oyen 04], detection of recurrent tumor [Schmid 03, Hicks 01] and evaluation of response to therapy [Hicks 09]. FDG is



a glucose analogue in which a hydroxyl group (-OH) (present at C-2 position) is substituted by a radioactive isotope  $^{18}\text{F}$  as shown in figure 1.1.

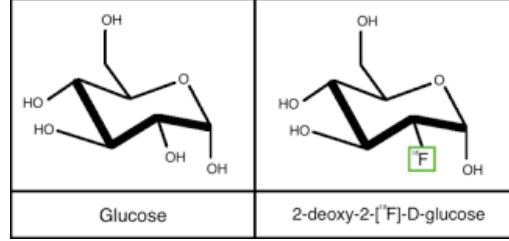


Figure 1.1 – Glucose and FDG molecule

After injection, FDG being a glucose analogue, is transported from the blood, via glucose transporters (predominantly GLUT-1) to the different cells. The uptake of FDG is higher in the cells consuming more glucose, such as brain, kidney and cancer cells. In the cell, FDG is phosphorylated (a process of attachment of a phosphate group) by a group of enzymes called hexokinase (example HK 2) to form FDG - 6 - phosphate [Castell 08]. In contrast to glucose-6-phosphate as shown in figure 1.2, FDG-6-phosphate cannot be further metabolized along the glycolytic pathway and gets accumulated within the cells in direct proportion to their metabolic activity [Rudd 10].

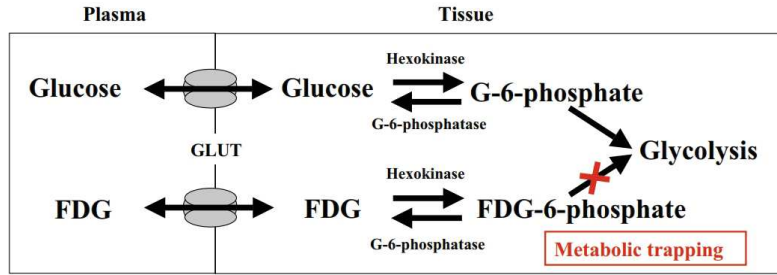


Figure 1.2 – Metabolic trapping of fluorodeoxyglucose (FDG) in the cell. (Reprinted from [Rudd 10])

Being a positron emitting radiotracer, FDG decays by emitting positrons, which interact in the body. The interaction process is described in section 1.2.2 and it results in the emission of two gamma photons of 511 keV energy, which are eventually detected by the PET scanners. When a tissue (other than normal tissues requiring glucose) absorbs a lot of glucose (or FDG), it indicates higher metabolism. Figure 1.3 illustrates the bio-distribution of FDG in different normal and malignant tissues of human body.

## 1.2 Physical process

### 1.2.1 Positron decay

When the positron emitting radiotracer decays, a positron is emitted. A positron is a particle which has the same mass but opposite electric charge as of the electron and thus it has a very short lifetime in electron rich material such as tissue. Positron decay is denoted as:

$$X_Z^A \rightarrow Y_{Z-1}^A + \beta^+ + \nu_e \quad (1.1)$$

where  $X_Z^A$  denotes the parent nuclide with mass  $A$  and atomic number  $Z$ , and  $Y_{Z-1}^A$  denotes the daughter nuclide. The decay products include a daughter nuclide, a positron ( $\beta^+$ ) and a neutrino ( $\nu_e$ )

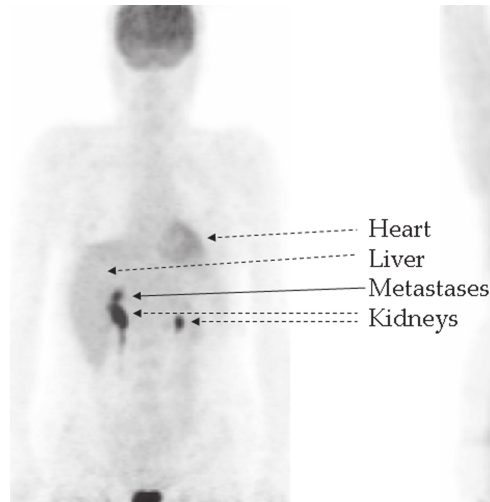


Figure 1.3 – PET scan showing a small metastasis in the liver, just above the kidney. (Reprinted from [Fine 12])

and the energy released in decay is shared between these particles. Positrons are thus emitted with a range of kinetic energies, from zero upto a maximum endpoint energy  $E_{max}$ , which depends on each radionuclide. Figure 1.4 shows the kinetic energy distribution with which positrons are emitted from  $^{18}\text{F}$  radionuclide, with a maximum kinetic energy of 0.635 MeV.

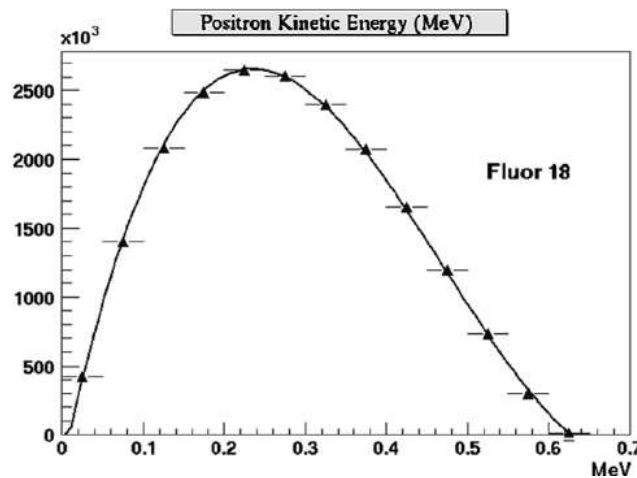


Figure 1.4 – Positron emission spectrum for F-18 radionuclide. (Reprinted from [Jan 05a])

### 1.2.2 Annihilation

The emitted  $\beta^+$  rapidly loses its kinetic energy due to its inelastic interactions with atomic electrons in the tissue. When its energy is dissipated (usually within a range of  $10^{-1}$  to  $10^{-2}$  cm, depending on its energy), the  $\beta^+$  interacts with electron. The positron interaction leads either to  $\beta^+ - e^-$  annihilation (as a result of matter-anti-matter encounter) or to the formation of a hydrogen like state known as positronium (a hydrogen analogue, where the proton that forms the nucleus in a hydrogen atom is substituted via  $\beta^+$  [Phelps 06]). The positronium state lasts for about  $10^{-10}$  seconds and eventually

leads to annihilation. In the annihilation process, the mass of  $\beta^+$  and  $e^-$  is converted to electromagnetic energy. The energy released can be computed using Einstein's mass-energy equivalence given as:

$$E = mc^2 = m_e c^2 + m_{\beta} c^2 \quad (1.2)$$

where  $m_e$  and  $m_{\beta}$  represents the mass of electron and positron respectively and  $c$  is the speed of light. Substituting the values for  $m_e = m_{\beta} = 9.1 \times 10^{-31}$  kg in equation 1.2 and using the conversion between eV and joules i.e.,  $1\text{eV} = 1.6 \times 10^{-19}\text{J}$ , the energy released can be shown to be 1.022 MeV. As the  $\beta^+$  and  $e^-$  are almost at rest when annihilation occurred, the net momentum is close to zero. Because of the momentum as well as energy conservation principle, two photons are emitted simultaneously, in a direction opposite to each other with an energy equal to half of the total energy released i.e., 511 keV. Annihilation which results in more than two photons is also possible, but the probability of such process is very low (<1% probability) [Phelps 06]. The emitted gamma photons are detected by a pair of detectors defining a Line Of Response (LOR), as represented in figure 1.5 with green line.

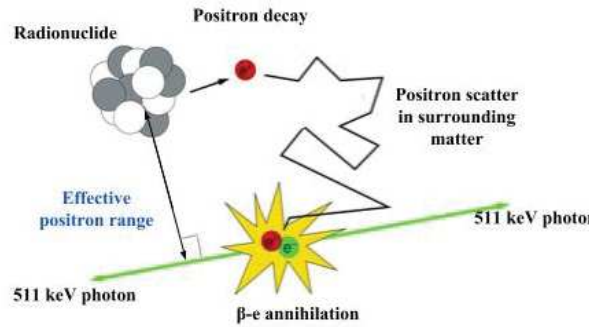


Figure 1.5 – Positron emission followed by positron scatter in the surrounding medium and subsequent positron-electron annihilation producing two 511 keV gamma photons emitted at  $180^\circ$ . (Adapted from [Phelps 06])

### 1.2.3 Positron range

For precise localization of radiotracer uptake in the subject, it is important to determine, as accurately as possible, the position of the positron emission. However, the PET scanners record an event by detecting two gamma photons in coincidence along a LOR, which in turn indicates the position of the  $\beta^+ - e^-$  annihilation. As shown in figure 1.5, the position of the positron emission is different from the position where it annihilates and the shortest distance between the LOR and the  $\beta^+$  emission site is known as the positron range. Since  $\beta^+ - e^-$  annihilation process is isotropic in nature with respect to the positron emission site, their distribution can be modeled by cusp-like function as shown in figure 1.6 for positrons emitted from  $^{18}\text{F}$ . The measured positron range is reported to be 0.10 mm Full Width at Half Maximum (FWHM) in water [Levin 99], accounting for uncertainty in the precise localization of the radiotracer uptake.

Positron range limits the ultimate spatial resolution achievable by PET scanners. To achieve PET scans with good possible spatial resolution for a given scanner geometry, it is preferred to use radionuclides with relatively small positron range. The positron range increases with the energy with which the positron is emitted and it also depends on the electron density of the medium. Positrons emitted from  $^{18}\text{F}$  have the shortest positron range as compared to other positron emitters such as  $^{11}\text{C}$ ,  $^{13}\text{N}$ ,  $^{15}\text{O}$  and thus  $^{18}\text{F}$  is a preferred radionuclide for PET imaging. Positron-emitting radionuclides along with their characteristics are listed in Table 1.1.

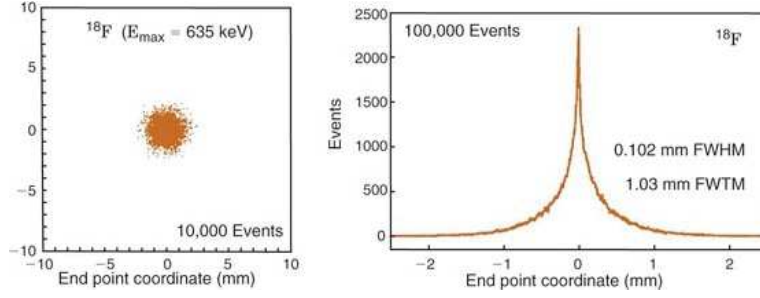


Figure 1.6 – Left: Distribution of positron annihilation sites in water for positrons emitted from F-18 at the center (0,0) of a 2D histogram; Right: Profile through the distribution shown on left, measuring FWHM and FWTM (Full Width at Tenth Maximum) of the distribution. (Reprinted from [Levin 99])

Radionuclide	Half-Life (min)	Emax [MeV]	Eaverage (MeV)	FWHM in water (mm)
C-11	20.39	0.959	0.385	0.19
N-13	9.97	1.197	0.491	0.28
O-15	2.04	1.738	0.735	0.50
F-18	109.77	0.635	0.242	0.10
Zr-89	4704.00	0.902	0.402	0.49

Table 1.1 – Common positron-emitting nuclides. The Full Width at Half Maximum (FWHM) of point source profiles in water (which is a major component of biological tissues) are results of MC simulations where positron-emitting point sources are placed in water [Levin 99, Le Loirec 07, Jødal 14].

#### 1.2.4 Photon noncolinearity

In addition to positron range, there is one more factor that can further affect the precise localization of radio-tracer uptake in the subject. Since it is assumed that both the electron and positron are at rest during annihilation, the momentum conservation imposes that the two resulting gamma photons would be emitted back-to-back, namely at  $180^\circ$  with respect to each other as shown via green line in figure 1.7. However, it may also be the case that the positron has some residual kinetic energy during annihilation which, in turn, will result in the emission of two gamma photons not exactly at  $180^\circ$ . This non-colinear emission of the two gamma photons is known as photon noncolinearity. Once the two non-colinear photons are detected, PET scanner assumes that the emission occurred exactly back-to-back, resulting in some error in locating the LOR as shown in the dotted line in figure 1.7. The distribution of angles has been modeled as a Gaussian distribution with  $180^\circ$  as mean and  $0.25^\circ$  FWHM [Phelps 06]. Photon noncolinearity can be estimated by the following equation:

$$R_{180^\circ} = 0.0022D \quad (1.3)$$

where  $D$  is the diameter of the PET scanner and thus it can be noted that the error increases linearly with the diameter of the PET scanner.

Positron range and photon noncolinearity are the two phenomenons relating to the basic of positron emission and annihilation process, that adds uncertainties in the determination of precise localization of radiotracer uptake in the subject or in other words, that degrades the spatial resolution of the PET scanners.

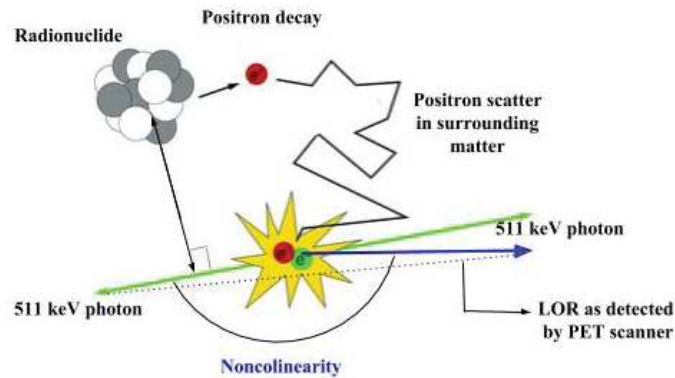


Figure 1.7 – Photon noncolinearity process resulting in emission of two gamma photons (one in blue and the other in green line) emitted at an angle other than  $180^\circ$ . Green line represents two gamma photons emitted at  $180^\circ$  and dotted line represents the LOR as detected by the PET scanner due to noncolinearity. (Adapted from [Phelps 06])

### 1.2.5 Types of coincidence events

The two gamma photons detected in coincidence results in an event and these events can be categorized as defined below:

1. True coincidence events: When the two gamma photons emitted in opposite direction detected in respective detector elements without any prior scattering or energy loss, are counted as true coincidence event as shown in the figure 1.8A.
2. Scattered coincidence events: If one or both gamma photons interact with the imaging object or within the detector, then the event is known as scattered event. These kind of events are responsible for mis-positioning of the event as shown in figure 1.8B.
3. Random coincidence events: When photons generated via two different positrons, are detected in the same coincidence window, this leads to the random coincidence event as shown in figure 1.8C. Such events create background noise and degrade the contrast in the reconstructed image.
4. Multiple coincidence events: When more than two gamma photons are detected in a given coincidence window, such events are known as multiple coincidence events and these events are usually discarded as can be seen in figure 1.8D.

The total number of coincidence events detected by the PET scanner are referred to as prompt coincidences and it consists of all the above mentioned types of coincidences. Other than the true coincidence events, all the other types of events have a degrading impact on the estimation of true radioactivity distribution and thus it is important to estimate what fraction of the measured prompt coincidences arise from scattered and accidental coincidences for each of the LORs [Tarantola 03].

## 1.3 511 keV gamma photon detectors for PET imaging

A PET scanner is composed of a set of detectors surrounding the subject to be imaged. Several different configurations of detectors have been used for commercial PET scanners. These include detectors mounted on a rotating ring configuration (Figure 1.9a), detectors arranged in a circular ring (Figure 1.9b), or detectors arranged in a polygonal ring (Figure 1.9c).

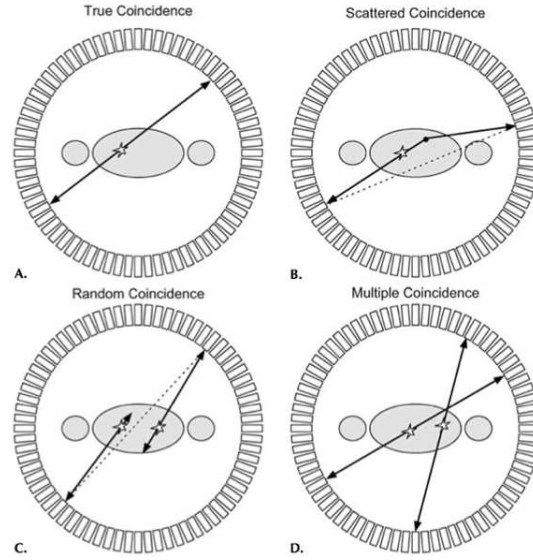


Figure 1.8 – Types of coincidence events detected by PET scanner: A. True coincidence event, B. Scattered coincidence event, C. Random coincidence event, D. Multiple coincidence event. (Reprinted from [Phelps 06])

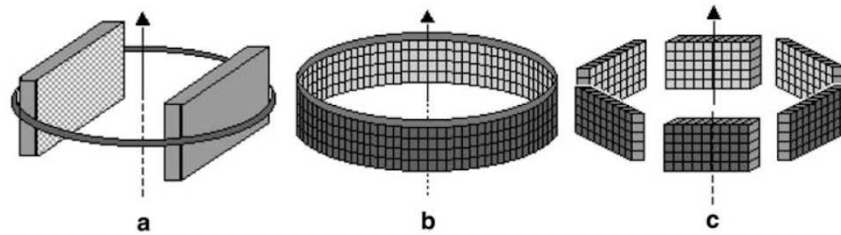


Figure 1.9 – Different configurations of PET detectors. a) rotating ring configuration; b) detectors arranged in a circular ring; c) detectors arranged in a polygonal ring configuration (Reprinted from [Humm 03])

For gamma photons detection, different types of detectors can be used such as Gas filled detectors (ionization chambers, G.M. counters), Scintillation detectors or Semiconductor detectors [Knoll 10]. However, for PET imaging, scintillation detectors are generally used and these detectors are made up of inorganic scintillator materials. Before going further, it is important to understand how the 511 keV gamma photon interacts with the surrounding tissue and with the detector material.

### 1.3.1 Interaction of 511 keV gamma photon with matter

As the gamma photon traverses through the matter, it interacts with the atoms in the matter and the type of interaction depends on the energy of the gamma photon and atomic number ( $Z$ ) of the matter. The 511 keV gamma photon interaction mechanisms involve Photoelectric absorption, Compton and Rayleigh scattering. These mechanisms result in either scattering of gamma photon at significant angles (with and without loss of energy) or in complete disappearance of gamma photons. All these mechanisms are discussed below. Photoelectric absorption and Compton scattering are the major interaction mechanisms for 511 keV gamma photons.

## Photoelectric absorption

This process results in complete disappearance of the gamma photon. In this process, a gamma photon interacts with an atomic electron as shown in figure 1.10B and is completely absorbed by transferring its energy to that electron. This leads to the ejection of that electron from the atom. The energy with which the electron is emitted ( $E$ ) is given as the kinetic energy ( $h\nu$ ) of the incident gamma photon minus the binding energy ( $E_b$ ) of the electron:

$$E = h\nu - E_b \quad (1.4)$$

with  $h$  is the Planck's constant. The probability of photoelectric absorption per unit distance depends on the atomic number ( $Z$ ) of the medium and for 511 keV gamma photon the probability of photoelectric absorption is proportional to  $Z^n$  with  $n$  being equal to 3 or 4 [Phelps 06, Wernick 04].

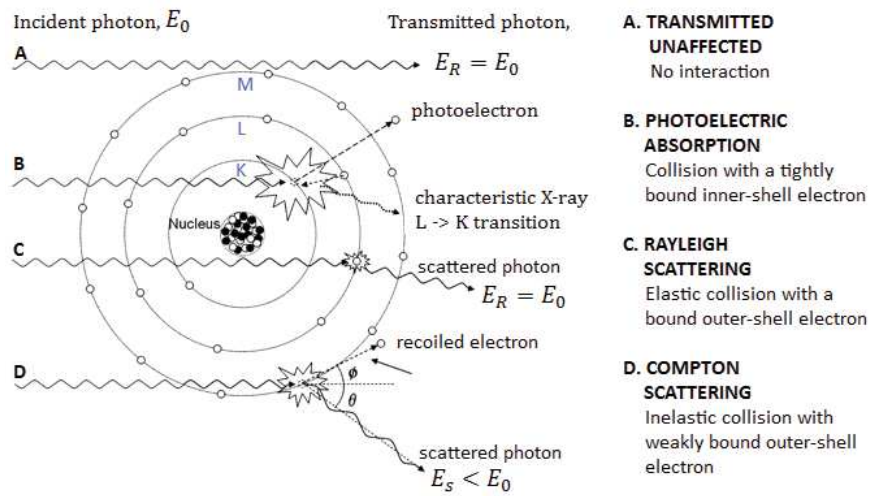


Figure 1.10 – Types of interaction of 511 keV gamma photons; B. Photoelectric absorption (generating a photoelectron); C. Rayleigh scattering (elastic collision with a bound outer shell electron); D. Compton scattering (Inelastic collision resulting in a scattered photon and recoiled electron) (Reprinted from [O’Hea 15])

## Rayleigh scattering

When elastic scattering occurs between the gamma photon and an atomic electron, the gamma photon is scattered without ionization or any energy loss in excitation of the internal states of the constituents of the material. This process is known as Rayleigh scattering, as shown in the figure 1.10C.

## Compton scattering

In Compton scattering, the incident gamma photon interacts with free or loosely bound electron present in the medium as shown in figure 1.10D. The interaction causes the electron to recoil, and a new photon emerges at an angle  $\theta$  from the photon’s incoming path. With the help of the equation of conservation of energy and conservation of momentum, the relation between its scattering angle ( $\theta$ ), original energy( $E$ ) and the energy of gamma photon after scattering ( $E'$ ) is given below:

$$E' = \frac{mc^2}{(mc^2/E) + 1 - \cos(\theta)} \quad (1.5)$$



where  $m$  is the mass of the electron and  $c$  is the speed of light. The energy transferred to an electron can be deduced as  $E - E'$ . The energy transferred to the electron varies from zero (when  $\theta = 0$ ) to a value when  $\theta = \pi$ , forming a continuum of energies. The probability of Compton scattering per unit length of the absorbing medium is linearly proportional to the atomic number ( $Z$ ) of the medium [Wernick 04].

The interaction of 511 keV gamma photon resulting in its absorption or scattering within the matter can be given as:

$$I = I_0 e^{-\mu x} \quad (1.6)$$

where  $I_0$  is the initial flux of 511 keV gamma photon incident on the medium of thickness  $x$  and  $I$  is the flux that passes through the medium without interaction.  $\mu$  is the linear attenuation coefficient and is defined as the probability per unit distance that an interaction will occur. To account for photoelectric absorption, rayleigh scattering and compton scattering, the total linear attenuation coefficient is given as:

$$\mu = \mu_{photoelectric} + \mu_{rayleigh} + \mu_{compton} \quad (1.7)$$

The 511 keV gamma photons, based on the above discussed interaction mechanisms, can interact with the body tissue as well as with the detector material. In order to be detected by the gamma detectors, the 511 keV gamma photons must pass through the body tissue. However, Compton scattering is the dominant interaction mechanism of 511 keV gamma photons in the tissue [Phelps 06]. Scattering redirects the 511 keV gamma photons from their original trajectory and if the photons still escape the body, the scattered gamma photons will result in incorrectly located LOR. This also results in the scattered events.

Both scatter and photoelectric interactions lead to the emission of an energetic electron, which further interacts in the detector material (scintillators) and leads to the production of scintillation light as discussed in the next section.

### 1.3.2 Scintillation process and detectors

Scintillator materials can be organic (liquid and plastic based) or inorganic (crystal based). Inorganic scintillators have the best light output and linearity (i.e., emitted light is proportional to the energy deposited by the radiation in the material) whereas organic scintillators are generally faster but have low light output. The high value of  $Z$  and density of inorganic scintillators make them suitable for gamma photon detection [Humm 03] and on the other side, organic scintillators are suitable for beta and neutron detection. Upon absorption of radiation, inorganic scintillators emit visible (scintillation) light proportional to the energy deposited by the radiation in the scintillator material, as described in the next section. This linearity between light output and energy deposited is an important property that further makes the inorganic scintillator a suitable detector for gamma detection.

#### Scintillation process

It can be explained on the basis of energy band model. In materials like insulators and semiconductors, electrons have available discrete bands of energy. The lower band, known as valence band, represents electrons which are essentially bound at the lattice sites, whereas, conduction band consists of electrons having sufficient energy to be free to migrate throughout the crystal. In between the two bands, there exists an intermediate band of energies, known as forbidden energy gap or band gap as shown in figure 1.11. In inorganic scintillators the conduction band is completely empty at room temperature and since they have a forbidden energy gap of around 4 to 6 eV, no electron can reach the conduction band from the valence band due to thermal excitation [Humm 03]. Thus, the electrons present in the valence



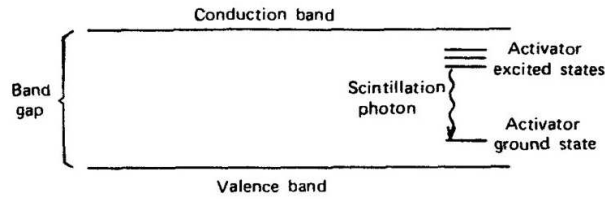


Figure 1.11 – Illustration of energy bands and activated acceptor site (energy states in band gap) in a doped inorganic scintillator. (Reprinted from [Knoll 10])

band require a minimum amount of energy to cross the forbidden band gap and reach the conduction band and this minimum amount of energy is known as activation energy.

The energetic electron created via 511 keV gamma interaction, elevates the electron located in the valence band to the conduction band, leaving behind holes in the valence band. This process depends on the kinetic energy of the electron generated in 511 keV gamma photon interaction and the number of electron-holes produced is given by the kinetic energy of the electron divided by the activation energy of the scintillator. These elevated electrons fall back onto the less energetic states, releasing the excess energy in the form of scintillation light as shown in figure 1.11. In pure crystals, the elevated electrons fall back onto the holes present in the valence band releasing energy, in the form of scintillation photons, equal to the forbidden band gap energy. The energy of the resulting photons is higher than the energy of the photons in the visible range. This emitted energy, being equal to the energy gap would be reabsorbed in the crystal itself. Thus, to enhance the probability of visible photon emission (instead of re-absorption) during the de-excitation process, small amounts of impurities are commonly added to pure inorganic scintillators, which represents the activated acceptor sites. These activated acceptor sites represent energy states created within the forbidden energy gap, through which an electron can de-excite back to the valence band, emitting energy in the form of photons. Since the energy is less than that of the full forbidden energy band gap, thus the resulting photons would lie in the visible range and would be able to escape the crystal. These emitted visible photons can be detected by photodetectors (section 1.3.3). In order to summarize the scintillation process, the 511 keV gamma photon interacts and deposits its energy within the scintillator crystal, which results in isotropic emission of optical photons, proportional to the deposited energy, which are further detected via photodetectors.

### Scintillation crystal properties for 511 keV gamma photon detection

The selection of the scintillator crystal is an important parameter for PET scanners performance. Scintillators can be characterized on the basis of several factors such as higher interaction cross-section, stopping power, light yield, the time over which the light is produced, hygroscopic properties [Melcher 00] etc,. These requirements and their purpose are summarized in table 1.2. The choice of scintillator crystal is an end result from the trade-off of several parameters as mentioned in table 1.2 and of its cost. At present, the most commonly used scintillator in commercial PET scanners is Cerium doped lutetium oxyorthosilicate (LSO:Ce) and cerium doped lutetium yttrium orthosilicate (LYSO:Ce). These two crystals are suitable candidates offering a good combination of properties for PET of any scintillation known today, such as high density and high atomic number for good gamma ray detection efficiency, high light output, non hygroscopic nature etc. LSO has been used in a high resolution brain PET scanners [Schmand 98], whereas LYSO has been used in several research prototype scanners (discussed in chapter 2).

Scintillator property	Purpose	LSO(Ce)	BGO	NaI(Tl)	LYSO(Ce)
High density (g/cc)	To stop a large fraction of the incident 511 keV gamma photons	7.40	7.13	3.67	7.10
High atomic number (Z)	Increases the number of photoelectric occurrences with respect to Compton scattering	65	76	51	60
High light output (photons / keV)	Helps to determine the location of the interaction and helps in direct energy measurement	28	8	38	31
High linear attenuation at 511 keV ( $cm^{-1}$ )	To maximize the probability per unit distance of an interaction	0.87	0.92	0.34	0.86
Hygroscopic nature	To simplify packaging	No	No	Yes	No

Table 1.2 – Comparison of LSO, BGO, NaI(Tl), LYSO scintillator crystals on the basis of different properties required for 511 keV gamma ray detection

### 1.3.3 Photodetectors

The use of scintillation crystals for gamma ray detection is incomplete without a photodetector to convert the scintillation or light photons into an electronic signal as shown in figure 1.12. An ideal photodetector should have the property of detecting extremely weak light signal down to a single optical photon and, secondly it should produce an output electronic signal proportional to the incident light intensity.

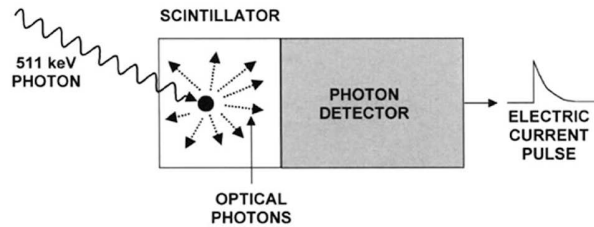


Figure 1.12 – A schematic representation of scintillator detector. (Reprinted from [Phelps 06])

Photo-Multiplier Tube (PMT) is an example of commonly used photodetector whereas the rapid development of solid-state detectors [Renker 09] has provided some promising candidates such as Avalanche Photodiodes (APDs) and Silicon PhotoMultipliers (SiPMs). The following section provides a brief introduction to PMT and other photodetectors along with their advantages and limitations.

#### Photo-Multiplier Tubes (PMT)

A simplified schematic of a PMT is shown in figure 1.13 and it contains two major components as given below:

1. A photosensitive layer, known as photocathode, that ejects electron when optical photon strikes onto their surface following photoelectric effect.

2. Electron multiplier structure, contains dynodes kept at positive voltage relative to the previous one. Electrons liberated from the photocathode are accelerated towards the first dynode, thus gain sufficient kinetic energy to eject secondary electrons, on the order of 3 to 4. Same process occurs between subsequent dynodes, causing an avalanche as can be seen from figure 1.13.

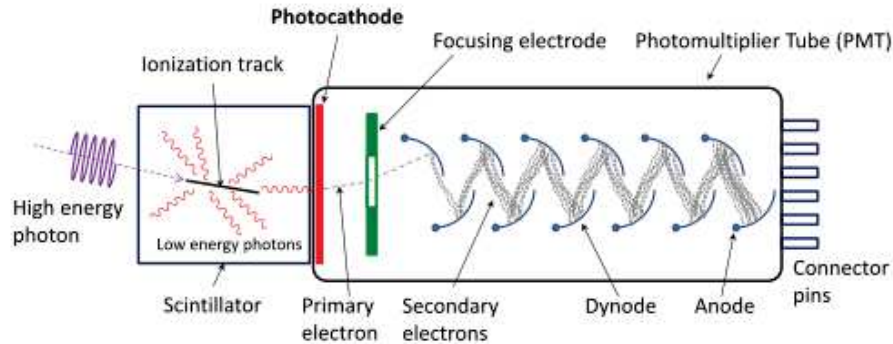


Figure 1.13 – A schematic representation of PET detector, consisting of a scintillator crystal coupled to PMT. An incoming photon deposits its energy in the scintillator, generating low energy (optical photons) shown in red color, which further strikes at the surface of photocathode, liberating a primary electron, that falls on a dynode and generates secondary electrons (Reprinted from [Commons 03])

A gain (as much as  $10^6$  to  $10^8$ ) usually is achieved with 9 to 12 dynodes. Finally the electrons reach the anode and produce a relatively large pulse of current proportional to the amount of incoming optical photons. In this manner, PMT can detect and amplify incoming very weak light signals and generate an electric pulse proportional to the incoming light intensity. A detailed description on the working of PMT is given in [Knoll 10].

One of the several limitations of PMT includes its requirement of high voltage supply, which has to be very stable since the multiplication factor is sensitive to change in the dynode potential. Another limitation is due to the bulkiness of PMT. Most importantly, PMTs are sensitive to the magnetic field limiting the use of PET scanners in PET - MRI multimodal imaging. Furthermore, in the conventional PMT the spatial information of the intensity is lost and summed by one large anode that receives all the secondary electrons. Casey and Nutt in 1986 [Casey 86a], introduced a solution to gather the spatial information and this solution is the “block detector”, as shown in figure 1.14.

### Block detectors

In block detector design, a scintillator crystal block is segmented into an array of small detector elements as shown in figure 1.14 [Townsend 04]. The saw cuts creating the segmented smaller crystals are filled with a reflective material (the purpose of which is to optically isolate individual elements within the block). The scintillator crystal matrix is attached to 4 PMTs (PMT A, PMT B, PMT C, PMT D) and thus the optical photons generated in each crystal are shared among these PMTs. The depth of the saw cuts is empirically determined in order to share scintillation light in a linear fashion among four PMTs. The scintillation light is shared as a function of the position of the 511 keV gamma photon interaction within the block.

For a gamma photon interacting in the corner detector element, because of the deep cuts all the scintillation light photons that are produced from the interaction end up in the PMT sitting directly underneath that element. Similarly, an event interacting towards the middle of the block, where the cuts are shallower, results in a roughly equal spread of scintillation light among all four PMTs. If the

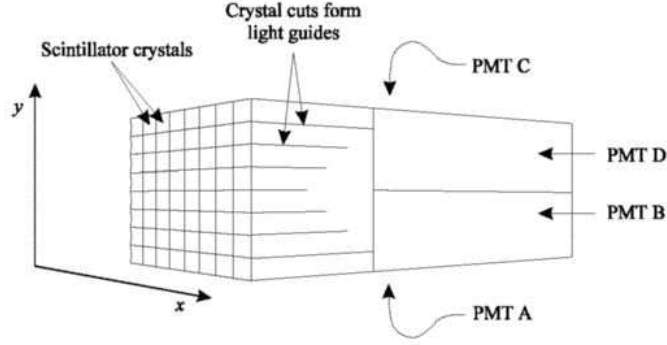


Figure 1.14 – Schematic representation of a scintillator block segmented into an 8x8 array, coupled to PMT block detector. (Reprinted from [Phelps 06])

signal from the four PMTs are  $S_A$ ,  $S_B$ ,  $S_C$  and  $S_D$  respectively, then the (x,y) location of each 511 keV gamma photon interaction within the segmented scintillator block, is determined by the simple ratio given as:

$$x = \frac{S_A + S_B - S_C - S_D}{T} \quad (1.8)$$

$$y = \frac{S_A + S_C - S_B - S_D}{T} \quad (1.9)$$

where T is the summed signal  $S_A + S_B + S_C + S_D$ . The depth of the cuts and with the sufficient scintillation light, the interaction of the incident gamma photon in each segmented crystal element will produce a unique distribution of scintillation light, as can be seen in figure 1.15. Figure 1.15 is a result of an experiment where the surface of a block detector is uniformly irradiated with 511 keV gamma photons.

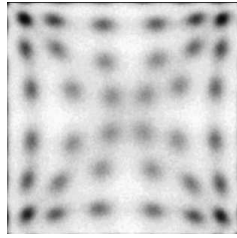


Figure 1.15 – Image obtained as a result of flood irradiating the front surface of a block detector with 511 keV photons (Reprinted from [Phelps 06])

The performance, in terms of intrinsic spatial resolution (discussed in section 1.5.2), of PET scanners is, however, limited by the PMT block detector design. To achieve a higher spatial resolution, segmentation of scintillator crystals to a higher level is required (section 1.5.2). Multi-anode PMT is a solution to resolve the segmentation of scintillator crystals as discussed in the next section.

### Multi-anode PMT

One of the major requirements of photodetectors is to use an electron multiplying structure. It maintains spatial separation between multiplied electron clouds originating from photo-electrons generated at different locations on the photo-cathode. Multi-anode PMT is one example of such a photodetector.

In multi-anode PMT as shown in figure 1.16, the PMT structure is segmented into multiple independent PMT elements. These elements are typically arranged on a square grid. Each PMT element has its own anode and each anode has its own output connection to a pin at the base of the PMT housing. This design of the electron-multiplication incorporating multi-anodes enables the spatial integrity of photo-electrons, which comes from the particular location of the photo-cathode. It consists of several dynode stages for electron multiplication. Coupling a scintillator array to a multi anode PMT is analogous to building a block detector with a large number of small PMT's.

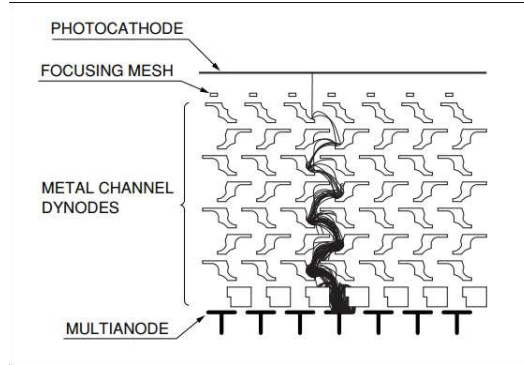


Figure 1.16 – Cross-section of dynode structure of a multi-anode PMT and one of the associated electron trajectories (adapted from Hamatsu, 2006)

Multi-anode PMTs are commercially available and a 256 channel (16 x 16) Hamamatsu H9500 multi-anode PMT photodetector is used in one of the scanners in this thesis. Further details on the specifications of this photo-detector are discussed in chapter 3 (section 3.2.4).

Solid state detectors (semiconductor detectors) can be used as an alternative to photomultiplier tubes [Humm 03]. In the next section we discuss the principle of operation of solid state photodetectors.

### Solid state photodetectors

Solid state detectors being insensitive to the magnetic field and small in size are used as an alternative to PMTs. Furthermore, these detectors, require much smaller voltage to operate as compared to PMTs. Solid state photodetectors are based on p-n junction working in reverse biased (negative voltage to the p-side relative to n-side of the p-n junction) mode. Under small reverse bias voltages, all free majority charge carriers on the p-n junction leave the p and n regions to form a depletion layer, which represents a space charge ( $-Q$  and  $+Q$  in figure 1.17left) of ionized impurities situated between p and n regions. This space charge causes an electric field ( $E$ ) from the  $+Q$  to the  $-Q$  side of the depletion layer. When a photon with sufficient energy (greater than the band gap energy of 1.12 eV for Si, corresponding to a wavelength shorter than 1100 nm) strikes the photodiode, it produces an electron-hole pair. Due to the presence of the electric field in the depletion region, the electron and hole quickly drift in opposite direction, inducing a charge.

Figure 1.17(left), depicts the basic idea, as explained above, about the working of a photodiode which results in unity gain ( $M$ ), as one incident light photon will produce only an electron-hole pair, which is around  $10^6$  to  $10^8$  for PMTs. Although photodiodes are robust, small and operate at very low voltages as compared to PMTs however, their unit gain (and thus high electrical noise) is their major limitation. The photodiodes working at small reverse bias voltages belong to the first part of the plot, in figure 1.17 (right), showing the variation of log of gain ( $M$ ) as a function of applied reverse bias voltage. When the applied reverse voltage is increased, the electrons produced in the depletion

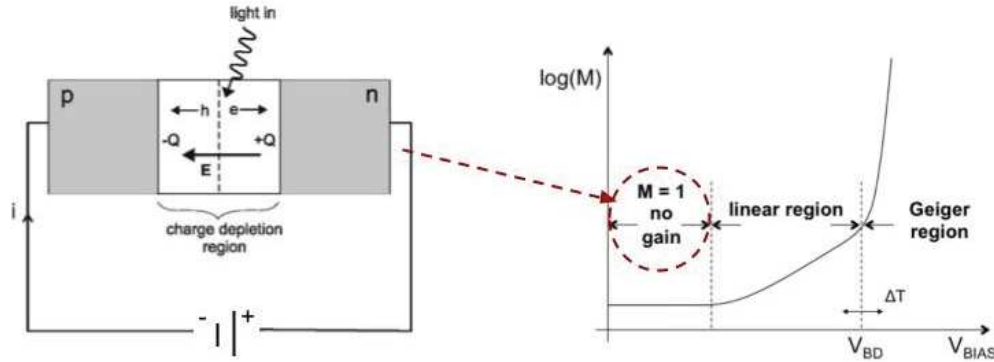


Figure 1.17 – On the left, a reverse bias pn junction, with a depletion region. When a light photon is incident on the depletion region, it produces an electron hole pair, which are drifted apart due to the electric field. On the right a plot showing variation of Gain ( $M$ ) as a function of applied reverse bias voltage  $V_{BIAS}$ . It shows three regions first, where  $M = 1$ ; second where  $M$  varies linearly with  $V_{BIAS}$  and third where  $M$  is infinite.

region ionize the Si atom by colliding with them and thus lead to the production of secondary charge carriers. This collision process occurs repeatedly leading to an avalanche effect thus resulting in an output signal being amplified by a certain gain, which is linear and is represented by the linear region on the same plot (figure 1.17right). The photodetectors designed to work in this region are known as Avalanche PhotoDiodes (APDs) [Pansart 97]. APDs have an advantage of better SNR value due to higher gain as compared to photodiodes. However, currently available APDs have low gains, of the order of few hundreds of eV, when compared with the gain achievable with PMTs [España 10].

In APD, the avalanche is not self sustained and comes to an end by itself. However, if the reverse biased voltage exceeds the breakdown voltage (the voltage at which the gain becomes infinite), the avalanche enters into Geiger mode, as shown in figure 1.17 (right). Once the avalanche begins, it sustains by itself unless it is stopped by using proper quenching mechanism (mechanism that is able to reduce the reverse bias voltage below breakdown voltage). The photodetectors designed to operate above breakdown voltage are known as GM-APDs [España 10]. The GM-APDS provides a gain of the order of  $10^6$ , which is comparable to PMT. Their detailed working procedure can be found in [Dinu 13], where they are reported to be working as a binary device (a 1 or a 0, where a 1 means that an avalanche occurred for a given time and a 0 represents no avalanche). However, being a binary device, GM-APDs does not give information on light intensities, the signal is the same if one or more photons reach at the same time. To overcome this limitation, a structure known as Silicon PhotoMultiplier (SiPM) has been proposed consisting of an array of GM-APDs [Golovin 04, Sadygov 14].

SiPM is a pixelated device, consisting of pixels or micro-cells. The number of micro-cells varies from several of 100's to several of 1000's, with their pitches (distance from the center of one pixel to the center of next pixel) ranging from  $25\ \mu\text{m}$  to  $100\ \mu\text{m}$ . Each micro-cell is a series combination of an APD operating at a voltage above breakdown voltage and a quenching resistor  $R_Q$  [Castro 15] as shown in figure 1.18 and all the micro-cells are connected in parallel. Because all SiPM micro-cells work together in parallel, the output signal is the sum of the signals from all fired micro-cells. So such a device, where each micro-cell operates digitally as a binary element, works as an analogue device and it can measure the light intensity. The output charge of a SiPM is, in principle, proportional to the number of incident photons in different cells. The probability that 2 or more photons hit the same micro-cell depends on the size of the micro-cell itself. SiPM is thus, used by almost all the device for PET imaging due to its high internal gain making it capable to detecting low light levels, compactness

and low power consumption. However, there are some drawbacks of SiPMs such as significant level of dark current and significant dead space between adjacent micro-cells.

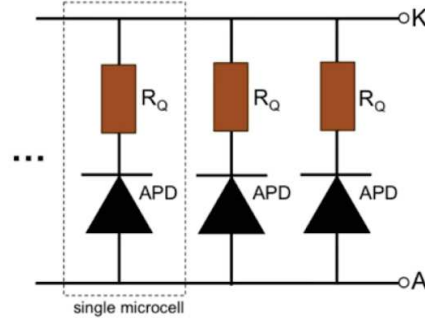


Figure 1.18 – Parallel combination of several micro-cells. Each micro-cell represents a series combination of a APD (designed to operate in GM mode) and a quenching resistance  $R_Q$ . A and K represents anode and cathode respectively.

Table 1.3 summarizes and compares different photodetectors such as PMT, Photodiode, APD and SiPM in terms of parameters such as gain, external bias voltage requirements, influence of magnetic field (in case of the PET scanners to be used with Magnetic Resonance Imaging MRI modality), and some other properties.

Parameters	PMT	Photodiode	APD	SiPM
Gain	$10^6$ to $10^8$	1	100	$10^6$ to $10^8$
Bias voltage	1000 V	few V	200 V	60 V
Dark output	Quiet	Limited by amplifier	Limited by amplifier	Noisy
Mechanical robustness	Good	Rugged	Rugged	Rugged
Magnetic field influence	Not immune	Immune	Immune	Immune
Ambient light exposure	Can be damaged	No Damage	No Damage	No Damage

Table 1.3 – Comparison of different photodetectors such as PMT, Photodiode, APD and SiPM

To summarize, PET scanner detects coincidence events on the basis of scintillation detectors which detects the annihilation gamma photons and emits light proportional to energy deposited, which in turn is detected by the photodetectors, that provides the position of the annihilation photon interaction in the scintillator. The acquired data is then stored (section 1.4) and corrected (if required) and is given as an input to image reconstruction algorithms (section 1.4.1).

## 1.4 Data acquisition and Image reconstruction

When a coincidence event is detected in a PET scanner, the associated LOR need to be stored in a specific data format that can be further used as an input to image reconstruction process. There are two different formats to record the acquired LORs; List mode and histogram mode. In List mode, each coincidence event (characterized by a LOR) is individually stored in a list-type format on an event-by-event basis as the events are detected. Each event is stored along with the information about the two locations at which the annihilation photons interacted, the energy deposited, time of interaction etc. In Histogram mode, a memory location is assigned to each possible LOR and each time a



valid coincidence event is detected along that LOR, that assigned memory location gets incremented by one. For 2D imaging, the histogram format can be more compact as compared to list mode since the average number of events per LOR is often more than one. However, for 3D imaging, the number of coincidence events increases and thus the size of the histograms, resulting in histograms that have an average number of events less than one. Thus in 3D imaging the list mode format is more compact for data acquisition. Furthermore, the list mode stores each event along with its measured attributes (energy, time etc), it is possible to represent the measured data as a function of its measured attributes, which is not possible in case of histogram mode, once the acquisition is done [Barrett 97]. In this thesis, the acquired data is stored in list mode format.

On the basis of the assumption that annihilation must have occurred at any point along the LOR (for no attenuation and scattered events), the number of coincidence events detected by a particular detector pair is proportional to the integral of the radionuclide concentration  $f(x,y,z)$  along the LOR joining those two detectors. The image reconstruction algorithms discussed in the next section, attempts to recover this radionuclide distribution  $f(x,y,z)$  from the line integrals.

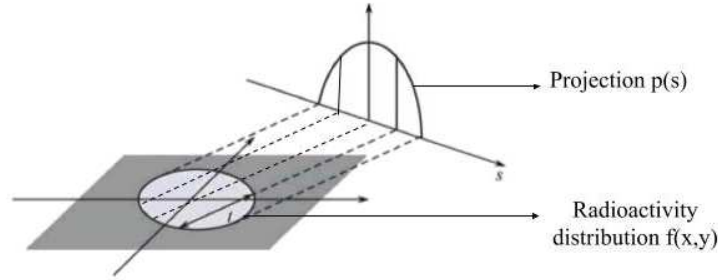


Figure 1.19 – The line integral of parallel LORs for a given radioactivity distribution  $f(x,y)$ . The line integral of all parallel LORs denotes a projection profile  $p(s, \phi)$ ;  $s$  being the radial distance and  $\phi$  being the given projection angle

The set of all line integrals intersecting the tracer distribution at the same given angle, but at different spatial positions is known as parallel projection. A one-dimensional parallel projection  $p(s, \phi)$  of a 2D object for a given projection angle  $\phi$  and for different radial distances  $s$  is shown in figure 1.19. For 3D imaging case, as shown in figure 1.20, projections are 2D line integrals for a given azimuthal angle  $\phi$  and co-polar angle  $\theta$ . After acquiring the data, image reconstruction step can be performed as discussed below.

#### 1.4.1 Image reconstruction

The objective of image reconstruction process is to estimate the distribution of the  $\beta^+$  emitting radio pharmaceuticals in the object that is being scanned. In PET imaging, LORs are collected from many different angles around the object. The recorded LOR only defines the annihilation location along the line joining the detector pair. The total number of counts measured by a particular detector pair is proportional to the integrated radioactivity along the line joining the two detectors. and it is known as line integral data. In this section, we discuss the image reconstruction process to convert the line integral data set recorded at different angles to the images showing the distribution of the  $\beta^+$  emitting atom. There are two basic approaches to reconstruct images i.e., analytical approach, and iterative approach. One of the objective of this thesis is to investigate the feasibility of an open source software CASToR to reconstruct images for data collected. The current version of CASToR reconstructs image only through iterative approach (MLEM). Thus, in this chapter we will only discuss the iterative approach to reconstruct the images.



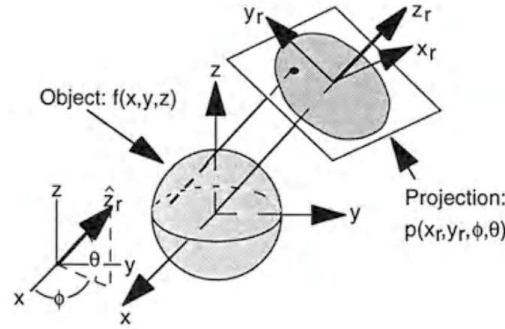


Figure 1.20 – The 2D line integral for a given 3D radioactivity distribution  $f(x,y,z)$  for a given azimuthal angle  $\phi$  and co-polar angle  $\theta$ . (Reprinted from [Bendriem 13])

### Iterative image reconstruction

The basic idea behind the iterative reconstruction is to discretize the image space in several image voxels and consider each voxel value as an unknown. On the basis of scanner geometry and the physics, a system of linear equations can be set up. Figure 1.21 presents the setup of system of equations, represented in the matrix form as given below:

$$FA = P \quad (1.10)$$

where each element  $F_j$  in  $F$  represents the voxel value and each element  $P_i$  in  $P$  represents the projection measurement. Each element  $A_{ij}$  in  $A$  represents a coefficient that is the contribution from voxel  $j$  to the  $i^{th}$  detector pair. The matrix  $A$  is known as System Matrix (SM) and it models the detector response function to the image space. Each element  $A_{ij}$  of SM represents the probability that the event has originated from the  $j^{th}$  voxel and is recorded by the  $i^{th}$  detector pair. [Li 15]. In chapter 4 (section 4.7.3), we discuss two different approaches to compute SM elements.

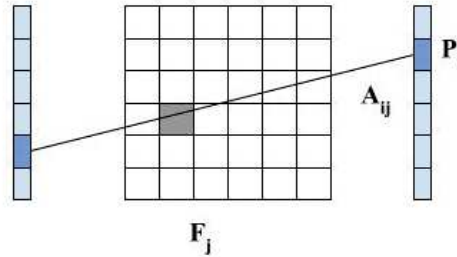


Figure 1.21 – Illustration of discretize image space and a LOR joining the detector pair. A system of equation ( $FA = P$ ) is setup to describe the scanner geometry and physics. Each element  $F_j$  and  $P_i$  of matrix  $F$  and  $P$  respectively represents the voxel value and the projection measurement. Elements  $A_{ij}$  of matrix  $A$  represents the SM elements.

The equation 1.10 can be solved by an iterative algorithm. Figure 1.22 presents the basic approach of using an iterative algorithm. The initial estimate of the image is usually a blank scan where all image voxels are filled with a constant value (either 0 or 1 depending on the algorithm being used). The next step involves calculation of projections (by performing forward projection) based on this initial activity distribution estimate. The forward projection is performed by summing up all the

activity in the voxels that are intersected by the line joining the detector pair and considering the respective SM elements  $A_{ij}$ . Once the forward projection process is performed, we have a projection data set calculated on the basis of initial guess of activity distribution. This calculated projection data set is compared with the actual measured projection data set. On the basis of the result of the comparison, the initial estimate is modified, thereby creating a new estimate. Each loop in figure 1.22 represents one iteration. The whole process is repeated, thereby generating updated image estimates that will start to converge towards the radiotracer distribution. The objective is to progressively refine an estimate of activity distribution to converge as much as possible with true activity distribution.

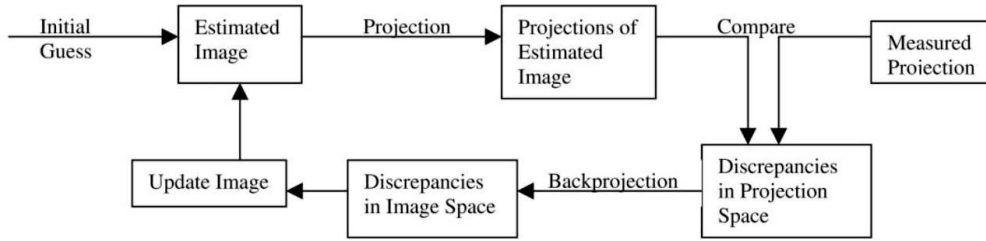


Figure 1.22 – Basic flow chart for iterative image reconstruction process. (Reprinted from [Zeng 10])

There are many types of algorithms to perform the iterative image reconstruction. The algorithms differ in the way, the measured and estimated projections are compared, and also the kind of correction applied to the current estimate. In the scope of my work, MLEM (Maximum Likelihood expectation maximization) algorithm is used since MLEM is the only implemented algorithm in CASToR software version 1 (which is used to perform all the image reconstruction process), which is discussed in details in chapter 4 (section 4.7). MLEM algorithm is discussed below:

### MLEM Algorithm

Proposed by Shepp and Vardi in 1982 [Shepp 82], it is one commonly used iterative reconstruction algorithm. It is developed based on the Poisson probabilistic nature of the emission of photons. The objective of the MLEM algorithm is to find a best estimate for the matrix  $F$  which has the highest probability of generating the observed projection data  $P$  [Bruyant 02]. Considering  $A_{ij}$  as the SM elements, the expected projections  $q_i$  for a given image matrix is given as:

$$q_i = \sum_{j=1}^N F_j A_{ij} \quad i = 1, 2, \dots, M \quad (1.11)$$

The MLEM algorithm consist of 2 steps: The first step is the expectation step, in which the formula expressing the likelihood is formed. (Likelihood represents a statistical measure that is maximized when the difference between the measured and estimated projections is minimized). The likelihood  $L(F)$  that the image  $F$  has generated the projection values  $P$  (the observed projection data) is given by:

$$L(F) = \prod_{i=1}^M e^{-q_i} \frac{q_i^{P_i}}{P_i!} \quad (1.12)$$

The second step of MLEM algorithm is the maximization step, the image that has the highest values of likelihood to give the measured data is found. The highest value of likelihood  $L(F)$  is found by calculating its derivative with respect to each image element  $F_j$ . However, in order to calculate the derivative of the likelihood, one usually consider the logarithm of it, as given below:

$$\ln L(F) = -\sum_{i=1}^M q_i + \sum_{i=1}^M P_i \ln(q_i) - \sum_{i=1}^M \ln(P_i!) \quad (1.13)$$

using equation 1.11 to introduce  $F_j$ , we obtain:

$$\ln L(F) = -\sum_{i=1}^M \sum_{j=1}^N F_j A_{ij} + \sum_{i=1}^M P_i \ln\left(\sum_{j=1}^N F_j A_{ij}\right) - \sum_{i=1}^M \ln(P_i!) \quad (1.14)$$

Equation 1.14 represents the likelihood function and it allows to calculate the probability to observe a projection data set for any given image estimate  $F$ . Since objective is to get an image which has the maximum probability to yield  $P$ , the image matrix  $F$  for which  $L(F)$  is maximal is considered as the best estimate for the observed data set  $P$ . The maximum is found when the derivative of  $L(F)$  is zero.

$$\frac{\partial \ln L(F)}{\partial F_j} = -\sum_{i=1}^M A_{ij} + \sum_{i=1}^M P_i \frac{A_{ij}}{\sum_{j=1}^N F_j A_{ij}} = 0 \quad (1.15)$$

Multiplying the above equation with  $F_j$  and simplifying it, one can write:

$$F_j = \frac{F_j}{\sum_{i=1}^M A_{ij}} \sum_{i=1}^M \frac{P_i}{\sum_{j=1}^N F_j A_{ij}} A_{ij} \quad (1.16)$$

Equation 1.16 results in MLEM iterative algorithm as described by Lange and Carson and is given as:

$$F_j^{k+1} = \frac{F_j^k}{\sum_{i=1}^M A_{ij}} \sum_{i=1}^M \frac{P_i}{\sum_{j=1}^N F_j^k A_{ij}} A_{ij} \quad (1.17)$$

where  $F_j^k$  represents the value of the reconstructed image at the  $j^{th}$  voxel for  $k^{th}$  iteration,  $k$  being the iteration number. The factor  $\frac{P_i}{\sum_j F_j^k A_{ij}}$  represents the ratio of the measured number of counts to the number of counts of the current estimate in bin  $i$ . The factor  $\sum_i A_{ij} \frac{P_i}{\sum_j F_j^k A_{ij}}$  represents the back-projection of this ratio for detector pair  $i$ . A set of successive projection and back-projection are performed in MLEM algorithm. In this thesis MLEM algorithm has been used to evaluate the performance of different scanners. In the next section, we discuss the figure of merits used in this thesis to evaluate the performance of the scanners.

## 1.5 Figure of Merits

### 1.5.1 Detection efficiency ( $\eta$ )

Detection efficiency refers to the capability of a detector to record annihilation gamma photons. It is one of the most important factors that affects the statistical quality of the acquired coincidence events. High statistical quality is required to realize the scanner spatial resolution potential in the reconstructed images. Detection efficiency of a PET scanner depends on two components, firstly on the geometric efficiency of the scanner, and secondly on the intrinsic efficiency of the scintillator crystal. The two components are given as:

1. Geometric efficiency of the scanner: It refers to the fraction of emitted annihilation gamma photons that hit the scintillator detectors and this efficiency is determined by two factors, a) the overall solid angle ( $\Omega$ ) coverage of the detector with respect to the source location and b) the

packing fraction ( $P_F$ ) (representing small gaps between the crystal elements). The solid angle subtended for a point source at the centre of FOV of a circular PET scanner is given as:

$$\Omega = 4\pi \sin \tan^{-1} \frac{A}{D} \quad (1.18)$$

where A represents the maximum axial extent over which coincidence events are recorded and D represents the diameter of the scanner [Phelps 06]. The packing fraction is the ratio of the active area (i.e., scintillator crystal) to the total surface area (scintillator crystal plus the dead space, if any). To maximize the geometric efficiency, the detectors should be close to the source i.e., the patient (smaller diameter scanners), the detector area should encompass the entire patient (enough length of the scanner) and less dead space in the crystal matrix.

2. Intrinsic efficiency of the scintillator crystal: It refers to the fraction of those incident annihilation gamma photons that hit the detector and are detected. For individual crystal, it is given by the product of the detection probability of the incoming photon in the crystal and the fraction of these events,  $\Phi$ , that fall within the selected energy window [Phelps 06]. The efficiency is given as:

$$\epsilon = (1 - e^{-\mu L})\Phi \quad (1.19)$$

where  $\mu$  is the attenuation coefficient of the scintillator crystal and L is the crystal depth. Longer crystals will thus increase the number of detected events.

The overall detection efficiency of the PET scanner is thus given as the product of square of intrinsic efficiency ( $\epsilon^2$ : due to detection of two coincidence events per LOR) of the crystal and the geometric efficiency of the scanner. Thus the overall detection efficiency ( $\eta$ ) of a PET scanner for a point source placed at the center of a ring scanner is given as:

$$\eta = 100 \times \frac{\epsilon^2 P_F \Omega}{4\pi} \quad (1.20)$$

### 1.5.2 Spatial resolution

Another important parameter that impacts the performance of PET scanners is spatial resolution and it represents the ability of a scanner to distinguish between two points. In PET imaging, it is defined as the FWHM of the reconstructed one dimensional profile of a point source in the center of the FOV. The spatial resolution is affected by a number of factors among which is the positron range and the annihilation photon non-collinearity mentioned in section 1.2. Intrinsic spatial resolution ( $R_{det}$ ) of the scintillation detectors is another important factor that affects the spatial resolution of the PET scanners. The limit of spatial resolution achievable by the scintillator crystal and positioning electronics, ignoring other causes (such as positron range), is called the intrinsic spatial resolution of the PET scanner.

For PET scanners, two types of crystal configurations are used, namely, monolithic (continuous) and pixelated crystals as shown in figure 1.23. For pixelated crystal design, the intrinsic spatial resolution is determined by the size of the crystal used. At the centre of the FOV, the intrinsic resolution in this case can be described by a triangular shaped coincidence response function where the FWHM equals one half the detector width ( $d/2$ ), d being the crystal size. Most commercial and academic PET systems are based on pixelated crystal design. On the other hand, for the scanners employing monolithic detectors [González 13], the intrinsic resolution depends on several factors such as the light yield of the scintillator crystal, coating of the crystal, crystal depth affecting the spread of light photons before

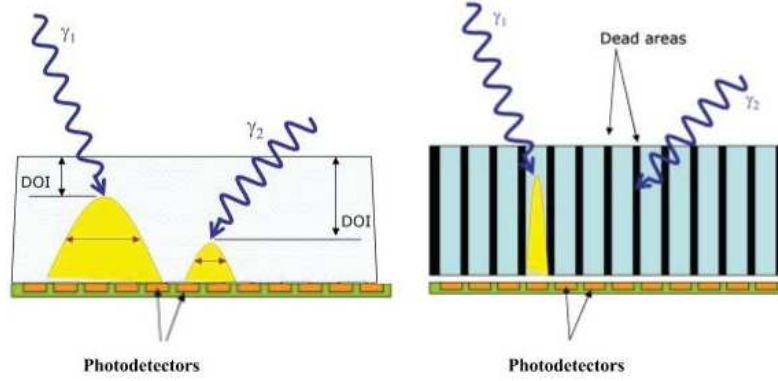


Figure 1.23 – Modules showing monolithic (left) and pixelated (right) crystal configurations (Adapted from [González 13])

they reach the photodetectors etc. If the intrinsic spatial resolution is a Gaussian function with FWHM =  $w$ , then the spatial resolution of the detector pair is also a Gaussian function. At the cFOV, the intrinsic resolution in this case is given as  $\frac{w}{\sqrt{2}}$ . Another important factor limiting the intrinsic spatial resolution (for both the pixelated and monolithic crystal design) is multiple scattering of gamma photons within the crystal. Apart from positron physics and intrinsic spatial resolution, factors like depth of interaction effect, sampling and reconstruction algorithm also impacts the achievable spatial resolution. Considering all these factors, the PET scanner spatial resolution is given as:

$$R_{sys} = k \sqrt{R_{det}^2 + R_{range}^2 + R_{180}^2 + R_{DOI}^2 + b^2} \quad (1.21)$$

where  $k$  is a constant due to the reconstruction algorithm,  $R_{det}$  is the intrinsic spatial resolution limit due to scintillator crystal,  $R_{range}$  represents the finite limit on spatial resolution due to positron range,  $R_{180}$  represents the limit due to photon nonlinearity,  $R_{DOI}$  represents the limit due to depth of interaction (chapter 3) and  $b$  represents the limit due to coding between crystals and photodetectors.

To conclude for the performance parameters of PET scanners, detection efficiency and spatial resolution are two important parameters. It is desirable for a PET scanner to detect 511 keV gamma photons with highest possible detection efficiency and with the best achievable spatial resolution in order to optimize lesion detection. Although, there are certain factors that impact both the spatial resolution and detection efficiency, but not in the same manner. Some examples of these factors are discussed below:

1. Depth of the scintillator crystal (L): As discussed earlier, the depth of the scintillator crystal is an important factor for system detection efficiency and the use of long crystals is desired for increasing detection efficiency. However, this also increases the parallax error leading to degraded spatial resolution.
2. Diameter of PET scanners (D): Since detection efficiency decreases with increasing diameter of the PET scanner due to solid angle coverage with respect to the source, it is desirable to have the detectors as close to the source as possible. However, reducing the diameter of the scanner, increases the angle at which the gamma photons will be incident onto the surface of the scintillator crystals, thereby increasing parallax error.

However, there are some more factors that influence this trade-off between spatial resolution and detection efficiency of PET scanners such as insertion of reflector materials between the scintillator crystals, width of the scintillator crystals impacting the scintillator light output [Peng 10].

## 1.6 Conclusion

This chapter provides an overview of the basics of PET imaging. Based on suitable characteristics of  $^{18}\text{F}$  (such as appropriate half-life, short positron range), FDG is the candidate of choice for cancer detection. A PET scanner should have maximum detection efficiency and best achievable spatial resolution. In order to develop a scanner with such desirable performance, selection of scintillator crystal plays an important role. LYSO and LSO are reported in this chapter to be the suitable candidates for scintillation crystals for PET imaging due to their properties such as high light yield, higher atomic number etc. Currently most of the commercial scanners are based on LSO and LYSO crystals. A brief introduction to PMT and Solid State Photodetectors along with their working principle, advantages and limitations is also described. SiPM is reported to be used in most of the available commercial PET scanners to date. Spatial resolution and detection efficiency are described as two figure of merits used that characterize the performance of PET scanners. Spatial resolution is limited by several factors such as positron range, photon non-collinearity, intrinsic spatial resolution etc., whereas detection efficiency depends majorly on the length of the scanner, its diameter, choice of scintillator crystal and on the length of the crystal. It further provides a description to the factors that play an important role in determination of both the spatial resolution and detection efficiency together. However, in the next chapter we discuss the need to develop the small animal PET scanners and the challenges associated with the small animal PET scanners. It also provides a state-of-art on different available small animal PET scanners along with their performance characteristics.



## Chapter 2

# Small animal imaging via PET

### Contents

<b>2.1</b>	<b>Introduction</b>	<b>47</b>
<b>2.2</b>	<b>Background of small animal PET imaging</b>	<b>48</b>
<b>2.3</b>	<b>Challenges in designing small animal PET scanner</b>	<b>49</b>
<b>2.4</b>	<b>Currently available preclinical PET scanners</b>	<b>51</b>
<b>2.5</b>	<b>Summary</b>	<b>52</b>

## 2.1 Introduction

Animal models are living, non-human beings that are used to study the biological processes or the human diseases without the risk of harming humans. Several animal models have been developed and can be classified into different categories. Induced animal models (involving a healthy animal in which the condition to be investigated is experimentally induced) [Hau 08], spontaneous animal models (involving naturally developed genetic mutations) [Hansen 04], genetically modified models (involving genetic engineered animals to develop disease) are some examples of these animal model categories. The choice of the animal model and its category is dependent on the disease or the biological process under investigation. Mouse serves as a suitable animal model in the field of oncology, whereas rat is an important experimental animal, due to its larger brain size as compared to the mouse, in neuro-science research [Chatziioannou 02]. Other laboratory animals such as dogs, pigs, and non-human primates also play an important role in some experiments, such as in the study of central nervous system and in cardiology [Cherry 01]. Despite other animals, mouse is a preferred choice as an animal model of human disease [Kuntner 14, Cherry 01, Vandamme 14] due to the following reasons:

1. Mouse genome is close to human genome (99%).
2. Fast breeding cycle and low maintenance cost.
3. Highly developed methodology for genetic manipulation.

The imaging of the animal model can be performed both by ex-vivo (with the animal death) and in-vivo (with living animal) imaging techniques. Ex-vivo imaging involves injection of radiotracers in many animals and sacrificing them at various time points to investigate the tracer bio-distribution [Kiessling 11]. Here, each animal provides only a single set of information and cannot provide a continuous insight into the tracer bio-distribution [Tornai 99, Cherry 01]. Whereas, in-vivo imaging such as PET enables imaging of living animals over time, so the bio-distribution of the radiotracer can be



studied within the same animal for hours or days [Phelps 04, Rudin 03]. Since the bio-distribution is studied within the same animal over time, it reduces the number of animals to be used, reduces error due to animal to animal variations, offers possibility of multiple time course studies, lowers the overall time needed to obtain results.

The current thesis work is based on in-vivo PET imaging modality. Imaging of animal models like mouse and rat is known as small animal imaging and the PET scanners designed to scan small animals are known as preclinical PET scanners or small animal PET scanners. The objectives of this chapter are divided into three parts and are given below:

1. To discuss the need to develop pre-clinical PET scanners.
2. To present the challenges involved in designing pre-clinical PET scanners.
3. To review the list of currently available different preclinical PET scanners along with their performance parameters.

## 2.2 Background of small animal PET imaging

PET has become an established medical imaging modality in the field of oncology, cardiology and neurology [Riemann 08, Schnöckel 10, Yao 12, Lancelot 10]. However, it is not feasible to derive all the studies related to human biology, physiology and pharmacology from human body itself due to several ethical, economical, religious and practical reasons [Hau 08]. Thus, animal models (such as rats and mice) of human diseases serve as a suitable candidate for PET imaging. In 1991, Ingvar et al published the first PET images of a rat brain using a human brain PET scanner [Ingvar 91]. Around the same time in 1992, another research group Hume et al performed another study on a rat model using a human PET scanner [Hume 92]. It was reported that, the performance of human PET scanners was insufficient in terms of spatial resolution. The spatial resolution of the human PET scanners used was 5 mm, which was not sufficient to visualize separately the bio-distribution of the radiotracer in the different organs of small animals. A comparison of size difference between a human and a rat brain is presented in figure 2.1.

These studies on small animals using human PET scanners along with the advancement of animal model of human diseases, drove the need to develop small animal dedicated PET scanners. Table 2.1 provides the details on the first dedicated animal PET scanners developed to improve the spatial resolution using existing clinical PET technology i.e., BGO scintillator crystals coupled to PMTs block design or PS-PMTs.

PET scanner	Spatial resolution (mm) <sup>1</sup>	Axial FOV (cm)	Transaxial FOV (cm)	References
Hamamatsu SHR 2000 <sup>2</sup>	3.0 / 4.8	4.6	34.8	[Oehr 03, Watanabe 92] 1992
CTI ECAT 713 <sup>2</sup>	3.8 / 4.4	5.4	64.0	[Oehr 03, Cutler 92]; 1992
Hammersmith RAT-PET <sup>2</sup>	2.8 / 4.7	5.4	11.7	[Oehr 03, Rajeswaran 92]; 1992
Hamamatsu SHR 7700 <sup>3</sup>	2.6 / 3.3	11.4	33.0	[Watanabe 97]; 1997

Table 2.1 – First dedicated animal PET scanners employing BGO scintillation crystal coupled to PMTs block detectors or PS-PMTs

<sup>1</sup>Transaxial / axial spatial resolution at the CFOV

<sup>2</sup>using PMTs block detector design

<sup>3</sup>using PS-PMT

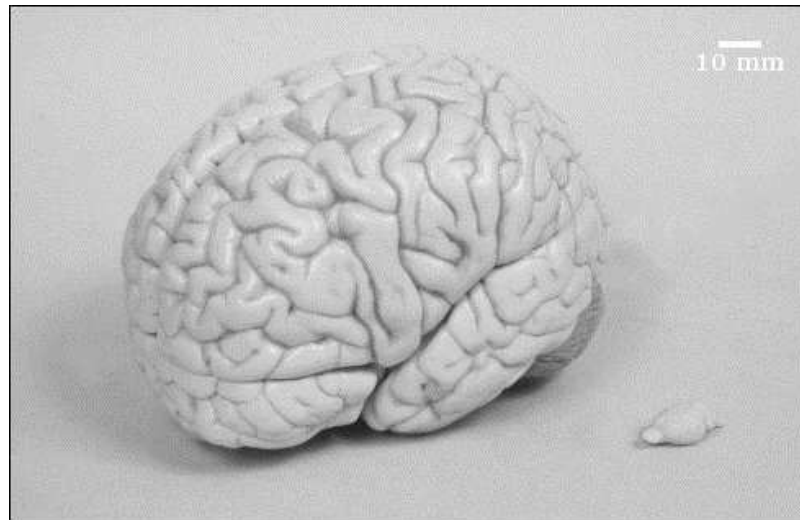


Figure 2.1 – Models of human and rat brain shown for size comparison. The human brain measures approximately 105 mm from top to bottom while the rat brain measures approximately 10 mm across the same scale. (Adapted from [Myers 02])

## 2.3 Challenges in designing small animal PET scanner

Developing dedicated small animal PET scanner enables us to perform more accurate and efficient studies on small animals as compared to the studies performed using human scanners. However, there are certain major challenges in designing small animal PET scanners and these challenges are given below:

1. **Accounting for the size difference between humans and small animals:** The first major challenge of designing small animal PET scanner comes from the size difference between humans and small animals. In order to investigate the same biological process or disease situation in small animals that has to be investigated for humans, the PET scanners must have similar ratios of volumetric spatial resolution to the volume of the object imaged.

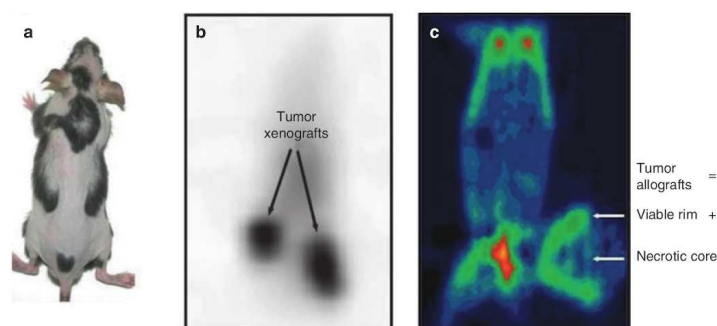


Figure 2.2 – Comparative study of PET images of mice having comparable size xenograft tumors; a) orientation of the mouse during the imaging process; b) image acquired via clinical PET scanner; c) image acquired via preclinical PET scanner (Reprinted from [Kiessling 11])

Figure 2.2 presents the orientation of mice during the PET scan (figure 2.2a) and the PET scan images of tumor bearing mice (figure 2.2b and figure 2.2c) [Kiessling 11]. The images are recon-

structured for the data acquired by a clinical PET scanner (figure 2.2b) having a spatial resolution of 6 mm and by a small animal PET scanner (figure 2.2c) having a spatial resolution of 2.2 mm. The tumors in the two images are of comparable size (1–1.5 cm in the largest dimension). It can be observed that the images reconstructed for clinical PET scanner show high-contrast uptake of the radiotracer by the two tumors without any heterogeneity of uptake, whereas, the image acquired by a small animal PET scanner enables the identification of differential uptake of the radiotracer within biologically distinct cells of the tumor i.e., in the viable rim and in the necrotic core as shown.

Thus, improving the scanner spatial resolution to visualize the heterogeneity of radiotracer uptake in small animals is one of the major challenges in the field of designing small animal PET scanner.

**2. Trade-off between spatial resolution and detection efficiency:** As explained in Chapter 1 (section 1.5.2), crystal size is one of the major factors that limits the scanner spatial resolution. Furthermore, thicker crystal degrades the spatial resolution due to parallax error. However, reducing the crystal size or reducing the crystal depth for improving spatial resolution, adversely impacts the scanner performance in terms of its detection efficiency. As explained in chapter 1 (section 1.5.1), the detection efficiency is determined by the product of solid angle, intrinsic efficiency and packing fraction. Following are some examples that create the trade-off between spatial resolution and detection efficiency.

- (a) Crystal depth is one of the major factors that affects the scanner detection efficiency as explained in chapter 1. In order to reduce the parallax error (not to degrade the spatial resolution), crystal depth is reduced, which in turn adversely impacts the scanner detection efficiency. Thus, crystal depth is an important factor that plays an important role affecting the trade-off between spatial resolution and detection efficiency.
- (b) Reducing the crystal size allows more number of crystals to be accommodated on a given photodetector surface area as shown in figure 2.3. The finite thickness (around 50 - 100  $\mu\text{m}$ ) of the reflective material between the crystals contributes to the non-scintillation material i.e., dead space, which reduces the packing fraction and thus the detection efficiency [Levin 07].

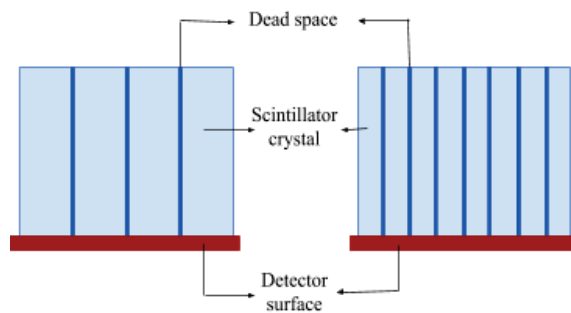


Figure 2.3 – Comparison of pixelated crystal matrices coupled to a detector surface. The crystal matrix on the left consists of crystals with larger crystal sizes as compared to the crystals of crystal matrix present on right side.

- (c) In order to improve the geometric efficiency and eventually scanner detection efficiency, the scanner should have possibly smaller diameter (which brings the scintillator crystals closer to the source). However, this will lead to gamma photon entering the crystals at large

oblique angles, causing parallax error and ultimately degraded spatial resolution [Levin 07].

3. **Light collection efficiency from scintillator crystals:** As gamma photon interacts within the scintillator crystal and deposits its energy, optical photons are produced isotropically. The fraction of the optical photons arriving at the photodetector surface, is known as the light collection efficiency. The optical photons undergo multiple reflections and since the reflective coating of the crystal surface is never ideal, a fraction of optical photons are lost. For scanners employing pixelated crystal matrix, the collection efficiency depends on the aspect ratio of the crystal, which is defined as the ratio of the crystal readout area to its length [Levin 02]. The longer (for improved detection efficiency) and the narrower is the crystal (for better spatial resolution), the lesser are the optical photons collected. It is important to maximize the light collection efficiency because, the number of optical photons detected indicate the energy deposited by the gamma photon in the scintillation crystal. A weak light collection efficiency degrades the energy resolution, affects the energy window settings and potentially degrades the spatial resolution [Levin 07]. [Siegel 95] further explains the problems associated with making the crystal narrower for improved spatial resolution.
4. **Different scales for injected radioactivity in humans and small animals:** For humans, the average injected activity is around 5 MBq per kilogram. It leads to  $\sim 350$  MBq of activity for a human weighing 70 kgs [Oehr 03] (this value is decreasing nowadays due to the improvement of scanner efficiency). On the linear scale, in a mouse weighing around  $\sim 20$  g, the injected activity should be close to a few hundreds of kBq. This injected activity of few hundreds of kBq is not enough to yield sufficient event statistics to reconstruct small volumes. Thus, higher doses of radioactivity is usually injected. As an example, for a 16 module variant of Quad Hidac pre-clinical PET scanner [Schäfers 05], the average injected activity in a mouse varies between 4 to 23 MBq (approximately 100 times more as compared to linear scaling with humans). However, injecting higher activity can impact the normal physiology of the small animal making it different from human disease conditions especially for diagnostic purposes [Oehr 03]. Thus, improving the detection efficiency of small animal PET scanner is an important factor.
5. **Cost:** Cost is another important factor in designing the small animal PET scanner [Cherry 01]. Employing pixelated crystal matrices, consisting of thin crystals or increasing the axial extent of the scanner [Levin 07], leads to higher cost. Thus, the technology of small animal imaging must evolve to a point where the PET imaging becomes relatively low-cost, high-throughput technique.

## 2.4 Currently available preclinical PET scanners

In order to visualize and quantify the radiotracer biodistribution in the small structures of mice and rats, several research groups lead to the development of numerous research prototype and commercial small animal PET scanners. Table 2.2 presents some examples for the first generation preclinical PET scanners along with the achievable spatial resolution values (at 5 mm from the cFOV as specified in NEMA NU-4 2008 standards) and the peak detection efficiency values. The axial and transaxial FOV for different scanners are also reported. The scanners reported in the table employs different scintillation crystals such as BGO, GSO, LSO or LYSO.

The table 2.2 shows that for the scanners which provide a spatial resolution close to 1 mm have smaller detection efficiency values, for example, Quad-HIDAC (1.20%) and TransPET (2.04%). It should be noted that all the spatial resolution values reported in table 2.2 corresponds to transverse

spatial resolution at 5 mm from the cFOV as mentioned by NEMA NU-4 2008 standards. We can observe that the improvement in spatial resolution comes at the expense of the detection efficiency. In parallel, we can observe that there are other scanners which have better detection efficiency values, such as IRIS PET (8%) and MuPET (6.38%) for a degraded spatial resolution (i.e., 1.78 mm and 1.50 mm respectively). Which of these scanners providing better spatial resolution or better detection efficiency values can be considered as the most suitable for small animal imaging ?

Model	Spatial resolution (mm) <sup>1</sup>	Peak detection efficiency (%)	Axial FOV (cm)	Transaxial FOV (cm)	Reference
MicroPET P4	2.29	1.19	7.80	19.0	[Tai 01b]
MicroPET R4	2.13	2.06	7.80	10.0	[Knoess 03a]
Mosaic HP	2.32	2.83	11.90	12.8	[Huisman 07]
Quad-HIDAC <sup>3</sup>	1.08 <sup>2</sup>	1.20	28.00	16.5	[Schäfers 05]
microPET FOCUS 120	1.92	3.42	7.60	10.0	[Laforest 07]
microPET FOCUS 220	1.75	2.28	7.60	19.0	[Goertzen 12]
ClearPET	1.94	3.03	11.00	12.0	[Ziemons 05]
Argus (GE eXplore Vista)	1.63	4.32	4.80	11.8	[Wang 06]
VrPET	1.52	2.22	4.50	14.0	[Lage 09]
LabPET 4	1.65	1.40	3.75	10.0	[Bergeron 14]
LabPET 8	1.65	2.36	7.50	10.0	[Bergeron 09]
LabPET 12	1.65	5.40	11.4	10.0	[Bergeron 14]
ClairvivoPET	2.16	8.72	15.10	10.2	[Sato 15]
FLEX Triumph X-PET Scanner	2.20	5.90	11.60	10.0	[Prasad 10]
NanoScan PET/MRI	1.50	8.40	9.40	12.30	[Nagy 13]
Albia Trimodal PET/SPECT/CT	1.50	6.30	14.80	8.00	[Spinks 14]
TransPET BioCaliburn	1.0	2.04	5.30	13.00	[Wang 14]
MuPET	1.48	6.38	11.60	10.0	[Wong 12]
NanoPET/CT	1.03 <sup>2</sup>	7.70	9.48	12.30	[Szanda 11]
Inveon DPET	1.63	6.72	12.7	16.1	[Constantinescu 09]
IRIS PET	1.78	8.0	9.5	8.0	[Belcari 17]

Table 2.2 – Comparison of first generation preclinical PET scanners in terms of their performance parameters (radial spatial resolution (mm) measured at 5 mm radial distance and peak detection efficiency (%) at the cFOV) as mentioned in NEMA NU 4-2008 standards.

## 2.5 Summary

One of the major challenge in the field of preclinical PET scanner design is to find the optimal balance between the spatial resolution and the detection efficiency. In this chapter we observe the trade-off between these two parameters for the available preclinical PET scanners. The motivation of this thesis is to understand how by optimizing the geometry of the scanners, both the spatial resolution and the detection efficiency can be improved simultaneously. Another motivation is to understand the importance of improving these performance parameters for preclinical PET imaging. Currently, the scanner geometry design has been improved to an extent so as to provide a spatial resolution close to or even less than 1 mm at the cFOV [Sato 15].

In order to investigate the objectives of the thesis, we discuss four different scanner geometries based on different geometrical approach as well as on the prior research work performed in our lab. In the next chapter we discuss about the geometries of the designed scanners.

<sup>1</sup>radial spatial resolution at 5 mm from the cFOV

<sup>2</sup>at the radial center of the FOV

<sup>3</sup>evaluation as per NEMA NU 2-2001 standards for human PET scanners

# Chapter 3

## Scanner geometries

### Contents

<b>3.1</b>	<b>Introduction</b>	<b>53</b>
<b>3.2</b>	<b>Fixed parameters for defining scanner geometries</b>	<b>54</b>
3.2.1	Scintillator crystal	54
3.2.2	Scanner diameter	54
3.2.3	Scanner axial coverage	55
3.2.4	Photo-detector	55
3.2.5	Photo-detector readout	56
3.2.6	Number of PET head modules	56
<b>3.3</b>	<b>Variable parameters for defining scanner geometries</b>	<b>57</b>
3.3.1	Crystal size	58
3.3.2	Crystal depth	58
<b>3.4</b>	<b>Scanners geometries</b>	<b>59</b>
3.4.1	Scanner A: 2D detection technique	60
3.4.2	Scanner B: 2D detection technique + binary sampling	63
3.4.3	Scanner C: 2D detection technique + continuous sampling	65
3.4.4	Scanner D: 3D detection technique	68
3.4.5	IRIS PET Scanner	70
<b>3.5</b>	<b>Summary</b>	<b>71</b>

### 3.1 Introduction

As discussed earlier the geometrical factors of PET scanner create a compromise between scanner spatial resolution and detection efficiency. To overcome this compromise, multiple scanner designs have been proposed such as pixelated crystal scanner, tapered edge crystal scanner, axially elongated crystal scanner, multi layer pixelated crystal scanner etc [Weber 04, Levin 07, Ito 11]. Scanner designs here refer to the arrangement of scintillation crystals and photodetectors which affects the estimation of the position of gamma photon interaction in the scanner. One of the objectives of this thesis is to study the impact of PET scanner designs to optimize the trade-off between spatial resolution and detection efficiency. To achieve the objective, four scanners based on different designs (Scanner A, Scanner B, Scanner C and Scanner D) are investigated. These scanner designs have been selected based on the prior research work performed in the lab.

In this chapter, we describe the geometry and the technical details of these scanners. Since the objective is to study the impact of scanner design (i.e., the arrangement of crystals on the photodetector), factors like crystal material, scanner diameter, axial coverage of the scanner etc., which also influence the performance of the PET scanner, are kept fixed. Keeping these factors fixed while designing the geometries enable us to study the effect of scanner design independently of other factors. The details on the fixed parameters are discussed in section 3.2. As the objective is to optimize the trade-off between spatial resolution and detection efficiency, all four scanner geometries are defined in a way that the spatial resolution is less than or equal to 1 mm at the cFOV, while detection efficiency is varied for different designs. Some factors like crystal size or crystal depth are varied depending upon the requirements of each scanner design. These varied parameters and their impact on scanner performance are discussed in section 3.3. Later, section 3.4 describes individually the proposed scanner designs, their technical details, advantages and limitations. The IRIS PET, a commercially available high resolution preclinical PET scanner [Belcari 17], installed at our facility, is considered as state of art scanner in this work. In section 3.4.5, we discuss the technical details of the IRIS PET scanner.

## 3.2 Fixed parameters for defining scanner geometries

As described in chapter 1, parameters like axial scanner coverage (section 1.5), scanner diameter (section 1.5), crystal material (section 1.3.1) etc., impact the scanner performance. For example, employing high atomic number ( $Z$ ), high density scintillator crystals in a scanner increase the probability of photoelectric effect with respect to the Compton scattering. Decreasing scanner diameter improves the detection efficiency, while degrading the spatial resolution. In this chapter, we define four scanners based on different designs, keeping the above mentioned geometrical parameters fixed. This is done to avoid the impact on scanner performance coming from these factors and not from scanner design. The fixed factors are discussed below:

### 3.2.1 Scintillator crystal

Among all the scintillator crystals mentioned in chapter 1; (section 1.3.1), the selected crystal should have a good combination of high density, good light yield, high photoelectric to compton scattering interaction cross-section ratio. The crystals based on Cerium (Ce) doped lutetium oxyorthosilicate (LSO and LYSO) satisfy all these criteria simultaneously. Their attenuation length of 11.4 mm and 12.2 mm respectively, attenuate more than 90 % of the incident 511 keV gamma photons with 36 mm of material. Among the two lutetium oxyorthosilicate crystals, LSO presents a better photoelectric to compton cross section as compared to LYSO. However, LYSO provides higher light yield per keV gamma energy deposited, lesser self absorption of scintillation light [Ramirez 05] and weaker afterglow phenomena (i.e., delayed emission of photons in the crystal) as compared to LSO. Thus, LYSO is the preferred choice while designing all the four scanners.

### 3.2.2 Scanner diameter

Scanner diameter is an important parameter that influences the trade-off between spatial resolution and detection efficiency. As mentioned in chapter 1 (section 1.2.4), increasing scanner diameter degrades the spatial resolution due to photon noncolinearity, whereas, decreasing the diameter improves the scanner detection efficiency (section 1.5). Thus we try to keep the diameter to be a fixed parameter while designing all the scanner geometries. Due to the limitations of the size of available photodetector packaging and other design constraints, the diameter may vary from 50 mm to 70 mm among the four studied scanner designs. However, varying diameter from 50 mm to 70 mm, impacts the detection efficiency by 10% and spatial resolution by 0.1 mm at the cFOV as can be estimated from the graphs presented in figure 3.1.



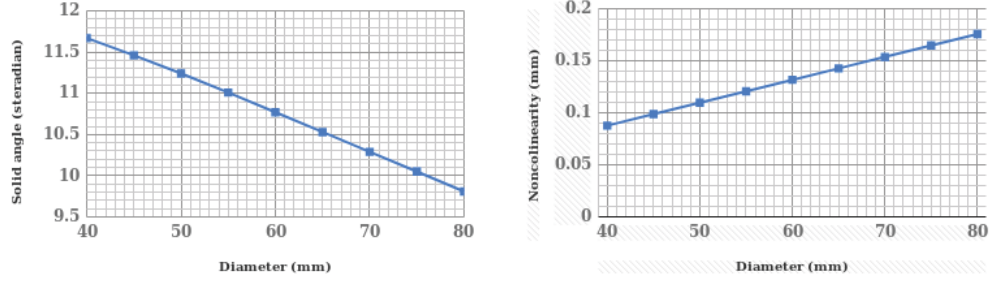


Figure 3.1 – Impact of scanner diameter ‘D’ (mm) at the cFOV on (left) detection efficiency via solid angle ( $\Omega$ ), calculated as  $\Omega = 4 \sin[\tan^{-1}(A/D)]$  where A denotes the axial length of the scanner (= 100 mm); (right) Spatial resolution (mm) via photon noncolinearity calculated as  $\Delta_c = 0.0022D$ .

### 3.2.3 Scanner axial coverage

Scanner axial coverage is another important factor that impacts the scanner performance in a manner similar to scanner diameter. The detection efficiency increases as the length of the scanner increases whereas increasing length of the scanner leads to photon entering at more oblique angles, degrading the spatial resolution due to parallax error. We keep the axial length of scanners to be around 100 mm for all 4 geometries, in order to image the whole body of a mouse.

### 3.2.4 Photo-detector

SiPM is the most promising photodetector, to date (as discussed in chapter 1), and thus it is used while designing the scanner geometries. SiPM is also known as Multi Pixel Photon Counter (MPPC) and consists of several micro pixels or GM-APDs. Normally, the preferred MPPC pixel size is  $50 \mu m$  or greater, so as to achieve high fill factor that leads to high photon detection efficiency. A MPPC of size 13 mm x 13 mm ( $50 \mu m$  pixel size) is selected as the final choice of photodetector. Figure 3.2 (top row) presents a 13 mm x 13 mm module of MPPC (Hamamatsu) used which consists of 4 x 4 channels, with a 3.2 mm pitch (The number of micro-pixels or SPAD is equal to 3600 in this configuration).

Parameters	MPPC	Multianode PMT
Size of a module ( $mm^2$ )	$13.0 \times 13.0$	$52.0 \times 52.0$
Number of channels per module	$16(4 \times 4)$	$256(16 \times 16)$
Effective photosensitive area/channel ( $mm^2$ )	$3.00 \times 3.00$	$3.04 \times 3.04$
Fill factor (%) or effective area/external size	74	89
Refractive index of window material	1.55	1.47

Table 3.1 – Technical details of the MPPC and multianode PMT photodetector used for designing scanner geometries [Hamamatsu 16]

Furthermore, as an exception for a scanner design, Scanner D, a 256 channel (16 x 16) multianode PMT photodetector is used. This detector is used since all the dedicated electronics have already been developed for it in the lab and the preliminary results were obtained using this photodetector [Boisson 17]. Figure 3.2 (bottom row) presents a 52 mm x 52 mm module of multianode PMT photodetector assembly (Hamamatsu H9500). The technical details of these two photodetectors are given in table 3.1.



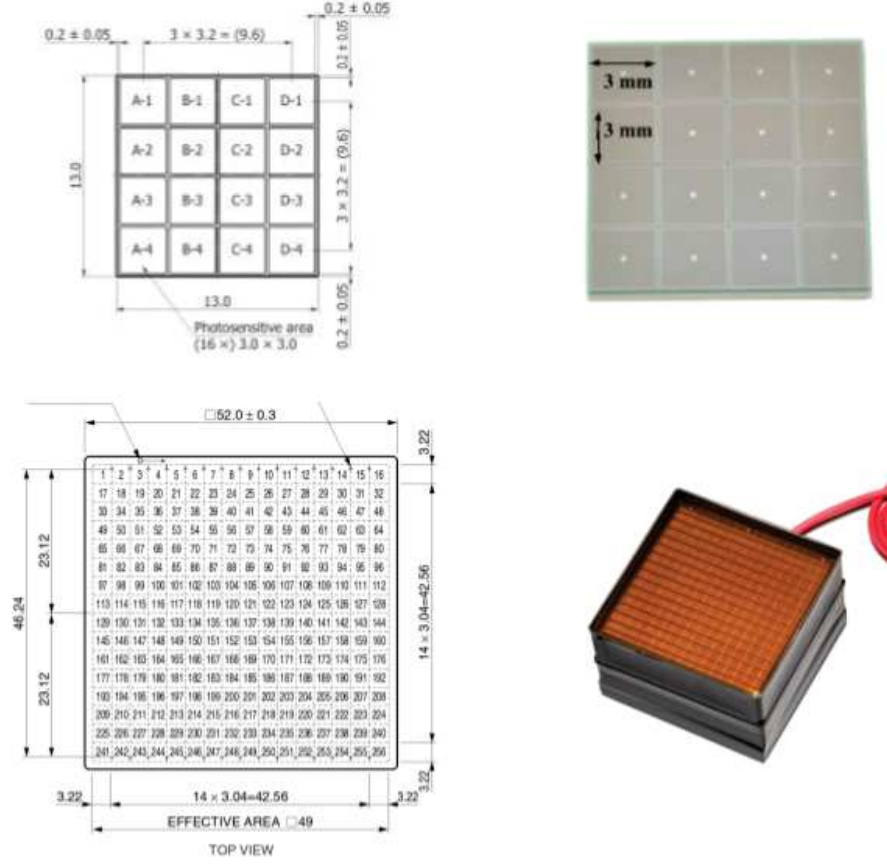


Figure 3.2 – Schematic illustration (left) and the image (right) of the photodetector modules used for designing scanner geometries; Top row: a 13 mm x 13 mm MPPC module consisting of 4 x 4 array of 3mm x 3mm channel; Bottom row: a 52 mm x 52 mm multianode PMT module consisting of 16 x 16 channels [Hamamatsu 16]

### 3.2.5 Photo-detector readout

In order to determine the position of interaction of gamma photon, it would be interesting to read each and every channel of the photodetector individually. However, it becomes very expensive to read each channel individually. The readout electronics for all the geometries in this thesis is based on Symmetric Charge Division (SCD) circuit that reduces the total number of readout channels [Popov 03]. For a circuit consisting of  $n \times m$  channels, SCD reduces the readout channels from  $n \times m$  to  $n + m$ . F. Boisson et al presented in their work [Boisson 17], the theory and working principle of SCD circuit, the associated software method used to retrieve the x- and y- coordinates of the gamma photon interaction and the optical photon distribution behaviour (to retrieve the z-coordinate for monolithic crystals).

### 3.2.6 Number of PET head modules

Since flat panel photodetectors such as MPPC's and multianode PMTs are used, the scanner geometry can be polygonal instead of completely circular in shape in the transverse plane, as shown in figure 3.3. The number of modules used to design the scanner is also an important factor that impacts both spatial resolution and detection efficiency simultaneously. Scanner geometry with less number

of modules, results eventually in higher detection efficiency due to less number of gaps between the modules through which the gamma photon can escape [Levin 07].



Figure 3.3 – Transverse cross section of PET scanner geometries consisting of 4, 6, 8, 10, 12 modules respectively.

In case of PET modules employing pixelated crystals matrix, the depth of the crystal leads to a geometric effect that degrades the spatial resolution. This effect, known as Depth Of Interaction (DOI) effect or parallax error, is due to the fact that the annihilation gamma photons can interact at any depth in the scintillation crystal. Consider a circular scanner geometry as shown in figure 3.4a, at the cFOV, all the emitted gamma photons will enter the scintillator crystal perpendicular to their surface. However, as the radial distance increases, the incident gamma photons enter the crystal at more and more oblique angles. Since there is lack of information regarding the depth of interaction of gamma photon within the crystal, it degrades the spatial resolution when the source is located at a radial offset. However as shown in figure 3.4b, less number of modules cause gamma photons to enter at oblique angles and thus degrades the spatial resolution even at the cFOV. Thus, the number of modules play an important role (for a fixed diameter) characterizing the scanner performance.

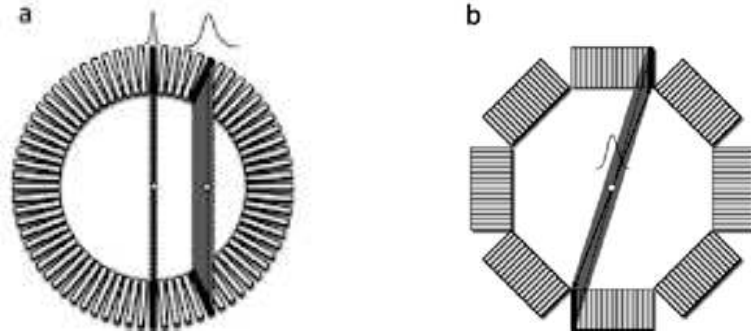


Figure 3.4 – Left (a): A circular scanner geometry showing parallax error for a LOR passing at a radial distance from the cFOV; Right (b): An octagonal scanner geometry, causing gamma photons to be incident at oblique angles even at the cFOV, resulting degraded spatial resolution at the cFOV. (Reprinted from [Ito 11])

To avoid the additional effect of number of modules on scanner performances, we design the scanner geometries using 8 modules. However, for scanner D, which is designed using 52 mm x 52 mm multianode PMT, only 4 modules are arranged in the transaxial plane so as to satisfy the limit of scanner diameter as mentioned in the fixed parameter section.

### 3.3 Variable parameters for defining scanner geometries

Since the objective of the work is to study the impact of scanner design, or arrangement of crystal and photodetector, on scanner performance, the geometrical factors are kept fixed as much as possible.

However to arrange the crystals and photodetectors in different scanner designs, certain parameters vary significantly from one scanner design to another. These parameters and their impact on scanner performance are listed below:

### 3.3.1 Crystal size

The crystal size is varied for different scanners due to the following requirement of different scanner designs:

1. For designs employing pixelated crystal matrix and monolithic crystals, the size of the crystal varies.
2. For the scanner designs employing axially elongated crystals (section 3.4.3), longer crystals are generally used so to reduce the number of modules in the axial direction. Although, as crystal length increases, the crystal cross sectional size should also increase so as to improve the light collection efficiency (the fraction of the available optical photons that are collected at the end of the crystal) which depends on the aspect ratio (which is defined as the ratio of crystal cross-sectional area to its depth). The crystals with low aspect ratio result in a large number of optical photon interactions with the crystal surfaces and thus the associated losses.

Since crystal size is a dominant factor affecting the scanner spatial resolution, achieving a spatial resolution of 1 mm, puts a limit to crystal size. Figure 3.5 shows the variation in spatial resolution as a function of crystal size at the cFOV for a range of scanner diameter. As discussed before, the scanner diameter varies between 50 mm to 70 mm for the four scanner geometries studied, we study the variation of spatial resolution for three different diameter values i.e., 50 mm, 60 mm and 70 mm. Since all the scanner geometries are designed so that the spatial resolution at the cFOV is equal to or less than 1 mm, the selected crystal size should be less than 2.0 mm. The final choice of the crystal size corresponding to each design is described later in this chapter.

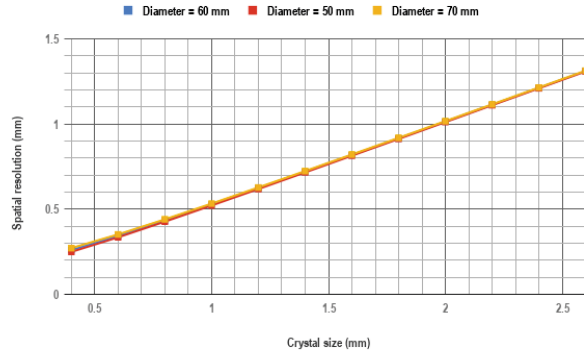


Figure 3.5 – Spatial resolution (mm) estimated at the cFOV for a scanner as a function of crystal size (d) using the equation  $R_{sys} = k((d/2)^2 + R_{range}^2 + R_{180^\circ}^2)^{\frac{1}{2}}$ . Where k, the constant to reconstruction is taken to be equal to 1,  $R_{range}$ , the factor representing the positron range is taken to be 0.1 mm,  $R_{180^\circ}$ , the factor representing the positron range is taken to be equal to  $0.0022 \times diameter$  (for diameter = 60 mm)

### 3.3.2 Crystal depth

Crystal depth is varied among the proposed scanner designs due to different requirements specific to each design as also mentioned for crystal size. However, crystal depth is an important factor since it

impacts both the spatial resolution and detection efficiency in a different manner. As mentioned in chapter 1, increasing the crystal depth increases the detection efficiency whereas, for radially elongated crystals, due to no information about DOI, parallax error degrades the spatial resolution. Figure 3.6 and figure 3.7 present the effect of varying crystal depth on detection efficiency and on spatial resolution for a general case of circular PET scanner geometry.

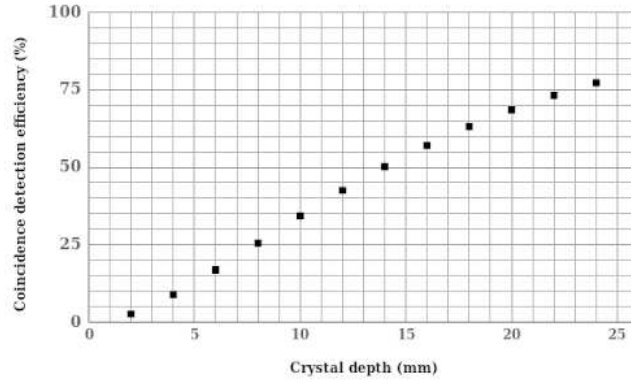


Figure 3.6 – Coincidence detection efficiency ( $\epsilon^2$ ) as a function of crystal depth ( $x$ ), where  $\epsilon = 1 - e^{-\mu x}$ .

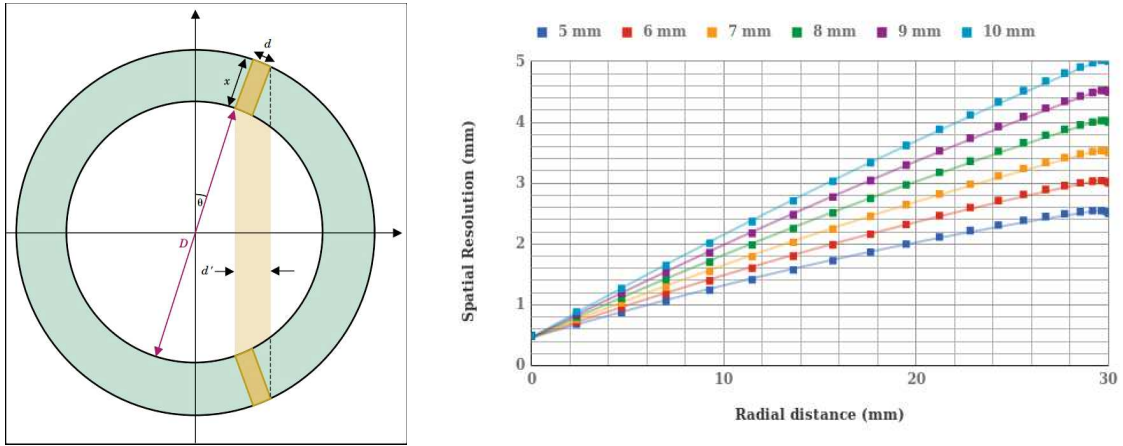


Figure 3.7 – Left: Illustration of a circular geometry scanner, where  $D$ ,  $d$  and  $x$  represent the scanner diameter, crystal size and crystal depth respectively. Due to the inability of determining the DOI,  $d'$  ( $d' = d \cos \theta + x \sin \theta$ ) represent the apparent width of the crystal (Reprinted from [Cherry 12]). Right: Analytically calculated spatial resolution ( $d'/2$ ) for a source kept at different radial positions and for different crystal depths varying from 5 mm to 10 mm (represented via different colours).

The final choice for crystal depth corresponding to each scanner and its requirement is explained later in this chapter.

### 3.4 Scanners geometries

All the scanner geometries studied in this thesis are based on different scanner designs. This different arrangement of crystals and photodetectors results in different detection technique. The detection

technique characterizes the level at which the position of interaction of gamma photon can be estimated. For example, some detection techniques enable us to extract the position of interaction up to crystal ID whereas other detection techniques can result in estimation of position of interaction to a more precise level i.e., x-, y-, z- coordinates inside the crystal.

The idea behind the selected scanned designs studied in this thesis is to progressively add an extra dimension in the estimated position of interaction of the gamma photon. The first design consists of a radially arranged pixelated crystal matrix which enables the 2D detection of gamma interaction. The second design consists of two layers of radially arranged pixelated crystal matrices which enables us a 2D detection as well as a binary sampling in the radial dimension. The third scanner design consists of an axially oriented crystal matrix, which enables a 2D detection as well as a continuous sampling in the axial dimension. Finally, the last scanner design employs a monolithic crystal, enabling the complete 3D estimation of the detection position. All the above scanner geometries are explained in detail in the following sections. We also describe the specifications for each scanner along with their respective advantages and disadvantages.

### 3.4.1 Scanner A: 2D detection technique

Over the last 20 years, most of the preclinical PET scanners [Lage 08, Tai 01a, Knoess 03b, Kim 07, Bao 09] were developed using radially elongated pixelated crystal matrix coupled to photodetectors. The crystal matrix is coupled to photodetector either via one-to-one coupling with the photodetector or via light guide for light sharing. Scanner A, the first preclinical PET scanner geometry studied in this thesis, is based on this classical design of employing pixelated crystal matrix coupled to photodetector via light guide. When an incoming gamma photon interacts within a crystal of pixelated crystal matrix, a large fraction of resulting optical photons arrive at the photodetector surface via light guide. Light guide shares the optical photons generated in a crystal over many photo-detector channels as shown in figure 3.8. This scanner design or the detection technique provides the position of interaction of the gamma photon in terms of crystal ID (i.e., x- and y- coordinates) and no DOI in the crystal can be extracted. Thus the detection technique is regarded as a 2D detection technique.

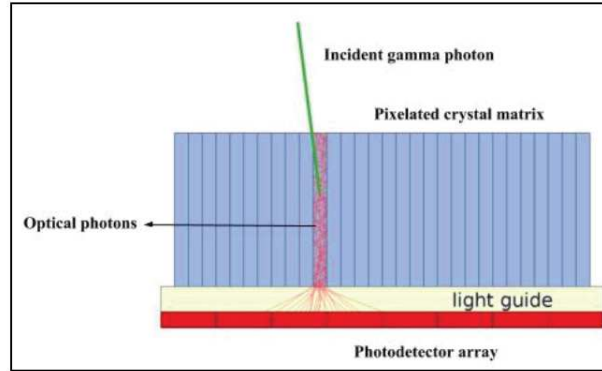


Figure 3.8 – 2D illustration of a module of scanner A. The optical photons (red lines) generated in a crystal is spread by the light guide (white) over several channels of the photodetector array (red)

### Scanner specifications

The LYSO scintillator crystal is used and is coupled to a 13 mm x 13 mm MPPC photodetector. The size of the crystal for scanner A is decided initially on the ability of the photodetector to distinguish each and every crystal in the crystal matrix. Based on in-house experiment, the 13 mm x 13 mm

MPPC photodetector permits us to distinguish each and every crystal of the crystal matrix down to a size of 0.56 mm.

Furthermore, the size of the crystal is decided on the basis of the trade-off between the packing fraction (i.e., active area / total area) of the crystal matrix for the given photodetector and the cost of a crystal matrix. Figure 3.9 presents the estimated packing fraction for a range of crystal sizes placed over a 13 mm x 13 mm MPPC module. However, the cost of the crystal matrix increases as the size of the crystal decreases, thus selecting a crystal matrix made up of very small sized crystals increases the manufacturing cost of the scanner.

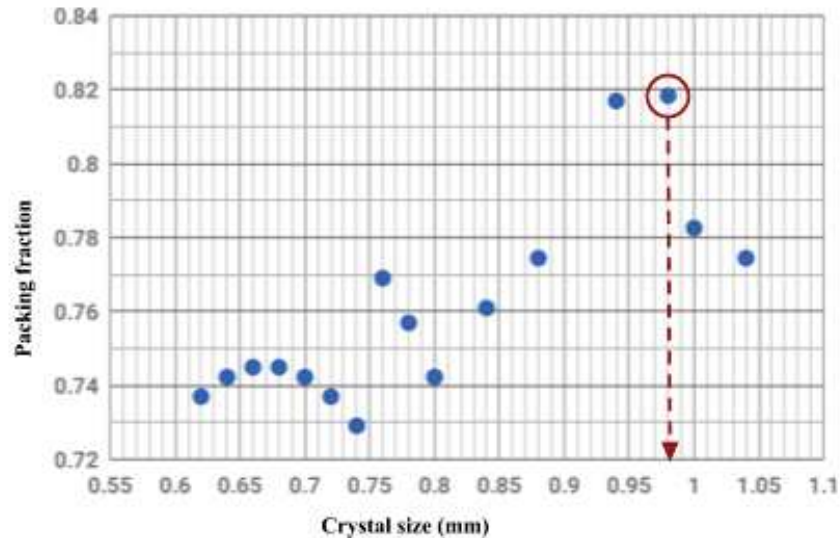


Figure 3.9 – Packing fraction (active area/total area) as a function of crystal size (mm)

Crystal size of 0.98 mm x 0.98 mm (with a pitch of 1.065 mm x 1.065 mm) has maximum value of packing fraction and is selected as a suitable option for designing the scanner A geometry. Figure 3.10 shows a photograph, taken in the lab, of two crystal matrices consisting of crystals with a cross sectional size of 0.98 mm x 0.98 mm.

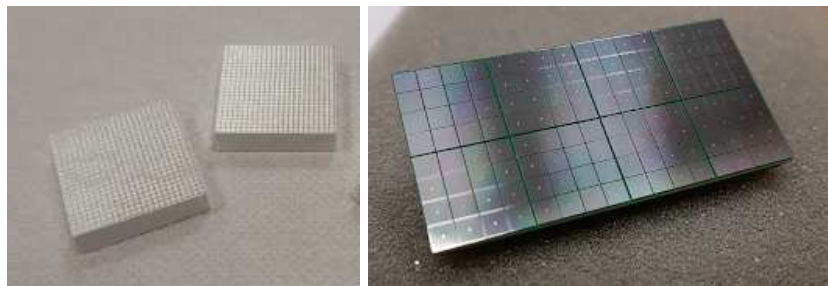


Figure 3.10 – Photograph of the (Left) LYSO crystal matrix where each crystal is having a size of 0.98 mm x 0.98 mm; (Right) MPPC photodetector array consisting of 2 x 4 modules each having a size of 13 mm x 13 mm. Each MPPC consists in 4 x 4 pixels of 3 x 3 mm with a pitch of 3.2 mm

Once the crystal size has been decided, the choice of crystal depth depends on several factors such as light collection efficiency, trade-off between spatial resolution and detection efficiency, availability of crystal lengths etc. It is interesting to study scanners with varying crystal depths due to the above mentioned factors. However, in this thesis a crystal depth of 8 mm has been investigated due to time



constraints.

An array of 2 x 4 (as shown in figure 3.10 right) forms a PET head for scanner A. Two such heads are arranged in axial direction, whereas eight heads are arranged in the transaxial direction to meet the fixed parameter requirements as described in section 3.1. The arrangement of crystal matrix over the photodetector array is shown in figure 3.11 (top). As per the available area of the 2 x 4 MPPC array and the size of the crystal, a matrix of 23 x 48 crystals is selected for each head.

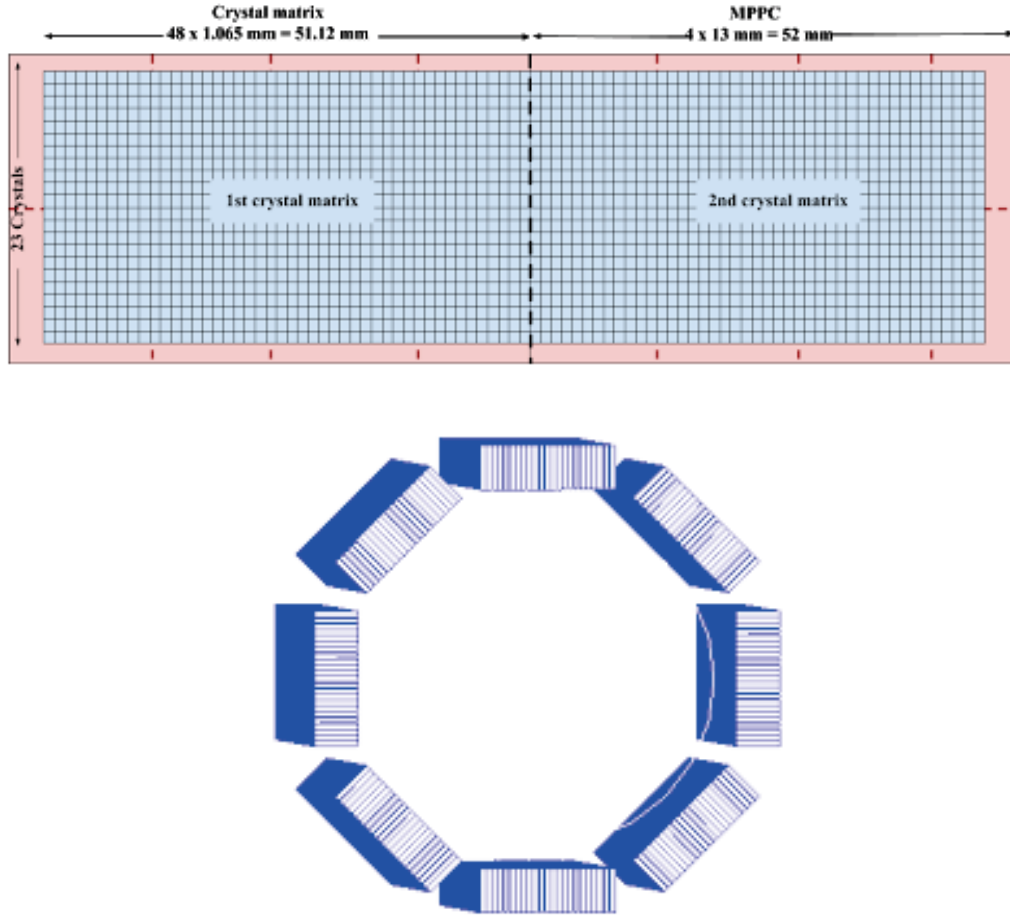


Figure 3.11 – Top: Illustration of two axial modules, each consisting of a crystal matrix (23 x 48 crystals) and a photodetectors array (2 x 4); Bottom: Transverse arrangement of radially elongated crystal matrices for scanner A generated via GATE MC simulation platform.

It can be noted from figure 3.11 (top row), that the crystal matrices are arranged in a manner such that there is no dead space between the two axial modules. Figure 3.11 (bottom row) presents the complete arrangement of crystal matrices in the transverse direction for scanner A.

### Discussion on 2D detection technique

Although this geometry is used at present by several commercially available preclinical PET scanners, there are certain limitations which are discussed below:

1. Improving spatial resolution in such geometries require reducing crystal size, which leads to increased cost as well as reduced fill factor that adversely impacts the scanner detection efficiency. However, with smaller crystal size we can distinguish the first Compton interaction when we have a one to one coupling or improved algorithm to localize this first interaction.
2. The information about the position of interaction can only be extracted at the level of crystal index (2D) and no information about the DOI in the crystal can be obtained. Therefore, increasing crystal depth, to improve the scanner detection efficiency, degrades the spatial resolution via parallax error and optimization of trade off between spatial resolution and detection efficiency becomes complicated.

Thus in order to optimize the trade-off between spatial resolution and detection efficiency, DOI measurement is an important requirement. DOI measurement improves the performance the spatial resolution and detection efficiency simultaneously. In the next section, we describe scanner B based on a different detection technique, which is an approach to optimize the complication faced in scanner A i.e., to provide the DOI measurement to a certain extent there by, optimizing spatial resolution and detection efficiency simultaneously.

### 3.4.2 Scanner B: 2D detection technique + binary sampling

Scanner B, is based on dual layer arrangement of crystal matrices, with a relative offset of half the crystal size in both x- and y- direction. This scanner geometry is basically an extension of scanner A, where an additional crystal matrix is radially coupled to the existing crystal matrix of Scanner A as illustrated in figure 3.12.

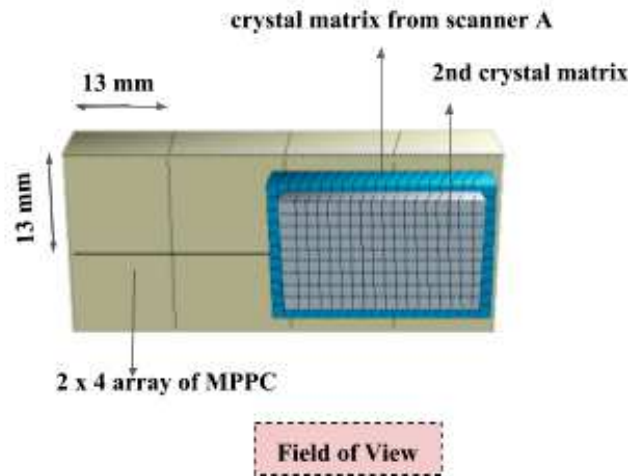


Figure 3.12 – Illustration of 2 layer of crystal matrix (in different shades of blue colour) radially coupled to each other with a relative offset of half the crystal size in both the directions.

When an incident gamma photon deposits its energy in the upper crystal matrix layer (or 2nd layer of figure 3.12), the scintillation photons propagate towards the lower crystal matrix and are divided among four lower crystals. Therefore, the centroid of the output optical photons distribution is located in the middle of the four lower crystals, which corresponds to the position of the upper crystal in which the gamma photon interaction has occurred. On the other hand, if an incident gamma photon deposits its energy in a crystal in the lower crystal matrix layer, the scintillation light output is distributed directly over the photodetector channels and provides the information on the crystal ID in which gamma photon has interacted. Since the two crystal matrices have a shift relative to each other, the centroid



of the output optical photon distribution corresponding to the gamma interactions in the upper and lower layer is shifted as well, as shown in figure 3.13.

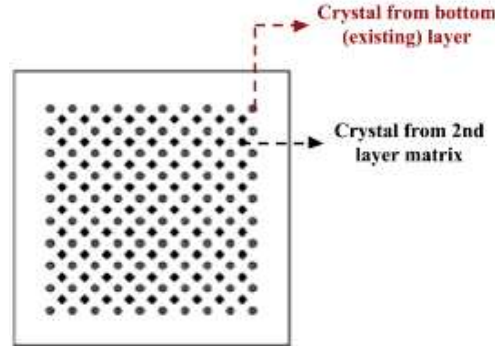


Figure 3.13 – The flood histogram pattern for dual layer crystal PET scanner, showing the flood positions corresponding to crystals belonging to different crystals. (Adapted from [Ito 11])

With this technique we can approximate the DOI determination up to crystal layer ID level and thus it is referred as 2D detection technique with binary sampling for DOI encoding. This technique improves the detection efficiency due to increased depth (contribution of both layers) of the crystal in the radial direction, with no further additional spatial resolution degradation due to parallax error. On the other hand, if we have the same crystal depth in scanner A (pixelated single layer crystal matrix) and scanner B (pixelated dual layer crystal matrix), scanner B improves the spatial resolution due to DOI decoding.

### Scanner specifications

Since this scanner geometry is an extension of scanner A, it is designed using the same scanner specifications (crystal matrix, crystal size, crystal depth, photodetector array etc.,) as described for scanner A. Scanner B consists of an additional layer of crystal matrix, coupled to the existing matrix of scanner A, with an offset. The coupling of two matrices is done in such a way that the center of each crystal of second layer lies at the center of four crystals of the existing crystal matrix. This arrangement makes it possible for optical photons generated in top layer, to be distributed over the photodetector via 4 crystals of the bottom layer and the event is positioned separately in the flood histogram. Thus the two crystal layers are distinguished and such distinction requires accurate positioning of the crystal layers, and essentially the same crystal size in both the layers. The bottom layer crystal size selection has been made for scanner A, thus the top layer is composed of crystals having a cross-sectional size of 0.98 mm x 0.98 mm. The crystal length of the second matrix layer is made shorter than the crystal length of the existing (bottom) crystal layer to make the probability of interaction the same in both layers.

Thus the second matrix layer consists of crystals having a size of 0.98 mm x 0.98 mm and a depth of 6 mm and is coupled to the crystal matrix from scanner A. In order to identify in which crystal layer the interaction has occurred, we make the top layer with one less row and column and offset it by half the crystal size. Thus the top layer for scanner B consists of 22 x 47 crystals per PET module. Considering both the crystal layers in a PET module, the scanner B consists of total 22 x 47 (top layer) + 23 x 48 (bottom layer) crystals. Since the scanner B is designed using scanner A, there is no dead space between the axial modules. Figure 3.14 illustrates the arrangement of crystal matrices (the crystal matrix from scanner A is shown in blue colour, whereas, the second layer is shown in red colour).

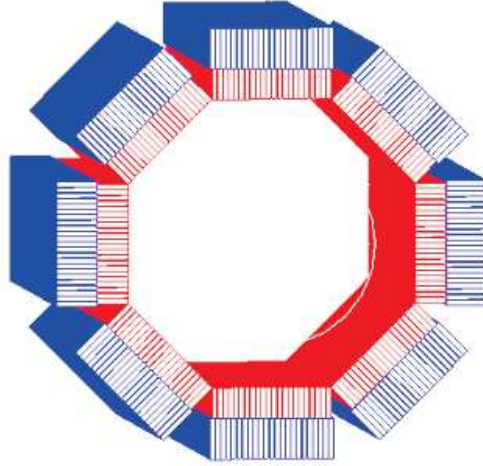


Figure 3.14 – Transverse arrangement of crystals for scanner B generated via GATE MC simulation tool. The scanner consist of two crystal matrices (layer shown in blue - crystal matrix layer from scanner A consisting of 23 x 48 crystals; layer shown in red - second crystal matrix consisting of 22 x 47 crystals)

### Discussion on 2D detection technique + binary sampling

This detection technique has been already developed for commercially available dedicated breast cancer detection PET scanner [Thompson 95, Murthy 00] and for small animal imaging PET scanners [Chung 04]. The major advantage of this technique is the performance improvement without adding the complications of using more photodetectors and associated electronics. However, there are certain challenges, which are discussed below:

1. This technique requires an accurate arrangement of 2 layers of crystal matrices, so that the optical photon distribution from a crystal of a layer does not overlap with the other distribution from another crystal.
2. Another disadvantage of this technique lies in light collection efficiency due to light dispersion resulting from the top layer on to the bottom layer.

Other designs that permit higher level of DOI encoding have been proposed and can be found in the literature ([Ito 11]). Two different scanner designs making use of different DOI techniques, have been already investigated at our facility. Based on those detection techniques and the results obtained via previous work, geometries for scanner C and scanner D are designed and are discussed in the two succeeding sections.

### 3.4.3 Scanner C: 2D detection technique + continuous sampling

Scanner C is designed using axially elongated pixelated crystal matrix as shown in figure 3.15 (Left), making it different from the conventional scanner geometries as discussed before. Once an incident gamma photon deposits its energy in a crystal, the optical photons generated propagate throughout the length of the crystal and get detected at both the ends. The crystal matrix is readout at both ends by a set of photodetectors. In the transverse direction (x,y) (figure 3.15 right), spatial resolution is given by the crystal section and the spatial resolution in the axial direction is given by the light

sharing between both photodetectors [Salvador 09b].

We estimate the axial interaction position ( $z$ ) of the incident gamma photon by using the contrast ( $C$ ) between the amounts of light recorded at both the ends of the crystal as given below:

$$C = \frac{S_R - S_L}{S_R + S_L} \quad (3.1)$$

where  $S_R$  and  $S_L$  represent the signals detected at the right and the left side of the crystal. By fitting the experimental contrast, a calibration curve is obtained for the entire crystal axial length ( $z$ ) as explained in [Salvador 09b, Brasse 04]. Thus, for a given signals ( $S_R$  and  $S_L$ ) detected at the respective side of the crystal, the contrast is calculated using equation 3.1. The corresponding axial position is derived with the help of the calibration curve.

Based on the crystal arrangement, this detection technique permits the 2D estimation of the interaction position in the transverse plane, based on the crystal size. It also provides the continuous readout in the axial direction of the scanner. Thus the technique is named as 2D detection technique + continuous sampling. The detection efficiency, for this scanner, depends on the number of crystals in the transverse direction and the geometry of the system. The principle advantage of this detection technique is that, due to a simplification in the depth encoding procedure, the spatial resolution and the detection efficiency are not correlated. This makes it possible to improve the detection efficiency along with the spatial resolution.

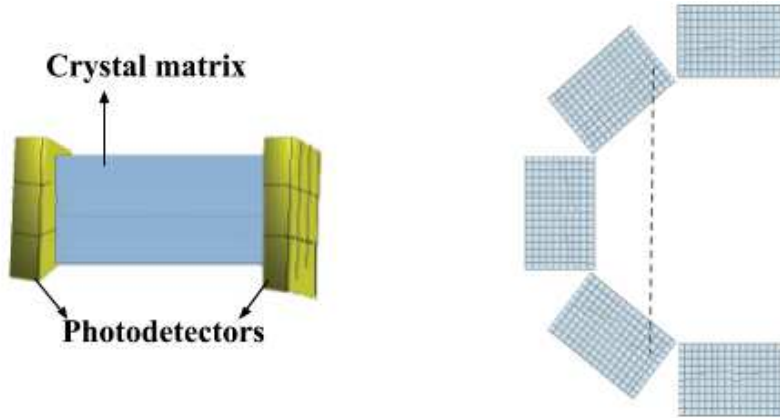


Figure 3.15 – Left: A module consisting of axially elongated crystal matrix readout at both the ends; Right: Illustration of the transverse view of scanner C presenting 5 modules (consist of 8 modules)

### Scanner specifications

This scanner configuration has already been studied and reported in the lab [Brard 13, Salvador 09b, Salvador 10]. The operative principles, the preliminary simulated performance, the effect of crystal coating and the crystal axial length on light sharing can be found in the literature [Jan 00, Shao 08, Yang 08]. In order to obtain a spatial resolution close to 1 mm in the axial direction, it has been demonstrated using both simulations and experimental acquisition by [Salvador 09b], that a 1.5 mm x 1.5 mm (transverse direction) x 20 mm (axial direction) LYSO:Ce crystal is a good candidate. The crystal dimensions for Scanner C are selected on the basis of this previous work performed in our lab. Figure 3.16 shows the transverse cross-section of a ring, presenting the arrangement of crystals in eight modules. A module consists in 16 x 24 crystals. The thickness of the 24 combined layers leads to 36 mm of LYSO crystal in the transverse direction, which corresponds to about three attenuation lengths

in order to absorb more than 90 % of the incident photons. The axial crystal length along with twice the photodetector depth accounts for axial length of a ring, i.e.,  $20 + 2 \times 1.3 = 22.6$  mm. In order to achieve the limit of axial FOV, as mentioned in fixed parameters, five such rings are arranged axially, to form the scanner C.

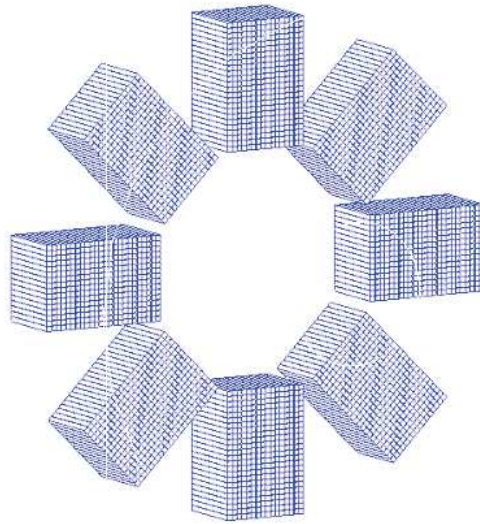


Figure 3.16 – Transverse arrangement of crystals for scanner C generated via GATE MC simulation platform. Crystals are axially (z- direction) elongated and are arranged in a matrix of  $16 \times 24 \times 1$  to form a module. The image presents only one ring consisting of 8 modules. The complete scanner C consists in 5 such rings

### Discussion on 2D detection technique + continuous sampling

The arrangement of crystals in scanner C allow to have DOI information (in terms of crystal ID), improving spatial resolution at the cFOV and even at the radial distances. Axially elongated crystal arrangement further allows us to arrange several layers of crystals in the transverse direction, thereby, improving detection efficiency simultaneously. However, there are certain drawbacks of this scanner geometry as discussed below:

1. Since the crystal length impacts the spatial resolution in the axial direction, increasing the crystal length deteriorates the spatial resolution [Salvador 10]. The selected crystal axial length of 20 mm is not sufficient to scan the entire length of small animal in a single scan. Thus five such crystal matrices are arranged axially in scanner C and each crystal matrix is readout at both ends. The presence of two photodetectors per crystal matrix contributes to the dead space as shown in figure 3.17.
2. Due to the presence of two photodetectors per crystal matrix, it also requires an increased number of photodetector channels and associated readout electronics. Thereby, potentially escalating the cost of the scanner. Thus, for commercial feasibility, this technique brings an issue concerning the manufacturing cost.

The foregoing scanner designs (scanner B and scanner C) improve the performance, as compared to the conventional design (scanner A) for small animal imaging by simultaneously optimizing the spatial

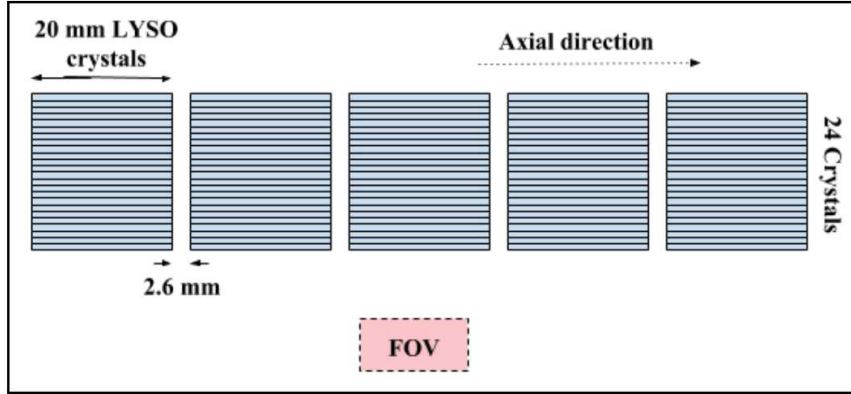


Figure 3.17 – Illustration of arrangement five axial modules, each consisting of 24 x 16 crystals. The axial arrangement of modules is consist of dead spaces ( = 2.6 mm) due to the presence of photodetectors

resolution and detection efficiency. However, these designs always require additional crystal matrices or additional photodetectors that escalate the cost. The next scanner, i.e., scanner D is a cost effective approach to improve the performance.

### 3.4.4 Scanner D: 3D detection technique

Most of the developed and commercially available small animal PET scanners are based on pixelated crystal matrix design [Marcinkowski 16]. The achievable spatial resolution in such scanner designs depends directly on the size of the crystal. However, as discussed before, there are certain drawbacks of employing pixelated crystal matrices such as complexity of fabricating finely pixelated crystal matrix, presence of dead spaces between the crystals, high cost, etc,. In order to overcome these limitations, the use of monolithic scintillator crystal has been proposed. Several research groups are developing preclinical PET scanners employing monolithic crystals [Bruyndonckx 06, Maas 06, Miyaoka 10, Carles 12, Cabello 13]. Furthermore, the position of gamma ray interaction in monolithic crystals is estimated from the optical photon distributions measured on the photodetector. The interaction position is typically estimated using a statistical based positioning algorithm such as Maximum-Likelihood (ML) estimation. Several positioning algorithm such as Mean Nearest Neighbour (MNN) positioning algorithm, neural networks, etc., can be found in the literature [Bruyndonckx 04, Li 10, Miyaoka 10, van Dam 11a, Marcinkowski 16, Tabacchini 17] to estimate the transverse coordinates. Different positioning algorithms to estimate the DOI of gamma photon can also be found in [Lerche 05, Ling 07, Van Dam 11b, Müller 18].

The last scanner design studied in this thesis, Scanner D, is designed using monolithic crystal. Figure 3.18 illustrates a module of Scanner D consists in monolithic scintillator crystal coupled to a multianode PMT. We estimate the transverse coordinate of interaction of gamma photon based on the centroid of the light spread on the photo detector. The DOI information is extracted using SCD circuit as explained in section 3.2.5 instead of using the conventional approach that depends on the extent of light spread. This scanner geometry enables us to estimate the DOI of gamma photon along with the estimates of x- and y- positions, thus this detection is regarded as 3D detection technique.

### Scanner specifications

The geometry of scanner D is designed on the basis of previous work performed at our facility [Boisson 17]. A module consists of a  $50 \text{ mm} \times 50 \text{ mm} \times 8 \text{ mm}^3$  (x-, y-, z- direction) monolithic

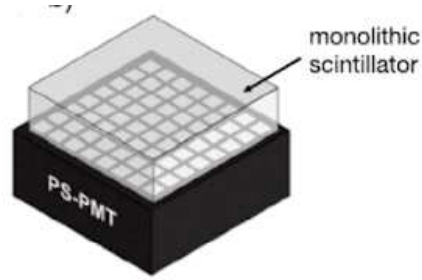


Figure 3.18 – Schematic illustration of monolithic scintillator crystal coupled to a multianode PMT. (Reprinted from [Ito 11])

LYSO crystal (Saint-Gobain) coupled to a H9500 PMT. The specifications are given in table 3.1. In the previous work, the spatial resolution in x- and y- direction for a module was measured using the resistive network. The mean spatial resolution value of 1.10 mm with an uncertainty of  $\pm 0.12$  mm FWHM was reported.

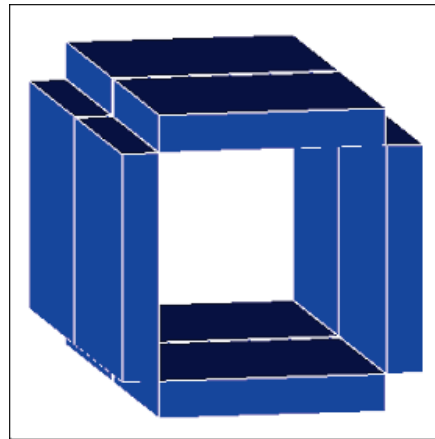


Figure 3.19 – Arrangement of crystals of scanner D generated via GATE MC simulation tool. Crystals are arranged in a square geometry and the size of each crystal is 50 mm x 50 mm x 8 mm. The image presents two rings, each consisting of 4 modules.

The final geometry of scanner D (figure 3.19) is designed using four modules per ring since the size of H9500 PMT is 52 mm x 52 mm, and the transaxial FOV is fixed to be close to 60 mm. In order to achieve the axial FOV close to 100 mm, scanner D consist of 2 rings. The size of the monolithic crystal is 50 mm and is coupled to 52 mm photodetector, this creates a 2 mm dead space between the two rings.

### Discussion on 3D detection technique

As compared to other three scanner geometries, this is the only scanner that consists of four modules per ring in the transverse plane. This factor impacts the scanner detection efficiency as well as spatial resolution when comparing with other scanner geometries. However, DOI capability of this design makes this scanner a very promising candidate for high resolution as well as high detection efficiency scanners. Measurements performed on this scanner design have shown that the intrinsic scanner resolution is comparable to that of scanners using arrays of small crystals. Further benefits of this scanner design are discussed below:



1. Since no dead spaces are present in case of pixelated crystal arrays to make them optically isolated, this scanner provides highest packing fraction among all the geometries discussed and thus improves the detection efficiency.
2. Scanner geometries employing pixelated crystal matrices also encounter issues like light collection losses. However, employing monolithic crystal faces no such complications (except at the edge where black paint is usually used) [Cherry 95].
3. Scanners employing monolithic crystal slabs are easier to manufacture as compared to other scanner geometries and is also a cheaper solution.

One important limitation of this scanner geometry is that for the increased amount of incoming events, the optical distribution can be merged and the determination of the barycenter can be difficult. This problem increases with the activity present in the FOV. This effect is reduced when using crystal matrix. The four discussed scanner geometries are evaluated to measure their performances. The measured performances are also compared to the performance of the state-of-art scanner, IRIS PET. In the next section, we discuss the geometry and other technical details of the IRIS PET scanner.

### 3.4.5 IRIS PET Scanner

It is a commercially available preclinical PET scanner installed at our facility. The scanner consists of two rings, each consisting of 8 modules. Each module consists in 27 (transaxial) and 26 (axial) LYSO: Ce crystals. The size of each crystal is 1.6 mm x 1.6 mm x 12 mm. All these modules are arranged in a manner to provide a 95 mm axial FOV and 80 mm transaxial FOV coverage. The 64 anode PMT (Hamamatsu H8500) is used as the photodetector and is directly coupled to the crystal matrix with no light guide between them. Each module can acquire coincidences with the six opposing modules (three in the same ring and three in another ring). Figure 3.20 (Left) shows the arrangement of radially elongated crystal matrices of IRIS PET scanner. Figure 3.20 (Right) presents an image of the IRIS PET scanner installed at the facility.

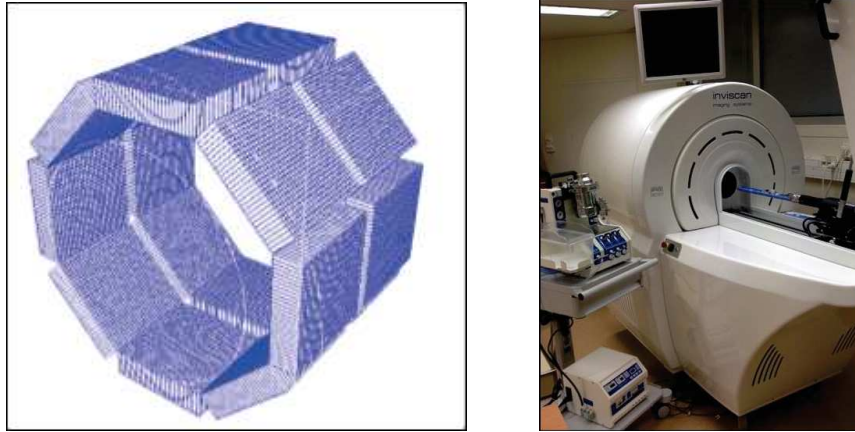


Figure 3.20 – Left: Arrangement of crystals in IRIS PET scanner generated via GATE MC simulation platform. Crystals are radially elongated and 27 x 26 crystal makes a module. The image presents two rings, each consisting of 8 modules. Right: image of the IRIS PET scanner installed at our facility

The scanner is based on the same detection technique as described for scanner A, i.e. 2D detection with no DOI information. The interaction position of gamma photon is decoded using Anger logic [Belcari 17].

### 3.5 Summary

The four different scanner geometries are discussed in this chapter. All the geometries are based on different arrangement of crystals and photodetectors. In the first scanner geometry (Scanner A), the idea is to improve the spatial resolution by reducing the crystal size and improving the detection efficiency by employing the thicker crystals. However, due to the lack of DOI encoding capabilities, the parallax error degrades the spatial resolution. Scanner B improves the scanner performance by improving the detection efficiency (by adding more crystals in the radial direction) and without further degrading the spatial resolution. Scanner C further improves the trade-off between spatial resolution and detection efficiency by incorporating high level of DOI encoding. So far, optimizing spatial resolution and detection efficiency simultaneously leads to escalating cost as the designs include more crystal matrices and photodetectors array. Scanner D, based on monolithic crystals, is a cheaper solution to improve the scanner performance and optimize the spatial resolution and detection efficiency trade off. Table 3.2 presents the summary for the specifications of all the scanners discussed in this chapter.

	Scanner A	Scanner B	Scanner C	Scanner D	IRIS
<b>Module</b>					
<b>Crystal material</b>	LYSO:Ce	LYSO:Ce	LYSO:Ce	LYSO:Ce	LYSO:Ce
<b>Crystal pixel size</b> $mm^3$	$0.98 \times 0.98 \times 8$	$0.98 \times 0.98 \times 6$ + $0.98 \times 0.98 \times 8$	$1.45 \times 1.45 \times 20$	$50 \times 50 \times 8$	$1.6 \times 1.6 \times 12$
<b>Crystal pixel pitch</b> $mm^2$	$1.065 \times 1.065$	$1.065 \times 1.065$	$1.5 \times 1.5$	$50 \times 50$	$1.68 \times 1.71$
<b>No. of crystals/module</b> $mm^2$	$23 \times 48$	$22 \times 47$ + $23 \times 48$	$24 \times 16$	$1 \times 1$	$27 \times 26$
<b>Scanner</b>					
<b>No. of modules</b>	$16(8 \times 2)$	$16(8 \times 2)$	$40(8 \times 5)$	$8(4 \times 2)$	$16(8 \times 2)$
<b>No. of crystals</b>	17,664	34,208	15,360	8	11,232
<b>Diameter (mm)</b>	68.60	56.60	66.80	50.50	110.80
<b>Length (mm)</b>	102.24	102.24	110.40	102.00	100.00

Table 3.2 – Summary of specifications of all the scanners discussed in this chapter

Once the scanner geometries have been defined, we require certain tools such as simulation platform, image reconstruction algorithms, quantification parameters etc., to reach the objectives of the thesis. All the discussed scanner geometries are simulated using GATE, a MC simulation platform. The details concerning the simulation settings (such as geometry and physics definition, setting coincidence energy and timing window etc), output data format and the output data analysis process are discussed in the next chapter. After the analysis part, the collected coincidence events are used to reconstruct the images. Two different approaches for reconstruction are used and are discussed in the next chapter.





## Chapter 4

# Simulation and Image reconstruction process

### Contents

---

<b>4.1</b>	<b>Introduction</b>	<b>73</b>
<b>4.2</b>	<b>Monte Carlo (MC) simulations</b>	<b>74</b>
<b>4.3</b>	<b>GATE simulation software</b>	<b>75</b>
4.3.1	Defining PET scanner geometry	75
4.3.2	Source, Phantom and underlying physics processes	76
4.3.3	Digitizer	76
<b>4.4</b>	<b>Data acquisition approach: Customized</b>	<b>78</b>
4.4.1	Introduction	78
4.4.2	Validation of the simulated model	79
<b>4.5</b>	<b>Image reconstruction process</b>	<b>80</b>
4.5.1	System Matrix (A)	81
4.5.2	MC generated SM elements ( $a_{ij}$ )	81
4.5.3	Analytical computation of SM elements ( $a_{ij}$ )	83
<b>4.6</b>	<b>CASToR: image reconstruction platform</b>	<b>85</b>
4.6.1	Main features	85
<b>4.7</b>	<b>CASToR's image reconstruction process</b>	<b>86</b>
4.7.1	Identification of geometrical information of the scanner geometry	86
4.7.2	Conversion of LM data to the CASToR data file format	88
4.7.3	Sensitivity profile generation	88
4.7.4	Image reconstruction process	89
4.7.5	Summary	90
<b>4.8</b>	<b>NEMA NU 4 Standards</b>	<b>90</b>
<b>4.9</b>	<b>Conclusion</b>	<b>91</b>

---

### 4.1 Introduction

In the field of nuclear medicine, optimization of scanner geometries for better performance is one of the active subjects [Selfridge 18, Schmall 16, Mikhaylova 15]. In order to optimize the scanner geometry, it is important to assess individually all the factors that influence its performance. In this thesis we are investigating four different scanners to study the effect of scanner performance parameters on the

reconstructed image quality. In order to reach our objectives, we are using a simulation platform, data analysis approach, image reconstruction software and NEMA NU-4 standards. In this chapter we describe all these approaches and standards used to investigate the scanners performance.

Computer simulations plays a valuable role to investigate new scanner designs, since computer simulations are usually inexpensive, faster and easily repeatable as compared to the experimentation. MC simulation is a widely used computer simulation approach and is used since 1960 in the field of medical physics [Loudos 07, Buvat 05]. Several PET dedicated MC computer codes are available today to simulate a variety of scanners. In the section 4.2 we provide a general introduction to MC simulations and to available simulation platforms. GATE (the Geant4 Application for Tomographic Emission) MC simulation software is used in the scope of this thesis to perform all the required simulations. Working of GATE software and simulation process at the user level is discussed in section 4.3. GATE simulation platform enables us to acquire the output coincidence events for a given set of input parameters (such as scanner geometry, material choice, energy, timing window, etc.) following an in-built signal processing chain. However, in this thesis instead of using the signal processing chain unit as provided by GATE software, the raw output data is extracted and is analyzed separately following some conditions which are discussed in the section 4.4. The analyzed GATE output events can be reconstructed to form meaningful images and several image reconstruction tools are available to perform the reconstruction process. Section 4.5 presents the details of the image reconstruction approach used along with the process of SM generation. An image reconstruction open source software CASToR (Customizable and Advanced Software for Tomographic Reconstruction) is used in this thesis to reconstruct simulated events. Section 4.6 and 4.7 describes CASToR's main characteristics and image reconstruction process. In order to estimate the scanner performance and to make comparisons, it is important to characterize their performance in terms of objective parameters, which can be evaluated via a standardized methodology. NEMA NU 4 standards [Goertzen 12] published in 2008 for preclinical PET scanners presents the objective parameters such as detection efficiency, spatial resolution, scatter function etc., along with the standard methodologies to estimate these parameters. In section 4.8, we provide an introduction to NEMA NU-4 2008 standards established for preclinical PET scanners. In section 4.8 we conclude the main points discussed in this chapter.

## 4.2 Monte Carlo (MC) simulations

The basic idea behind MC simulations is to generate a model as similar as possible to the real model of interest. The model is created to study the behaviour of a process based on known occurrence probabilities using random sampling of probability density functions (PDFs). When a photon or any other charged particle interacts with a medium, it gets scattered or absorbed depending upon the medium and the energy of the incident radiation. All these phenomenons are statistical in nature and thus serve as a perfect candidate to apply MC simulation techniques [Andreo 91, Turner 85]. In case of photon interaction investigation, the partial and total cross section data (based on the medium) represents known probabilities and are used to estimate the path length and the type of interaction occurred.

MC simulation techniques are nowadays commonly used in nuclear medicine to study the medical imaging devices, to predict their performance in a varied range of situations and to optimize their design [Zaidi 99]. A detailed description of the principles and application of MC simulations in the field of nuclear imaging can be found in [Zaidi 02, Loudos 07, Staelens 09, Ljungberg 12]. Two types of MC codes suitable for PET scanners in public domain [Buvat 02] are discussed below:

1. The general purpose codes: The Electron Gamma Shower (EGS) [Hirayama 05], Monte Carlo N-Particle (MCNP) [Briesmeister 00] and GEometry ANd Tracking (Geant4) [Barca 03] are some examples of general purpose simulation codes which simulate particle transportation and have been developed for high energy physics or for dosimetry. These codes require a lot of expertise to model and simulate the scanner configurations.

2. The dedicated codes for specific applications: PET-EGS based on EGS code [Nelson 90], Geant4 based GATE (Geant4 Application for emission Tomography) [Jan 04] are some examples of dedicated codes which are specifically designed to perform nuclear medicine PET and SPECT simulations. These codes are more user friendly as compared to the general purpose code.

MC simulations heavily depend on generation of random numbers to model the random behaviour of the studied system. The random number generator should deliver uncorrelated, uniform and reproducible random number sequences for a long period. A detailed description on different random number generators can be found in [Feldman 09]. In order to perform MC simulations to investigate the performance of different scanner designs, GATE software is used in the scope of this thesis. The next section provides a discussion on the simulation procedure used in GATE for the proposed scanner geometries described in chapter 3.

## 4.3 GATE simulation software

GATE is a widely used open source MC simulation software based on Geant4 libraries. It is designed based on the idea that the user may not be from the coding background thus it can be used without having programming knowledge. Benefiting from the Geant4 physics libraries, GATE can accurately model the underlying physical processes of the complicated emission tomography scanners. GATE simulations have been validated by several research groups through extensive studies by comparing them with the experimental results for a number of commercial PET systems [Jan 05c, Lamare 04, Lamare 06, Schmidtlein 06] as well as preclinical small animal PET systems [Jan 05b, Merheb 06, Baghaei 07, Yang 10, Lu 16]. To perform simulations in GATE, one needs to provide the description of different components necessary for the accurate modelling of a PET scanner, starting from the geometry configuration, radioactive source used, object geometry, the associated physics processes, the output format and the formulation of the processing chain for the detected events. In the following sections, we will describe the basic approach required to simulate a scanner in GATE such as defining the scanner geometry in section 4.3.1, defining the source, phantom and the underlying physics processes in section 4.3.2 and the data acquisition approach in section 4.3.3. The basic architecture of GATE for in depth knowledge can be found in literature [Jan 04] and it should be noted that only the application layer of GATE, which is used to perform simulations is discussed in the proceeding sections.

### 4.3.1 Defining PET scanner geometry

To simulate a scanner in GATE platform, the geometry and the arrangement of its components need to be defined accurately in a sequential manner. All the components of the scanners are defined as 'Volumes' and each volume is characterized by its shape, size, position and material composition (default material assigned is air). The very first volume defined is known as 'world', which is basically a box, centered at the origin. The world volume should be as big as to include the entire scanner geometry. The particle tracking stops when particle leaves this world volume. The second volume is defined as daughter of the world volume and this daughter volume specifies the type of scanner to be simulated (example: SPECTHead, cylindricalPET, ecat etc). For all the scanner geometries studied in this thesis work, the systems are cylindricalPET systems, which assume that the scanners are based on a cylindrical configuration. Each system (cylindricalPET in our case) has a predefined tree level structure of different volumes with each volume having its own specific order. For example, the tree structure of cylindricalPET scanner system consists in rsectors, modules, submodules, crystals and layers. All these volumes are linked together following a tree like structure where each branch represents a volume. Particles are then tracked through these sequentially arranged volumes.

When the user defines a scanner geometry, the volumes can be defined using any name (except for the volume specifying the scanner type). However, once the geometry is defined, all these volumes are required to be linked to the system i.e., defining which volume corresponds to rsectors, modules,

submodules, crystals and layers. Further, in order to store information about the particle interaction withing a specific volume, a Sensitive Detector (SD) should be attached to that volume. The complete geometrical configuration as per GATE definitions for all the scanners discussed in chapter 3 is given in appendix 1. In order to assign the material properties to a given volume ID, GATE uses Geant4 material libraries in combination with user defined material compositions. All the information concerning the material properties and composition are stored in the GateMaterial.db file.

#### 4.3.2 Source, Phantom and underlying physics processes

In order to define a source, one has to first specify the type of source (such as back-to-back, gamma, positron etc.). Once the type has been specified, the distribution and the shape of the source is defined. A source can have different possible spatial distributions such as volume, point, beam, plane, or surface (default distribution is point distribution). For each defined distribution, different shapes can be assigned such as for a plane source, the source shape can be defined as circle, annulus, ellipsoid, square or rectangle. For both surface and volume sources, it can be a sphere, ellipsoid or cylinder. After specifying the shape, the user needs to define the parameters corresponding to the defined shape (such as specifying the radius value for a circular shape). After the source type, the distribution, the activity of the source has to be defined. Other characteristics such as the direction of emission (solid angle), the energy distribution can also be defined by the user. Once the characteristics of the object to be imaged have been defined, GATE makes use of Geant4 General Particle Source (GPS) and database to shoot particles. The decay rate of the defined source depends on the specified activity and on the simulated time specified.

The phantom geometries created in this thesis are based on the same approach as to build the scanner geometries. This is defined as an analytical approach which involves creating various basic shapes of phantom, e.g. sphere, cylinder, box etc. The material of these phantoms can be set to any material of choice by inserting the associated keyword as given in the materials file. Phantom is also defined as the daughter volume of world volume. Further, in order to extract the particles interaction information inside the phantom, the phantom geometry should be attached with a phantom sensitive detector following the keyword 'attachPhantomSD'.

In order to model different physical processes such as radioactive source decay, particle interaction process for a range of energies and within a range of material compositions etc., GATE makes use of Geant4 libraries [Agostinelli 03]. User can also interactively select the required different interaction processes such as Photoelectric effect, Compton scattering, Rayleigh scattering etc. The purpose of defining which physics processes are used in simulations is to decide which interaction will take place. For MC simulations, this is done using pseudo-random numbers which are uniformly distributed in the interval  $[0,1]$ . These random numbers are used to determine the Mean Free Path (MFP), i.e., the length between two consecutive interactions, for each interaction process and the process for which the determined MFP is shortest, is chosen.

After defining the scanner geometry, the required source and the underlying physics processes, in order to perform simulations and get the output file containing information on the interactions of the particles, one needs to specify the signal processing chain to analyze the interactions. The signal processing chain analyzing the particles interactions is known as Digitizer module and this module is discussed in the next subsection.

#### 4.3.3 Digitizer

Once the user has specified the required details on scanner geometry, materials, source, physics involved, simulation time and has initiated the simulation, the particles are generated corresponding to their parameters (initial type, time, energy and momentum). An elementary trajectory step, which

is defined as 'step' in Geant4, is applied and it represents the path of a particle between discrete interactions. The particle's energy, momentum and trajectory step length changes from one interaction to another depending on the nature of interaction, type of particles, and the material through which particle is traversing. If the volume ID through which the particle is traversing and interacting have an attached a SD, only then the interaction information between the particle and the volume ID is stored and such interactions are known as 'hits'. The information stored for each hit corresponds to the deposited energy, time of interaction, type of interaction, volume ID where interaction has occurred etc. The same particle will continue to interact and the corresponding hits will be registered until the particle's energy becomes lower than a predefined energy value (specified by the user), or until the particle goes out of the sensitive volume. The information on the total trajectory of a particle is thus registered with the help of all the hits generated along its track.

However, the real scanners do not provide sequential information for each hit generated by each particle. Thus, in order to build the acquired hits into physical observables as given by a realistic scanner, a module called 'digitizer' is added and it enables the user to specify the sampling methods for the registered hits. Digitizer filters all the hits generated by a particle during its trajectory and generates a single entry in a file called 'Singles', which characterizes a single value of energy deposited by a particle and a position of the interaction of the particle. To process a single from a set of hits generated, digitizer module makes use of a series of signal processors as shown in figure 4.1. The output at each step along the processor series is defined as a pulse. Introduction to the signal processing units is given below:

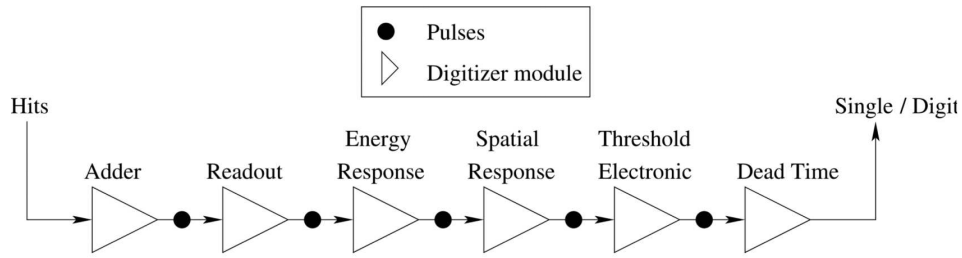


Figure 4.1 – Digitizer module consisting of a series of signal processing units to process hits into a single. (Reprinted from [Loudos 07])

1. Adder: The first unit of digitizer module is 'Adder'. For a particle interacting at multiple positions (i.e. creating multiple hits) within a crystal, the adder sums the deposited energy of these hits to yield a pulse or a Single. This is due to the fact that the electronics always measure an integrated signal, and do not have the time or energy resolution necessary to distinguish between the individual interactions of the particle within a crystal. The position of each single is given on the basis of the energy-weighted centroid of the hit positions. The time of the pulse is set to that of the first hit within the volume. Furthermore, if a particle interacts in several SDs, the hit adder module will provide a list of individual singles for each SD.
2. Readout: The second unit of the digitizer module is 'Readout'. This unit adds the multiple singles generated by a particle interacting within different crystals of the scanner. This yields a final pulse containing the total energy deposited within all the crystals. The position of the single depends on the policy defined by the user. There are two possibilities of defining the policies. First being the 'winner-takes-all' policy, the position of the pulse is the one that has the maximum energy [Jan 04]. For the second one 'energy-centroid' policy, the position is determined by weighting the crystal indices of each pulse by the deposited energy in order to get the energy centroid position. In this case, only the crystal index is determined, and the actual Cartesian coordinates of the resulting pulse are reset to the center of this crystal.

3. Following the above two units which group hits into singles and then sum singles, other units, as shown in figure 4.1, are also present in GATE such as energy resolution, energy window, spatial resolution, time resolution etc, which transform the resulting singles into the physical observables as expected following the behaviour of the photo-detector, electronics and acquisition system. The other modules are not mandatory modules and can be used to further mimic the details of the realistic scanner output as per user's requirements. The energy response unit serves two functions, first to apply a Gaussian blur to the energy of the pulse for a user defined FWHM; and secondly to provide an upper and a lower energy threshold window. A further in depth description on energy response unit and on other shown units can be found in [Jan 04].

Once the simulated events are analyzed by the digitizer chain, singles that are in coincidence are then sorted to find the coincidence events. Whenever the time interval between the two singles is less than what is specified by the user, those pairs of singles can be considered as coincidence events. GATE generates output files, namely Hits.dat, Singles.dat, Coincidences.dat (if user turns the flags ON for all these files).

These files contain detailed information on the interaction process, energy deposition, location and time of interaction, number of interactions that took place in the object and in the scanner geometry. However, as explained in chapter 3 (section 3.2.5), SCD readout approach and electronics have been developed in our lab to determine the position of interaction of gamma photons in a given module. In this thesis work, the hits are analyzed as per the data acquisition system developed in our lab and the different units of digitizer modules are not used. Only the mandatory units such as Adder and Readout are used to acquire hits and singles. The process of analyzing the hits to form the coincidence events as we get in real experiments using the SCD approach developed in our lab is given in the next section.

## 4.4 Data acquisition approach: Customized

### 4.4.1 Introduction

Digitizer module analyzes the recorded hits of a particle interacting within a SD volume and provides the user with output coincident events. In our lab a readout detection system has been developed to efficiently analyze the acquired events as per real scanner acquisition. However, the designed readout detection system's behaviour is different from the output of the digitizer chain. Unlike the GATE platform, the detection system designed for scanners do not perform a barycentric calculation for the estimation of the detection position. Following are the key points that explain the difference in the behaviours of the designed readout detection system:

1. The designed detection system is capable of discarding the events in which an incident gamma photon interacts in two different rsectors because estimating the barycenter of such events will lead to LOR positioning error.
2. The designed detection system can discriminate or identify two interactions occurring in two different crystals separated by a single crystal. E.Brard in his work [Brard 13] estimated the probability of the number of interactions of 511 keV gamma photons per module (of LYSO crystal). In his work, he simulated a cylindrical source of uniform activity without taking into account the scattering and attenuation of 511 keV gamma photons in the FOV. It has been reported that for and beyond the 3 interactions, the probability of occurrence becomes low. The occurrence probability is reported to be 10% for 3 interactions, only 2% for 4 interactions and 0.2% for 5 interactions. He further demonstrated that for the cases where incident gamma photon interacts in two different crystals of a module, in 70% of the cases, the first interaction results in lower deposited energy. Thus, the crystal in which minimum energy is deposited by the incident gamma photon is considered as the first interaction position. It should be noted that this approach is exactly opposite to the digitizer as discussed in the previous section.



3. In case of interactions within two consecutive crystals, the detection system cannot discriminate between two different positions of interaction and thus provides the crystal ID on the basis of barycenter estimation.

In order to mimic the expected behaviour of the developed readout system, a computer processing approach has already been developed in our lab and the same was used in this thesis to analyze the simulated events to sort coincidence events. The developed approach is described below:

1. The GATE output files ("hits" and "singles") are read in parallel. For each event contained in the .singles file, the corresponding "hits" are searched and if the interaction leads to an ionization, which will lead to its detection by the system (emission of optical photons), then the interaction is considered. Such events are stored in an output binary file along with its characteristics such as energy deposited value, interaction position, type of interaction etc. However, if an event in .singles file includes multiple rsectors, or several interactions, then the events are discarded.
2. Once the events are stored in a binary file, the events are further treated on the basis of their energy deposited (minimum energy deposited hit position is selected or following the Anger logic in case of IRIS PET scanner) to provide the crystal indices of the affected crystals. At the end of this step, the coincident events are stored in the output List Mode (LM) files.
3. The last step includes the system characteristics, such as energy window, timing window etc. Depending on the values obtained, the events are rejected or accepted.

It should be noted that the same approach has been developed for the IRIS PET scanner. However, the position of interaction of the incident gamma photons is estimated following the Anger logic (discussed in chapter 1). GATE platform allows the user to store the simulated data as ASCII or root output files. Following the simulation approach as explained in this chapter, we simulate IRIS PET scanner. In the next section, we will compare the simulated detection efficiency with the real acquisition for the IRIS PET scanner installed in our facility to validate the developed simulation geometry and the readout data analysis approach.

#### 4.4.2 Validation of the simulated model

As discussed in the previous sections, all the scanner geometries are defined in GATE. In order to validate the scanners definition, the simulation environment and the readout detection system, we designed the GATE simulation model of the IRIS PET scanner installed in our facility and simulated it to estimate the detection efficiency for a point source located at different axial positions at the central axis (radial distance = 0) in the scanner and to compare the nature of the curve obtained with the curve obtained via experimental acquisition. To compare the two approaches (simulation and experimental), all the acquisition conditions are kept the same and these conditions are discussed below:

1. The coincidence events are acquired for a Na22 point source located at different axial locations.
2. The coincidence energy window is set as 250 keV - 750 keV.
3. The coincidence timing window for acquiring coincidence events is set as 5.2 ns.

Figure 4.2 shows the comparison for the detection efficiency curve obtained via simulations and experimental acquisition for a point source initially kept at the cFOV of the scanner and is then moved in the either axial direction at an interval of 10 mm. The energy resolution used to perform the simulations is 14% at 511 keV. The experimental acquisition (in red) is reported to have a maximum detection efficiency of  $6.73 \pm 1.0\%$  at the cFOV. For the same scanner, the reported detection efficiency



value is obtained via MC simulation (in blue), following customized readout analysis approach (section 4.4) is  $7.18 \pm 1.1\%$ . The detection efficiency is estimated as the ratio of the number of photons detected to the number of photons emitted. The efficiency value obtained experimentally is lower than the simulated efficiency. This underestimation can be explained by measuring the fluctuations related to the detection system itself. The two curves shows the same behaviour such as sharp central peak followed by the plateau on both sides. Since IRIS PET scanner consists in two axial rings, separated by a distance equal to four times the pixel size (acting as a dead space), we get the plateau on either side.

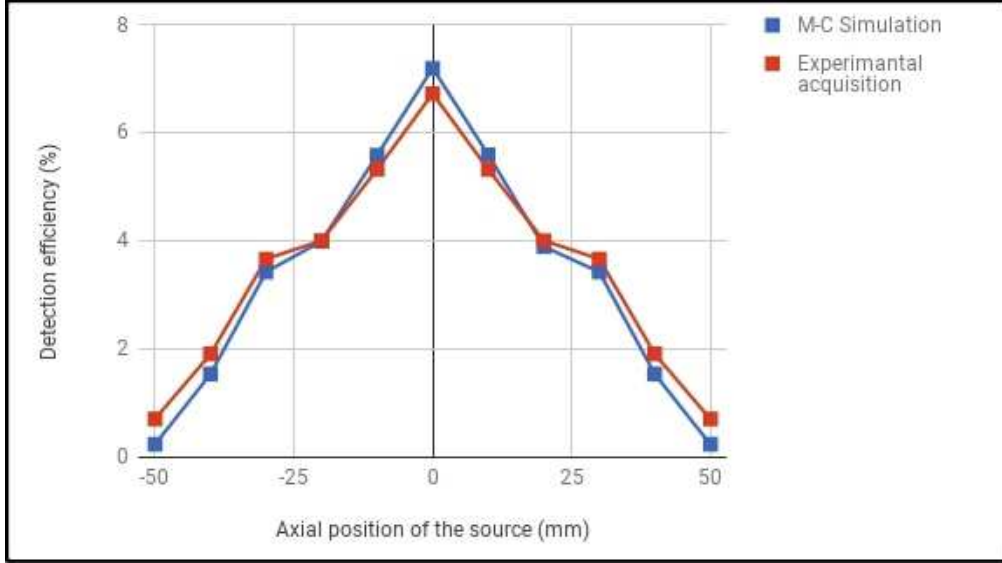


Figure 4.2 – Graph showing the comparison of detection efficiency curve obtained for a point source placed at different axial positions along the radial center of the scanner. The blue curve presents the detection efficiency values obtained via MC simulations and the red curve represents the real acquisition values.

Further, S.Salvador [Salvador 09a] validated in his thesis work, the simulation model and the read-out data analysis approach (same as discussed in the previous section) for the scanner employing axially oriented crystals. The same scanner geometry is used in this thesis work and the scanner is designated as scanner C.

Once the simulated geometry is validated for detection efficiency and the data analysis approach, these coincidence events are used as input to the image reconstruction process. In this thesis, iterative image reconstruction process (MLEM) is used to generate the images as discussed in chapter 1. In the next section, we describe the image reconstruction process along with the different approaches to compute SM elements.

## 4.5 Image reconstruction process

As mentioned in chapter 1, one of the objectives of my thesis is to investigate the feasibility of an open source software CASToR to reconstruct images from the collected data. The version of CASToR, used in the thesis work reconstructs images only through MLEM algorithm. Thus, MLEM algorithm is used in this work to reconstruct the simulated coincidence events. In iterative image reconstruction process, an initial estimate of an image ( $f^0$ : 3D image matrix) is made and the forward projections ( $q_i$ ) are estimated based on the SM elements and image estimate as given below:

$$q_i = \sum_{j=1}^N a_{ij} \times C_j \quad (4.1)$$

where  $C_j$  represents the events in the  $j^{th}$  voxel of an image estimate,  $q_i$  represents a projection for  $i^{th}$  detector pair and  $a_{ij}$  represents the probability that the event has originated from the  $j^{th}$  voxel and is recorded by the  $i^{th}$  detector pair. These forward projections are then compared with the acquired projections. After comparing, based on the ratio between the two sets of projections (estimated and acquired), the corrections are made to improve the previously considered image estimate and get a new image estimate ( $f^1$ ) as shown in the equation below:

$$f_i^{k+1} = \frac{f_i^k}{\sum_{j=1}^m a_{ij}} \sum_{j=1}^m a_{ij} \frac{p_j}{\sum_{i'=1}^n a_{i'j} C_{i'}^k} \quad (4.2)$$

Further iterations are performed to compare the two sets of projections and successively improve the image estimate till the two projections start converging as explained in chapter 1 (section 1.4.1). As it can be seen from equation 4.1, the projections computed for an image estimate is strongly influenced by the accuracy of the system matrix elements and further equation 4.2 presents the impact of SM elements on the next image estimate. Thus, it can be concluded that for the iterative image reconstruction algorithms, such as MLEM, SM is regarded as a central element and therefore, it is essential to accurately estimate it. In the next section, we discuss two different approaches to generate the SM elements.

#### 4.5.1 System Matrix (A)

The estimation and storage of the SM elements  $a_{ij}$  can be a very laborious task due to the large size of the matrix. A SM should include all the process such as positron range, photon non collinearity, and detector-related effects (including crystal widths, inter-crystal scattering and inter-crystal penetration). SM ( $A$ ) can be factorized into several small matrices [Rahmim 13], where each small matrix corresponds to a relevant aspect as shown below:

$$A = A_{det.blur} A_{geom} A_{det.sens} A_{attn} A_{positron} \quad (4.3)$$

where  $A_{positron}$  is an image space matrix component which models the positron range effect [Qi 05].  $A_{attn}$  and  $A_{det.sens}$  matrices contain the attenuation and the normalization factors [Badawi 98] respectively.  $A_{geom}$  matrix models the effect due to the scanner geometry accounting for the geometrical efficiency and  $A_{det.blur}$  models detector blurring effects due to inter crystal scatter, crystal depth interaction, photon non collinearity [Tohme 09]. There are different approaches to estimate the system matrix elements such as estimation via MC simulations, estimating SM elements via analytical projectors or estimating experimentally via a real scanner acquisition. In this thesis, we will use two approaches to obtain SM i.e., via MC simulations and using analytical projectors and these two approaches are discussed in the next subsections.

#### 4.5.2 MC generated SM elements ( $a_{ij}$ )

As suggested by Veklerov et al [Veklerov 88] for clinical PET imaging, MC simulations can be used to generate SM elements. SM elements estimated via MC simulations take into account all the physical and geometrical phenomenons occurring in the scanner and in the scanning object such as inter crystal scattering, crystal depth, attenuation and scattering in the object, positron range, non collinearity etc. It requires the user to define the scanner geometry, along with required physics processes and simulated the whole arrangement in GATE. The source is defined in the form of a cylinder with a volume covering essentially the complete FOV of the defined scanner. The used source only takes into account the physics of the detection and since no attenuation and scattering mediums are used, the

attenuation and scatter events are not considered. Once the acquisition is done, the FOV is voxelized to determine the probability of emission in a particular voxel. We are generating the SM for the discussed scanners using MC simulations and the factors like positron range, positron non collinearity are not considered. Thus, the simulation consists of an isotropically emitting back-to-back 511 keV gamma photons source. The simulations were performed to obtain several coincidence events emitted by each image voxel. However, it should be noted that the number of events recorded to generate SM, influence the overall quality of the SM and thus also the image quality of the reconstructed images. The effect of number of recorded coincidence events used to estimate SM elements is studied in the next chapter. Each element  $a_{ij}$  is determined by estimating the number of coincidence event originated from each image voxel  $j$  as well as by estimating the number of events detected along the  $i^{th}$  LOR. Thus

$$a_{ij} = \frac{N_i^D}{N_j^E} \quad (4.4)$$

where  $N_i^D$  corresponds to the number of photons detected along the  $i^{th}$  LOR and  $N_j^E$  corresponds to the number of photons emitted from the voxel  $j$ . MC simulation is a validated approach to generate accurate SM elements, however, there are certain limitations of this approach such as:

1. Storage complications: The space on the disk occupied by the SM is completely dependent on the number of elements present in it (i.e., product of  $i$  LORs and  $j$  image voxels). For the four scanner geometries investigated in this thesis, we are trying to keep the same axial and transaxial FOV. Thus the voxelized FOV or the image space is also defined to have the same number of voxels for all the scanners i.e., 100 x 100 x 270 voxels. In other words, the image space consists in 100 x 100 voxels in each transverse slice and complete scanners contains 270 transverse slices. Each voxels has a size of 0.4 mm x 0.4 mm x 0.4 mm (voxel size is a compromise between the scanner spatial resolution and storage space. Reducing the voxel sizes, increases the total voxel number). Furthermore, the number of LORs is a fixed value for a given scanner geometry depending upon the number of crystals present in the scanner. Table 4.1 provides the information on number of crystals, LORs, image voxels and thus the size of resulting system matrix for all four scanners as a product of crystal pairs and image voxels.

Scanners	Crystals ( $n$ )	Crystal pair's (LOR's $\frac{n(n-1)}{2}$ )	Image space	SM elements
A	17,664 (23 x 48 x 8 x 2)	$1.5 \times 10^8$	2,700,000	$4.05 \times 10^{14}$
B	34,208 (17,664 + 22 x 47 x 8 x 2)	$5.8 \times 10^8$	2,700,000	$15.66 \times 10^{14}$
C	307,200 (16 x 20 x 8 x 5 x 24)	$471.8 \times 10^8$	2,700,000	$12.73 \times 10^{16}$
D	160,000 (50 x 50 x 8 x 4 x 2)	$127.9 \times 10^8$	2,700,000	$3.45 \times 10^{16}$

Table 4.1 – Summary of SM elements for all the scanners investigated in this thesis as a function of crystal pairs and image voxels

The major limitations of this approach of SM generation are, firstly the huge in-memory storage cost of the SM elements and secondly the computational cost of looking up the data due to the huge size of the SM.

2. Computation time: As mentioned before, the accuracy of SM elements depends on the number of coincidence events recorded. In order to improve the quality of the SM and thus the resulting

image quality, a large number of photons must be simulated. In order to acquire large number of events, instead of running one single and long simulation, we used grid computing environment available in our laboratory and divided one long simulation into several small simulations running in parallel. Furthermore, both computation time and storage complication can be reduced by the use of some symmetries depending on the scanner geometry.

Scanner D as explained in chapter 3, employs monolithic crystal to detect the coincidence events. This scanner configuration has been already experimentally evaluated and reported to have an intrinsic spatial resolution close to 1.0 mm in all three directions. Thus, in order to discretize the continuous sampling offered by monolithic crystal, we voxelize the monolithic crystal into small crystals of size 1.0 mm x 1.0 mm x 1.0 mm. Similarly, axially elongated crystals of Scanner C are also voxelized in the axial direction into small crystals each having an axial length of 1 mm.

In the next section we will discuss another approach to compute the SM elements i.e., using analytical projectors.

### 4.5.3 Analytical computation of SM elements ( $a_{ij}$ )

MC simulations accurately models the  $A_{geom}$  and  $A_{det.blur}$  sub-matrices of the SM but brings the challenges associated with long simulation times and storage of SM elements. Furthermore, sub-matrices corresponding to factors like positron range, non collinearity, attenuation are not modeled since we are simulating back-to-back gamma photon source without any attenuation or scattering medium present in the FOV. These sub-matrix elements ( $A_{geom}$  and  $A_{det.blur}$ ) can also be computed analytically on-the-fly which reduces the storage complication of all the elements as well as the long simulation time issue. The analytical approach to populate a SM is based on the usage of different projectors estimating elements via line integral model [Joseph 82] or area integral model. There are also some accurate projectors which can be used to estimate  $A_{det.blur}$  elements [Strul 03, Selivanov 00]. In this thesis, we are estimating the SM elements using the geometrical projectors. The reason behind using only the geometrical projectors is that we are using an image reconstruction software (CASToR) which has implemented only the geometrical projectors. This software is described in detail in section 4.6.

Following are some examples of geometrical projectors which can be used to perform projection and back projection operations:

1. **Pixel driven projector:** One of the simplest algorithm to perform projection step involves pixel-driven projectors (Peters 1981). This projector works by visiting each pixel in a loop and the center of each pixel is projected on the detector as shown in figure 4.3 (left). The pixel-driven projector is rarely used to perform forward projection because it tends to introduce high-frequency artifacts [Levakhina 14]. The pixel-driven projector is preferred to perform back projection.
2. **Ray driven projector:** The projector works by connecting the detector elements by straight lines according to the scanner geometry and the projection value is calculated as a weighted sum of all pixels that lie on the line. This projector is preferred for forward projection operations (such as in estimation of SM elements) where a value from the detector element is distributed along the line using some weighting. To date, several ray driven projectors are available (Siddon, variants of Siddon [Siddon 85, Jacobs 98], Joseph [Joseph 82] etc) and the most commonly used example is siddon projector. In 1984, Siddon published a fast and consistent analytical projector approach called Siddon's projector. In siddon projector, each matrix element is calculated as the intersection length of a specific LOR in a given image voxel as shown in the figure 4.4. Siddon projector results in accelerated projection speed since the system matrix element is calculated by line integral instead of volume integral. However, the siddon's projector does not take into account the crystal size since the LOR is drawn from the center of one crystal to another and thus the intrinsic resolution provided by the detector cannot be modelled accurately. This limitation

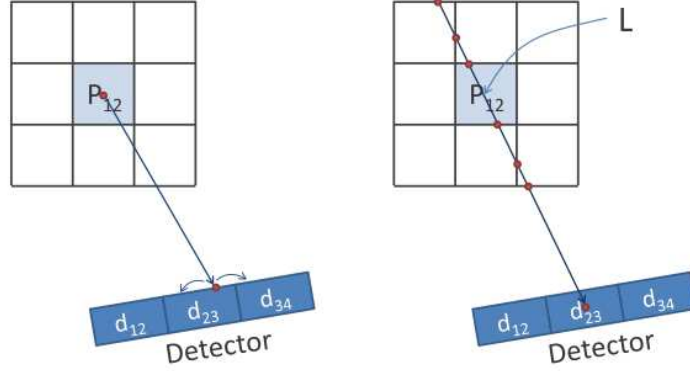


Figure 4.3 – Illustration of pixel driven (left) and ray driven (right) projectors. The mapping is shown only for a detector module of the detector pair.

of the projector impacts the accuracy of estimating the system matrix element and thus the image quality.

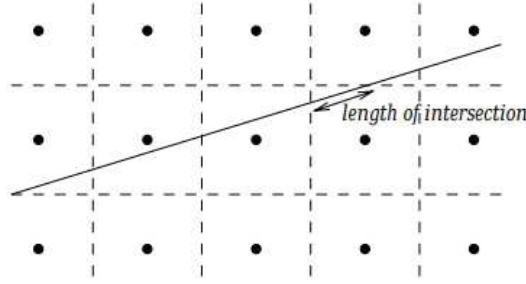


Figure 4.4 – Illustration of a three dimensional voxel grid along one axis. The SM elements  $a_{ij}$  for  $i^{th}$  LOR and  $j^{th}$  voxel is computed as the length of the intersection between the  $i^{th}$  LOR and  $j^{th}$  voxel (Reprinted from [Turbell 01])

3. **Distance driven projector:** In 2002, De Man and Basu introduced the concept of distance-driven projector [De Man 02] and later extended it to 3D [De Man 04]. Distance-driven projection is essentially a combination of ray-driven projection and pixel-driven techniques. In 2D distance-driven projection, pixel boundaries and detector-pair boundaries are mapped to a common axis. Then, the length of the overlap between detector-pair and pixel boundaries is used to determine the weight, used in the projection of a pixel or the back-projection of a detector-pair element. Figure 4.5 (right) shows the overlap mapped for an image pixel on a common axis and the detectors are also mapped on the same axis.

Further, [Manjeshwar 06] extend the distance-driven approach described by [De Man 02] for PET scanners. Consider a 1D example, figure 4.5 (left), the activity in pixels  $x_1, x_2, x_3, \dots$  is represented by  $X_1, X_2, X_3, \dots$  where as the measurement in detector-pairs  $u_1, u_2, u_3, \dots$  is represented by  $U_1, U_2, U_3, \dots$ . The distance-driven projector uses the length-of the overlap ( $w_0, w_1, w_2, \dots$ ) to calculate the weighted sum of activities from pixel to estimate the measurement in detector-pairs.

$$U_2 = w_1 \times X_2 + w_2 \times X_3 \quad (4.5)$$

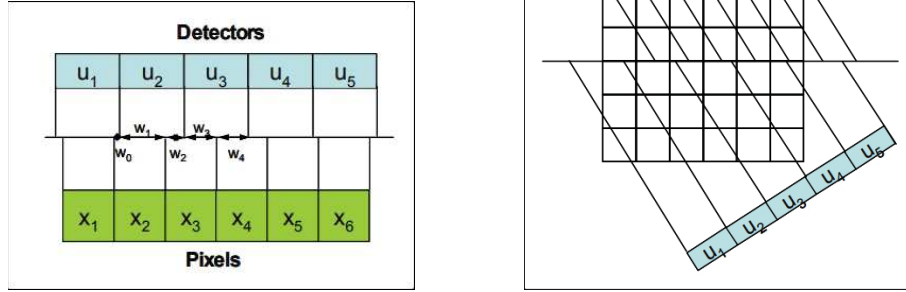


Figure 4.5 – Illustration of distance driven projection process (Reprinted from [Manjeshwar 06])

In the equation above  $w_1$  corresponds to the element of the system matrix between the pixel  $x_2$  and the detector-pair  $u_1$ , whereas  $w_2$  corresponds to the element of the system matrix between the pixel  $x_3$  and detector-pair  $u_2$ . In 3D distance-driven model, a common plane is used instead of a common axis. The boundaries of voxels are mapped to the plane along with the boundaries of the detectors. The area of the overlap is used to compute the projection weights.

The distance driven projector has been recognized as far to be the most exact projector which can accurately account for finite-width of the detectors. It is also reported [De Man 04] that distance driven projector does not introduce the artifacts in the reconstructed image as introduced by other projectors such as Siddon. The distance driven projector is used in the thesis to estimate the SM elements on-the-fly for all the discussed scanner geometries. Once the SM elements are estimated, images are reconstructed using MLEM algorithm. However, in order to generate images using analytical (distance driven) projector, an open source software CASToR is used. In the next section, we will discuss in detail the main features, the complete working process, advantages and limitations of this open-source reconstruction platform for emission tomography.

## 4.6 CASToR: image reconstruction platform

Customizable and Advanced Software for Tomographic Reconstruction (CASToR) platform is an open source software to perform tomographic image reconstruction. The whole software is written in C++. It is designed to use directly the GATE input and output files. The complete process of image reconstruction is divided into different parts, such as identification of scanner geometry, conversion of GATE output data into its readable format, sensitivity profile generation and finally the reconstruction process. Since the software recognizes the GATE files, it facilitates the description of the scanner geometry and the coincidence events. CASToR framework is used to reconstruct images in this thesis. The research presented in this thesis was developed using different versions of CASToR from version 1.0 (released on March 23, 2017) to version 2.0.1 released on April 27, 2018. In the proceeding section, we present some main characteristics of CASToR tool.

### 4.6.1 Main features

The main features of current versions of CASToR are given below:

1. It only performs iterative image reconstruction and the supported imaging modalities include PET and SPECT scanners.

2. Both list mode and histogram PET data format are supported. For both data formats, CASToR defines a data file as a collection of events.
3. In the current version, only MLEM algorithm is implemented which supports the reconstruction of list mode data. It uses interfile I/O format for storing images and data.
4. It supports reconstruction of images for GATE simulated data. However, in the current version only root format of the output data can be used.
5. It takes into account the attenuation and normalization corrections if an input binary file, containing appropriate corrections, and a header file is provided.
6. It works by using projectors (as discussed in section 4.5.2) and implemented projectors include original and accelerated versions of the Siddon [Siddon 85, Jacobs 98], Joseph [Joseph 82] (in version 1) and Distance driven [De Man 04] (in version 2).
7. It has two-level parallelism: a high level splitting of the data using MPI (Message Passing Interface) and a low-level multi-threading of the loops over the events using the Open-MP (Open Multi-Processing) libraries.

CASToR also has some added features such as it performs reconstruction of multi-frames and respiratory/cardiac gated acquisitions, image convolution and spatial regularization. However, these features are not used in the thesis work and thus are not discussed. In the current scope of my work, only the features related to PET imaging are discussed. We are only using list mode data format to generate CASToR readable files. As mentioned earlier, only the distance driven projector is used to perform forward and backward projections and even to compute the SM elements on-the-fly. In the next section we will discuss the different steps required to reconstruct images starting from list mode data as given by GATE.

## 4.7 CASToR's image reconstruction process

CASToR completes the whole process of image reconstruction in 4 steps. In step 1, the scanner geometry is identified following a specific approach as given in subsection 4.7.1 where each crystal is assigned a specific identification number, also called as CASToR ID. Once the CASToR IDs have been assigned, in step 2 CASToR reads the input list mode data and store each event in terms of CASToR IDs in a binary file and also generates a header file as explained in subsection 4.7.2. Later, in step 3, CASToR generates a sensitivity map before launching the iterations and in step 4, it performs the iterations to reconstruct the image. All the steps are explained below:

### 4.7.1 Identification of geometrical information of the scanner geometry

The first part of CASToR code is dedicated to generate an ASCII file (.geom) containing mandatory and optional fields to describe a scanner geometry. The mandatory field includes total number of crystals in the scanner, number of layers in which crystals are arranged, scanner radius, the number of rsectors, size of the crystal etc, whereas the optional parameters include the angle at which the first rsector is located, the direction in which the second rsector is located (clockwise or anticlockwise), number of modules and submodules in a rsector, the gap between the modules, submodules and crystals etc. CASToR defines the scanner geometry following the cylindrical PET system of GATE simulation and thus the whole scanner geometry is decomposed into 5 levels, referred as rsector, module, submodule, crystal and layer. All these nested levels are considered to be rectangular in shape. The interconnections between these nested levels are illustrated in figure 4.6.

The current implementation of CASToR code simply uses a command line to generate this ASCII file. Launching the command line 'castor-GATEMacToGeom' without arguments display only the main



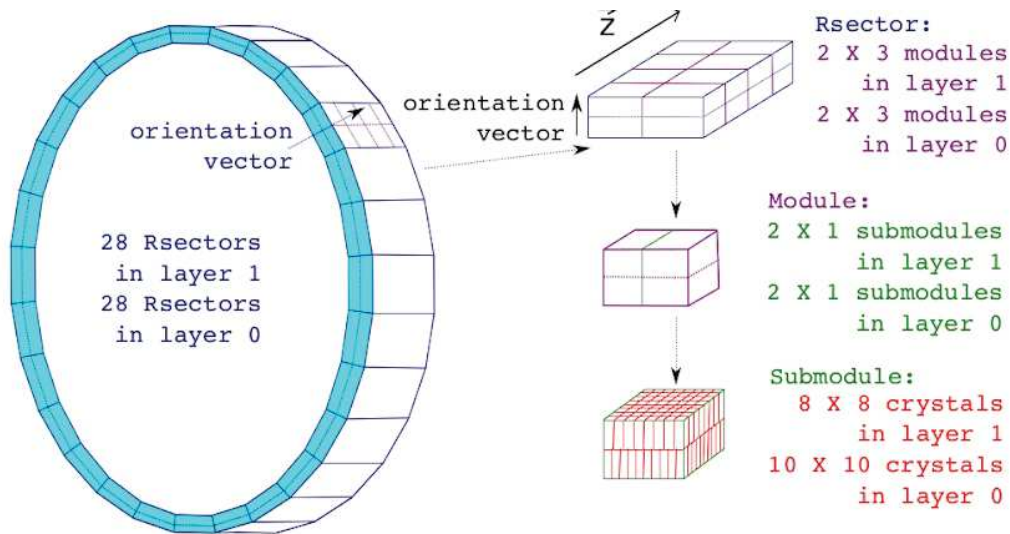


Figure 4.6 – Illustration of different nested levels of PET scanner geometry as read by CASToR. The figure presents a cylindrical PET system consisting of 2 layers and each layer contains 28 rsectors. Each rsector is composed of modules (2 in the transverse direction and 3 in the axial). Each module further contains 2 submodules in the transverse direction and each submodule contains pixelated crystal matrix. Layer 1, (having larger radius) contains a 8 x 8 crystal matrix and layer 0 (with smaller radius) contains a 10 x 10 crystal matrix ) presenting Rsectors, Modules, Submodules, Crystals and Layers. (Reprinted from [Merlin 18])

usage options. The command line interface for step 1 is shown in figure 4.7, where an input macro file (the one used in GATE to perform simulations), an output file name (to store the information on scanner geometry following CASToR's format) is required. The output file is saved by default in a subfolder named 'config/scanner' in the CASToR source tree.

```

File Edit View Search Terminal Tabs Help
/work/biosave/kaggarwa... x /biosave/kaggarwa/IRIS... x /biosave/kaggarwa/IRIS... x / x
sbgat352:/: castor-GATEMacToGeom
Invalid number of arguments. Please read the help section.

Usage: castor-GATEMacToGeom -m input_mac_file
                             -o output_geom_file
                             -v verbose

[Input settings]:
-m input_mac_file      : give the path to a GATE macro file describing a cylindricalPET, ecat or SPECThead system
-o output_geom_file    : give the alias of the output geom file which will be generated in the scanner repository
                        (default location: config/scanner/)

This program is part of the CASToR release version 2.0.1.

```

Figure 4.7 – Command line interface for step 1 illustrating the required input files and commands. CASToR requires input macro file as used in GATE and the output file name in which CASToR's readable format of scanner geometry will be stored

The user can also manually define or modify this ASCII file by providing the appropriate details of the scanner geometry. On the basis of the information provided in this ASCII file, all the crystals in the scanner are assigned with a unique identification number known as CASToR ID. Based on the angle at which the first rsector is located, the first crystal in that rsector is assigned CASToR ID 0.

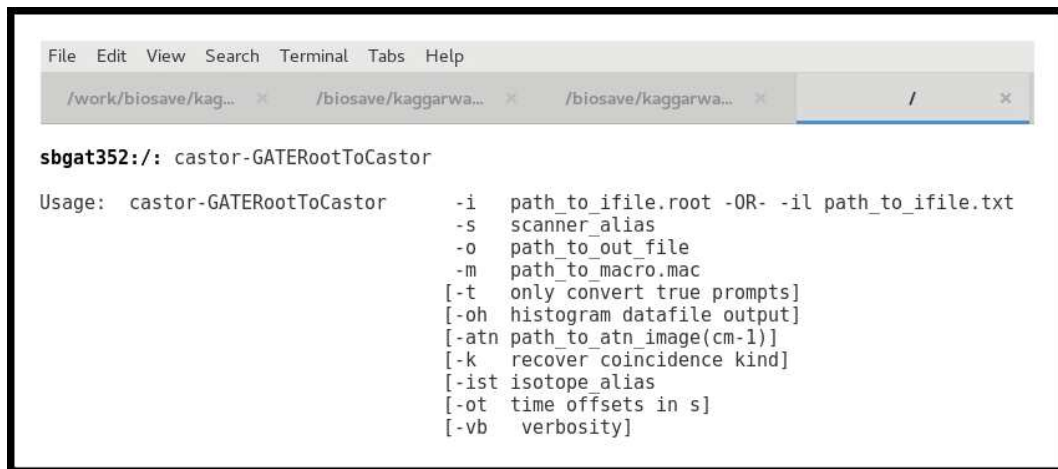


Given the direction of rotation, further CASToR IDs are assigned to other crystals. Crystals are first assigned CASToR IDs transversely along the crystal ring, following the given direction in the ASCII file (clockwise by default), and then axially across the crystal rings. If the scanner consists in multiple layers, all the crystals in the first layer are assigned CASToR IDs before switching to the crystals in the next layer. Once the unique CASToR IDs are assigned to all the crystals in the scanner, all the events or the correction data in the data files or in the correction files are recorded using these unique identification number. The geometry files generated by CASToR for the four scanners studied in this thesis are provided in the appendix A2.

The second step of CASToR code performs the function of converting the input data files consisting of events represented in the form of different nested levels (rsectors, modules, submodules, crystals, layers) into output files where each event is recorded in terms of CASToR IDs. The details on second step is given in the next subsection.

#### 4.7.2 Conversion of LM data to the CASToR data file format

CASToR has another command line interface which generates the CASToR readable format data files. This step converts an input LM data file (.root) consisting of coincident events defined in terms of crystal IDs, submodule IDs, module IDs, rsector IDs and layer IDs into two separate files: an ASCII header and a binary data file. The header file contains all the mandatory information about the data type (LM or histogram mode), the scanner file name (generated via step 1), as well as the information on the correction factors (if any) embedded into the data file. The binary data file contains the raw data from the acquisition or simulation in the form of CASToR IDs, time (in ms) and other correction factors (such as attenuation correction factors, normalization factors, if provided). Figure 4.8 presents the command line interface for data conversion step.



```

File Edit View Search Terminal Tabs Help

/work/biosave/kag...  /biosave/kaggarwa...  /biosave/kaggarwa...  /

sbgat352:/: castor-GATERootToCastor

Usage: castor-GATERootToCastor      -i path_to_ifile.root -OR- -il path_to_ifile.txt
                                   -s scanner_alias
                                   -o path_to_out_file
                                   -m path_to_macro.mac
                                   [-t only convert true prompts]
                                   [-oh histogram datafile output]
                                   [-atn path_to_atn_image(cm-1)]
                                   [-k recover coincidence kind]
                                   [-ist isotope alias]
                                   [-ot time offsets in s]
                                   [-vb verbosity]

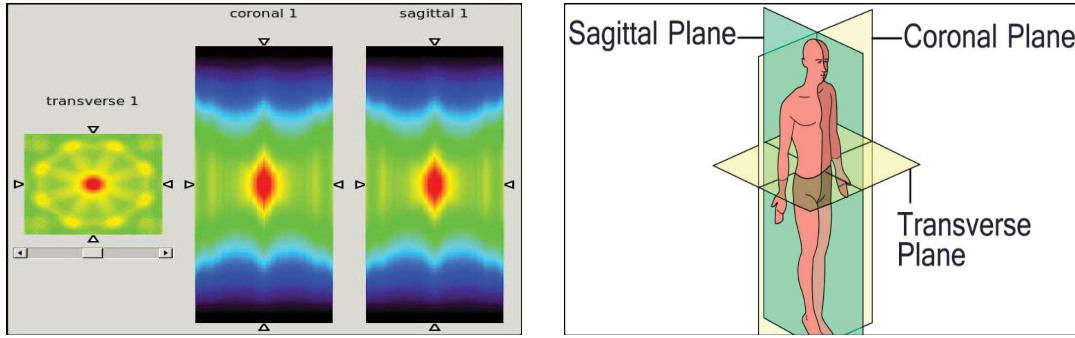
```

Figure 4.8 – Command line interface for step 2 illustrating the required input files and commands. For this step CASToR requires an input data file of root format as given by GATE, the name of the geometry file as generated in step 1, a name to store CASToR readable format output data file, input geometry file as also provided in step 1. The other required parameters are optional and are not used in this thesis

#### 4.7.3 Sensitivity profile generation

Before the image reconstruction step, CASToR computes a sensitivity profile where a backward projection step is performed over all possible detection elements present in the scanner. The sensitivity profile

generation process solely depends on the characteristics of the scanner geometry description as identified during the first step (Identification of geometrical information of the scanner geometry). Based on the description (scanner radius, size of the crystals, number of crystals etc), CASToR computes the Cartesian coordinate of the crystals and once the crystal Cartesian coordinates are determined, the back-projection step is performed (in order to estimate the  $\sum_{j=1}^m a_{ij}$  term present in the denominator of equation 4.2). While generating the profile, detection efficiency values for the crystals are not considered. If the user provides externally the normalization, attenuation correction file, these correction factors can also be used while generating the sensitivity profile.



(a) Sensitivity profile generated for Scanner A consisting of 8 head modules in a transverse ring and 23 x 48 crystals per head module. Sensitivity profile generated solely depends on the crystals of the scanner even if no event is detected by any crystal pair. This image basically presents summation of all  $a_{ij}$ 's for all  $i$ 's for a given  $j$ .

(b) The figure illustrates the three different planes 'Transverse' (the plane that is perpendicular to the axis of rotation of the scanner), 'Sagittal' (plane divides the body into its medial and lateral sides) and 'Coronal' (plane perpendicular to previous two planes). These three notations will be used to present the reconstructed images throughout in the thesis

Figure 4.9 – Illustration of: (a) an example of the sensitivity profile generated by CASToR; (b) the notation concerning the planes of imaging

Sensitivity profile is a 3D array having the same size of the image matrix. Each element of the sensitivity profile represents the summation of probability values for an event originated from that image voxel and detected by any detector pairs. Figure 4.9 (a) presents an example of sensitivity profile generated for Scanner A using distance driven projector. The size of the sensitivity profile generated is 100 x 100 x 270 where each voxel size is 0.4 mm x 0.4 mm x 0.4 mm. Figure 4.9 (b) illustrates the notations concerning the planes of imaging.

#### 4.7.4 Image reconstruction process

During the image reconstruction step, each event is processed one by one as it is stored in the CASToR binary file (generated during step 2). For each event recovered from the data file buffer, following sub-steps are performed:

1. Calculation of SM elements  $a_{ij}$  associated with the first event entry (i.e., the probability for a  $i^{th}$  event corresponding to all the  $j$  voxels, or in other words, one row of the SM). This sub-step is performed using on-the-fly projectors and the projector type can be specified by the user.
2. Once the SM elements are computed for a given event, the optimizer module computes forward model along the event ray for the current image estimate.
3. As per the optimization algorithm, the optimizer module computes the update term in the data space.

4. In the last sub-step, the optimizer module performs the back-projection process of the update term in the image space along the event ray.

The above mentioned sub-steps are performed for all the events stored. Also it should be noted that in the scope of this thesis work, distance driven projector is used for all the projection and back-projection process.

#### 4.7.5 Summary

CASToR is a research tool developed to reconstruct images for acquired or simulated data-sets, either from the clinical or experimental systems. Since each event is processed individually, CASToR provides another advantage of parallel execution to speed up the image reconstruction process. Further, since it estimates the SM elements on-the-fly, the complications for storing and accessing computationally heavy SM is not an issue which we generally need to face in case of MC generated SM. Despite the above mentioned advantages of CASToR, following are some challenges faced while using it to reconstruct images for the scanners discussed in chapter 3

1. While reconstructing image for the scanner employing continuous crystals, a virtually pixelized geometry is defined to perform step 1 and step 2.
2. During the computation of the SM elements, projectors do not take into account the detection efficiency of the different crystal pairs, which leads to the artifacts in the reconstructed images. To correct the images for the variations in detection efficiency, it is important to provide the correction values to account for these variations. This process of correcting detector efficiency variations is discussed in chapter 6.

In the next chapter, we will present the images reconstructed using CASToR software for all the scanner geometries.

## 4.8 NEMA NU 4 Standards

As we are comparing different scanner geometries, it is important to have a standard method to evaluate the scanner performance parameters. National Electrical Manufacturers Association (NEMA) propose a standard methodology [Li 15] to evaluate the performance of preclinical PET scanners. The aim of the standard is to establish a baseline for scanner performance measured under identical imaging conditions and to be independent of scanner geometry. NEMA NU-4 2008 standard states that the procedure to evaluate the scanner performance is applicable to all the preclinical PET scanner geometries i.e., scanners employing discrete crystals, monolithic crystals, rotating scanners, TOF scanners, single slice and multi slice scanners. Prior to NEMA NU-4, there were no specific defined standards to evaluate the performance of preclinical PET scanners. The NEMA NU 4-2008 standard provides a standard methodology to estimate the following performance parameters of preclinical PET scanners:

1. Spatial resolution
2. Sensitivity
3. Counting rate capabilities such as scatter fraction.
4. Image quality in terms of Recovery Coefficient (RC) and Uniformity.

To estimate the above mentioned parameters, NEMA also provides information on the data acquisition approach along with the source type, source position, activity, phantom, simulation run time etc. In this thesis, we are estimating spatial resolution, detection efficiency and image quality, discussed in chapter 5, for all the scanners. Once the performance parameters are estimated, we compare the

scanners on the basis of these estimated parameters. Since we are not evaluating the performance parameters for routine testing, comparison with other commercially available PET scanners, we are adapting some modifications from NEMA NU-4 standards such as iterative image reconstruction approach is used for all sorts of reconstruction mentioned. The modified techniques are applied to all the scanners investigated in this thesis so as to maintain the common baseline for the comparison.

## 4.9 Conclusion

This chapter presents all the simulation, data processing and the image reconstruction approaches used in this thesis. We have seen in this chapter, the implementation for an accurate modeling of the PET scanner geometry in GATE MC simulation platform. The latter has been validated for its detection efficiency with the experimentally obtained values for a point source located at different axial locations inside the scanner. The developed simulation model will thus be considered as a reference in the rest of this manuscript and on the similar basis, the geometry for four scanners (discussed in chapter 3) is made. The files defined to perform simulations for the scanners is given in appendix 1.

The data analysis approach discussed in this chapter is also used for all the scanners to analyze the GATE output files, to sort the coincidence events following the real output of the scanners. In this thesis work, MLEM algorithm is used to perform all the image reconstruction process. MC simulations to generate the SM element is considered to be a preferred choice, since it models accurately all the matrix elements by considering all the physical and geometrical effects, provided sufficient statistics are acquired. However as mentioned before, generating SM via MC simulations is a time consuming task and we are investigating four different geometries, thus generation of SM for all the scanners is a very long process. The time duration for which the scanner geometries are simulated to populate the SM are reported in the next chapter. In the meantime, we reconstructed the images for these scanners using on-the-fly generated SM elements via CASToR. CASToR, being capable of parallel computing, enables us to compute SM elements on the fly and thus, reconstruct the images in a very less time duration as compared to the SM generation via MC simulations. The comparison of image quality for the images reconstructed via CASToR and using MC generated SM is also reported in the next chapter.

In the next chapter, we characterize the performance parameters such as spatial resolution, detection efficiency and image quality for all the scanners using all the tools discussed in this chapter.



## Chapter 5

# Performance measurement of the proposed geometries

### Contents

---

<b>5.1</b>	<b>Introduction</b>	<b>93</b>
<b>5.2</b>	<b>Characterization of SM generated using MC simulations</b>	<b>94</b>
<b>5.3</b>	<b>Estimation of spatial resolution</b>	<b>97</b>
5.3.1	Simulation method	98
5.3.2	Data processing and analysis	98
5.3.3	Results and discussion	99
<b>5.4</b>	<b>Estimation of detection efficiency</b>	<b>100</b>
5.4.1	Simulation approach	102
5.4.2	Data process and analysis	102
5.4.3	Results	103
<b>5.5</b>	<b>Estimation of image quality</b>	<b>104</b>
5.5.1	Simulation approach	104
5.5.2	Data process and analysis	104
5.5.3	Results	106
<b>5.6</b>	<b>Conclusion</b>	<b>111</b>

---

### 5.1 Introduction

Once we gather all the tools to perform simulations, data analysis and image reconstruction, we estimate the performance parameters of all the investigated scanners. MLEM algorithm is used to perform image reconstruction process and for MLEM algorithm, we need to generate SM for all the scanner geometries. MC simulations serve as an ideal approach to generate a SM with accurate enough description of the scanner response, however, at the cost of longer simulation time and storage complications. Since SM elements are used both in forward and backward projection operations for each iteration of MLEM algorithm, the accuracy of SM elements strongly affect the quality of the reconstructed image. Thus it is important to characterize the MC generated SM for accuracy before using them to perform image reconstruction. In section 5.2, we discuss the parameters used for characterization of SM generated for the thesis work. We also reconstruct the images using CASToR software where projectors are used to estimate the SM elements on-the-fly.

The performance of all the designed scanner geometries are estimated in terms of spatial resolution and detection efficiency. The MC simulation, data analysis and image reconstruction is performed as described in NEMA NU-4 standards and are reported in section 5.3 and 5.4. It should be noted that a few methodologies as proposed in NEMA NU-4 2008 standards are modified and the modifications adapted to estimate the objective parameters are discussed in the respective sections. Once the scanners are characterized to estimate their performance parameters, the impact of these estimated parameters is studied on the overall image quality. The impact is studied by simulating IQP following the methodology given in NEMA NU-4 standards (section 5.5). SNR and RC values are reported to study the effect of scanner performance parameters on the image quality.

To conclude, following are the major objectives discussed in this chapter:

1. Characterization of MC simulation generated SM for all the discussed scanner geometries.
2. Estimation and comparison of performance parameters (spatial resolution and detection efficiency) following the standard methodology given in NEMA NU-4 2008.
3. Qualitative and quantitative comparison of the images reconstructed by two approaches (using MLEM algorithm): pre-computed SM generated via MC simulations; and using CASToR software where distance driven projector is used to estimate the SM elements on-the-fly.
4. Estimation of RC and SNR values from the reconstructed IQP images to study impact of investigated scanner designs on the overall image quality.

## 5.2 Characterization of SM generated using MC simulations

MC simulations mimic all the random processes associated with the emission and detection process, thus the SM generated using MC simulations account for all the involved physical effects. As a result, SM elements provide an accurate relationship between the imaging space and the scanner response as compared to the approach where SM elements are computed via projectors. However, the time consumption and storage of MC generated SM elements are two major limitation factors of this approach. Since SM is the central element of all the iterative reconstruction algorithms and is used in both forward and back projection operations in each iteration of image reconstruction process, the reconstructed image quality is highly dependent on the accuracy of the SM [Li 15, Rahmim 13, Rafecas 04]. In order to generate the SM via MC simulations, a uniform source placed over all the image voxels is simulated. Each SM element value is estimated by recording how many events are detected by a given detector pair divided by how many events are emitted from a given voxel. Since it is a probability, longer simulation time duration leads to high accuracy of the SM elements and reduces the statistical variations. We cannot run the simulations for life time to keep on improving the accuracy of SM elements so, we need to decide a stopping point where the SM elements have been accurately enough estimated so as to begin the image reconstruction process.

In literature [Li 15, Rafecas 04, Rafecas 03], two parameters are given to characterize the accuracy of the SM elements. These two parameters are:

1. **The number of non-zero matrix elements ( $N^{non-zero}$ ):** For a scanner geometry and given total number of image voxels, the number of SM elements is equal to the total number of crystal pairs multiplied by number of image voxels. As more events are detected in the scanner,  $N^{non-zero}$  increases (i.e., events originated from new image voxels are detected by new crystal pairs, filling zero elements of the SM). Once we reach the complete SM, new simulations would not imply an increase in the number of non-zero elements.

2. **The Mean Relative Error (MRE) per voxel ( $\sigma_{rel}$ ):** The second parameter used to characterize the SM is the MRE value per voxel [Rafecas 04] and is calculated as:

$$\sigma_{rel} = \frac{\sum_{i=0, j=0}^{(i-1)(j-1)} \frac{\sigma_{A_{ij}}}{A_{ij}}}{N} \quad (5.1)$$

where  $\sigma_{A_{ij}}$  is the standard deviation of the element  $A_{ij}$  and  $N$  is the total number of non-zero matrix elements. On the basis of the assumption that the emission and detection of photons are Poisson processes, the standard deviation  $\sigma_{A_{ij}}$  can be written as:

$$\sigma_{A_{ij}} = \sqrt{A_{ij}} \quad (5.2)$$

$A_{ij}$  being the number of detected events generated from an image voxel  $j$  and detected by  $i^{th}$  detector pair. Once we generate SM for which new simulations do not increase the number of non-zero elements, we estimate the MRE value per voxel. Once we reach the minimum MRE value per voxel for a given number of simulated events, we can conclude that the resulting SM consists of reasonably good statistics.

In order to reconstruct images using MLEM algorithm, we have performed MC simulations to generate SM elements for all the scanners. Generation of SM elements of a scanner is a long process and since we are investigating four different scanner geometries along with the state-of-art IRIS PET scanner, we have generated currently a first version of SM for all these scanners. To further speed up the simulation, photon non-collinearity and positron range were not included in the simulation. The SM for all the scanners are generated following the same approach as explained in chapter 4.

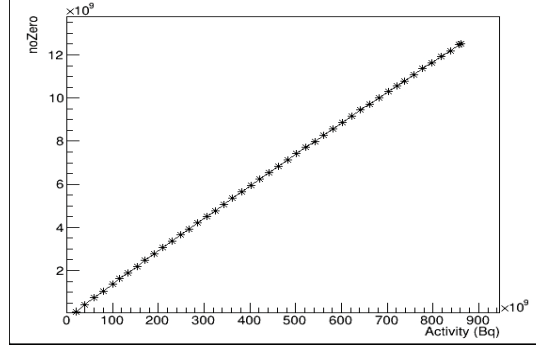
Scanner	Simulation run time (years)
IRIS	3.66
A	3.84
B	2.67
C	1.01
D	2.16

Table 5.1 – Summary on the simulation run time (years) for all the scanners to generate the SM via MC simulations. The given time corresponds to the simulation run time where simulations are running on a single thread (Intel Xeon E5-2670 @ 2.6 GHz)

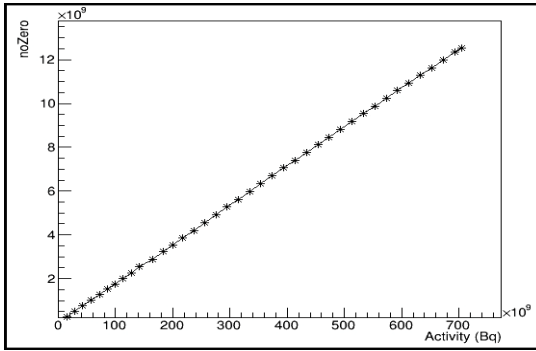
Table 5.1 reports the simulation run time (years) for the generation of first version of SM for all the scanners, assuming that the simulations are performed on a single thread. The image matrix size is taken as  $0.4 \text{ mm} \times 0.4 \text{ mm} \times 0.4 \text{ mm}$ . In this section we characterize the generated SM elements. Initially the SM are characterized to estimate non-zero elements as the function of simulated activity. Figure 5.1 provides the graphs showing the non-zero elements of a SM as a function of simulated activity for all the scanners.

In figure 5.1, the dependency of the number of non-zero elements of the SM is presented against the activity simulated for different scanners. It can be noted that for all the scanners, the non-zero SM elements are still increasing as more simulations are being launched and thus it can be concluded that we have not yet generated the complete SM for any of the scanner geometries. We are required to perform more simulations to further populate the SM for each scanner. Once we obtain the complete SM, the SM elements are characterized for their MRE values. However, due to time constraint, we take the current versions of generated SM to reconstruct images. Images are also reconstructed using CASToR software where SM elements are computed on-the-fly and the reconstructed images are

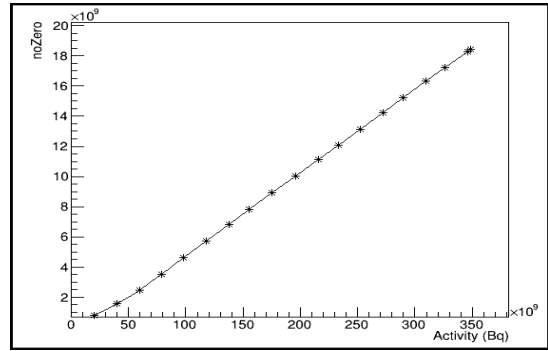




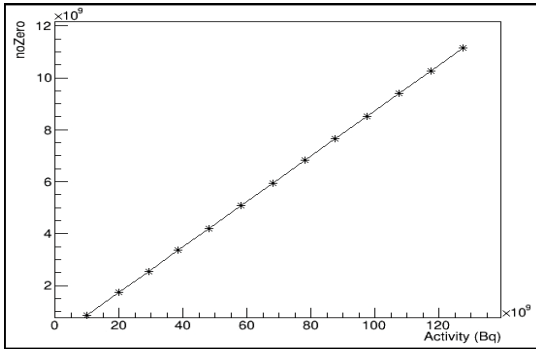
(a) SM characterization for IRIS PET consisting of  $1.7 \times 10^{14}$  SM elements



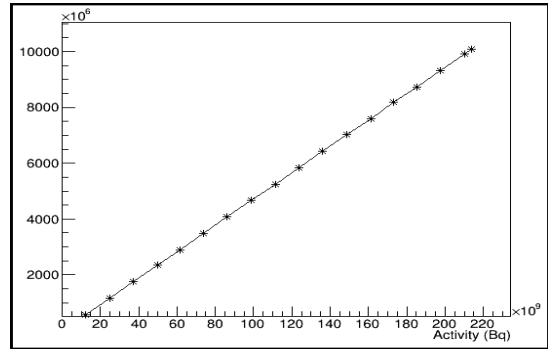
(b) SM characterization for Scanner A consisting of  $4.05 \times 10^{14}$



(c) SM characterization for Scanner B consisting of  $1.56 \times 10^{15}$



(d) SM characterization for Scanner C consisting of  $1.27 \times 10^{17}$



(e) SM characterization for Scanner D consisting of  $3.45 \times 10^{16}$

Figure 5.1 – Characterization of SM generated by performing MC simulations for IRIS PET scanner and for four designed scanners on the basis of non-zero elements.

compared with the images reconstructed via MC generated SM. In the next section we discuss the NEMA NU-4 standards established to evaluate the preclinical PET scanners performance.

### 5.3 Estimation of spatial resolution

Spatial resolution can be defined as the minimum distance at which two point sources are acquired and can be differentiated by the scanner [Goertzen 12]. The appropriate measure of spatial resolution would be to measure the width of the profile created when an object much smaller than the expected resolution of the system is imaged. A common method consists of imaging a point source and measuring the point spread function (PSF). Usually, the resolution is expressed as the FWHM of the profile. Very often this profile is approximated by a Gaussian function [Goertzen 12]. In this section, we calculate the theoretical values of different factors contributing to the achievable limit of the spatial resolution. Further we discuss the approach to estimate the spatial resolution as given in NEMA NU-4 standards. We also present the spatial resolution values estimated via simulations following the NEMA standard.

Positron physics (via non-zero positron range and photon non-collinearity ( $0.0022 \times \text{Diameter}$ )), and geometrical component of the scanner (via crystal width ( $d$ )) are two examples of the factors that put a limit to the spatial resolution. In chapter 1, we have discussed the impact of these factors. The ultimate scanner spatial resolution is given as the convolution of all the resolution response functions (Gaussian). The convolution of multiple Gaussian functions is another Gaussian with a FWHM given by adding the individual component FWHM in quadrature [Phelps 06]. The scanner spatial resolution at the cFOV  $R_{cFOV}$  thus can be written as:

$$R_{cFOV} \simeq \sqrt{R_{geom}^2 + (0.0022 \times D)^2 + \beta_+^2} \quad (5.3)$$

where  $R_{geom}$ ,  $D$  and  $\beta_+$  represents the resolution limit due to the geometric component of the scanner (i.e.,  $d/2$ ;  $d$  represents the crystal size); scanner diameter and positron range. The average positron range from a  $^{22}\text{Na}$  source embedded in an acrylic cube is also very close to 0.66 mm, the range of  $^{18}\text{F}$  positrons in water [Alessio 10]. Based on equation 5.3, table 5.2 provides the values of different factors contributing to the achievable limit of scanner spatial resolution and the resulting spatial resolution values for all the discussed scanner geometries and for the IRIS PET scanner at the cFOV.

Scanner	$R_{geom}$ ( $d/2$ )	Non-collinearity ( $0.0022 \times D$ )	Positron range (mm)	$R_{cFOV}$ (mm)
A	0.49	0.151	0.66	0.835
B	0.49	0.124	0.66	0.831
C	0.72	0.147	0.66	0.991
D	0.70	0.11	0.66	0.937
IRIS	0.84	0.244	0.66	1.200

Table 5.2 – Summary of factors contributing to the limit of spatial resolution and the calculated spatial resolution (mm) values at the cFOV based on these factors for all the scanner geometries.

It should be noted that Scanner D design employs monolithic scintillator crystal and for the geometries employing monolithic crystals, the intrinsic spatial resolution is not estimated by geometric component (i.e.,  $d/2$ ). It depends on the distribution of generated scintillation photons determining the position of the event. For monolithic crystals, the spatial resolution is given as (intrinsic spatial resolution  $/\sqrt{2}$ ) at the cFOV. For Scanner D, the intrinsic spatial resolution has been estimated to be  $\sim 1.0$  mm by experimentation [Boisson 17]. However, in order to generate SM elements and also to reconstruct images in CASToR, we are required to divide the monolithic crystal into discrete units.

Table 5.2 shows that all the scanner geometries are designed so as to provide a spatial resolution close to 1 mm at the cFOV. There are other factors as well that impacts the scanner spatial resolution

even at the cFOV such as incident angle of the photon at the detector, depth of interaction of the photon, reconstruction parameters and coding method for light spread. In the next subsections, we estimate the spatial resolution via MC simulations following the NEMA standard.

### 5.3.1 Simulation method

The section 3 of NEMA NU-4 2008 protocol presents a methodology to determine the spatial resolution using a  $^{22}\text{Na}$  point source. The source is embedded in an acrylic cube with no more than 0.3 mm active diameter in all the directions. The length of a side of the cube is 10 mm. By defining the scanner geometries and the above mentioned source, the simulations are performed using GATE platform. The source was initially kept at the cFOV to acquire the coincidence events and then the source was moved to 5, 10 and 15 mm radial offset to the cFOV as shown in figure 5.2. It should be noted that the radial positions specified in NEMA are 5, 10, 15 and 25 mm, however, Scanner D has a FOV of 50.50 mm and thus we are not estimating the spatial resolution at 25 mm radial position. It is mentioned in NEMA NU-4 standard that at least  $10^5$  prompt events shall be acquired at all the measurement positions and thus the simulations are performed (i.e. given activity and simulation time) so as to acquire  $2 \times 10^5$  prompt events for all the scanners.

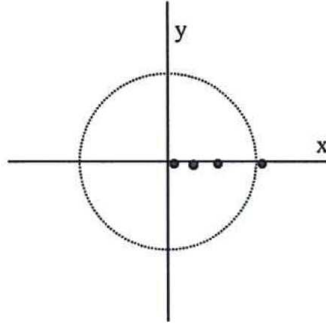


Figure 5.2 – Illustration of different radial positions where the source is simulated to estimate the scanner spatial resolution. (NEMA NU-4)

### 5.3.2 Data processing and analysis

The simulated data for all the scanners are reconstructed via MLEM algorithm, however, NEMA standard specifies 2D or 3D FBP algorithm. NEMA proposes that in order to measure the width of the point spread function as accurately as can practically be achieved, its expected FWHM should span at-least five pixels. The pixel size should be made no larger than one-fifth of the expected FWHM in the transverse direction during reconstruction and should be indicated as a condition for the spatial resolution measurement. Since all the scanner geometries are designed to provide the spatial resolution of 1 mm, we take the image voxel size to be  $0.2 \times 0.2 \times 0.4$  mm. Thus, to perform the image reconstruction, we need to generate a SM having the same voxel size for all the scanners. As discussed in the previous section, we generated SM using MC simulations for a voxel size of  $0.4 \times 0.4 \times 0.4$  mm, however, it has been reported that not all the elements of SM are estimated. Further reducing the voxel size, increases the SM elements and thus the number of non zero SM elements. Therefore, we reconstructed images using CASToR to estimate the spatial resolution.

Once the simulated data is reconstructed into images, the spatial resolution of the point source response function is determined in all three directions. The detector response function is formed in each direction by adding all one dimensional profiles that are parallel to the direction of measurement.

Following the NEMA recommendation, the maximum value of each of the 1D profile is determined by a parabolic fit using the peak point and its two nearest neighbouring points respectively. The adjacent pixels at half the maximum value obtained are linearly interpolated on both the sides of 1D profile to determine the FWHM. Values are then converted to distance (mm) by multiplying with the pixel size.

### 5.3.3 Results and discussion

Once the spatial resolution is estimated for all the scanner geometries, the observations are categorized into following three parts:

1. **Convergence test:** The spatial resolution for a point source located at the cFOV is estimated for different iterations of MLEM algorithm for all the scanners. Figure 5.3 presents the radial spatial resolution convergence curves estimated as the function of number of iterations of MLEM algorithm performed in CASToR.

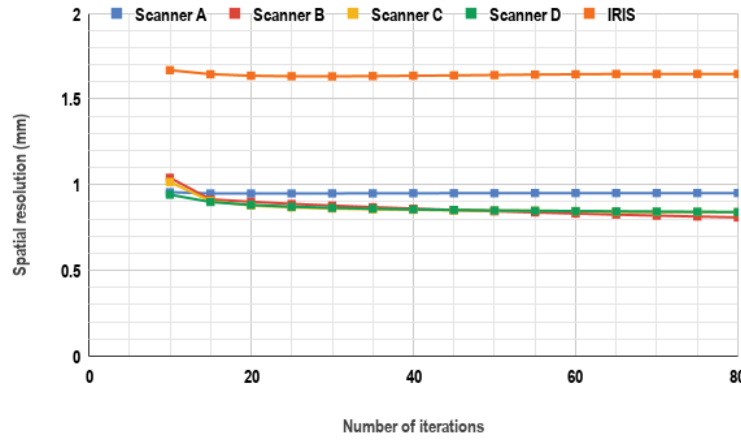


Figure 5.3 – Radial spatial resolution (mm) estimated via MC simulations for a point source placed at the cFOV as a function of number of iterations of MLEM algorithm for all the four scanner geometries and also for the IRIS PET scanner

From figure 5.3 it can be observed that IRIS PET scanner and Scanner A start to reach the convergent value from 20<sup>th</sup> iteration. Both the scanners (IRIS PET and Scanner A) are based on similar geometrical approach employing a single layer of pixelated crystals, arranged in an octagonal shape in the transverse plane. However, the spatial resolution values estimated for Scanner B, Scanner C and Scanner D does not show convergences and keep on decreasing with the number of iterations. This is due to the fact that as the scanner geometry gets complicated (i.e., crystal layers increases), the on-the-fly estimated SM elements based on projectors are not sufficient to map the detector response function to the image space. We will observe further in detail in section 5.5 that the images generated via CASToR (using on-the-fly computed SM elements) for Scanner B, Scanner C and Scanner D (employing several crystal matrices) contain artifacts.

2. **Spatial resolution values at the cFOV:** Table 5.3 presents the value of FWHM estimated at the cFOV for all the scanners via MC simulations. All the values are reported in mm. The values are reported for 20<sup>th</sup> iteration of the reconstructed image. It can be observed that all the FWHM values for all the designed scanners at the cFOV are close to 1 mm in all directions as expected.

Furthermore, all the four scanners provide a spatial resolution better than the IRIS PET scanner. However, it should be noted that, the Scanner D employs monolithic scintillator crystal and thus we pixelized the continuous distribution into discrete crystals. The monolithic crystal of 50 mm  $\times$  50 mm  $\times$  8 mm has been pixelized into smaller crystals of 1mm  $\times$  1mm  $\times$  1mm in each direction. This conversion has created an over estimation of the intrinsic spatial resolution from 0.70 (experimentally estimated) to 0.50 mm. As a consequence of making continuous distribution into discrete, we over estimate the achievable spatial resolution limit.

Scanners	Radial (x) mm	Tangential (y) mm	Axial (z) mm
A	0.92	0.95	0.86
B	0.87	0.85	0.85
C	0.88	0.89	0.75
D	0.85	0.79	0.85
IRIS	1.65	1.63	1.69

Table 5.3 – Spatial resolution (FWHM) values (mm) estimated via MC simulations for a point source placed at the cFOV for all the scanner geometries

3. **Spatial resolution at different radial distances:** Figure 5.4 presents the estimated spatial resolution for all the four scanners as the source is placed at different radial positions. The spatial resolution values are estimated and compared in the radial direction (Figure 5.4(a)), tangential direction (Figure 5.4(b)) and axial direction (Figure 5.4(c)).

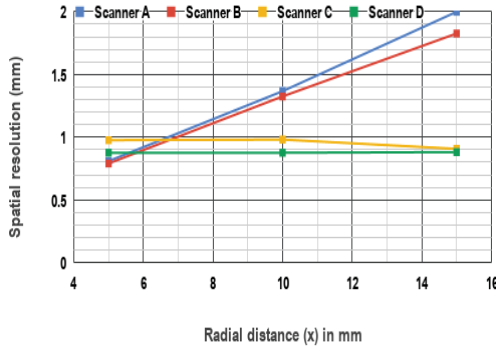
As the source moves away from cFOV in the radial direction, it can be observed that the radial spatial resolution degrades only for Scanner A and Scanner B. Further a difference in the spatial resolution between the axis can be observed only for Scanner A and Scanner B. The cause of this difference is the fact that as the source moves along the radial direction, it results in a larger parallax error in that direction, without impacting the spatial resolution in the tangential and in the axial direction. Scanner C is designed by employing a matrix of axially elongated crystals in order to compensate the parallax error and it can be noted that spatial resolution is not affected by parallax error for scanner C. Scanner D is also designed to incorporate the DOI and thus presents no spatial resolution degradation for source placed at different radial positions.

The image reconstruction process is performed via MLEM algorithm using CASToR where distance driven projector is used to calculate the SM elements on-the-fly. However it has been reported that on-the-fly calculation of SM elements does not map the detector response function to the image space by taking into account all the factors such as crystal depth, intrinsic detection efficiency of the crystal etc. This issue for on-the-fly calculation of SM elements gets worse as the scanner geometry gets more and more complicated, as in case of Scanner B, Scanner C and Scanner D, where multiple layers or continuous crystal distribution is used. We further characterize the effect of on-the-fly generated SM elements for these scanners when estimating the image quality (section 5.5).

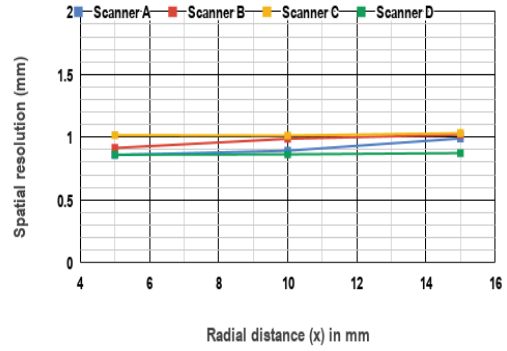
In the next section, we characterize the scanner geometries for their detection efficiency.

## 5.4 Estimation of detection efficiency

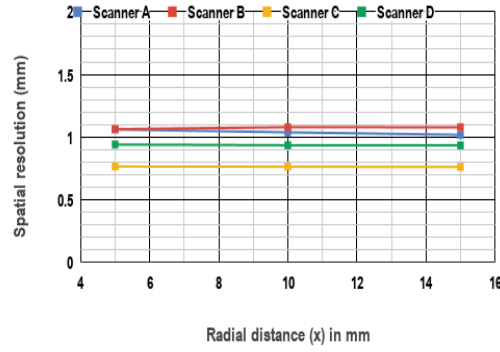
The detection efficiency of a PET scanner represents its ability of detecting coincident photons emitted from inside the FOV of the scanner. It is expressed as the fraction of the annihilation events detected as true coincidence events. In this section, we calculate the theoretical values of different factors



(a) FWHM (mm) measured in radial direction



(b) FWHM (mm) measured in tangential direction



(c) FWHM (mm) measured in axial direction

Figure 5.4 – Comparison of spatial resolution (mm) in all three direction estimated for all the scanner geometries with a point source placed at several radial distances i.e., 5 mm, 10 mm and 15 mm from the cFOV

contributing to the detection efficiency of scanners. Further we discuss the approach to estimate the detection efficiency as given in NEMA NU-4 standards (mentioned as sensitivity). We also present the detection efficiency values estimated via simulations following the NEMA standard.

As explained in chapter 1, the detection efficiency of the scanners is mainly determined by two parameters firstly the geometric efficiency, and secondly the intrinsic efficiency of the scintillator crystal via following factors:

1. **Geometric efficiency:** The factors impacting the geometric efficiency of a scanner are:
  - (a) The overall solid angle ( $\Omega$ ) coverage of the detector with respect to the source location. The solid angle depends on the scanner's axial coverage ( $A$ ) and on the diameter ( $D$ ).
  - (b) The packing fraction i.e., the ratio of the active area to the total surface area.
2. **Intrinsic efficiency:** The factors impacting the intrinsic efficiency of a scanner are:
  - (a) Scintillator crystal material (atomic number and density).
  - (b) Crystal length (d).

Table 5.4 presents the theoretical values of these factors based on the four scanner geometries designed and for the IRIS PET scanner as well. The theoretical detection efficiency values for a point source placed at the cFOV of the scanner is also calculated using the approximation of ring scanner as given in chapter 1 for all the scanners. LYSO:Ce is used as the scintillator crystal in all the scanner geometries and the intrinsic efficiency is calculated on the basis of LYSO. Since all the scanners are designed to have the similar diameter and axial FOV, thus the calculated solid angle is nearly the same for all the scanners. It can be noticed that the intrinsic detection efficiency varies a lot among the four scanner geometries due to the different values of crystal depth offered and thus this is one of the major factors impacting the scanner detection efficiency. Since Scanner C offers the maximum intrinsic efficiency as compared to the other scanner geometries, it provides the maximum detection efficiency.

Scanners	Solid angle ( $\omega$ )	Intrinsic efficiency ( $\epsilon^2$ )	Packing fraction	Detection efficiency (%)
A	10.43	0.25	0.85	6.40
B	10.99	0.49	0.85	13.27
C	10.75	0.91	0.95	26.76
D	11.26	0.25	1.00	8.12
IRIS	8.12	0.42	0.87	8.55

Table 5.4 – Theoretical values calculated, for a point source placed at the cFOV, for solid angle  $\Omega$ , intrinsic detection efficiency  $\epsilon^2$  and packing fraction for all the scanners based on the assumption that all the scanners are of ring geometry

However, there are certain factors such as dead space between the axial modules of the scanners, dead spaces between the rsectors in the transverse plane etc., that also impact the detection efficiency. Based on the scanner geometries design the simulations are performed following the approach given in NEMA standards. The simulation approach is explained in the following subsection.

#### 5.4.1 Simulation approach

The same  $22\text{Na}$  point source in an acrylic cubic phantom as specified to estimate the spatial resolution is mentioned by NEMA NU-4 standard to estimate the detection efficiency. A point source of activity of 10 MBq is simulated for all the scanners for a time duration of 10 min. The source is placed in the scanner in such a manner so as to be axially and transaxially centered. Counting rates are acquired at this location.

#### 5.4.2 Data process and analysis

As mentioned in NEMA NU-4 2008 section 5, Single slice re-binning is used to assign counts in oblique LORs to the image slice where the LOR crosses the scanner axis, so that each slice is represented by one sinogram. For each row of the sinogram (angle), the highest value shall be located, and all the pixels greater than 1 cm from this peak value are set to zero. The total of all pixels in the sinogram are then summed to form the total counts ( $c$ ) in that slice. No other corrections for scatter and random events are performed. The detection efficiency ( $\eta$ ) values, measured in counts per second per Bq ( $\frac{cps}{Bq}$ ), are thus calculated from the total counts obtained as shown below:

$$\eta = \frac{c}{T \cdot A} \quad (5.4)$$

Where  $T$  represents the time duration over which the counts are acquired and  $A$  is the input source activity. As the branching ratio of Na-22 is 0.9060, the absolute detection efficiency ( $\eta_{abs}$ )(%)

is given as:

$$\eta_{abs} = \frac{\eta}{0.9060} \times 100 \quad (5.5)$$

### 5.4.3 Results

The computed detection efficiency values for all the scanners are reported in table 5.5 along with the theoretically calculated values. As expected, the detection efficiency value for Scanner C is the highest as compared to all other scanners since the total depth provided by 24 layers of axially elongated crystals is  $1.5 \times 24 = 36$  mm (which is equivalent to the three LYSO attenuation lengths).

Scanners	Estimated Detection efficiency(%)	Theoretical Detection efficiency(%)
A	5.50	6.40
B	13.87	13.27
C	23.42	26.76
D	9.55	8.12
IRIS	8.08	8.55

Table 5.5 – Estimated and theoretically calculated detection efficiency values (%) at the cFOV for all the scanner geometries

On the other hand, Scanner A and Scanner D offer the thinner crystal depth (length of crystal being 8 mm). Scanner D results in higher detection efficiency as compared to Scanner A due to the following reasons:

1. As mentioned in chapter 3 (section 3.1.6), lesser the number of rsectors in the transverse plane, the lesser is the dead space between the rsectors and thus higher the detection efficiency.
2. Diameter of Scanner D is less than the diameter of Scanner A and as explained in chapter 3 (section 3.1.2, Figure 1), as the diameter increases, solid angle decreases, which leads to lesser detection efficiency.
3. The last point contributing to this difference of detection efficiency between Scanner A and Scanner D comes from the packing fraction. Scanner D is based on monolithic crystal whereas Scanner A employs pixelated crystal matrix consisting of dead spaces.

Scanner B is designed on the geometry of Scanner A having an additional layer of crystal matrix sitting at the surface of the existing crystal matrix of Scanner A. This additional crystal matrix contributes to the total depth of the crystals thereby stopping more incident gamma photons. The reported detection efficiency values of all the scanners show the same behaviour as expected (i.e., Scanner C designed to provide maximum detection efficiency is reported to provide maximum value of detection efficiency as compared to other scanners).

Since all the scanners have been characterized for their performance parameters (i.e., spatial resolution and detection efficiency), the aim is to investigate how these performance parameters will affect the image quality. In order to perform this study, an IQP is simulated, RC and SNR values are reported in the next section. Reconstruction of simulated IQP is performed via MLEM algorithm. In the next section we describe the IQP phantom, the simulation approach, parameters like RC and SNR used to investigate the impact of all the scanners performance on the image quality.



## 5.5 Estimation of image quality

Due to the complex interplay of different aspects of system performance, it is desirable to be able to compare the image quality of different scanners for a standardized imaging situation. IQP is used in NEMA NU-4 2008 standards. The IQP consisting of uniform hot and cold areas, serves as an imaging object similar to a small rodent consisting of hot lesions. The image quality is characterized by the following parameters:

1. **Recovery Coefficients (RC):** It is defined as the ratio of observed to true activity in a reconstructed PET image. The RC values measured in the hot rods are indicative of the spatial resolution of the PET scanners.
2. **Noise in the uniform region:** It is defined as the standard deviation of uniformity measurement in the uniform activity region. The noise in the uniform region of the phantom is indicative of the SNR. High detection efficiency scanners reduce the statistical noise in the reconstructed images and thus increase the SNR for more reliable lesion detection.

In the following sections we discuss the IQP structure, simulation and data analysis approach to estimate the image quality for all the discussed scanner geometries.

### 5.5.1 Simulation approach

The image quality parameters are estimated using the NEMA NU-4 2008 IQP. The material mentioned to built IQP is PMMA (Poly Methyl Meth Acrylate) and the internal dimensions specified are: 50 mm length and 30 mm diameter. The phantom consists of the following parts:

1. **Body:** It consists of two main parts as shown in figure 5.5(a). At the top, we have a large fillable cylindrical chamber with a 30 mm diameter and a 30 mm length. At the bottom, we have 20 mm longer solid part containing 5 fillable rods with diameters of 1, 2, 3, 4 and 5 mm respectively.
2. **Top cover:** It is a lid as shown in figure 5.5(b), attached to the top part of the body. It supports two cold region chambers, one filled with water and the other with air. The two chambers are 14 mm long and 8 mm in diameter.
3. **Bottom cover:** A lid on the bottom part of the IQP body as shown in the figure 5.5(c).

Figure 5.5(d) illustrates the complete IQP geometry used to perform simulations in the thesis. The phantom is placed inside the scanner such that the axis of its main cylindrical compartment is aligned with the axial axis of the scanner geometry. As per NEMA NU-4 standard,  $^{18}\text{F}$  source is used and the activity used in the whole phantom is 100 micro-Curie distributed between the hot cylinder of the upper part of the phantom, the uniform region and the five rods placed at the inferior part of the phantom. Simulations are performed for 20 minutes.

### 5.5.2 Data process and analysis

The simulation acquired LM data is reconstructed using MLEM algorithm. For IRIS PET, Scanner A and Scanner B, we reconstructed images using MC generated SM and compared with the images reconstructed using CASToR (where SM is calculated analytically). For the other two scanners (Scanner C and Scanner D), since the number of crystal pairs are enormous, the implemented MLEM algorithm (using SM stored on the disk) does not support image reconstruction. Thus, images for Scanner C and Scanner D are only reconstructed using CASToR (where SM elements are computed on the fly and are not stored on the disk). The voxel size of image matrix is taken as 0.4 mm x 0.4 mm x 0.4 mm for all the scanner geometries.

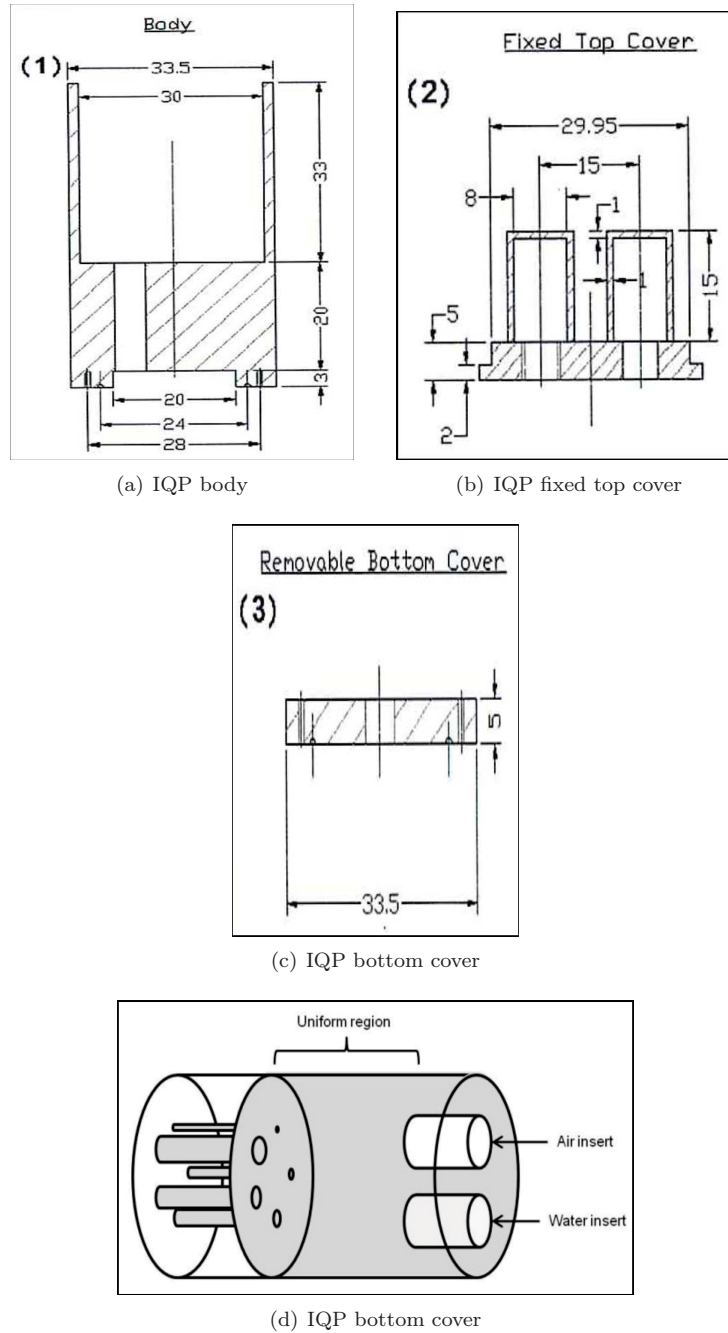


Figure 5.5 – Illustration of IQP geometry consisting of three parts: (1) Body, consisting of a large fillable cylindrical chamber at the top and a solid part at the bottom; (2) Top cover, supporting two cold regions; (3) Bottom cover, to cover the bottom part of the body (Reprinted from NEMA NU-4 2008). Complete IQP is shown at the bottom as used to estimate the quality of reconstructed image in terms of RC and uniformity (Reprinted from [Anizan 12])

RC and uniformity values are estimated following the approach given in NEMA NU-4 2008 standards. In order to calculate the uniformity value, a cylindrical Volume Of Interest (VOI) having a diameter of 22.5 mm and length 10 mm is drawn over the center of the uniform region of the IQP. The average activity concentration reported gives the estimated uniformity. To compute the RC values, the image slice covering the central 10 mm length of the hot rods are averaged to obtain a single slice of lower noise. Around each hot rod a circular Region Of Interest (ROI) is drawn with a diameter equal to twice the physical diameter of the hot rods and the maximum value in each of this ROIs is noted. The transverse image pixel coordinates for the location in each ROI with the maximum value is noted and is used to create a line profile along each of the rods in the axial direction. The pixel values measured along each profile, divided by the mean activity concentration found in the uniformity test is used to determine the mean of the RC value for each rod.

### 5.5.3 Results

Based on the simulation and data analysis approach, we simulated the scanners and reconstructed the images to estimate the image quality. The observations of this section are given below:

1. **Qualitative analysis of the reconstructed IQP images:** The images are reconstructed using a) pre-computed SM elements, generated via MC simulations as discussed in section 5.2 and; b) using CASToR where SM elements are computed on-the-fly via distance driven projector. Figure 5.6, 5.7 and 5.8 presents the IQP images reconstructed for IRIS PET, Scanner A and Scanner B through both the approaches (images reconstructed via pre-computed SM elements are on the left hand side whereas the CASToR reconstructed images are on right side). The figures present the transverse plane (showing reconstructed five hot rods) and the axial plane (presenting all three parts of reconstructed IQP).

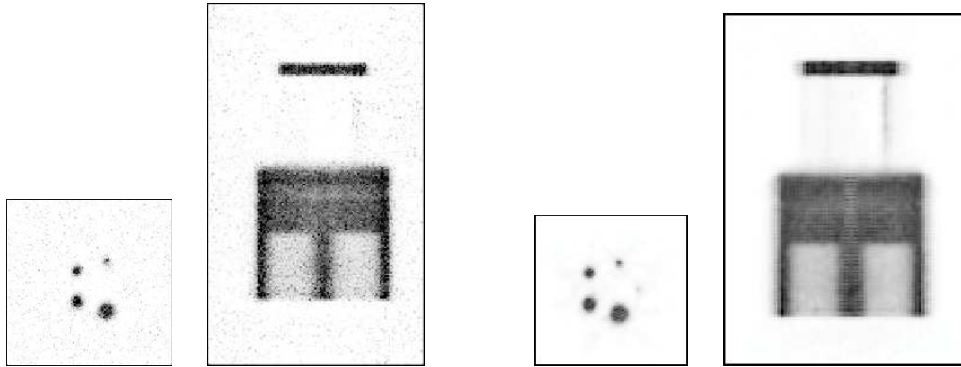


Figure 5.6 – IRIS PET: IQP reconstructed images showing the transverse plane consisting of 5 hot rods and the axial plane showing all three parts of the IQP phantom via pre-computed SM elements (left side) and via CASToR (right side)

With the MC generated SM, we are able to reconstruct the images for all the three scanners (IRIS, Scanner A and Scanner B). However, the reconstructed images are very noisy especially for Scanner A and Scanner B because the computed non-zero elements of SM elements for these two scanners are less when compared to IRIS PET. On the other hand, in the CASToR reconstructed images, we can observe a decreased intensity in the center of the IQP for all the reconstructed images. This is due to the fact that the MLEM algorithm is formulated on the assumption that the sensitivity of all the LORs in the scanner is the same. However, there are variety of factors, such as detection efficiency of the scintillator crystals, angle of incidence of gamma photons, scanner geometry etc., which influence the detection of certain LORs. Hence

the LORs have different detection efficiency values, thereby generating artifacts as can be observed in all the images reconstructed via CASToR.

As mentioned before, for Scanner C and Scanner D, images are only reconstructed using the analytical SM generated by CASToR. The reconstructed images are shown in figure 5.9 (Scanner C) and figure 5.10 (Scanner D). It can be noted that the artifacts present in the IQP images generated by IRIS, Scanner A and Scanner B, become worst for Scanner C and Scanner D. This is due to the fact that Scanner C and Scanner D employ multiple layers of crystals and thus further require the normalization for the variation in LOR detection efficiency values.

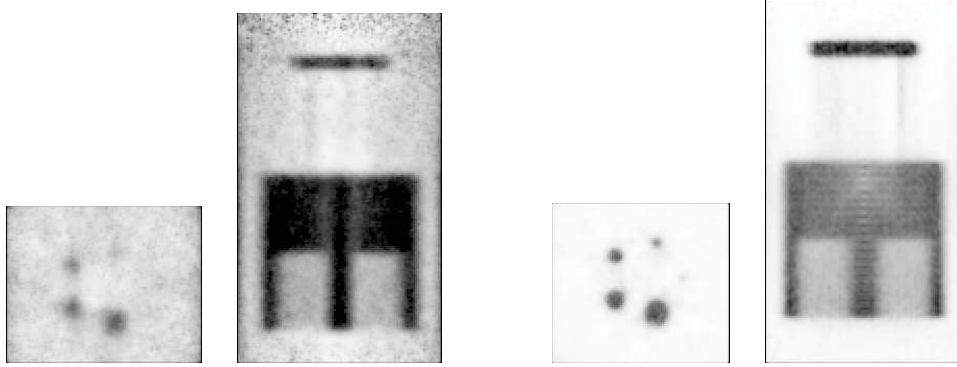


Figure 5.7 – Scanner A: IQP reconstructed images showing the transverse plane consisting of 5 hot rods and the axial plane showing all three parts of the IQP phantom via pre-computed SM elements (left side) and via CASToR (right side)

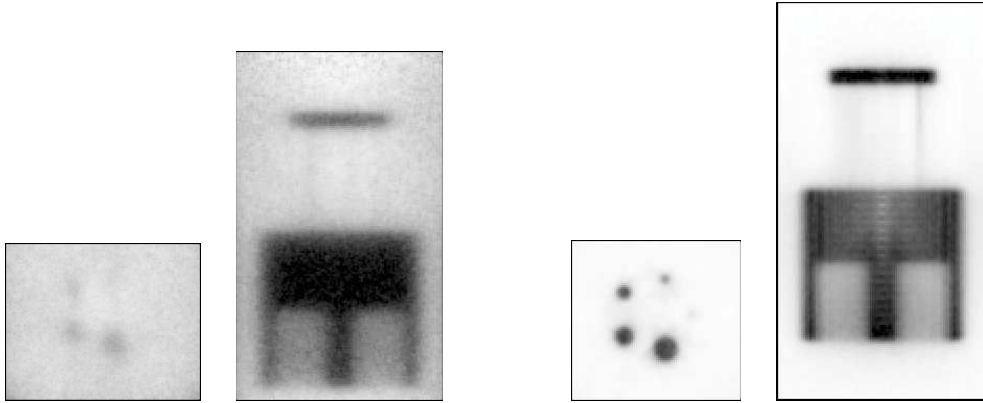


Figure 5.8 – Scanner B: IQP reconstructed images showing the transverse plane consisting of 5 hot rods and the axial plane showing all three parts of the IQP phantom via pre-computed SM elements (left side) and via CASToR (right side)

As mentioned in chapter 4, CASToR generates a sensitivity image, before starting MLEM iterations. The time taken for the sensitivity image is increased as the number of crystal pairs or the image voxel increase. Table 5.6 provides an idea on the time taken for the sensitivity profile generation for all the scanners using CASToR.

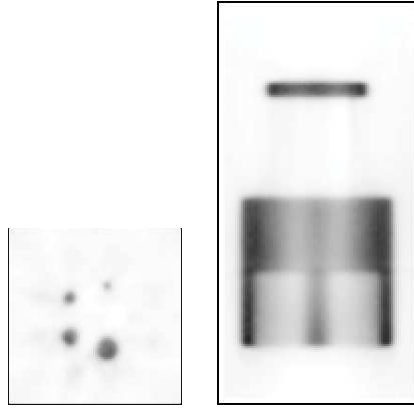


Figure 5.9 – Scanner C: IQP reconstructed image showing the transverse plane consisting of 5 hot rods and the axial plane showing all three parts of the IQP phantom using CASToR

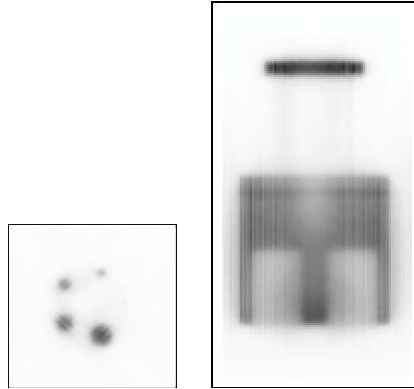


Figure 5.10 – Scanner D: IQP reconstructed image showing the transverse plane consisting of 5 hot rods and the axial plane showing all three parts of the IQP phantom using CASToR

Scanners	MC Simulation run time (years)	Castor Sensitivity image time (s)
A	3.84	1466
B	2.67	6182
C	1.01	435606
D	2.16	138066
IRIS	3.66	1699

Table 5.6 – Comparison of time duration for MC simulations to generate the first version of SM and by CASToR to generate a sensitivity profile for all the scanner geometries.

2. **Convergence for RC values estimated for all the scanners:** The images are reconstructed using both approaches (pre-computed SM and SM computed on the fly) for the same image voxel size. The RC values are then estimated for different iterations to test for convergence. Figure 5.11 presents the RC values estimated as a function of number of iterations for IRIS PET (at the top), Scanner A (center) and for Scanner B (bottom). Figure 5.11 presents a comparison between the RC values estimated from the images reconstructed using pre-computed SM via MC simulations (left) and from the image reconstructed via CASToR using distance driven projector to calculate SM elements on-the-fly (right). It can be observed that the RC values estimated from the images reconstructed using pre-computed SM for all the scanners cannot be used to quantify the images as the statistical uncertainties associated with insufficient events to compute the SM impacts the quantification of the reconstructed images and will require more statistics as reported in section 5.2.

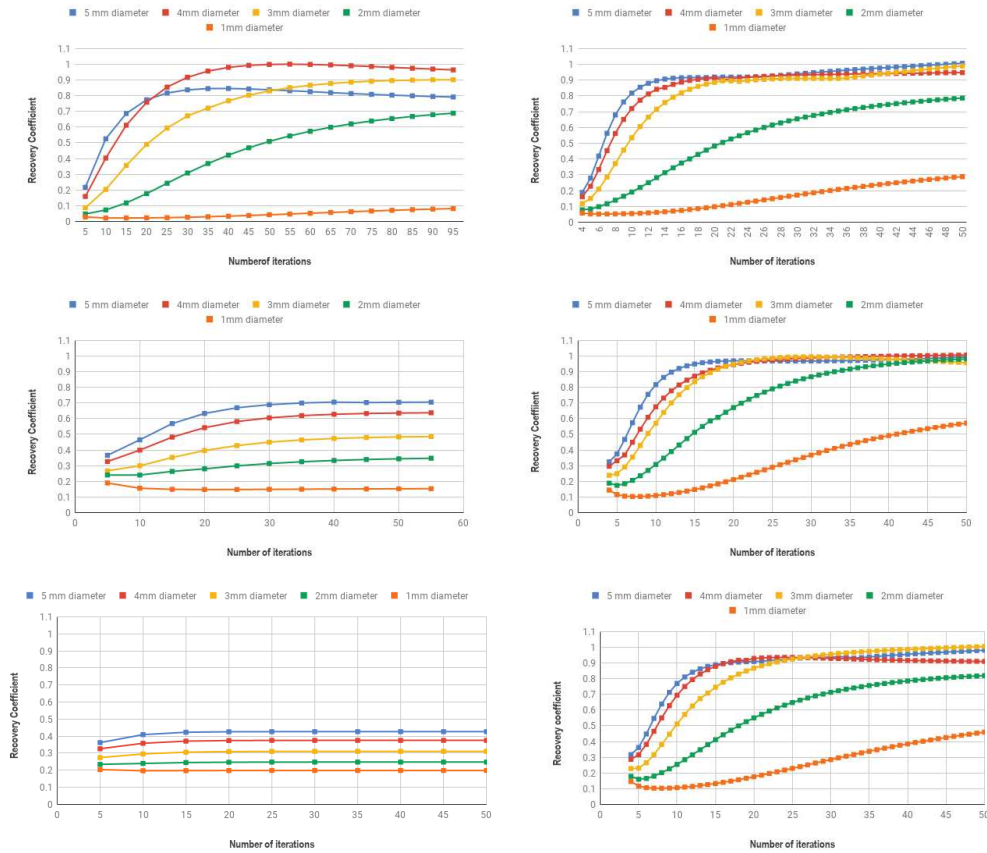


Figure 5.11 – Graphs presenting RC values estimated as a function of number of iterations for the images reconstructed using pre-computed SM via MC simulations (left) and for the images reconstructed with CASToR using distance driven projector to compute SM elements on-the-fly (right) for IRIS PET (top row), Scanner A (center row) and for Scanner B (bottom row).

Figure 5.12 presents the RC values estimated from the images reconstructed with CASToR for Scanner C and Scanner D as a function of number of iterations.

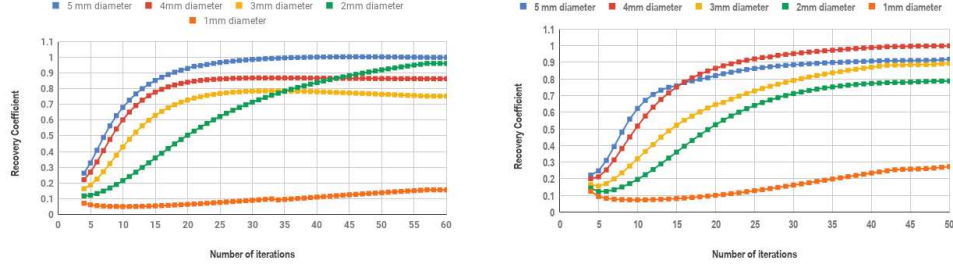


Figure 5.12 – Graphs presenting RC values estimated as a function of number of iterations for the images reconstructed using CASToR using distance driven projector to compute SM elements on-the-fly for Scanner C (left) and for Scanner D (right)

3. **RC values estimated for all the scanners:** Table 5.7 presents the RC values estimated for all the 5 hot rods.

Scanners	1 mm rod	2 mm rod	3 mm rod	4 mm rod	5 mm rod
A	$0.49 \pm 0.19$	$0.95 \pm 0.21$	$0.98 \pm 0.18$	$0.99 \pm 0.18$	$0.98 \pm 0.16$
B	$0.38 \pm 0.11$	$0.77 \pm 0.12$	$0.97 \pm 0.11$	$0.92 \pm 0.08$	$0.94 \pm 0.10$
C	$0.11 \pm 0.12$	$0.84 \pm 0.35$	$0.78 \pm 0.11$	$0.87 \pm 0.06$	$1.00 \pm 0.10$
D	$0.23 \pm 0.18$	$0.77 \pm 0.26$	$0.87 \pm 0.20$	$0.99 \pm 0.14$	$0.91 \pm 0.15$
IRIS	$0.24 \pm 0.12$	$0.74 \pm 0.17$	$0.93 \pm 0.19$	$0.94 \pm 0.10$	$0.98 \pm 0.12$

Table 5.7 – RC values estimated from the IQP reconstructed image ( $40^{th}$  iteration) using CASToR.

Since RC values are indicative of scanner spatial resolution, scanners with better spatial resolution should provide higher RC values for hot rods of much smaller diameter. The scanner geometries designed in this thesis are reported to provide an improved spatial resolution as compared to IRIS PET. However, no significant difference is observed between the RC values estimated by the designed scanners (providing improved spatial resolution) and IRIS PET. Furthermore, the error values on each RC values for all the scanners are significant.

In figure 5.13(a), we compares the RC values estimated for 5 hot rods of different diameters for all the scanners. It can be observed that for scanners employing more complex geometry (such as several crystal layers in case of Scanner B, Scanner C and Scanner D), we cannot quantify the RC values without normalization due to the presence of the artifacts. Since both IRIS PET and Scanner A employs only one crystal matrix, we compare the RC values estimated for these two scanners as shown in figure 5.13(b). As expected Scanner A having better spatial resolution as compared to IRIS PET, provides a better RC value for 2 mm and 1 mm diameter rod.

RC values are estimated as the ratio of observed to true activity in the reconstructed image and the true activity is extracted as the mean uniformity value in the uniform region of reconstructed image of the phantom. However, it can be observed in figure 5.6 and 5.7, due to lack of normalization, we get artifacts in the uniform region of the reconstructed IQP. Thus, we underestimate the true activity value (or the mean uniformity value) and thus the estimated RC values are



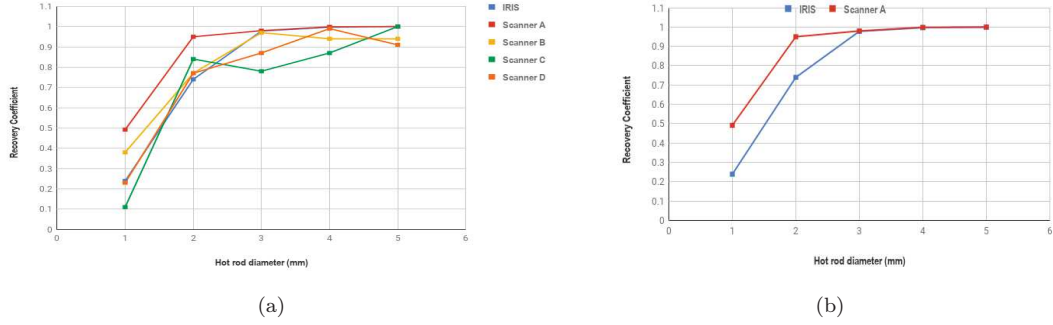


Figure 5.13 – Comparison of RC values estimated from IQP reconstructed images for IRIS PET scanner (blue) and for Scanner A (red) as a function of hot rod diameter

greater than 1. We have divided the estimated RC values for all the rods of a scanner by the RC value of the 5 mm rod.

4. **SNR values estimated for all the scanners:** Detection efficiency should be as high as possible to achieve good SNR for high spatial resolution images [Levin 07]. Improved SNR enhances the ability to identify and quantify a subtle signal in the presence of background noise. Table 5.8 provides SNR value computed for all the scanners by estimating uniformity value (mean) and the noise (standard deviation) in the uniform region of the CASToR reconstructed IQP image.

Scanners	SNR
IRIS	10.2
A	7.3
B	9.5
C	2.1
D	3.7

Table 5.8 – SNR values estimated from CASToR reconstructed images of IQP for all the scanners.

Despite having the maximum detection efficiency value, Scanner C is observed to have minimum SNR value. This is due to the presence of artifacts (resulting from the unaccounted variation in the sensitivity of the LORs) in the uniform region. The reported artifact results in increased noise (standard deviation) in the uniform region, thus impacting the estimated SNR value. Similarly, for other scanner geometries, noise due to artifacts impact the estimated SNR.

Furthermore, among IRIS PET and Scanner A (designed using single crystal layer), IRIS PET scanner is reported to provide a better SNR as compared to Scanner A since it offers improved detection efficiency.

## 5.6 Conclusion

All the four designed scanner geometries, along with IRIS PET are characterized in this chapter to estimate the performance parameters (i.e., spatial resolution and detection efficiency). We followed



NEMA NU-4 2008 standards as much as possible and all the deviations adapted from these standards are mentioned in the respective sections. All four designed scanners are reported to provide a spatial resolution close to 1 mm at the cFOV. The spatial resolution offered by all the designed scanner geometries is better than the state-of-art IRIS PET scanner. The estimated detection efficiency values are also in accordance with the predicted theoretical values. The maximum detection efficiency is offered by Scanner C.

Once the scanners have been characterized for their performance parameters, we study qualitatively and quantitatively the reconstructed image quality. IQP is used to estimate the image quality. Images are reconstructed using MLEM algorithm. As explained in chapter 4, MC generated SM provides an accurate mapping of the detector response function to the image space, thus the idea was to perform all the image reconstruction process by MLEM algorithm using MC generated SM. The SM for all the 5 scanners were generated by running MC simulations. The quality of the SM impacts the reconstructed images, thus it is important to characterize the generated SM elements. We characterize all the generated SM by determining the non-zero matrix elements as a function of detected coincidence events. As the number of detected coincidence events increases, the non-zero SM elements increase and eventually saturate. However, for all the MC generated SM, we reported that the number of non-zero SM elements are very less when compared to total number of SM elements. Running new simulations are resulting in increase in the number of non-zero SM elements. Thus, we need to run more simulations to generate more coincidence events to populate the SM till the number of non-zero elements saturates. However, due to time limitation, we have reconstructed the data acquired for IQP using the SM we have generated via MC simulations to study how the quality of SM impacts the quality of reconstructed images. It is observed that the images generated using MC generated SM cannot be used for quantification purposes. Furthermore, the algorithm developed in our lab requires to store the complete SM in memory and use it for image reconstruction process. However, due to memory constraints, it is not possible to reconstruct the images for scanner C and D with the current tools available, since Scanner C and Scanner D contain enormous number of crystal pairs. With the current algorithm, only the images for IRIS PET scanner and for Scanner A and Scanner B can be reconstructed.

Images are also reconstructed using CASToR where SM elements are computed on the fly via distance driven projectors. A comparison is also made for both image reconstruction approaches. We observed the artifacts in the CASToR reconstructed images at the center of the IQP for the scanner geometries especially for Scanner B, Scanner C and Scanner D. These artifacts are due to the fact that the reconstructed images are not normalized for the variation in detector sensitivities. Moreover, the artifacts increase as the scanner geometry becomes more and more complex as in case of Scanner B, Scanner C and Scanner D, which employs multiple crystal layers. The normalization process and the impact of normalization on the reconstructed image to remove the artifacts is discussed in the next chapter.

We have compared the estimated RC and SNR values of the reconstructed images for IRIS PET and Scanner A. Both scanners employ single layer of pixelated crystal matrix. Since Scanner A offers improved spatial resolution as compared to IRIS PET, it is observed that Scanner A provides better RC values for the hot rods with smaller diameter. However, the detection efficiency of Scanner A is lower than that of IRIS PET and thus the estimated SNR value for Scanner A is lower. It should be noted that the images reconstructed via CASToR are not normalized and have artifacts. Thus we need to normalize the images to better quantify the image quality.

In the next chapter, we investigate different approaches to perform the normalization process for Scanner A to be able to generate images free from artifacts. The image quality parameters are estimated for normalized images and are compared with the parameters of the image generated with the same scanner before normalization.

# Chapter 6

## Normalization

### Contents

<b>6.1</b>	<b>Introduction</b>	<b>113</b>
<b>6.2</b>	<b>Normalization process</b>	<b>114</b>
6.2.1	Standard technique for normalization	114
<b>6.3</b>	<b>Analytical approach of normalization</b>	<b>115</b>
<b>6.4</b>	<b>Component based normalization approach</b>	<b>117</b>
6.4.1	Normalization using MC simulations	119
<b>6.5</b>	<b>Comparison with and without normalization correction</b>	<b>123</b>
6.5.1	Qualitative comparison	123
6.5.2	Quantitative comparison	124
<b>6.6</b>	<b>Conclusion</b>	<b>125</b>

### 6.1 Introduction

The random processes associated with the emission and detection of gamma photons such as depth of interaction, type of interaction, angle of incidence, etc., impacts the sensitivity of LORs. MC simulations mimic all these random processes and thus, SM generated via MC simulations accurately maps the scanner detection response to the image space. On the other hand, the analytical projectors are unable to capture all these general characteristics of emission and detection of gamma photons [Sarrhini 12]. In this thesis, we use CASToR where SM elements are computed on-the-fly via projectors. Thus, we are not taking into account all these factors which create a variation in the detection efficiency of different LORs. Furthermore, the reconstruction algorithms are formulated on the assumption that the detection efficiency of all the LORs in the scanner is same. Thus, the reconstructed images where SM elements are calculated via projectors, result in artifacts, as we can see in figure 5.9 and 5.10 of chapter 5. Lack of consideration of variation in detection efficiency of different LORs is a major limitation for reconstructing images using CASToR. Thus, we need to find the appropriate factors accounting for the variation in the detection efficiency of LORs. These factors are known as the normalization factors. Incorporating the normalization factors in the image reconstruction process, correct for the variation in the detection efficiency of the LORs. Thus, we get images corrected of the artifacts. The process of generating factors and correcting the reconstructed images for the variation of LORs is known as normalization.

In this chapter, we are investigating analytical as well as MC simulation approaches to generate normalization factors and to study their effect on the reconstructed image. The normalization factors are generated using both methods only for Scanner A. The normalization factors generated via

MC simulations following the component based normalization model (section 6.4) result in improved reconstructed images. The major objectives of this chapter are as follow:

1. Discuss the normalization process to generate normalization factors (section 6.2).
2. Generate normalization factors using analytical (section 6.3) and MC simulation (section 6.4) approaches to reconstruct images.
3. Qualitative and quantitative comparison between images reconstructed with and without incorporating normalization factors in CASToR (section 6.5).

In the next section we discuss state-of-art of the normalization process for PET scanners.

## 6.2 Normalization process

As discussed in chapter 4, the SM generated using analytical projector models only the effect of the geometrical efficiency of the LORs due to the scanner geometry (i.e., linking the area defined by two crystals and the voxel). However, the used projector fails to model the impact of other factors such as crystal depth, intrinsic detection efficiency of the crystals, inter crystal scatter etc, while estimating the SM elements. Since the LORs have different detection efficiency values and all these differences are not accounted in the SM elements, the resulting images consist of artifacts. These artifacts degrade the quantitative accuracy of the reconstructed images. The process of estimating the correction factors accounting for the variation in the detection efficiency of LORs and incorporating these factors to reconstruct artifacts free images is known as normalization. The individual correction factors for each LOR are referred to as normalization factors.

Different approaches to perform normalization exist in the literature. The standard technique [Badawi 98] to estimate the normalization factors involve exposing all the crystals in the scanner to a calibrated source of activity for the same amount of time and measuring the response of each LOR. This calibration scan is known as blank scan and it provides the information on the variation of the sensitivity of each LOR [Defrise 91]. In the next section (section 6.2.1), we describe the standard technique for normalization.

### 6.2.1 Standard technique for normalization

The objective of normalization process is to generate a normalization factor for each LOR. For a theoretical case, assume that we have a source of known shape and position in the FOV and is equally illuminating all the crystal pairs forming a LOR (let  $A$  be the activity of the source). Also assume that appropriate attenuation, scatter, and random corrections have been applied, and there are no variations in the detection efficiency of LORs, then the count rate ( $C_{uivj}$ ) measured along the LOR for joining the crystal  $i$  to crystal  $j$  of ring  $u$  and  $v$  respectively can be given as [Theodorakis 13]:

$$C_{uivj} = A(\text{constant}) \quad (6.1)$$

It should be noted that equation 6.1 is not true for the case of real scanners. There are a number of factors affecting the detection efficiency of LOR and thus the resulting count rate is different and is given as:

$$C_{uivj} = AF_{uivj} \quad (6.2)$$

where  $F_{uivj}$  represents the factors affecting the detection efficiency of LORs. The normalization factor ( $N_{uivj}$ ) counteract on the effect of  $F_{uivj}$ . Thus we can write:

$$N_{uivj} = \frac{1}{F_{uivj}} \quad (6.3)$$

From a calibration scan we measure the count rate for a crystal pair ( $C_{uivj}$ ) and thus from equation 6.3 and equation 6.2, the normalization factors can be estimated as:

$$N_{uivj} = \frac{A}{C_{uivj}} \quad (6.4)$$

This is the standard technique to estimate the normalization factors and is also known as direct normalization [Defrise 91]. Thus, the standard technique to estimate normalization factors involve exposing all the crystals in the scanner to a calibrated source of activity for the same amount of time and measuring the response of each LOR.

One of the major drawback of this standard technique is its statistical accuracy [Badawi 98, Bai 02]. As explained for SM generation via MC simulations, the accuracy of the normalization factors in the blank scan increases as the number of events per crystal pair increases. Thus calculation of accurate normalization factors for each crystal pair of the scanner is a computationally expensive and time consuming task. In order to overcome these limitations of the standard technique, different approaches were proposed ([Pépin 11b, Casey 86a, Badawi 98]) to estimate the normalization factors in the time span less than that of a blank scan. In the next section (section 6.3), we estimate the normalization factor for each LOR analytically. The objective is to take into account the angle of incidence (between the crystals of same plane and also of different planes) and the crystal depth depending on the angle of incidence.

### 6.3 Analytical approach of normalization

In the first attempt to normalize all the LORs, we used analytical approach. We generate the normalization coefficients for each crystal pair on the basis of intrinsic efficiency and the angular dependence between the crystal pair. The angular dependence is accounted by extrapolating the length of LOR inside the crystals as shown in figure 6.1. The detection efficiency of a LOR joining the crystal pair (a,b) is less as compared to the detection efficiency of the LOR joining crystal pair (c,d).

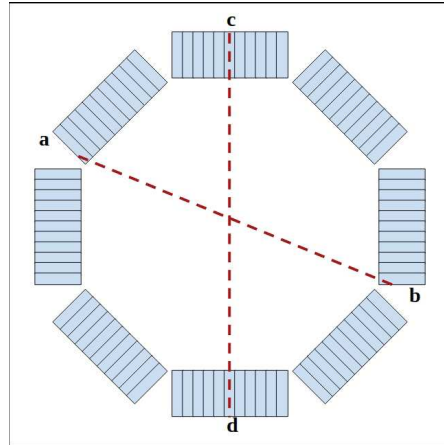


Figure 6.1 – Illustration of an octagonal preclinical PET scanner geometry (as used for Scanner A). Two LORs joining crystal pairs (a,b) and (c,d) are drawn. The detection efficiency of the LOR joining crystal (a,b) is less as compared to the LOR joining the crystal pair (c,d).

The detection efficiency is less because the crystal pair (c,d) offers more depth to the incoming photons. The efficiency for LOR joining the crystal pair (a,b)  $\epsilon_{ab}$  is given as:

$$\epsilon_{ab} = (1 - e^{-\mu d_a}) \times (1 - e^{-\mu d_b}) \quad (6.5)$$

where  $d_a$  and  $d_b$  represents the length of the LOR inside the crystal a and crystal b respectively. Similarly the efficiency of LOR joining the crystal pair (c,d)  $\epsilon_{cd}$  is given as:

$$\epsilon_{cd} = (1 - e^{-\mu d_c}) \times (1 - e^{-\mu d_d}) \quad (6.6)$$

where  $d_c$  and  $d_d$  represents the length of the LOR inside the crystal c and crystal d respectively. The length of LOR inside the crystal (i.e.,  $d_a, d_b, d_c, d_d$ ) is calculated analytically by joining the center of crystal surface facing the cFOV to the point where LOR finally goes out of the crystal as shown in figure 6.2 (black dotted lines). The normalization factors  $\eta_{uivj}$  are thus computed as  $\epsilon_{ui} \times \epsilon_{vj}$  for all the crystal pairs of scanner.

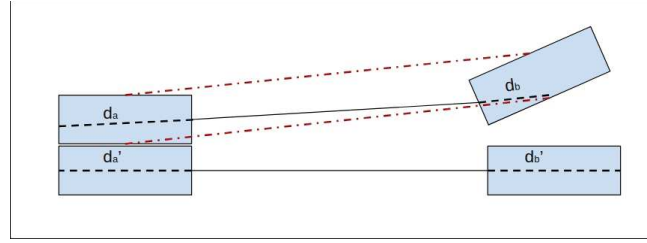


Figure 6.2 – Illustration of two crystal pairs (a,b) and (a',b'). The red dotted lines represent the mapping performed by distance driven projector, joining all the surfaces of one crystal center to another. The black line joining the centers, at the surface facing the cFOV, of the two crystals represents the LOR and the dotted line presents the extrapolation of LOR inside the crystal.

In order to calculate the values for all the  $\eta_{uivj}$ , we have updated a part of CASToR code. Before starting image reconstruction algorithm, CASToR generates a sensitivity profile for the scanner by mapping all the crystal pairs one by one. Because of the updated code, when CASToR runs a loop on all the crystal pairs, instead of mapping crystals for sensitivity profile, we draw a LOR joining the centers of the two crystals. Each end of the LOR is extrapolated inside the respective crystals as shown in figure 6.2. Extrapolated length inside the crystal varies depending upon the angle of incidence of LOR onto that crystal. The crystal surface and the position on the surface where the extrapolated LOR first interacts is determined and the extrapolated length ( $d_a$  and  $d_b$ ) is estimated. Following the equation 6.6, the normalization factors  $\eta_{uivj}$  are calculated and stored in a binary file. Once the loop on all the crystal pairs is performed, we obtain a binary file consisting of normalization factors as a function of crystal pairs. We keep the same structure of the binary file as specified in the CASToR manual where a normalization factor is given with the crystal IDs and the crystal IDs are written in the form of CASToR IDs as explained in chapter 4. The computed normalization factors (or the generated binary file) are then used by CASToR (with no changes in the algorithm) to initially generate the sensitivity profile incorporating the normalization factors and then to reconstruct the images.

The reconstructed IQP image incorporating the analytically generated normalization factors is given in figure 6.3. The reconstructed image presents a sharp drop in the intensity at the center and also for several LoRs. This is because computing the normalization factor, as shown in figure 6.1, for the crystal pair (a, b), the distance seen by the gamma photon before exiting the crystal is very less as compared to that in the case for the crystal pair (c,d). The difference between the distance covered in two crystal pairs, result in a variation of detection efficiency by a factor of 300 between the

normalization factor of (a,b) and (c,d). Thus, the resulting reconstructed image of IQP (figure 6.3) shows a sharp drop in the intensity where the calculated  $d$  is very small.

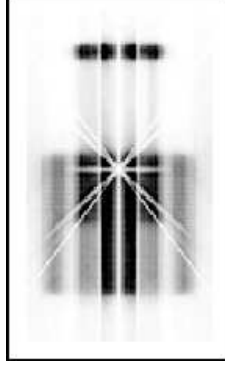


Figure 6.3 – IQP image reconstructed using CASToR for Scanner A for GATE simulated data. Normalization coefficients calculated by analytical approach discussed in section 6.3 are Incorporated in CASToR for the reconstruction process.

In this analytical approach, we only consider one LOR per crystal pair (joining the center of one crystal to the center of another) and extrapolate it to estimate the normalization factors. This is a major limitation of our approach since there can be other possible LORs joining the same crystal pair and not passing through the center of the crystal surface as shown in figure 6.4. The dotted red lines in figure 6.4 represent the other possible LORs connecting the same pair of crystal (a,b) and not passing through the center of the crystal. We did not take into account all these possible LOR and thus we got the artifacts in figure 6.3.

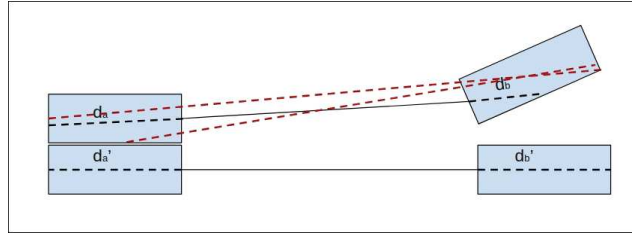


Figure 6.4 – Illustration of two crystal pairs (a,b) and (a',b'). The black line represents the LOR joining the two crystals along with the extrapolation of LOR inside the crystals. The red dotted line are some examples of other LORs joining the same crystal pair.

Thus, this approach of calculating the normalization factors based on the extrapolation length of the LOR inside the crystals is not appropriate, without taking into account all possible coincidences between the two crystals. In the next section we use component-based normalization model approach [Badawi 98] to determine the normalization factors.

## 6.4 Component based normalization approach

[Casey 86b] in 1986 proposed a technique to estimate the normalization factors and also to overcome the accuracy limitation of the standard technique. The idea behind their technique is that each crystal is in coincidence with several other crystals. When the normalization factors are determined, several

LORs and their respective normalization factors involve a common crystal which makes the normalization factors correlated to each other. Thus, this technique assumes that the detection efficiency of each LOR (depends on whether both the crystals in a crystal pair can detect the gamma photons) is given by the product of intrinsic efficiency ( $\epsilon$ ) of the respective crystal pair in coincidence. The proposed idea was to estimate the normalization factors by determining the intrinsic efficiency values of all the crystals. For a scanner consisting of  $n$  crystals, the direct normalization approach (the standard technique) measures the detection efficiency of  $n^2$  LORs, whereas with the assumption of [Casey 86b], by determining the intrinsic efficiency of  $n$  crystals we can estimate all the normalization factors. The importance of this proposed model was due to the fact that normalization scans are possible with less events, in less time duration and without compromising the accuracy of the results [Theodorakis 13]. Thus their assumption leads to reduction in the number of parameters to be estimated. However, there were limitations of their model such as presence of artifacts at the edges of the FOV in the reconstructed images and was later addressed by [Hoffman 89].

[Hoffman 89] afterwards proposed another improved model that includes the fact that for a ring scanner, the detection efficiency of a LOR also depends on the radial distance from the cFOV with which it is passing. The LOR passing through the centre of FOV is incident perpendicularly on the surface of all the crystals, thereby encountering more crystal material as compared to the LOR passing at a certain radial distance. Thus depending upon the radial distance through which LOR is passing by (or the angle of incidence of gamma photon on the crystal surface), the probability of detection of gamma photon is affected. Thereby, impacting the detection efficiency of LORs. This model, thus incorporates a radially dependent geometric factor in the previous model as given below:

$$\eta_{d1,d2} = \epsilon_{d1} \times \epsilon_{d2} \times f_{geom}^r \quad (6.7)$$

where  $f_{geom}^r$  represents the effect due to the radial factor and  $\epsilon_{d1}$  and  $\epsilon_{d2}$  represent the intrinsic detection efficiency of a crystal pair. This model improved the earlier model but failed to account for other factors such as axial geometric factor (variation in detection efficiency of LOR joining crystals of different rings due to difference in incidence angle) existing in a similar way of radial geometric factor. It is because at that time, 3D acquisition was not introduced. Septa was used to acquire data in 2D mode and the data was reconstructed using 2D algorithms.

Afterwards, [Badawi 98], described in their work a component based normalization technique similar to that used by [Ollinger 95], but modified to allow full separation of geometric and intrinsic detector efficiency effects. The normalization model presented in their work is given as:

$$\eta_{uivj} = \epsilon_{ui} \times \epsilon_{vj} \times b_u^{ax} \times b_v^{ax} \times f_{uv} \times g_{uv}^{ax} \times g_{uv}^r \quad (6.8)$$

where  $\eta_{uivj}$  represents the overall efficiency for the LOR joining the crystals  $i$  and  $j$  of ring  $u$  and  $v$  respectively.  $\epsilon_{ui}$  and  $\epsilon_{vj}$  represent the individual efficiency of crystal  $i$  of ring  $u$  and crystal  $j$  of ring  $v$  respectively.  $b_u^{ax}$  and  $b_v^{ax}$  represent the axial block profile factors.  $f_{uv}$  characterizes the crystal interference pattern.  $g_{uv}^{ax}$  represents the axial geometric factor and  $g_{uv}^r$  represents the radial geometric factor. All these factors are explained below:

1. **Crystal efficiency variation factor ( $\epsilon_{ui}$  and  $\epsilon_{vj}$ ):** A crystal intrinsic efficiency demonstrates its ability to convert incoming photon into scintillation light. Factors like presence of impurities in the crystal, smallest difference in the aspect ratio of different crystals of same scanner etc, affects the crystal efficiency.
2. **Axial block profile factor ( $b_u^{ax}$  and  $b_v^{ax}$ ):** The axial block profile factors represent the relative efficiency of each axial ring of the scanner. These factors are obtained by considering only the events in the same ring (i.e., when  $u = v$ ).



3. **Crystal interference pattern factor ( $f_{uv}$ ):** The crystal interference is a geometric response factor between a crystal and all the crystals present in the opposite module. This geometric response factor repeats itself after every  $N_m$  crystals, where  $N_m$  is the number of radial crystals in a module [Bailey 97].
4. **Axial geometric factor ( $g_{uv}^{ax}$ ):** The axial geometric factor accounts for the relative efficiency for each axial ring combination of the scanner.
5. **Radial geometric factor ( $g_{uv}^r$ ):** The radial geometric factor accounts for the variation in the LOR incidence angle and in the solid angle subtended as a function of radial distance ( $r$ ) from the center of the ring.

Using the model proposed by Badawi et al., [Pépin 11a] performed normalization in their work and presented the effectiveness of this model to normalize the reconstructed images with significant reduction in non uniformity index. In the following section, we estimate the component based normalization factors as discussed above by performing MC simulations.

#### 6.4.1 Normalization using MC simulations

In this section we follow the model proposed by Badawi et al to normalize the PET scanner (Scanner A) to account for the variation in the detection efficiency of the LORs. The procedure is based on MC simulations, performed using GATE to estimate all the normalization factors. Each component of the component based approach contributes differently depending on its nature. Two different types of sources are used to perform the MC simulations as discussed below:

1. **Cylindrical volume source:** The first source is an uniform cylindrical source having a radius of 20 mm centered on the scanner axis. The length of the source is such that it covers the complete axial FOV of the scanner. The uniform cylindrical source will uniformly illuminate all the crystal rings. This source is used to estimate the axial factors such as axial block profile factors ( $b_u^{ax}$  and  $b_v^{ax}$ ) and axial geometric factors ( $g_{uv}^{ax}$ ).
2. **Cylindrical surface source:** The second source is a surface source having a radius of 30 mm to estimate the radial geometric factor. The radius of the surface source is kept as close to the radius of the scanner A (34.3 mm). The source is long enough to cover the entire axial FOV of the scanner. The surface source is used on the basis of an assumption that it uniformly illuminates all the crystals of all the rings, so that no analytical corrections are required.

It should be noted that since we are only performing the MC simulations in the scope of this thesis work, thus the intrinsic crystal efficiency values (resulting from crystal impurities) are not estimated. Once the simulations are performed for both sources with GATE, we use the LM data to calculate the normalization factors. The different components of the model and thus the normalization factors are estimated as given below:

1. **Axial correction factors:** The axial block profile factor is determined by dividing the mean value of detected events in a ring index by the number of coincidence events recorded in each event and is as given below [Pépin 11b]:

$$b_u^{ax} = \sqrt{\frac{\frac{1}{M} \sum_{v=1}^M \sum_{i,j} t_{vivj}^{cyl}}{\sum_{i,j} t_{uivj}^{cyl}}} \quad (6.9)$$

where  $t_{uivj}^{cyl}$  is the number of true coincidence events recorded for a LOR joining crystal  $i$  to crystal  $j$  of rings  $u$  and  $v$ .  $M$  denotes the total number of axial rings in the scanner. The block profile factor is estimated by considering only the direct planes (i.e., ring difference is zero). Figure



6.5 presents the number of detected coincidence events (blue line) in respective ring index for Scanner A. The number of coincidences are recorded by simulating a uniform cylindrical source illuminating uniformly all the rings of the scanner. However, we can observe a lower detection efficiency at the edges of the scanner. The red line in the same graph is the corrected number of events obtained after calculating  $b_u$  factor values using equation 6.9.

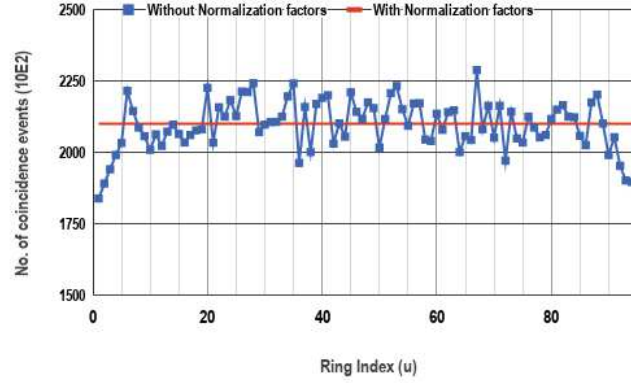


Figure 6.5 – The graph presents number of detected coincidence events as a function of ring index (blue curve) for Scanner A. Red line represents the normalized detected events after applying axial block profile correction factor.

Similarly, we have recorded the number of coincidence events for the IRIS PET scanner (simulated model) as a function of ring index as shown in figure 6.6 left. In figure 6.6 right, the graph presents the correction values  $b_u^{ax}$  estimated for the IRIS PET scanner as a function of ring index.

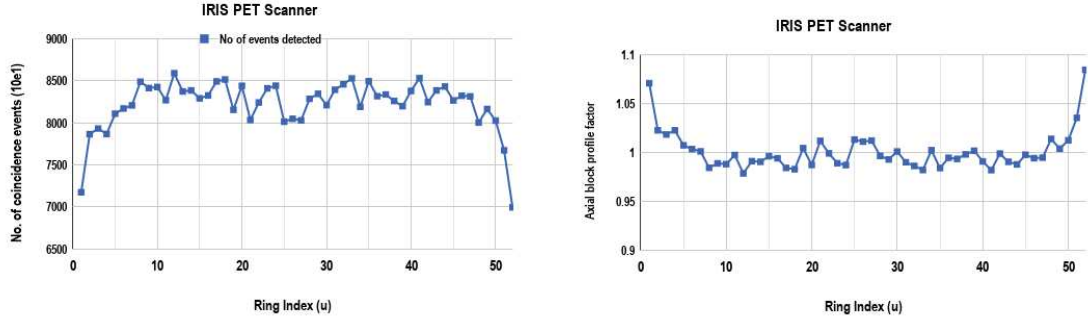


Figure 6.6 – Block profile correction  $b_u^{ax}$  factors for IRIS PET scanner; Left: the number of detected coincidence events as a function of ring index. Right: the axial block profile factors as a function of ring index.

It should be noted that the number of coincidence events per ring index are recorded following GATE simulations running for a short time duration ( $\sim 1 - 2$  hours). The idea behind the calculation of  $b_u^{ax}$  values presented in figure 6.6 right is to show the effectiveness of the axial block profile correction factor.

The axial geometric factors  $g_{uv}^{ax}$  are also calculated using the same simulation source following the

same approach i.e., by dividing the average number of coincidence events in a ring combination by the number of events detected in a ring combination. This factor incorporates the detection efficiency variations between rings which arise due to incidence angle effects and solid angle subtended as a function of ring difference. The formula to estimate the axial geometric factor is given as [Pépin 11b]:

$$g_{uv}^{ax} = \frac{\frac{1}{M^2} \sum_{u',v'}^M b_{u'}^{ax} b_{v'}^{ax} \sum_{i,j} t_{u'iv'j}^{cyl} \cos\theta}{b_u^{ax} b_v^{ax} \sum_{i,j} t_{uivj}^{cyl} \cos\theta} \quad (6.10)$$

where  $\theta$  is the co-polar angle between the LOR and the transverse plane.

2. **Transverse geometric factor:** The transverse geometric factor is estimated by simulating the surface cylindrical source. The radius of the surface cylindrical source is comparable to the radius of the scanner. Thus, the source uniformly irradiates all the crystals and we need not to provide the analytical corrections for the non uniformity of the source. The transverse geometric factor is estimated by averaging all the LORs sharing the common radial distance 'r' and is given as:

$$g_{uv}^{tr} = \frac{\frac{1}{k} \sum_{r'} \sum_{uv} \sum_{x=r'} C_{uivj}^{surf}}{\sum_{uv} \sum_{x=r'} C_{uivj}^{surf}} \quad (6.11)$$

where  $k$  is the number of radial elements and  $C_{uivj}^{surf}$  represents the number of coincidence events for LOR  $uivj$  after applying all the previously calculated correction factors and is given as:

$$C_{uivj}^{surf} = b_u^{ax} b_v^{ax} g_{uv}^{ax} t_{uivj}^{cyl} \quad (6.12)$$

Figure 6.7 presents the calculated transverse geometric factors as a function of radial distance  $r$  from the cFOV. It can be noted that the geometrical component is higher at the cFOV as compared to the edges.

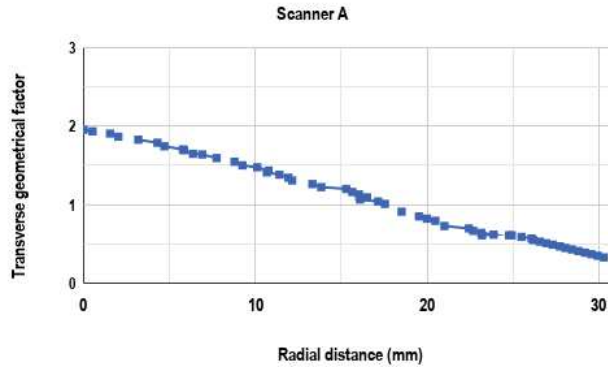


Figure 6.7 – Transverse geometrical factor  $g_{uv}^{tr}$  as a function of radial distance from the cFOV estimated for Scanner A.

3. **Crystal interference pattern:** The crystal interference is a geometric response factor between a crystal and all the crystals present in the opposite module. This geometric response

factor repeats itself after every  $N_m$  crystals, where  $N_m$  is the number of radial crystals in a module. We can further understand the impact of crystal interference pattern in the reconstructed image by observing the IQP reconstructed image of scanner A (figure 6.8 left) as also presented in chapter 5. The image contains a pattern of white lines. This white line pattern is due to the crystal interference effect. The white line pattern appears because in CASToR, to perform the projection and back-projection process, the projectors always maps the center of a crystal to the center of another crystal as shown in figure 6.2.

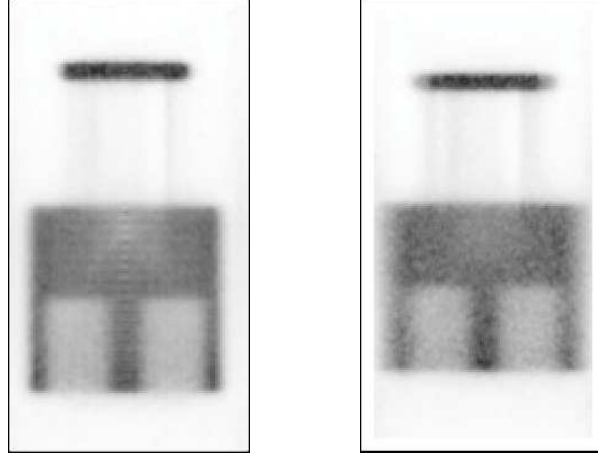


Figure 6.8 – IQP images reconstructed using CASToR for Scanner A for GATE simulated data without (left) and with (right) analytical corrections implemented for crystal interference effect. The IQP reconstructed image on the left shows white lines in the uniform region of the phantom which is corrected in the reconstructed image on the right side.

In the thesis work, we used analytical approach to correct for the interference pattern. In order to correct for this effect while reconstructing images using CASToR, we have updated a part of CASToR algorithm (in the distance driven projector algorithm). Because of the updated part of the code, when the projector maps one crystal to another, it randomly selects a value along the length. Thus while mapping a crystal pair to each other, the distance driven projector starts from a random length of the crystal and maps till another random point of its pair crystal.

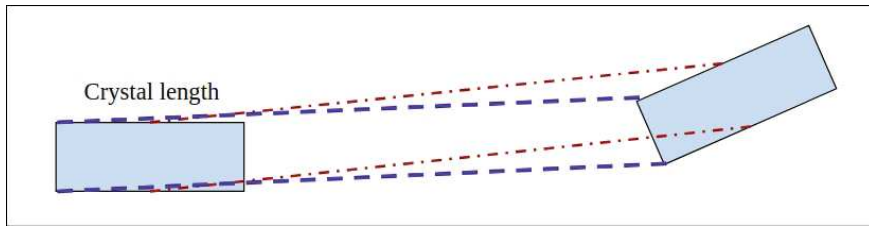


Figure 6.9 – Illustration of a crystal pair where red dotted lines represent the mapping performed by the distance driven projector in CASToR, joining all four side surfaces of the two crystals from the center of a crystal (i.e., half the crystal length) to the center of another. Blue dotted lines are an example of random selection of starting and end point of the projector.

Figure 6.9 presents a crystal pair where red dotted lines show the mapping of the two crystals as

done in CASToR i.e., from center to center. The blue lines in the same figure show an example of the mapping after the code has been updated. Figure 6.8 right, presents the reconstructed IQP with random selection of mapping points for all the crystal pairs and we can observe that there are no white lines as are there in figure 6.8 left. We do not observe these white line pattern because we are randomly selecting the projector starting point and end point (as shown in figure 6.9). Thereby, correcting for the crystal interference pattern effect.

Once all the above mentioned normalization correction factors are estimated (both via MC simulations and analytical approach), we provide these factors in CASToR as a separate binary file containing normalization factors for all the crystal pairs. CASToR while reconstructing the sensitivity profile and the images, reads the input binary normalization file to look for the appropriate normalization value for a particular crystal pair. In the next section we discuss the reconstructed IQP image for Scanner A with the calculated normalization factors. The image reconstructed using normalization factors is also compared with the image reconstructed without the normalization factors.

## 6.5 Comparison with and without normalization correction

In chapter 5, we study the image quality of the reconstructed images for all the scanners. Images were reconstructed using CASToR and no normalization factors were incorporated. We observed artifacts in all the reconstructed images without incorporating the normalization factors. In this chapter, we have estimated the normalization factors and reconstructed images incorporating these factors. In this section we present the qualitative and quantitative comparison of the images reconstructed with and without incorporating the normalization factors.

### 6.5.1 Qualitative comparison

Figure 6.10 presents the transverse image of the uniform region of the IQP reconstructed images without including (left) and including (right) the MC simulation estimated normalization factors. The transverse image on the left side presents a drop in intensity at the cFOV. Incorporating estimated normalization factors in the image reconstruction process, the drop in intensity reduces. Further, in figure 6.11 we compare the line profile passing through the center of figure 6.10.

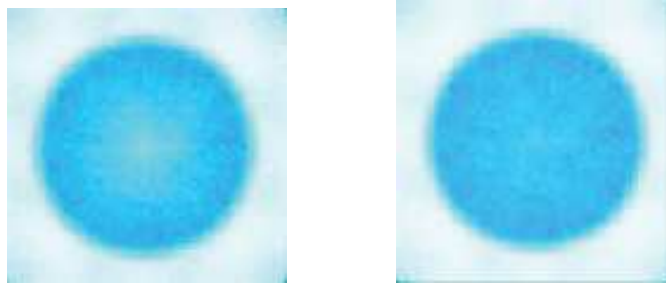


Figure 6.10 – Comparison of the radial profile of the uniform region of the IQP reconstructed using CASToR without normalization factors (left) and with normalization factors (right) estimated following component based normalization model.

Figure 6.12 presents the axial profile of the IQP reconstructed without (left) and with normalization factors (right). The intensity drop can be observed in the image reconstructed without normalization (left), which is corrected using the normalization factors as shown in the image (right). We can observe qualitatively that the drop in the intensity is significantly less when the images are reconstructed using

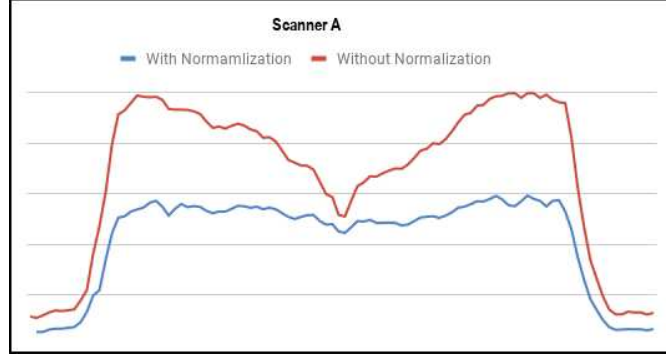


Figure 6.11 – Comparison of the line profile passing through the center of figure 6.10. Red curve presents the line profile for the radial profile of the uniform region of IQP without incorporating normalization factors. The blue curve presents the same for the image reconstruction process incorporating the normalization factors.

normalization factors. However, it should be noted that the MC simulations to estimate the normalization factors are performed for very short duration of time ( $\sim 1-2$  hours). Thus, we did not generate enough statistics to compute accurate normalization factors. The accuracy of the normalization factors and thus the image quality will improve as more statistics will be generated.

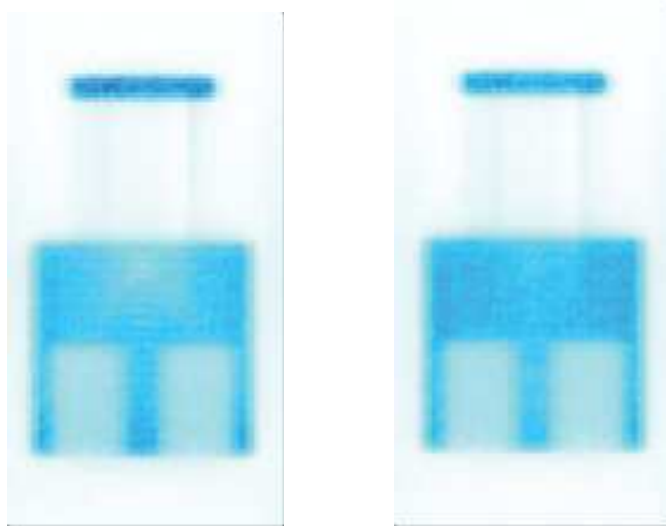


Figure 6.12 – Comparison of axial profile of GATE simulated IQP reconstructed using CASToR without (left) and with (right) incorporating the normalization factors.

### 6.5.2 Quantitative comparison

The quantitative parameters to report the image quality are estimated at the 40<sup>th</sup> iteration. Table 6.1 presents a comparison of the estimated values for RC without and with incorporating the normalization correction factors.

Scanners	1 mm rod	2 mm rod	3 mm rod	4 mm rod	5 mm rod
Without normalization	$0.49 \pm 0.19$	$0.95 \pm 0.21$	$0.98 \pm 0.18$	$0.99 \pm 0.18$	$0.98 \pm 0.16$
With normalization	$0.48 \pm 0.05$	$0.94 \pm 0.10$	$0.92 \pm 0.10$	$0.99 \pm 0.09$	$0.92 \pm 0.07$

Table 6.1 – Comparison of RC values estimated from the IQP reconstructed image ( $40^{th}$  iteration) using CASToR without and with incorporating normalization factors estimated using equations 6.9, 6.10, 6.11, 6.12

We can observe that the estimated RC value for all the hot rods, having different diameters, remains the same with and without incorporating the normalization factors. However, the standard deviation in each RC value for each hot rod reduces significantly with the normalization factors. Furthermore, the SNR value estimated from the image reconstructed with normalization factor shows an improvement of 16 %. The normalization factors reduce the standard deviation (i.e., noise and the artifact) in the reconstructed image, thereby improving the SNR and the accuracy.

## 6.6 Conclusion

In this chapter we discuss the need to normalize the reconstructed images to account for the variation in the detection efficiency of different LORs of a scanner. Different approaches to generate normalization corrections have been presented. We present an analytical approach to correct for crystal interference pattern factor and the resulting image shows improvement. It has been shown further that MC simulation generated normalization factors (following component based normalization approach) are appropriate to normalize the reconstructed images.

The normalization factors for Scanner A are generated by performing the MC simulations with GATE for a short duration of time. However, we need to simulate both the sources for long duration in order to generate accurate normalization coefficients. As we have characterized the accuracy of SM elements generated via MC simulations in Chapter 5, we are also required to test the accuracy of the MC simulation generated normalization factors. Due to time constraint reasons, we did not perform the accuracy test and generated normalization factors with less statistics itself. As a perspective for this chapter, we can investigate the accuracy of normalization factors by performing simulations over longer duration. Similarly, the images generated by other scanners can also be normalized to improve the image quality for accurate quantification.

It has been reported that with the MC generated normalization factor following component based normalization model, the SNR shows an improvement of 16 % as compared to the SNR estimated from the images reconstructed without normalization. With the reconstructed images incorporating MC estimated normalization factors, we can conclude that it is possible to normalize the reconstructed images to improve the image quality for quantitative purpose. Furthermore, since the estimated normalization factors are incorporated on-the-fly while estimating the SM element, thus it improves the image quality without any storage complications.



## Chapter 7

# Concluding Remarks and Perspectives

The advancement of PET modality and the development of animal models of human disease have lead to the development of PET technology for small animals (preclinical PET imaging). Mice are a suitable choice for modelling human diseases because of their faster reproduction cycles, shorter life span, similarity with human genes and advancement of molecular biological technology etc,. Rat is also a favourable animal model for neurological research due to its bigger brain size as compared to mouse. However, the small structures of mice and rats bring the need to design scanners to improve visualization of the radio tracer distribution in the individual organs and in their substructures. Furthermore, in order to maintain the natural biological state of small animals, less radioactivity is injected and lower injected radioactivity results in less event statistics and thus impacts the SNR. Thus for small animal imaging, a PET scanner should have both a) high detection efficiency and b) high spatial resolution.

From positron emission to image reconstruction, many factors have a significant impact on the spatial resolution, detection efficiency and on their trade off. For example, improving spatial resolution led to the development of scanners with small crystals, which results in fewer counts per crystal, thus impacting the SNR. Several research groups have developed dedicated small animal PET scanners starting from the 1997 and some of these scanners are commercially available. However, as discussed in this thesis, most of the developed dedicated small animal PET scanners present a trade-off between the spatial resolution and detection efficiency. The important question is how to decide which of the scanners providing improved spatial resolution or higher detection efficiency will better quantify the radiotracer distribution in the small animals ? or is it possible to improve both simultaneously ? If yes, how much improvement in the quantification of tracer distribution could be observed ?

In order to investigate the above mentioned questions, we simulated four different scanners designs. All the four scanners are designed to provide a spatial resolution of less than 1 mm at the cFOV. Further, based on different geometrical approaches, these scanners provide different detection efficiency values. Quantification accuracy of the radiotracer distribution may vary from one imaging condition to another. Thus, in order to investigate the impact of spatial resolution and detection efficiency on the quantification accuracy independent of the imaging conditions, a standard imaging protocol is followed as provided in NEMA NU - 4 2008. The overall image quality is characterized in terms of recovery coefficient and uniformity. To address the above mentioned questions, we used tools like GATE to perform MC simulations, an approach for data analysis which has been developed in our lab, and an image reconstruction software CASToR. CASToR is a new open source iterative image reconstruction software, where the MLEM algorithm is used to reconstruct the simulated data. CASToR makes use of different analytical projectors to compute the SM elements on-the-fly. We also computed the system matrix for all the scanners using MC simulations.



Based on the above mentioned questions, investigation approaches and the studied scanner designs, the main conclusions of the thesis are:

1. **Simultaneous optimization of the spatial resolution and detection efficiency:** We have investigated four scanner geometries (Scanner A, Scanner B, Scanner C and Scanner D) based on different geometrical approaches. The idea behind the selected geometrical approaches is to progressively add the third dimension in the estimated position of interaction of the gamma photon. The first geometry, Scanner A consists of a radially arranged pixelated crystal matrix which enables the 2D detection of gamma interaction. The second scanner geometry, Scanner B, is designed to improve the detection efficiency of Scanner A without degrading the spatial resolution. It consists of two layers of radially arranged pixelated crystal matrices (same crystal dimension as used for Scanner A). Two radial layers enable 2D detection as well as binary sampling in the radial dimension. The third design, Scanner C, further improves the trade-off between spatial resolution and detection efficiency by incorporating high level of DOI encoding. It consists of axially oriented crystal matrix, which enables 2D detection in the transverse direction as well as continuous sampling in the axial dimension. Thus, optimizing spatial resolution and detection efficiency simultaneously leads to escalating cost as the designs include more crystal matrices (also the photodetectors). Finally, the last design, Scanner D is a simplified solution and employs a monolithic crystal, enabling the complete 3D estimation of the detection position.

By performing MC simulations, following the standard procedure provided in NEMA-NU 4, we estimated the spatial resolution and detection efficiency of all the four scanners as summarized in table 7.1.

Scanners	Spatial Resolution (mm)	Detection efficiency (%)
A	0.92	5.50
B	0.87	13.87
C	0.88	23.42
D	0.85	9.55

Table 7.1 – Spatial resolution (mm) and detection efficiency (%) values estimated via MC simulations for a point source placed at the cFOV for all the four scanner geometries

As designed, all the four scanner geometries are reported to provide a spatial resolution close to 1 mm at the cFOV. Furthermore, Scanner C, enabling us to employ several crystal layers in the radial direction (providing more depth for incoming photon to interact as compared to other scanners), provides the maximum detection efficiency at the cFOV. On the other hand, Scanner A, as expected provides the least value of detection efficiency. Thus, the values obtained are in accordance with the expected behaviour. It is also observed and reported (section 5.3.3) that the spatial resolution for Scanner A and Scanner B degrades as we move the source radially outwards due to parallax error. On the basis of the estimated value of the performance parameters, figure 7.1 compares the studied scanners with the commercial and the research prototype scanners.

Thus, we can observe that the spatial resolution and detection efficiency are decoupled, as we move from 2D to 3D estimation of interaction position of the gamma photon. Decoupling these two enable us to improve both performance parameters simultaneously. Furthermore, it should be noted that we did not investigate the dead time and the pile-up phenomena, which can further impact the scanner detection efficiency values.

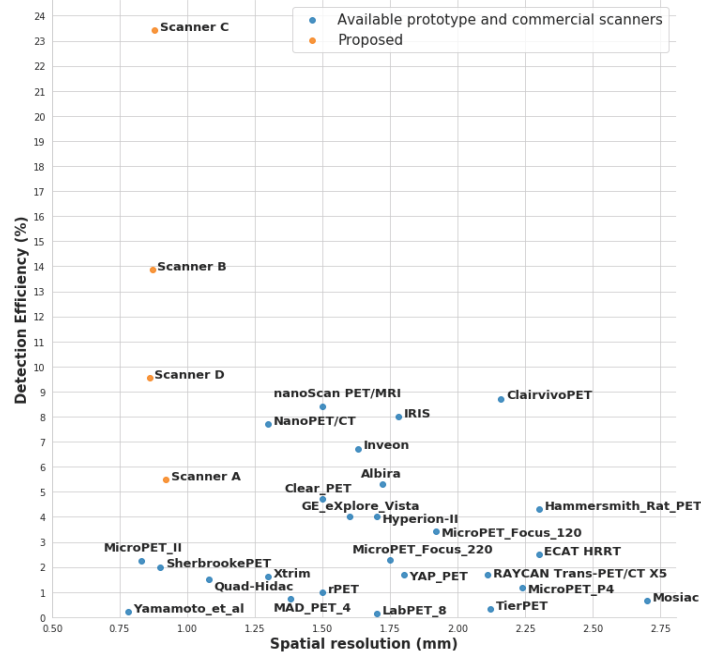


Figure 7.1 – Comparison of studied scanners with other commercial and research prototype scanners in terms of spatial resolution and detection efficiency.

## 2. CASToR: A faster approach to reconstruct images for newly designed scanners:

In this thesis, MLEM algorithm is used to reconstruct images for all the investigated scanner geometries. SM is a central element of all the iterative algorithms. SM can be generated following different approaches such as using projectors, MC simulations, and experimental acquisitions. We used two approaches a) by performing MC simulations and b) using analytical projectors to generate the SM for all the scanners. The outcomes of both approaches are discussed below:

- (a) via MC simulations: The advantage of generating SM elements via MC simulations is that it takes into account all the physical processes associated with the emission and detection of gamma photons. This results in modeling accurately the detector response to the image space. However, this approach requires long simulation scans to pre-compute the SM for all the scanners and store it on the disk for further use during the image reconstruction process. The space on the disk occupied by the SM is completely dependent on the number of elements present in it (i.e., product of  $i$  LORs and  $j$  image voxels). Thus, a major limitation of this approach is the storage of SM elements. However, scanner symmetries linked to each geometry can reduced the size of the matrix [Ortuno 10, Liu 13, Camarlinghi 18].

Another drawback of generating SM via MC simulations comes from long simulation time. All these simulations are performed using a computer grid facility which permits us to use the power of several computers in parallel. If we use the computing power of a single computer (example: Intel Xeon E5-2670 @ 2.6 GHz), the MC simulations will take several years for each scanner. Table 7.2 presents an approximate idea on the simulation run time for the generation of SM for all the four scanners, assuming that the simulations are performed on a single computer. However, it has been reported (section 5.2) that after several years equivalent simulations, the non-zero SM elements keep on increasing as more simulations are being launched. Thus, it can be concluded that we have not generated yet the complete

SM for any of the scanner geometry. Due to this reason the resulting reconstructed image fails to converge towards the estimation of quantitative parameters.

Scanner	MC Simulation run time (years)	Castor Sensitivity image time (s)
A	3.84	1466
B	2.67	6182
C	1.01	435606
D	2.16	138066

Table 7.2 – Comparison of time duration for MC simulations to generate the SM and by CASToR to generate a sensitivity profile for all the scanner geometries.

- (b) via projectors (as implemented in CASToR): CASToR computes the SM elements on-the-fly using analytical projectors and thus no storage of SM elements is required. Before the image reconstruction step, CASToR computes a sensitivity profile where a backward projection step is performed over all possible detection elements present in the scanner. Sensitivity profile is a 3D array having the same size of the image matrix. Each element of the sensitivity profile represents the summation of probability values for an event originated from that image voxel and detected by any detector pair ( $\sum_{j=1}^m a_{ij}$ ). Table 7.2 also presents the time taken by CASToR to generate a sensitivity profile for all the scanners. Where MC simulations take years to generate the SM and thus reconstruct the images, we have shown that using CASToR we can reconstruct the images for the same set of data in a couple of days. Thus we can conclude that CASToR is a faster approach to reconstruct images when investigating several different scanner geometries.

However, it should be noted that in CASToR the projectors estimating the SM elements do not take into account the variation in the detection efficiency of different LORs due to the scanner geometry. Thus we observe artifacts in the reconstructed images. We need to normalize the SM elements to incorporate the detector response function. Furthermore as the scanner geometry gets more and more complicated (i.e., consisting of several crystal layers), the variation in the detection efficiency of different LORs further increases, resulting in more degraded images.

- 3. Effect of scanner performance on the reconstructed image quality:** We simulated the IQP as per the procedure given in NEMA NU-4 2008. The reconstructed image quality is characterized in terms of RC and SNR values. As discussed in the previous point, images reconstructed using pre-computed SM (generated via MC simulations) cannot be used to provide any quantitative information, thus the images reconstructed with CASToR are used for quantification purposes. Table 7.3 provides the RC and SNR values estimated for all the scanners.

Scanner	Recovery Coefficient	Signal-to-Noise Ratio
A	$0.94 \pm 0.18$	7.3
B	$0.76 \pm 0.11$	9.5
C	$0.84 \pm 0.23$	2.1
D	$0.78 \pm 0.09$	3.7

Table 7.3 – Estimated RC (for 2 mm hot rod diameter) and SNR values for CASToR reconstructed images of IQP for all the studied scanners

Scanners having limited spatial resolution as compared to the imaging object, leads to underestimation of the activity due to the Partial Volume Effect (PVE). RC values are indicative of the

spatial resolution, thus scanners with better spatial resolution should provide higher RC values for hot rods of much smaller diameter. All the investigated scanners, with the estimated spatial resolution close to 1 mm, provide comparable RC values for 2 mm diameter rod. However, the error associated with the respective RC values are not insignificant. The error values majorly depend on the SNR value (reported for all the scanners in table B.4), which further depends on the scanner detection efficiency. Detection efficiency should be as high as possible to achieve good SNR and thus more accurate quantification. As reported earlier, Scanner C provides the highest detection efficiency as compared to other scanners, however, the reported SNR value is the least for Scanner D. This is due to the fact that the SNR value and thus the error also depends upon the image reconstruction process and the corrections implemented. As mentioned before, the images are reconstructed using CASToR software where corrections for normalization (or variation in detection efficiency of different LORs) are not accounted for and it results in increased error values. In this case, the error values resulting due to non-normalized images overpower the expected impact of detection efficiency.

All these investigated scanners present a trade off between spatial resolution and detection efficiency to a different extent. Scanner C provides a very high value of detection efficiency as well as spatial resolution close to 1 mm (i.e., providing maximum optimization). However, the impact of optimizing this trade off for Scanner C on the overall image quality is not observed when compared to Scanner A (providing the minimum optimization between the spatial resolution and detection efficiency). It is observed that image reconstruction approach as well as the normalization corrections play a significant role. Thus, it can be concluded that the overall image quality is dominated by the normalization correction and not by the intrinsic performance.

4. **Normalization plays a significant role in image reconstruction process:** We observed the artifacts in the CASToR reconstructed images at the center of the IQP for all the scanner geometries. For this reconstruction process, the projectors are used to estimate the SM elements on-the-fly. However, the projectors are unable to model the detector response for the computed SM elements. As a result the reconstructed images present a lack of intensity at the cFOV as shown in figure 7.2(a) (left).

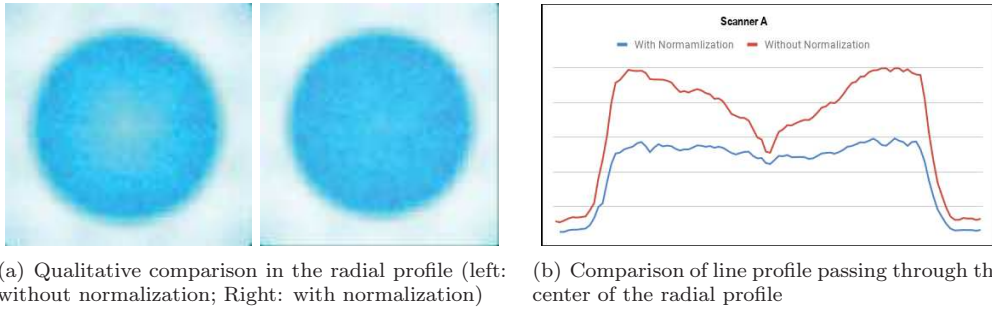


Figure 7.2 – Comparison of the radial profile of the uniform region of the IQP reconstructed using CASToR without and with normalization factors.

These artifacts are due to the fact that the reconstructed images are not normalized for the variation in the detection efficiency of different LORs, whereas the MLEM algorithm assumes that the detection efficiency of all the LORs is the same. We estimated the axial and transaxial normalization factors using component based approach for Scanner A. The normalization factors are estimated following MC simulations, however the simulations are performed for a very short

time duration due to time constraints. We provided all the estimated normalization factors for respective crystal pairs to CASToR to compute the normalized SM elements. We showed that the reconstructed images incorporating normalization factors (computed for a short simulation  $\sim 1$  hour) shows significant improvement qualitatively (figure 7.2(a) left) resulting in 16% improvement in SNR value and thus the estimated RC values are more accurate. Thus, we observed that the normalization correction plays a significant role.

The initial objective of this thesis was to study the feasibility of optimizing the spatial resolution and detection efficiency simultaneously and to study the impact of this optimization on the overall image quality. We have demonstrated that it is possible to decouple the spatial resolution and detection efficiency by using different scanner designs. To further study the impact of these geometries on the quantification of radiotracer distribution, we used iterative image reconstruction algorithm (MLEM). SM were generated using MC simulations, however, it has been observed that SM generation is a very long and time consuming process. With incomplete and inaccurate SM, it is not possible to reconstruct and study the reconstructed images. Furthermore, for Scanner C and Scanner D, due to significant increase in the SM elements, storage has also been reported as one of the major limitations. Thus, an open source image reconstruction software CASToR is used to perform all the reconstruction processes. One of the objectives behind using iterative algorithm was to study the usefulness of CASToR. CASToR is developed to reconstruct images for a scanner geometry employing pixelated crystal matrices. Thus, we adapted CASToR code to take into account the different scanner geometries and reconstructed the IQP simulated data to obtain the images. Since CASToR reconstructs image using analytical projectors and does not take into account the variation in the detection efficiency of different LORs, we observed artifacts in the reconstructed images. These artifacts do impact significantly the noise component of the quantification parameters.

The error in the quantification parameter due to our reconstruction approach (artifact in the reconstructed images) overpowers the impact of optimizing scanner spatial resolution and detection efficiency. We investigated different normalization techniques to account for the variation in the detection efficiency of different LORs. Based on component based method, normalization factors are generated by performing MC simulations for a scanner geometry. CASToR code is also modified to incorporate the generated normalization factors during image reconstruction process. We observed significant improvement in the reconstructed image and also in the quantification accuracy. Based on the improvement, it can be concluded that with appropriated image reconstruction process and the implemented corrections, we can improve the quantification accuracy of the radiotracer distribution more than when compared to optimizing along the spatial resolution and detection efficiency.

Based on our findings, conclusions and the research work performed on four scanner geometries, following could be the perspectives of the current research work:

1. **To correct the reconstructed images for normalization for all the scanners:** As discussed in the thesis, component based normalization factors generated by performing MC simulation improves the reconstructed image quality. An important perspective of this research work would be to estimate the normalization factors for all the remaining scanners and characterize the estimated factors for their accuracy. Once all the normalization factors are estimated and are characterized for the accuracy, it will be used to reconstruct the images using CASToR. We will then be able to quantify the impact of the optimization of spatial resolution and detection efficiency on the reconstructed image quality.

Current version of CASToR works by loading an input correction file (containing the correction factors for all the LORs) and store it on memory. Since Scanner C and scanner D involves a large number of crystal pairs, it is not possible (with current version of CASToR) to perform

the reconstruction process. Thus, another perspective could be to incorporate a solution to fix this limitation and successfully reconstruct the images by taking into account all the estimated normalization factors.

2. **Extraction of kinetic parameters for quantification:** Once the images are corrected for the artifacts, it would be interesting to study the impact of optimization of scanner performance by performing tracer kinetic modelling. Tracer kinetic modelling explains mathematically the transportation mechanism and biochemical reactions of the tracer in tissue. It requires imaging the dynamics of the radiotracer distribution over time in the local tissue to extract the transfer rate constants, volume of distribution or binding potentials from the radiotracer to the target. An important perspective of this research work is to investigate the impact of improving intrinsic performance of the scanner on the estimation of kinetic modelling parameters.



# Appendix A

## Gate simulation macros

### A.1 Scanner A

```
# CYLINDRICAL
/gate/world/daughters/name          cylindricalPET
/gate/world/daughters/insert        cylinder
/gate/cylindricalPET/placement/setTranslation 0.0 0.0 0.0 mm
/gate/cylindricalPET/geometry/setRmax    60.0 mm
/gate/cylindricalPET/geometry/setRmin    30.0 mm
/gate/cylindricalPET/geometry/setHeight  110.0 mm
/gate/cylindricalPET/setMaterial        Air
/gate/cylindricalPET/vis/forceWireframe
/gate/cylindricalPET/vis/setColor       white
/gate/cylindricalPET/vis/setVisible     1

# RSECTOR
/gate/cylindricalPET/daughters/name    rsector
/gate/cylindricalPET/daughters/insert  box
/gate/rsector/placement/setTranslation 35.3 0.0 0.0 mm
/gate/rsector/geometry/setXLength      14.0 mm
/gate/rsector/geometry/setYLength      26.0 mm
/gate/rsector/geometry/setZLength      104.0 mm
/gate/rsector/setMaterial              Air
/gate/rsector/vis/setVisible           0
/gate/rsector/vis/setColor             red

# MODULE
/gate/rsector/daughters/name          module
/gate/rsector/daughters/insert        box
/gate/module/placement/setTranslation 0.0 0.0 0.0 mm
/gate/module/geometry/setXLength      14.0 mm
/gate/module/geometry/setYLength      26.0 mm
/gate/module/geometry/setZLength      51.12 mm
/gate/module/setMaterial              Air
/gate/module/vis/setVisible           0
```



```

# BLOCK
/gate/module/daughters/name block
/gate/module/daughters/insert box
/gate/block/placement/setTranslation 3.0 0.0 0.0 mm
/gate/block/geometry/setXLength 8.0 mm
/gate/block/geometry/setYLength 26.0 mm
/gate/block/geometry/setZLength 51.12 mm
/gate/block/setMaterial Plexiglass
/gate/block/vis/setVisible 0

# C R Y S T A L
/gate/block/daughters/name crystal
/gate/block/daughters/insert box
/gate/crystal/placement/setTranslation 0.0 0.0 0.0 mm
/gate/crystal/geometry/setXLength 8.0 mm
/gate/crystal/geometry/setYLength 0.98 mm
/gate/crystal/geometry/setZLength 0.98 mm
/gate/crystal/setMaterial LYSOPET
/gate/crystal/vis/setVisible 0
/gate/crystal/vis/setColor blue

# LYSO layer
/gate/crystal/daughters/name LYSO
/gate/crystal/daughters/insert box
/gate/LYSO/placement/setTranslation 0.0 0.0 0.0 mm
/gate/LYSO/geometry/setXLength 8.0 mm
/gate/LYSO/geometry/setYLength 0.98 mm
/gate/LYSO/geometry/setZLength 0.98 mm
/gate/LYSO/setMaterial LYSOPET
/gate/LYSO/vis/setColor blue

# R E P E A T C R Y S T A L
/gate/crystal/repeaters/insert cubicArray
/gate/crystal/cubicArray/setRepeatNumberX 1
/gate/crystal/cubicArray/setRepeatNumberY 23
/gate/crystal/cubicArray/setRepeatNumberZ 48
/gate/crystal/cubicArray/setRepeatVector 0.0 1.065 1.065 mm

# R E P E A T M O D U L E
/gate/module/repeaters/insert cubicArray
/gate/module/cubicArray/setRepeatNumberX 1
/gate/module/cubicArray/setRepeatNumberY 1
/gate/module/cubicArray/setRepeatNumberZ 2
/gate/module/cubicArray/setRepeatVector 0.0 0.0 51.12 mm

```

```
# R E P E A T R S E C T O R
/gate/rsector/repeaters/insert ring
/gate/rsector/ring/setRepeatNumber 8
```

## A.2 Scanner B

```
# CYLINDRICAL
/gate/world/daughters/name cylindricalPET
/gate/world/daughters/insert cylinder
/gate/cylindricalPET/placement/setTranslation 0.0 0.0 0.0 mm
/gate/cylindricalPET/geometry/setRmax 60.0 mm
/gate/cylindricalPET/geometry/setRmin 20.0 mm
/gate/cylindricalPET/geometry/setHeight 110.0 mm
/gate/cylindricalPET/setMaterial Air
/gate/cylindricalPET/vis/forceWireframe
/gate/cylindricalPET/vis/setColor white

# RSECTOR
/gate/cylindricalPET/daughters/name rsector
/gate/cylindricalPET/daughters/insert box
/gate/rsector/placement/setTranslation 35.3 0.0 0.0 mm
/gate/rsector/geometry/setXLength 14.0 mm
/gate/rsector/geometry/setYLength 26.0 mm
/gate/rsector/geometry/setZLength 104.0 mm
/gate/rsector/setMaterial Air
/gate/rsector/vis/setVisible 0
/gate/rsector/vis/setColor red

# MODULE
/gate/rsector/daughters/name module
/gate/rsector/daughters/insert box
/gate/module/placement/setTranslation 0.0 0.0 0.0 mm
/gate/module/geometry/setXLength 14.0 mm
/gate/module/geometry/setYLength 26.0 mm
/gate/module/geometry/setZLength 51.12 mm
/gate/module/setMaterial Air
/gate/module/vis/setVisible 0
/gate/module/vis/setColor white

# BLOCK
/gate/module/daughters/name block
/gate/module/daughters/insert box
/gate/block/placement/setTranslation 0.0 0.0 0.0 mm
/gate/block/geometry/setXLength 14.0 mm
/gate/block/geometry/setYLength 26.0 mm
```

```

/gate/block/geometry/setZLength      51.12 mm
/gate/block/setMaterial               Plexiglass
/gate/block/vis/setVisible           0

# C R Y S T A L
/gate/block/daughters/name           crystal
/gate/block/daughters/insert         box
/gate/crystal/placement/setTranslation 0.0 0.0 0.0 mm
/gate/crystal/geometry/setXLength    14.0 mm
/gate/crystal/geometry/setYLength    26.0 mm
/gate/crystal/geometry/setZLength    51.12 mm
/gate/crystal/setMaterial             Plexiglass
/gate/crystal/vis/setVisible          0
/gate/crystal/vis/setColor            white

# LYSO layer
/gate/crystal/daughters/name         LYSO1
/gate/crystal/daughters/insert       box
/gate/LYSO1/placement/setTranslation -4.0 0.0 0.0 mm
/gate/LYSO1/geometry/setXLength      6.0 mm
/gate/LYSO1/geometry/setYLength      0.98 mm
/gate/LYSO1/geometry/setZLength      0.98 mm
/gate/LYSO1/setMaterial               LYSOPET
/gate/LYSO1/vis/setColor              red

/gate/crystal/daughters/name         LYSO2
/gate/crystal/daughters/insert       box
/gate/LYSO2/placement/setTranslation 3.0 0.0 0.0 mm
/gate/LYSO2/geometry/setXLength      8.0 mm
/gate/LYSO2/geometry/setYLength      0.98 mm
/gate/LYSO2/geometry/setZLength      0.98 mm
/gate/LYSO2/setMaterial               LYSOPET
/gate/LYSO2/vis/setColor              blue

# R E P E A T LYSO 1st layers
/gate/LYSO1/repeaters/insert          cubicArray
/gate/LYSO1/cubicArray/setRepeatNumberX 1
/gate/LYSO1/cubicArray/setRepeatNumberY 22
/gate/LYSO1/cubicArray/setRepeatNumberZ 47
/gate/LYSO1/cubicArray/setRepeatVector 0.0 1.065 1.065 mm

# R E P E A T LYSO 2nd layers
/gate/LYSO2/repeaters/insert          cubicArray
/gate/LYSO2/cubicArray/setRepeatNumberX 1
/gate/LYSO2/cubicArray/setRepeatNumberY 23
/gate/LYSO2/cubicArray/setRepeatNumberZ 48

```

```

/gate/LYSO2/cubicArray/setRepeatVector      0.0 1.065 1.065 mm

# R E P E A T M O D U L E
/gate/module/repeaters/insert                cubicArray
/gate/module/cubicArray/setRepeatNumberX     1
/gate/module/cubicArray/setRepeatNumberY     1
/gate/module/cubicArray/setRepeatNumberZ     2
/gate/module/cubicArray/setRepeatVector      0.0 0.0 51.12 mm

# R E P E A T R S E C T O R
/gate/rsector/repeaters/insert                ring
/gate/rsector/ring/setRepeatNumber            8

```

### A.3 Scanner C

```

# CYLINDRICAL
/gate/world/daughters/name                    cylindricalPET
/gate/world/daughters/insert                  cylinder
/gate/cylindricalPET/placement/setTranslation 0.0 0.0 0.0 mm
/gate/cylindricalPET/geometry/setRmax         80.0 mm
/gate/cylindricalPET/geometry/setRmin         20.0 mm
/gate/cylindricalPET/geometry/setHeight       120.0 mm
/gate/cylindricalPET/setMaterial              Air
/gate/cylindricalPET/vis/forceWireframe
/gate/cylindricalPET/vis/setColor             white

# RSECTOR
/gate/cylindricalPET/daughters/name            rsector
/gate/cylindricalPET/daughters/insert          box
/gate/rsector/placement/setTranslation         51.2 0.0 0.0 mm
/gate/rsector/geometry/setXLength              39.0 mm
/gate/rsector/geometry/setYLength              26.0 mm
/gate/rsector/geometry/setZLength              116.0 mm
/gate/rsector/setMaterial                      Air
/gate/rsector/vis/setVisible                   0
/gate/rsector/vis/setColor                     red

# MODULE
/gate/rsector/daughters/name                   module
/gate/rsector/daughters/insert                 box
/gate/module/placement/setTranslation          0.0 0.0 0.0 mm
/gate/module/geometry/setXLength               39.0 mm
/gate/module/geometry/setYLength               26.0 mm
/gate/module/geometry/setZLength               22.9 mm
/gate/module/setMaterial                       Air

```

```

/gate/module/vis/setVisible 0
/gate/module/vis/setColor yellow

# BLOCK
/gate/module/daughters/name block
/gate/module/daughters/insert box
/gate/block/placement/setTranslation 0.0 0.0 0.0 mm
/gate/block/geometry/setXLength 36.0 mm
/gate/block/geometry/setYLength 26.0 mm
/gate/block/geometry/setZLength 22.9 mm
/gate/block/setMaterial Plexiglass
/gate/block/vis/setVisible 0
/gate/block/vis/setColor black

# C R Y S T A L
/gate/block/daughters/name crystal
/gate/block/daughters/insert box
/gate/crystal/placement/setTranslation 0.0 0.0 0.0 mm
/gate/crystal/geometry/setXLength 1.45 mm
/gate/crystal/geometry/setYLength 1.45 mm
/gate/crystal/geometry/setZLength 20.0 mm
/gate/crystal/setMaterial LYSOPET
/gate/crystal/vis/setVisible 0
/gate/crystal/vis/setColor yellow

# LYSO layer
/gate/crystal/daughters/name LYSO
/gate/crystal/daughters/insert box
/gate/LYSO/placement/setTranslation 0.0 0.0 0.0 mm
/gate/LYSO/geometry/setXLength 1.45 mm
/gate/LYSO/geometry/setYLength 1.45 mm
/gate/LYSO/geometry/setZLength 20.0 mm
/gate/LYSO/setMaterial LYSOPET
/gate/LYSO/vis/setColor blue

# R E P E A T C R Y S T A L
/gate/crystal/repeaters/insert cubicArray
/gate/crystal/cubicArray/setRepeatNumberX 24
/gate/crystal/cubicArray/setRepeatNumberY 16
/gate/crystal/cubicArray/setRepeatNumberZ 1
/gate/crystal/cubicArray/setRepeatVector 1.5 1.5 0.0 mm

# R E P E A T M O D U L E
/gate/module/repeaters/insert cubicArray
/gate/module/cubicArray/setRepeatNumberX 1
/gate/module/cubicArray/setRepeatNumberY 1

```

```

/gate/module/cubicArray/setRepeatNumberZ 5
/gate/module/cubicArray/setRepeatVector 0.0 0.0 22.6 mm

# R E P E A T R S E C T O R
/gate/rsector/repeaters/insert ring
/gate/rsector/ring/setRepeatNumber 8

```

## A.4 Scanner D

```

# CYLINDRICAL
/gate/world/daughters/name cylindricalPET
/gate/world/daughters/insert cylinder
/gate/cylindricalPET/placement/setTranslation 0.0 0.0 0.0 mm
/gate/cylindricalPET/geometry/setRmax 100.0 mm
/gate/cylindricalPET/geometry/setRmin 20.0 mm
/gate/cylindricalPET/geometry/setHeight 110.0 mm
/gate/cylindricalPET/setMaterial Air
/gate/cylindricalPET/vis/forceWireframe
/gate/cylindricalPET/vis/setColor white

# — P L E X I G L A S S C A S K —
/gate/cylindricalPET/daughters/name headSyst
/gate/cylindricalPET/daughters/insert box
/gate/headSyst/placement/setTranslation 0.0 0.0 0.0 mm
/gate/headSyst/geometry/setXLength 89.0 mm
/gate/headSyst/geometry/setYLength 89.0 mm
/gate/headSyst/geometry/setZLength 104.0 mm
/gate/headSyst/setMaterial Plexiglass
/gate/headSyst/vis/forceWireframe
/gate/headSyst/vis/setVisible 0
/gate/headSyst/vis/setColor red

# — A I R G A P —
/gate/cylindricalPET/daughters/name module
/gate/cylindricalPET/daughters/insert box
/gate/module/geometry/setXLength 50.4 mm
/gate/module/geometry/setYLength 50.4 mm
/gate/module/geometry/setZLength 104.0 mm
/gate/module/placement/setTranslation 0.0 0.0 0.0 mm
/gate/module/setMaterial Air
/gate/module/vis/forceWireframe
/gate/module/vis/setVisible 0
/gate/module/vis/setColor blue

# — R S E C T O R — #

```

/gate/cylindricalPET/daughters/name	rsector
/gate/cylindricalPET/daughters/insert	box
/gate/rsector/geometry/setXLength	8.32 mm
/gate/rsector/geometry/setYLength	50.14 mm
/gate/rsector/geometry/setZLength	104.0 mm
/gate/rsector/setMaterial	Air
/gate/rsector/placement/setTranslation	29.21 0.0 0.0 mm
/gate/rsector/vis/forceWireframe	
/gate/rsector/vis/setVisible	0
/gate/rsector/vis/setColor	red

#### # — A L U M I N I U M C O A T I N G — #

/gate/rsector/daughters/name	alu
/gate/rsector/daughters/insert	box
/gate/alu/placement/setTranslation	-4.06 0.0 0.0 mm
/gate/alu/geometry/setXLength	0.2 mm
/gate/alu/geometry/setYLength	50.14 mm
/gate/alu/geometry/setZLength	104.0 mm
/gate/alu/setMaterial	Aluminium
/gate/alu/vis/forceWireframe	
/gate/alu/vis/setVisible	0
/gate/alu/vis/setColor	green

#### # — C R Y S T A L — #

/gate/rsector/daughters/name	crystal
/gate/rsector/daughters/insert	box
/gate/crystal/geometry/setXLength	8.12 mm
/gate/crystal/geometry/setYLength	50.14 mm
/gate/crystal/geometry/setZLength	50.14 mm
/gate/crystal/placement/setTranslation	0.1 0.0 0.0 mm
/gate/crystal/setMaterial	Air
/gate/crystal/vis/forceWireframe	
/gate/crystal/vis/setVisible	1

#### # — L Y S O L A Y E R — #

/gate/crystal/daughters/name	LYSO
/gate/crystal/daughters/insert	box
/gate/LYSO/geometry/setXLength	8.12 mm
/gate/LYSO/geometry/setYLength	50.14 mm
/gate/LYSO/geometry/setZLength	50.14 mm
/gate/LYSO/placement/setTranslation	0.0 0.0 0.0 mm
/gate/LYSO/setMaterial	LYSOPET
/gate/LYSO/vis/forceSolid	
/gate/LYSO/vis/setVisible 1	
/gate/LYSO/vis/setColor	blue

#### # R E P E A T C R Y S T A L

/gate/crystal/repeaters/insert	cubicArray
--------------------------------	------------

/gate/crystal/cubicArray/setRepeatNumberX	1
/gate/crystal/cubicArray/setRepeatNumberY	1
/gate/crystal/cubicArray/setRepeatNumberZ	2
/gate/crystal/cubicArray/setRepeatVector	0.0 0.0 52.0 mm
# — position — #	
/gate/rsector/repeaters/insert	ring
/gate/rsector/ring/setRepeatNumber	4





## Appendix B

# CASToR generated geometry files

### B.1 Scanner A

```
# MANDATORY FIELDS
modality : PET
scanner name : Scanner A
number of elements : 17664
number of layers : 1

scanner radius : 34.3
number of rsectors : 8
number of crystals transaxial : 23
number of crystals axial : 48

crystals size depth : 8
crystals size transaxial : 0.98
crystals size axial : 0.98

# OPTIONAL FIELDS
rsectors first angle : -90
number of rsectors axial : 1
rsector gap transaxial : 0
rsector gap axial : 0
number of modules transaxial : 1
number of modules axial : 2
module gap transaxial : 0
module gap axial : 0.085
number of submodules transaxial : 1
number of submodules axial : 1
submodule gap transaxial : 0
submodule gap axial : 0
crystal gap transaxial : 0.085
crystal gap axial : 0.085
mean depth of interaction : -1
rotation direction : CCW
```

## B.2 Scanner B

# MANDATORY FIELDS	
modality :	PET
scanner name :	Scanner B
number of elements :	34208
number of layers :	2
scanner radius :	28.3,34.3
number of rsectors :	8,8
number of crystals transaxial :	22,23
number of crystals axial :	47,48
crystals size depth :	6,8
crystals size transaxial :	0.98,0.98
crystals size axial :	0.98,0.98
# OPTIONAL FIELDS	
rsectors first angle :	-90,-90
number of rsectors axial :	1,1
rsector gap transaxial :	0
rsector gap axial :	0,0
number of modules transaxial :	1,1
number of modules axial :	2,2
module gap transaxial :	0,0
module gap axial :	0,0
number of submodules transaxial :	1,1
number of submodules axial :	1,1
submodule gap transaxial :	0,0
submodule gap axial :	0,0
crystal gap transaxial :	0.085,0.085
crystal gap axial :	0.085,0.085
mean depth of interaction :	-1,-1
rotation direction :	CCW

### B.3 Scanner C

[illegible]

[illegible][illegible]

## B.4 Scanner D

# MANDATORY FIELDS

modality :	PET
scanner name :	Scanner D
number of elements :	160000
number of layers :	8

scanner radius :	25.25,26.25,27.25,28.25,29.25,30.25,31.25,32.25
number of rsectors :	4,4,4,4,4,4,4
number of crystals transaxial :	50,50,50,50,50,50,50,50
number of crystals axial :	50,50,50,50,50,50,50,50

crystals size depth :	1,1,1,1,1,1,1,1
crystals size transaxial :	1.0,1.0,1.0,1.0,1.0,1.0,1.0,1.0
crystals size axial :	1.0,1.0,1.0,1.0,1.0,1.0,1.0,1.0

# OPTIONAL FIELDS

rsectors first angle :	-90,-90,-90,-90,-90,-90,-90,-90
number of rsectors axial :	1,1,1,1,1,1,1,1
rsector gap transaxial :	0
rsector gap axial :	0,0,0,0,0,0,0,0
number of modules transaxial :	1,1,1,1,1,1,1,1
number of modules axial :	2,2,2,2,2,2,2,2
module gap transaxial :	0,0,0,0,0,0,0,0
module gap axial :	1.86,1.86,1.86,1.86,1.86,1.86,1.86,1.86
number of submodules transaxial :	1,1,1,1,1,1,1,1
number of submodules axial :	1,1,1,1,1,1,1,1
submodule gap transaxial :	0,0,0,0,0,0,0,0
submodule gap axial :	0,0,0,0,0,0,0,0
crystal gap transaxial :	0,0,0,0,0,0,0,0
crystal gap axial :	0,0,0,0,0,0,0,0
mean depth of interaction :	-1,-1,-1,-1,-1,-1,-1,-1
rotation direction :	CCW

# Bibliography

- [Agostinelli 03] Sea Agostinelli, John Allison, K al Amako, John Apostolakis, H Araujo, P Arce, M Asai, D Axen, S Banerjee, G 2 Barrand *et al.* *GEANT4—a simulation toolkit*. Nuclear instruments and methods in physics research section A: Accelerators, Spectrometers, Detectors and Associated Equipment, vol. 506, no. 3, pages 250–303, 2003.
- [Alessio 10] Adam M Alessio, Charles W Stearns, Shan Tong, Steven G Ross, Steve Kohlmyer, Alex Ganin & Paul E Kinahan. *Application and evaluation of a measured spatially variant system model for PET image reconstruction*. IEEE transactions on medical imaging, vol. 29, no. 3, pages 938–949, 2010.
- [Andreo 91] Pedro Andreo. *Monte Carlo techniques in medical radiation physics*. Physics in Medicine & Biology, vol. 36, no. 7, page 861, 1991.
- [Anizan 12] Nadège Anizan, Thomas Carlier, Cecilia Hindorf, Jacques Barbet & Manuel Bardiès. *dAcquisition setting optimization and quantitative imaging for 124 I studies with the Inveon microPET-CT system*. EJNMMI research, vol. 2, no. 1, page 7, 2012.
- [Badawi 98] Ramsey D Badawi, MA Lodge & PK Marsden. *Algorithms for calculating detector efficiency normalization coefficients for true coincidences in 3D PET*. Physics in medicine & biology, vol. 43, no. 1, page 189, 1998.
- [Baghaei 07] Hossain Baghaei, Yuxuan Zhang, Hongdi Li, Yu Wang, Soonseok Kim, Rocio A Ramirez, Jiguo Liu, Shitao Liu & Wai-Hoi Wong. *GATE Monte Carlo simulation of a high-sensitivity and high-resolution LSO-based small animal PET camera*. IEEE Transactions on Nuclear Science, vol. 54, no. 5, pages 1568–1573, 2007.
- [Bai 02] Bing Bai, Q Li, CH Holdsworth, E Asma, Yuan-Chuan Tai, A Chatziioannou & Richard M Leahy. *Model-based normalization for iterative 3D PET image reconstruction*. Physics in medicine & biology, vol. 47, no. 15, page 2773, 2002.
- [Bailey 97] Dale Bailey, D.W. Townsend, Paul Kinahan, S Grootoonk & Terry Jones. *An investigation of factors affecting detector and geometric correction in normalization of 3-D PET data*. Nuclear Science, IEEE Transactions on, vol. 43, pages 3300 – 3307, 01 1997.
- [Bao 09] Q. Bao, D. Newport, M. Chen, D. B. Stout & A. F. Chatziioannou. *Performance Evaluation of the Inveon Dedicated PET Preclinical Tomograph Based on the NEMA NU-4 Standards*. Journal of Nuclear Medicine, vol. 50, no. 3, pages 401–408, February 2009.

- [Barca 03] G Barca, F Castrovillari, S Chauvie, D Cuce, F Foppiano, G Ghiso, S Guatelli, E Lamanna, MC Lopes, L Peralta *et al.* *A powerful simulation tool for medical physics applications: Geant4*. Nuclear Physics B-Proceedings Supplements, vol. 125, pages 80–84, 2003.
- [Barrett 97] Harrison H Barrett, Timothy White & Lucas C Parra. *List-mode likelihood*. JOSA A, vol. 14, no. 11, pages 2914–2923, 1997.
- [Belcari 17] Nicola Belcari, Niccolò Camarlinghi, Stefano Ferretti, Patricia Iozzo, Daniele Panetta, Piero A Salvadori, Giancarlo Sportelli & Alberto Del Guerra. *NEMA NU-4 performance evaluation of the IRIS PET/CT preclinical scanner*. IEEE Transactions on Radiation and Plasma Medical Sciences, vol. 1, no. 4, pages 301–309, 2017.
- [Bendriem 13] Bernard Bendriem & David W Townsend. The theory and practice of 3d pet, volume 32. Springer Science & Business Media, 2013.
- [Bergeron 09] Melanie Bergeron, Jules Cadorette, Jean-Francois Beaudoin, Martin D Lepage, Ghislain Robert, Vitali Selivanov, Marc-André Tetrault, Nicolas Viscogliosi, Jeffrey P Norenberg, Réjean Fontaine *et al.* *Performance evaluation of the LabPET APD-based digital PET scanner*. IEEE Transactions on Nuclear Science, vol. 56, no. 1, pages 10–16, 2009.
- [Bergeron 14] Melanie Bergeron, Jules Cadorette, Marc-Andre Tetrault, Jean-Francois Beaudoin, Jean-Daniel Leroux, Rejean Fontaine & Roger Lecomte. *Imaging performance of LabPET APD-based digital PET scanners for pre-clinical research*. Physics in Medicine & Biology, vol. 59, no. 3, page 661, 2014.
- [Boisson 17] Frederic Boisson, Virgile Bekaert, J Sahr & David Brasse. *Description and properties of a resistive network applied to emission tomography detector readouts*. Nuclear Instruments and Methods in Physics Research Section A: Accelerators, Spectrometers, Detectors and Associated Equipment, vol. 872, 08 2017.
- [Brard 13] E Brard & D Brasse. *Axially oriented crystal geometry applied to small-animal PET system: A proof of concept*. IEEE Transactions on Nuclear Science, vol. 60, no. 3, pages 1471–1477, 2013.
- [Brasse 04] D Brasse, I Piqueras & J-L Guyonnet. *Design of a small animal PET system high detection efficiency*. In IEEE Symposium Conference Record Nuclear Science 2004., volume 4, pages 2412–2416. IEEE, 2004.
- [Briesmeister 00] Judith F Briesmeister *et al.* *MCNPTM-A general Monte Carlo N-particle transport code*. 2000.
- [Bruyant 02] Philippe P. Bruyant. *Analytic and iterative reconstruction algorithms in SPECT*. Journal of nuclear medicine : official publication, Society of Nuclear Medicine, vol. 43 10, pages 1343–58, 2002.
- [Bruyndonckx 04] Peter Bruyndonckx, Sophie Léonard, Stefaan Tavernier, Cedric Lemaître, Olivier Devroede, Yibao Wu & Magalie Krieguer. *Neural network-based position estimators for PET detectors using monolithic LSO blocks*. IEEE Transactions on Nuclear Science, vol. 51, no. 5, pages 2520–2525, 2004.

- [Bruyndonckx 06] P Bruyndonckx, Cedric Lemaitre, Sophie Leonard, Dennis R Schaart, DJ Van Der Laan, Marnix C Maas, Olivier Devroede, Yibao Wu, Magalie Krieguer & Stefaan Tavernier. *Initial characterization of a nonpixelated scintillator detector in a PET prototype demonstrator*. IEEE transactions on nuclear science, vol. 53, no. 5, pages 2543–2548, 2006.
- [Buvat 02] I Buvat, I Castiglioni *et al.* *Monte Carlo simulations in SPET and PET*. QJ Nucl. Med, vol. 46, no. 1, pages 48–61, 2002.
- [Buvat 05] Irene Buvat, Isabella Castiglioni, Juliette Feuardent & Maria-Carla Gilardi. *Unified description and validation of Monte Carlo simulators in PET*. Physics in Medicine & Biology, vol. 50, no. 2, page 329, 2005.
- [Cabello 13] J Cabello, P Barrillon, J Barrio, MARIA GIUSEPPINA Bisogni, Alberto Del Guerra, C Lacasta, M Rafecas, H Saikouk, C Solaz, P Soleviet *et al.* *High resolution detectors based on continuous crystals and SiPMs for small animal PET*. Nuclear Instruments and Methods in Physics Research Section A: Accelerators, Spectrometers, Detectors and Associated Equipment, vol. 718, pages 148–150, 2013.
- [Cai 19] Zhengxin Cai, Songye Li, David Matuskey, Nabeel Nabulsi & Yiyun Huang. *PET imaging of synaptic density: A new tool for investigation of neuropsychiatric diseases*. Neuroscience letters, vol. 691, pages 44–50, 2019.
- [Camarlinghi 18] Niccolò Camarlinghi, Giancarlo Sportelli, Alberto Del Guerra & Nicola Belcari. *An automatic algorithm to exploit the symmetries of the system response matrix in positron emission tomography iterative reconstruction*. Physics in Medicine & Biology, vol. 63, no. 19, page 195005, 2018.
- [Carles 12] M Carles, Ch W Lerche, F Sánchez, A Orero, L Moliner, A Soriano & JM Benloch. *Performance of a DOI-encoding small animal PET system with monolithic scintillators*. Nuclear Instruments and Methods in Physics Research Section A: Accelerators, Spectrometers, Detectors and Associated Equipment, vol. 695, pages 317–321, 2012.
- [Casey 86a] ME Casey & R Nutt. *A multicrystal two dimensional BGO detector system for positron emission tomography*. Ieee transactions on nuclear science, vol. 33, no. 1, pages 460–463, 1986.
- [Casey 86b] Michael E Casey & Edward J Hoffman. *Quantitation in positron emission computed tomography: 7. A technique to reduce noise in accidental coincidence measurements and coincidence efficiency calibration*. Journal of computer assisted tomography, vol. 10, no. 5, pages 845–850, 1986.
- [Castell 08] F Castell & GJR Cook. *Quantitative techniques in 18 FDG PET scanning in oncology*. British Journal of Cancer, vol. 98, no. 10, page 1597, 2008.
- [Castro 15] Filipe Castro. *Silicon Photomultipliers*, 2015.
- [Chatziioannou 02] Arion F Chatziioannou. *Molecular imaging of small animals with dedicated PET tomographs*. European journal of nuclear medicine and molecular imaging, vol. 29, no. 1, pages 98–114, 2002.



- [Cherry 95] S.R. Cherry, Y. Shao, M.P. Tornai, S. Siegel, A.R. Ricci & M.E. Phelps. *Collection of scintillation light from small BGO crystals*. IEEE Transactions on Nuclear Science, vol. 42, no. 4, pages 1058–1063, 1995.
- [Cherry 01] Simon R Cherry & Sanjiv S Gambhir. *Use of positron emission tomography in animal research*. ILAR journal, vol. 42, no. 3, pages 219–232, 2001.
- [Cherry 12] Simon R. Cherry, James A. Sorenson PhD & Michael E. Phelps PhD. *Physics in nuclear medicine*. Saunders, 2012.
- [Chung 04] Yong Hyun Chung, Yong Choi, Gyuseong Cho, Yearn Seong Choe, Kyung-Han Lee & Byung-Tae Kim. *Characterization of dual layer phoswich detector performance for small animal PET using Monte Carlo simulation*. Physics in Medicine and Biology, vol. 49, no. 13, pages 2881–2890, jun 2004.
- [Commons 03] Wikimedia Commons. *Schematic view of a photomultiplier coupled to a scintillator, illustrating detection of gamma rays*, 2003.
- [Constantinescu 09] Cristian C Constantinescu & Jogeshwar Mukherjee. *Performance evaluation of an Inveon PET preclinical scanner*. Physics in Medicine & Biology, vol. 54, no. 9, page 2885, 2009.
- [Conti 91] PS Conti. *The applications of PET in clinical oncology*. 1991.
- [Cutler 92] P Duffy Cutler, Simon R Cherry, Edward J Hoffman, Ward M Digby & Michael E Phelps. *Design features and performance of a PET system for animal research*. Journal of nuclear medicine: official publication, Society of Nuclear Medicine, vol. 33, no. 4, pages 595–604, 1992.
- [De Man 02] Bruno De Man & S Basu. *Distance-driven projection and backprojection*. pages 1477 – 1480 vol.3, 12 2002.
- [De Man 04] Bruno De Man & Samit Basu. *Distance-driven projection and backprojection in three dimensions*. Physics in medicine and biology, vol. 49, pages 2463–75, 07 2004.
- [Defrise 91] M Defrise, DW Townsend, D Bailey, AMC Geissbuhler & T Jones. *A normalization technique for 3D PET data*. Physics in Medicine & Biology, vol. 36, no. 7, page 939, 1991.
- [Dinu 13] Nicoletta Dinu. *Instrumentation on Silicon Detectors: from properties characterization to applications*. PhD thesis, Université Paris Sud-Paris XI, 2013.
- [España 10] Samuel España, LM Fraile, JL Herraiz, José Manuel Udías, M Desco & JJ Vaquero. *Performance evaluation of SiPM photodetectors for PET imaging in the presence of magnetic fields*. Nuclear Instruments and Methods in Physics Research Section A: Accelerators, Spectrometers, Detectors and Associated Equipment, vol. 613, no. 2, pages 308–316, 2010.
- [Feldman 09] Richard M. Feldman & Ciriaco Valdez-Flores. *Basics of Monte Carlo Simulation*. In Applied Probability and Stochastic Processes, pages 45–72. Springer Berlin Heidelberg, November 2009.

- [Fine 12] Eugene J. Fine, C.J. Segal-Isaacson, Richard D. Feinman, Silvia Herszkopf, Maria C. Romano, Norica Tomuta, Amanda F. Bontempo, Abdissa Negassa & Joseph A. Sparano. *Targeting insulin inhibition as a metabolic therapy in advanced cancer: A pilot safety and feasibility dietary trial in 10 patients*. Nutrition, vol. 28, no. 10, pages 1028–1035, October 2012.
- [Goertzen 12] Andrew L Goertzen, Qinan Bao, Mélanie Bergeron, Eric Blankemeyer, Stephan Blinder, Mario Cañadas, Arion F Chatziioannou, Katherine Dinelle, Esmat Elhami, Hans-Sonke Janset *al.* *NEMA NU 4-2008 comparison of preclinical PET imaging systems*. Journal of Nuclear Medicine, vol. 53, no. 8, pages 1300–1309, 2012.
- [Golovin 04] V Golovin & Valeri Saveliev. *Novel type of avalanche photodetector with Geiger mode operation*. Nuclear Instruments and Methods in Physics Research Section A: Accelerators, Spectrometers, Detectors and Associated Equipment, vol. 518, no. 1-2, pages 560–564, 2004.
- [González 13] AJ González, A Peiró, P Conde, L Hernández, L Moliner, A Orero, MJ Rodríguez-Álvarez, F Sánchez, A Soriano, LF Vidale *al.* *Monolithic crystals for PET devices: Optical coupling optimization*. Nuclear Instruments and Methods in Physics Research Section A: Accelerators, Spectrometers, Detectors and Associated Equipment, vol. 731, pages 288–294, 2013.
- [Hamamatsu 16] Hamamatsu. *MPPC and MPPC module for precision measurement*. Hamamatsu, Japan, 3 2016.
- [Hansen 04] K Hansen & C Khanna. *Spontaneous and genetically engineered animal models: use in preclinical cancer drug development*. European Journal of Cancer, vol. 40, no. 6, pages 858–880, 2004.
- [Hau 08] Jann Hau. *Animal models for human diseases*. In Sourcebook of models for biomedical research, pages 3–8. Springer, 2008.
- [Hicks 01] Rodney J Hicks, Victor Kalff, Michael P MacManus, Robert E Ware, Allan F McKenzie, Jane P Matthews & David L Ball. *The utility of 18F-FDG PET for suspected recurrent non-small cell lung cancer after potentially curative therapy: impact on management and prognostic stratification*. Journal of Nuclear Medicine, vol. 42, no. 11, pages 1605–1613, 2001.
- [Hicks 09] Rodney J Hicks. *Role of 18F-FDG PET in assessment of response in non-small cell lung cancer*. Journal of Nuclear Medicine, 2009.
- [Hirayama 05] Hideo Hirayama, Yoshihito Namito, Walter R Nelson, Alex F Bielajew & Scott J Wilderman. *The EGS5 code system*. Rapport technique, 2005.
- [Hoffman 89] Edward J Hoffman, Thomas M Guerrero, Guido Germano, WM Digby & M Dahlbom. *PET system calibrations and corrections for quantitative and spatially accurate images*. IEEE Transactions on Nuclear Science, vol. 36, no. 1, pages 1108–1112, 1989.

- [Hoh 93] Carl K. Hoh, Randall A. Hawkins, John A. Glaspy, Magnus Dahlbom, Nielson Y. Tse, Edward J. Hoffman, Christiaan Schiepers, Yong Choi, Sheila Rege, Egbert Nitzsche, Jamshid Maddahi & Michael E. Phelps. *Cancer Detection with Whole-Body PET Using 2-[18F]Fluoro-2-Deoxy-D-Glucose*. Journal of Computer Assisted Tomography, vol. 17, no. 4, pages 582–589, jul 1993.
- [Huisman 07] Marc C Huisman, Sybille Reder, Axel W Weber, Sibylle I Ziegler & Markus Schwaiger. *Performance evaluation of the Philips MOSAIC small animal PET scanner*. European journal of Nuclear Medicine and Molecular imaging, vol. 34, no. 4, pages 532–540, 2007.
- [Hume 92] Susan P Hume, Ralph Myers, Peter M Bloomfield, Jolanta Opacka-Juffry, Jill E Cremer, Randall G Ahier, Sajinda K Luthra, David J Brooks & Adriaan A Lammertsma. *Quantitation of carbon-11-labeled raclopride in rat striatum using positron emission tomography*. Synapse, vol. 12, no. 1, pages 47–54, 1992.
- [Humm 03] John L Humm, Anatoly Rosenfeld & Alberto Del Guerra. *From PET detectors to PET scanners*. European journal of nuclear medicine and molecular imaging, vol. 30, no. 11, pages 1574–1597, 2003.
- [Ingvar 91] M Ingvar, L Eriksson, GA Rogers, S Stone-Elander & L Widen. *Rapid feasibility studies of tracers for positron emission tomography: high-resolution PET in small animals with kinetic analysis*. Journal of Cerebral Blood Flow & Metabolism, vol. 11, no. 6, pages 926–931, 1991.
- [Iskandrian 16] Ami E Iskandrian & Ernest V Garcia. *Nuclear cardiac imaging*, 2016.
- [Ito 11] Mikiko Ito, Seong Jong Hong & Jae Sung Lee. *Positron emission tomography (PET) detectors with depth-of- interaction (DOI) capability*. Biomedical Engineering Letters, vol. 1, no. 2, pages 70–81, May 2011.
- [Jacobs 98] Filip Jacobs, Erik Sundermann, Bjorn De Sutter, Mark Christiaens & Ignace Lemahieu. *A fast algorithm to calculate the exact radiological path through a pixel or voxel space*. Journal of computing and information technology, vol. 6, no. 1, pages 89–94, 1998.
- [Jacobson 14] Orit Jacobson, Dale O Kiesewetter & Xiaoyuan Chen. *Fluorine-18 radiochemistry, labeling strategies and synthetic routes*. Bioconjugate chemistry, vol. 26, no. 1, pages 1–18, 2014.
- [Jan 00] S Jan, J Collot & E Tournefier. *A liquid xenon PET camera-simulation and position sensitive PMT tests*. In 2000 IEEE Nuclear Science Symposium. Conference Record (Cat. No. 00CH37149), volume 3, pages 17–23. IEEE, 2000.
- [Jan 04] Sébastien Jan, G Santin, D Strul, Steven Staelens, K Assie, D Autret, S Avner, R Barbier, M Bardies, PM Bloomfield *et al.* *GATE: a simulation toolkit for PET and SPECT*. Physics in Medicine & Biology, vol. 49, no. 19, page 4543, 2004.
- [Jan 05a] S. Jan, C. Comtat, D. Strul, G. Santin & R. Trebossen. *Monte Carlo Simulation for the ECAT EXACT HR+ system using GATE*. IEEE Transactions on Nuclear Science, vol. 52, no. 3, pages 627–633, June 2005.

- [Jan 05b] Sébastien Jan, C Comtat, D Strul, G Santin & R Trebossen. *Monte Carlo simulation for the ECAT EXACT HR+ system using GATE*. Ieee transactions on nuclear science, vol. 52, no. 3, pages 627–633, 2005.
- [Jan 05c] Sébastien Jan, Claude Comtat, Daniel Strul, Giovanni Santin & Régine Trébossen. *Monte Carlo simulation for the ECAT EXACT HR+ system using GATE*. Nuclear Science, IEEE Transactions on, vol. 52, pages 627 – 633, 07 2005.
- [Joseph 82] Peter M Joseph. *An improved algorithm for reprojecting rays through pixel images*. IEEE transactions on medical imaging, vol. 1, no. 3, pages 192–196, 1982.
- [Jødal 14] Lars Jødal, Cindy Le Loirec & Christophe Champion. *Positron range in PET imaging: Non-conventional isotopes*. Physics in medicine and biology, vol. 59, pages 7419–7434, 11 2014.
- [Kiessling 11] Fabian Kiessling. *Small animal imaging : basics and practical guide*. Springer, Berlin Heidelberg, 2011.
- [Kim 07] J. S. Kim, J. S. Lee, K. C. Im, S. J. Kim, S.-Y. Kim, D. S. Lee & D. H. Moon. *Performance Measurement of the microPET Focus 120 Scanner*. Journal of Nuclear Medicine, vol. 48, no. 9, pages 1527–1535, August 2007.
- [Kitson 09] Sean L Kitson, Vincenzo Cuccurullo, Andrea Ciarmiello, Diana Salvo & Luigi Mansi. *Clinical applications of positron emission tomography (PET) imaging in medicine: oncology, brain diseases and cardiology*. Current Radiopharmaceuticals, vol. 2, no. 4, pages 224–253, 2009.
- [Knoess 03a] Christof Knoess, Stefan Siegel, Anne Smith, Danny Newport, Norbert Richerzhagen, Alexandra Winkeler, Andreas Jacobs, Rhonda N Goble, Rudolf Graf, Klaus Wienhard *et al.* *Performance evaluation of the microPET R4 PET scanner for rodents*. European journal of nuclear medicine and molecular imaging, vol. 30, no. 5, pages 737–747, 2003.
- [Knoess 03b] Christof Knoess, Stefan Siegel, Anne Smith, Danny Newport, Norbert Richerzhagen, Alexandra Winkeler, Andreas Jacobs, Rhonda N. Goble, Rudolf Graf, Klaus Wienhard & Wolf-Dieter Heiss. *Performance evaluation of the microPET R4 PET scanner for rodents*. European Journal of Nuclear Medicine and Molecular Imaging, vol. 30, no. 5, pages 737–747, May 2003.
- [Knoll 10] Glenn F Knoll. *Radiation detection and measurement*. John Wiley & Sons, 2010.
- [Kuntner 14] Claudia Kuntner & David B Stout. *Quantitative preclinical PET imaging: opportunities and challenges*. Frontiers in physics, vol. 2, page 12, 2014.
- [Laforest 07] Richard Laforest, Desmond Longford, Stefan Siegel, Danny F Newport & Jeffrey Yap. *Performance evaluation of the microPET®—FOCUS-F120*. IEEE Transactions on Nuclear Science, vol. 54, no. 1, pages 42–49, 2007.
- [Lage 08] Eduardo Lage, Juan Jose Vaquero, Alejandro Sisniega, Samuel Espana, Gustavo Tapias, Angel Udias, Veronica Garcia, Alexia Rodriguez-Ruano & Manuel Desco. *VrPET/CT: Development of a rotating multimodality scanner for small-animal imaging*. In 2008 IEEE Nuclear Science Symposium Conference Record. IEEE, October 2008.

- [Lage 09] E Lage, JJ Vaquero, A Sisniega, S Espana, G Tapias, M Abella, A Rodriguez-Ruano, JE Ortuno, A Udias & M Desco. *Design and performance evaluation of a coplanar multimodality scanner for rodent imaging*. Physics in Medicine & Biology, vol. 54, no. 18, page 5427, 2009.
- [Lamare 04] Frederic Lamare, Alexandra Turzo, Yves Bizais & Dimitris Visvikis. *Simulation of the Allegro PET system using GATE*. In Medical Imaging 2004: Physics of Medical Imaging, volume 5368, pages 890–898. International Society for Optics and Photonics, 2004.
- [Lamare 06] F Lamare, A Turzo, Y Bizais, C Cheze Le Rest & D Visvikis. *Validation of a Monte Carlo simulation of the Philips Allegro/GEMINI PET systems using GATE*. Physics in Medicine & Biology, vol. 51, no. 4, page 943, 2006.
- [Lancelot 10] Sophie Lancelot & Luc Zimmer. *Small-animal positron emission tomography as a tool for neuropharmacology*. Trends in pharmacological sciences, vol. 31, no. 9, pages 411–417, 2010.
- [Le Bars 06] Didier Le Bars. *Fluorine-18 and medical imaging: Radiopharmaceuticals for positron emission tomography*. Journal of Fluorine Chemistry, vol. 127, no. 11, pages 1488–1493, 2006.
- [Le Loirec 07] C Le Loirec & C Champion. *Track structure simulation for positron emitters of physical interest. Part II: The case of the radiometals*. Nuclear Instruments and Methods in Physics Research Section A: Accelerators, Spectrometers, Detectors and Associated Equipment, vol. 582, no. 2, pages 654–664, 2007.
- [Lerche 05] Christoph Lerche, J.M. Benloch, F Sanchez, N Pavon, B Escat, Eva Gimenez, M Fernandez, I Torres, Marc Gimenez, A Sebastia & J Martinez. *Depth of ??-ray interaction within continuous crystals from the width of its scintillation light-distribution*. Nuclear Science, IEEE Transactions on, vol. 52, pages 560 – 572, 07 2005.
- [Levakhina 14] Yulia Levakhina. *Forward and backprojection model (FP/BP)*. In Three-Dimensional Digital Tomosynthesis, pages 43–74. Springer Fachmedien Wiesbaden, 2014.
- [Levin 99] Craig S Levin & Edward J Hoffman. *Calculation of positron range and its effect on the fundamental limit of positron emission tomography system spatial resolution*. Physics in Medicine & Biology, vol. 44, no. 3, page 781, 1999.
- [Levin 02] Craig S Levin. *Design of a high-resolution and high-sensitivity scintillation crystal array for PET with nearly complete light collection*. IEEE Transactions on Nuclear Science, vol. 49, no. 5, pages 2236–2243, 2002.
- [Levin 07] Craig S Levin & Habib Zaidi. *Current trends in preclinical PET system design*. PET clinics, vol. 2, no. 2, pages 125–160, 2007.
- [Li 10] Zhi Li, M Wedrowski, P Bruyndonckx & G Vandersteen. *Nonlinear least-squares modeling of 3D interaction position in a monolithic scintillator block*. Physics in Medicine & Biology, vol. 55, no. 21, page 6515, 2010.

- [Li 15] Kaiyang Li, Mitra Safavi-Naeini, DR Franklin, Zhangbo Han, Anatoly B Rosenfeld, B Hutton & Michael LF Lerch. *A new virtual ring-based system matrix generator for iterative image reconstruction in high resolution small volume PET systems*. Physics in Medicine & Biology, vol. 60, no. 17, page 6949, 2015.
- [Ling 07] T Ling, TK Lewellen & RS Miyaoka. *Depth of interaction decoding of a continuous crystal detector module*. Physics in Medicine & Biology, vol. 52, no. 8, page 2213, 2007.
- [Liu 13] Yilong Liu, Mengdie Wang, Jing Bai & Hui Zhang. *System response matrix calculation using symmetries for dual-head PET scanners*. International Journal of Imaging Systems and Technology, vol. 23, no. 3, pages 205–214, 2013.
- [Ljungberg 12] M. Ljungberg, S.E. Strand & M.A. King. Monte carlo calculations in nuclear medicine, second edition: Applications in diagnostic imaging. Series in Medical Physics and Biomedical Engineering. Taylor & Francis, 2012.
- [Loudos 07] George K Loudos. *Monte Carlo simulations in Nuclear Medicine*. In AIP Conference Proceedings, volume 958, pages 147–150. AIP, 2007.
- [Lu 16] Lijun Lu, Houjin Zhang, Zhaoying Bian, Jianhua Ma, Qiangjin Feng & Wufan Chen. *Validation of a Monte Carlo simulation of the Inveon PET scanner using GATE*. Nuclear Instruments and Methods in Physics Research Section A: Accelerators, Spectrometers, Detectors and Associated Equipment, vol. 828, pages 170–175, 2016.
- [Maas 06] Marnix C Maas, DJ Van Der Laan, Dennis R Schaart, Jan Huizenga, JC Brouwer, Peter Bruyndonckx, Sophie Léonard, Cedric Lemaître & Carel WE Van Eijk. *Experimental characterization of monolithic-crystal small animal PET detectors read out by APD arrays*. IEEE Transactions on Nuclear Science, vol. 53, no. 3, pages 1071–1077, 2006.
- [Manjeshwar 06] Ravindra M Manjeshwar, Steven G Ross, Maria Iatrou, Timothy W Deller & Charles W Stearns. *Fully 3D PET iterative reconstruction using distance-driven projectors and native scanner geometry*. In 2006 IEEE Nuclear Science Symposium Conference Record, volume 5, pages 2804–2807. IEEE, 2006.
- [Marcinkowski 16] Radosław Marcinkowski, Pieter Mollet, Roel Van Holen & Stefaan Vandenberghe. *Sub-millimetre DOI detector based on monolithic LYSO and digital SiPM for a dedicated small-animal PET system*. Physics in Medicine & Biology, vol. 61, no. 5, page 2196, 2016.
- [Melcher 00] Charles L Melcher. *Scintillation crystals for PET*. 2000.
- [Merheb 06] Charbel Merheb, Stan Nicol, Yolande Petegnief, Jean-Noël Talbot & Irène Buvat. *Assessment of the Mosaic animal PET system response using list-mode data for validation of GATE Monte Carlo modelling*. Nuclear Instruments and Methods in Physics Research Section A: Accelerators, Spectrometers, Detectors and Associated Equipment, vol. 569, no. 2, pages 220–224, 2006.



- [Merlin 18] Thibaut Merlin, Simon Stute, Didier Benoit, Julien Bert, Thomas Carlier, Claude Comtat, Marina Filipovic, Frédéric Lamare & Dimitris Visvikis. *CASToR: a generic data organization and processing code framework for multi-modal and multi-dimensional tomographic reconstruction*. Physics in Medicine & Biology, vol. 63, no. 18, page 185005, 2018.
- [Mikhaylova 15] Ekaterina Mikhaylova, Valerio Tabacchini, Giacomo Borghi, Pieter Mollet, D’Hoe Ester, Dennis R Schaart & Stefaan Vandenberghe. *Geometric optimization of an ultralow-dose high-resolution pediatric PET scanner based on monolithic scintillators with dSiPM readout*. In EJNMMI physics, volume 2, page A23. SpringerOpen, 2015.
- [Miyaoka 10] Robert S Miyaoka, Xiaoli Li, William Hunter, Larry Pierce, Wendy McDougald, Paul E Kinahan & Tom K Lewellen. *Resolution properties of a prototype continuous miniature crystal element (cMiCE) scanner*. In IEEE Nuclear Science Symposium & Medical Imaging Conference, pages 2836–2840. IEEE, 2010.
- [Murthy 00] Kavita Murthy, Marianne Aznar, Christopher J Thompson, Antoine Loutfi, Robert Lisbona & Jean H Gagnon. *Results of preliminary clinical trials of the positron emission mammography system PEM-I: a dedicated breast imaging system producing glucose metabolic images using FDG*. Journal of Nuclear Medicine, vol. 41, no. 11, pages 1851–1858, 2000.
- [Myers 02] R Myers. *Small animal PET*. European Neuropsychopharmacology, vol. 12, no. 6, pages 545–555, December 2002.
- [Müller 18] Florian Müller, David Schug, Patrick Hallen, Jan Grahe & Volkmar Schulz. *A novel DOI Positioning Algorithm for Monolithic Scintillator Crystals in PET based on Gradient Tree Boosting*, 05 2018.
- [Nader 06] Michael A Nader, Drake Morgan, H Donald Gage, Susan H Nader, Tonya L Calhoun, Nancy Buchheimer, Richard Ehrenkaufer & Robert H Mach. *PET imaging of dopamine D2 receptors during chronic cocaine self-administration in monkeys*. Nature neuroscience, vol. 9, no. 8, page 1050, 2006.
- [Nagy 13] Kálmán Nagy, Miklós Tóth, Péter Major, Gergely Patay, Győző Egri, Jenny Häggkvist, Andrea Varrone, Lars Farde, Christer Halldin & Balázs Gulyás. *Performance evaluation of the small-animal nanoScan PET/MRI system*. Journal of Nuclear Medicine, vol. 54, no. 10, pages 1825–1832, 2013.
- [Nelson 90] W Ralph Nelson & Yoshihito Namito. *The EGS4 code system: solution of gamma-ray and electron transport problems*. Rapport technique, Stanford Linear Accelerator Center, Menlo Park, CA (USA), 1990.
- [Oehr 03] Peter Oehr, Hans-Jürgen Biersack & R Edward Coleman. *Pet and pet-ct in oncology*. 08 2003.
- [O’Hea 15] Inna O’Hea. *MSc Thesis "The development of Phase-contrast imaging techniques towards implementation in clinical mammography"*. PhD thesis, 09 2015.
- [Ollinger 95] John M Ollinger. *Detector efficiency and Compton scatter in fully 3D PET*. IEEE transactions on nuclear science, vol. 42, no. 4, pages 1168–1173, 1995.

- [Ortuno 10] JE Ortuno, G Kontaxakis, JL Rubio, P Guerra & A Santos. *Efficient methodologies for system matrix modelling in iterative image reconstruction for rotating high-resolution PET*. Physics in Medicine & Biology, vol. 55, no. 7, page 1833, 2010.
- [Oyen 04] Wim JG Oyen, Jan Bussink, Ad FT Verhagen, Frans HM Corstens & Gerben P Bootsma. *Role of FDG-PET in the diagnosis and management of lung cancer*. Expert Review of Anticancer Therapy, vol. 4, no. 4, pages 561–567, aug 2004.
- [Pansart 97] JP Pansart. *Avalanche photodiodes for particle detection*. Nuclear Instruments and Methods in Physics Research Section A: Accelerators, Spectrometers, Detectors and Associated Equipment, vol. 387, no. 1-2, pages 186–193, 1997.
- [Peng 10] Hao Peng & Craig S Levin. *Recent developments in PET instrumentation*. Current pharmaceutical biotechnology, vol. 11, no. 6, pages 555–571, 2010.
- [Pepin 11a] Audrey Pepin, Simon Stute, Sama Jan & Claude Comtat. *Normalization of Monte Carlo PET data using GATE*. pages 4196–4200, 10 2011.
- [Pépin 11b] Audrey Pépin, Simon Stute, Sébastien Jan & Claude Comtat. *Normalization of Monte Carlo PET data using GATE*. In 2011 IEEE Nuclear Science Symposium Conference Record, pages 4196–4200. IEEE, 2011.
- [Phelps 04] Michael E Phelps. Pet: molecular imaging and its biological applications. Springer Science & Business Media, 2004.
- [Phelps 06] Michael E. Phelps, editeur. PET. Springer New York, 2006.
- [Popov 03] V. Popov, S. Majewski & A.G. Weisenberger. *Readout electronics for multianode photomultiplier tubes with pad matrix anode layout*. In 2003 IEEE Nuclear Science Symposium. Conference Record (IEEE Cat. No.03CH37515). IEEE, 2003.
- [Prasad 10] Rameshwar Prasad, Osman Ratib & Habib Zaidi. *Performance evaluation of the FLEX triumph X-PET scanner using the national electrical manufacturers association NU-4 standards*. Journal of Nuclear Medicine, vol. 51, no. 10, pages 1608–1615, 2010.
- [Qi 05] Jinyi Qi & Ronald H Huesman. *Effect of errors in the system matrix on maximum a posteriori image reconstruction*. Physics in Medicine & Biology, vol. 50, no. 14, page 3297, 2005.
- [Rafecas 03] Magdalena Rafecas, Brygida Mosler, Melanie Dietz, M Pogl, David P McElroy & Sibylle I Ziegler. *Use of a Monte-Carlo based probability matrix for 3D iterative reconstruction of MADPET-II data*. In 2003 IEEE Nuclear Science Symposium. Conference Record (IEEE Cat. No. 03CH37515), volume 3, pages 1775–1779. IEEE, 2003.
- [Rafecas 04] Magdalena Rafecas, Guido Boning, Bernd J Pichler, Eckhart Lorenz, Markus Schwaiger & Sibylle I Ziegler. *Effect of noise in the probability matrix used for statistical reconstruction of PET data*. IEEE Transactions on Nuclear Science, vol. 51, no. 1, pages 149–156, 2004.



- [Rahmim 13] Arman Rahmim, Jinyi Qi & Vesna Sossi. *Resolution modeling in PET imaging: theory, practice, benefits, and pitfalls*. Medical physics, vol. 40, no. 6Part1, 2013.
- [Rajeswaran 92] S Rajeswaran, Dale Lindsay Bailey, SP Hume, David W Townsend, A Geissbuhler, J Young & T Jones. *2D and 3D imaging of small animals and the human radial artery with a high resolution detector for PET*. IEEE Transactions on medical imaging, vol. 11, no. 3, pages 386–391, 1992.
- [Ramirez 05] R.A. Ramirez, Wai-Hoi Wong, Soonseok Kim, H. Baghaei, Hongdi Li, Yu Wang, Yuxuan Zhang, Shitao Liu & Jiguo Liu. *A Comparison of BGO, GSO, MLS, LGSO, LYSO and LSO Scintillation Materials for High-Spatial-Resolution Animal PET Detectors*. In IEEE Nuclear Science Symposium Conference Record, 2005. IEEE, 2005.
- [Ratib 14] Osman Ratib & René Nkoulou. *Potential applications of PET/MR imaging in cardiology*. Journal of Nuclear Medicine, pages jnumed–113, 2014.
- [Renker 09] D Renker & E Lorenz. *Advances in solid state photon detectors*. Journal of Instrumentation, vol. 4, no. 04, page P04004, 2009.
- [Riemann 08] B Riemann, KP Schäfers, O Schober & M Schäfers. *Small animal PET in pre-clinical studies: opportunities and challenges*. The Quarterly Journal of Nuclear Medicine and Molecular Imaging, vol. 52, no. 3, page 215, 2008.
- [Rohren 04] Eric M Rohren, Timothy G Turkington & R Edward Coleman. *Clinical applications of PET in oncology*. Radiology, vol. 231, no. 2, pages 305–332, 2004.
- [Rudd 10] James H.F. Rudd, Jagat Narula, H. William Strauss, Renu Virmani, Josef Machac, Mike Klimas, Nobuhiro Tahara, Valentin Fuster, Elizabeth A. Warburton, Zahi A. Fayad & Ahmed A. Tawakol. *Imaging Atherosclerotic Plaque Inflammation by Fluorodeoxyglucose With Positron Emission Tomography*. Journal of the American College of Cardiology, vol. 55, no. 23, pages 2527–2535, June 2010.
- [Rudin 03] Markus Rudin & Ralph Weissleder. *Molecular imaging in drug discovery and development*. Nature reviews Drug discovery, vol. 2, no. 2, page 123, 2003.
- [Sadygov 14] Z Sadygov, Kh Abdullaev, G Akhmedov, F Akhmedov, S Khorev, R Mukhtarov, A Sadigov, A Sidelev, A Titov, F Zerrouket *al*. *Model of single-electron performance of micropixel avalanche photodiodes*. arXiv preprint arXiv:1410.2619, 2014.
- [Salvador 09a] Samuel Salvador. *Conception et réalisation d’un module de détection d’un tomographe à émission de positrons dédié à l’imagerie du petit animal*. PhD thesis, Strasbourg, 2009.
- [Salvador 09b] Samuel Salvador, Daniel Huss & David Brasse. *Design of a High Performances Small Animal PET System With Axial Oriented Crystals and DOI Capability*. IEEE Transactions on Nuclear Science, vol. 56, no. 1, pages 17–23, February 2009.

- [Salvador 10] Samuel Salvador, Jacques Wurtz & David Brasse. *Optimizing PET DOI Resolution With Crystal Coating and Length*. IEEE Transactions on Nuclear Science, vol. 57, no. 5, pages 2468–2474, October 2010.
- [Sarrhini 12] Otman Sarrhini & M’hamed Bentourkia. *A comparison of a Monte Carlo-based detection probability matrix with analytical probability matrix for small animal PET scanners*. Computerized Medical Imaging and Graphics, vol. 36, no. 4, pages 314–324, 2012.
- [Sato 15] K Sato, M Shidahara, H Watabe, S Watanuki, Y Ishikawa, Y Arakawa, YH Nai, S Furumoto, M Tashiro, T Shojiet *al.* *Performance evaluation of the small-animal PET scanner ClairvivoPET using NEMA NU 4-2008 standards*. Physics in Medicine & Biology, vol. 61, no. 2, page 696, 2015.
- [Schäfers 05] Klaus P Schäfers, Andrew J Reader, Michael Kriens, Christof Knoess, Otmar Schober & Michael Schäfers. *Performance evaluation of the 32-module quadHI-DAC small-animal PET scanner*. Journal of Nuclear Medicine, vol. 46, no. 6, pages 996–1004, 2005.
- [Schmall 16] Jeffrey P Schmall, Joel S Karp, Matt Werner & Suleman Surti. *Parallax error in long-axial field-of-view PET scanners—a simulation study*. Physics in Medicine & Biology, vol. 61, no. 14, page 5443, 2016.
- [Schmand 98] M. Schmand, L. Eriksson, M.E. Casey, M.S. Andreaco, C. Melcher, K. Wienhard, G. Flugge & R. Nutt. *Performance results of a new DOI detector block for a high resolution PET-LSO research tomograph HRRT*. IEEE Transactions on Nuclear Science, vol. 45, no. 6, pages 3000–3006, 1998.
- [Schmid 03] RA Schmid, H Hautmann, B Poellinger, W Kellner, A Moisseev, K Brinkbaeumer, M Weiss, K Hahn & S Dresel. *Staging of recurrent and advanced lung cancer with 18F-FDG PET in a coincidence technique (hybrid PET)*. Nuclear medicine communications, vol. 24, no. 1, pages 37–45, 2003.
- [Schmidtlein 06] C Ross Schmidtlein, Assen S Kirov, Sadek A Nehmeh, Yusuf E Erdi, John L Humm, Howard I Amols, Luc M Bidaut, Alex Ganin, Charles W Stearns, David L McDaniel *et al.* *Validation of GATE Monte Carlo simulations of the GE Advance/Discovery LS PET scanners*. Medical physics, vol. 33, no. 1, pages 198–208, 2006.
- [Schnöckel 10] Uta Schnöckel, Sven Hermann, Lars Stegger, Marilyn Law, Michael Kuhlmann, Otmar Schober, Klaus Schäfers & Michael Schäfers. *Small-animal PET: a promising, non-invasive tool in pre-clinical research*. European Journal of Pharmaceutics and Biopharmaceutics, vol. 74, no. 1, pages 50–54, 2010.
- [Selfridge 18] Aaron R Selfridge, Simon R Cherry & Martin S Judenhofer. *Optimization of a depth of interaction encoding PET block detector for a PET/MRI insert*. Physics in Medicine & Biology, vol. 63, no. 23, page 235031, dec 2018.
- [Selivanov 00] V.V. Selivanov, Y Picard, J Cadorette, S Rodrigue & Roger Lecomte. *Detector response models for statistical iterative image reconstruction in high resolution PET*. Nuclear Science, IEEE Transactions on, vol. 47, pages 1168 – 1175, 07 2000.

- [Shao 08] Yiping Shao, Rutao Yao & Tianyu Ma. *A novel method to calibrate DOI function of a PET detector with a dual-ended-scintillator readout*. Medical Physics, vol. 35, no. 12, pages 5829–5840, November 2008.
- [Shepp 82] L. A. Shepp & Y. Vardi. *Maximum Likelihood Reconstruction for Emission Tomography*. IEEE Transactions on Medical Imaging, vol. 1, no. 2, pages 113–122, October 1982.
- [Siddon 85] Robert L Siddon. *Fast calculation of the exact radiological path for a three-dimensional CT array*. Medical physics, vol. 12, no. 2, pages 252–255, 1985.
- [Siegel 95] Stefan Siegel, Simon R Cherry, Anthony R Ricci, Yiping Shao & Michael E Phelps. *Development of continuous detectors for a high resolution animal PET system*. IEEE transactions on nuclear science, vol. 42, no. 4, pages 1069–1074, 1995.
- [Spinks 14] TJ Spinks, D Karia, MO Leach & G Flux. *Quantitative PET and SPECT performance characteristics of the Albira Trimodal pre-clinical tomograph*. Physics in Medicine & Biology, vol. 59, no. 3, page 715, 2014.
- [Staelens 09] Steven Staelens & Irene Buvat. Monte carlo simulations in nuclear medicine imaging, pages 177–209. 12 2009.
- [Strul 03] D Strul, RB Slates, M Dahlbom, Simon R Cherry & Paul K Marsden. *An improved analytical detector response function model for multilayer small-diameter PET scanners*. Physics in medicine & biology, vol. 48, no. 8, page 979, 2003.
- [Szanda 11] Istvan Szanda, Jane Mackewn, Gergely Patay, Peter Major, Kavitha Sunassee, Gregory E Mullen, Gabor Nemeth, York Haemisch, Philip J Blower & Paul K Marsden. *National Electrical Manufacturers Association NU-4 performance evaluation of the PET component of the NanoPET/CT preclinical PET/CT scanner*. Journal of nuclear medicine, vol. 52, no. 11, pages 1741–1747, 2011.
- [Tabacchini 17] Valerio Tabacchini, Suleman Surti, Giacomo Borghi, Joel S Karp & Dennis R Schaart. *Improved image quality using monolithic scintillator detectors with dual-sided readout in a whole-body TOF-PET ring: a simulation study*. Physics in Medicine & Biology, vol. 62, no. 5, page 2018, 2017.
- [Tai 01a] Y C Tai, A Chatziioannou, S Siegel, J Young, D Newport, R N Goble, R E Nutt & S R Cherry. *Performance evaluation of the microPET P4: a PET system dedicated to animal imaging*. Physics in Medicine and Biology, vol. 46, no. 7, pages 1845–1862, June 2001.
- [Tai 01b] YC Tai, A Chatziioannou, S Siegel, J Young, D Newport, RN Goble, RE Nutt & Simon R Cherry. *Performance evaluation of the microPET P4: a PET system dedicated to animal imaging*. Physics in Medicine & Biology, vol. 46, no. 7, page 1845, 2001.
- [Tarantola 03] Gabriele Tarantola, Felicia Zito & Paolo Gerundini. *PET instrumentation and reconstruction algorithms in whole-body applications*. Journal of Nuclear Medicine, vol. 44, no. 5, pages 756–769, 2003.

- [Theodorakis 13] Lampros Theodorakis, George Loudos, Vasilios Prassopoulos, Constantin Kappas, Ioannis Tsougos & Panagiotis Georgoulas. *A review of PET normalization: striving for count rate uniformity*. Nuclear medicine communications, vol. 34, no. 11, pages 1033–1045, 2013.
- [Thompson 95] CJ Thompson, K Murthy, Y Picard, IN Weinberg & R Mako. *Positron emission mammography (PEM): a promising technique for detecting breast cancer*. IEEE transactions on nuclear science, vol. 42, no. 4, pages 1012–1017, 1995.
- [Tohme 09] Michel S Tohme & Jinyi Qi. *Iterative image reconstruction for positron emission tomography based on a detector response function estimated from point source measurements*. Physics in medicine & biology, vol. 54, no. 12, page 3709, 2009.
- [Tornai 99] Martin P Tornai, Ronald J Jaszczak, Timothy G Turkington & R Edward Coleman. *Small-animal PET: advent of a new era of PET research*, 1999.
- [Townsend 04] DW Townsend *et al.* *Physical principles and technology of clinical PET imaging*. Annals-Academy of Medicine Singapore, vol. 33, no. 2, pages 133–145, 2004.
- [Turbell 01] Henrik Turbell. *Cone-beam reconstruction using filtered backprojection*. PhD thesis, Linköping University Electronic Press, 2001.
- [Turner 85] JE Turner, HA Wright & RN Hamm. *A Monte Carlo primer for health physicists*. Health physics, vol. 48, no. 6, pages 717–733, 1985.
- [van Dam 11a] Herman T van Dam, Stefan Seifert, Ruud Vinke, Peter Dendooven, Herbert Lohner, Freek J Beekman & Dennis R Schaart. *Improved nearest neighbor methods for gamma photon interaction position determination in monolithic scintillator PET detectors*. IEEE Transactions on Nuclear Science, vol. 58, no. 5, pages 2139–2147, 2011.
- [Van Dam 11b] Herman T Van Dam, Stefan Seifert, Ruud Vinke, Peter Dendooven, Herbert Löhner, Freek J Beekman & Dennis R Schaart. *A practical method for depth of interaction determination in monolithic scintillator PET detectors*. Physics in Medicine & Biology, vol. 56, no. 13, page 4135, 2011.
- [Vandamme 14] Thierry F Vandamme. *Use of rodents as models of human diseases*. Journal of pharmacy & bioallied sciences, vol. 6, no. 1, page 2, 2014.
- [Veklerov 88] Eugene Veklerov, Jorge Llacer & Edward J. Hoffman. *MLE reconstruction of a brain phantom using a Monte Carlo transition matrix and a statistical stopping rule*. Nuclear Science, IEEE Transactions on, vol. 35, pages 603 – 607, 03 1988.
- [Wang 06] Yuchuan Wang, Jurgen Seidel, Benjamin MW Tsui, Juan J Vaquero & Martin G Pomper. *Performance evaluation of the GE healthcare eXplore VISTA dual-ring small-animal PET scanner*. Journal of Nuclear Medicine, vol. 47, no. 11, pages 1891–1900, 2006.
- [Wang 14] Luyao Wang, Jun Zhu, Xiao Liang, Ming Niu, Xiaoke Wu, Chien-Min Kao, Heejong Kim & Qingguo Xie. *Performance evaluation of the Trans-PET® BioCaliburn® LH system: a large FOV small-animal PET system*. Physics in Medicine & Biology, vol. 60, no. 1, page 137, 2014.

- [Watanabe 92] M Watanabe, H Uchida, H Okada, K Shimizu, N Satoh, E Yoshikawa, T Ohmura, T Yamashita & E Tanaka. *A high resolution PET for animal studies*. IEEE transactions on medical imaging, vol. 11, no. 4, pages 577–580, 1992.
- [Watanabe 97] M Watanabe, H Okada, K Shimizu, T Omura, E Yoshikawa, T Kosugi, S Mori & T Yamashita. *A high resolution animal PET scanner using compact PS-PMT detectors*. IEEE Transactions on Nuclear Science, vol. 44, no. 3, pages 1277–1282, 1997.
- [Weber 04] Simone Weber & Andreas Bauer. *Small animal PET: aspects of performance assessment*. European Journal of Nuclear Medicine and Molecular Imaging, vol. 31, no. 11, pages 1545–1555, October 2004.
- [Wernick 04] Miles N. Wernick & John N. Aarsvold. *Emission tomography: The fundamentals of pet and spect*. Academic Press, 2004.
- [Wong 12] Wai-Hoi Wong, Hongdi Li, Hossain Baghaei, Yuxuan Zhang, Rocio A Ramirez, Shitao Liu, Chao Wang & Shaohui An. *Engineering and performance (NEMA and animal) of a lower-cost higher-resolution animal PET/CT scanner using photomultiplier-quadrant-sharing detectors*. Journal of Nuclear Medicine, vol. 53, no. 11, pages 1786–1793, 2012.
- [Yang 08] Yongfeng Yang, Jinyi Qi, Yibao Wu, Sara St James, Richard Farrell, Purushottam A Dokhale, Kanai S Shah & Simon R Cherry. *Depth of interaction calibration for PET detectors with dual-ended readout by PSAPDs*. Physics in Medicine and Biology, vol. 54, no. 2, pages 433–445, December 2008.
- [Yang 10] Ching-Ching Yang, Jianhua Yu, Jason JS Lee & Benjamin MW Tsui. *Monte Carlo simulation of a GE eXplore VISTA system for quantitative small animal PET imaging*. Nuclear medicine communications, vol. 31, no. 1, pages 32–38, 2010.
- [Yao 12] Rutao Yao, Roger Lecomte & Elpida S Crawford. *Small-animal PET: what is it, and why do we need it?* Journal of nuclear medicine technology, vol. 40, no. 3, pages 157–165, 2012.
- [Zaidi 99] Habib Zaidi. *Relevance of accurate Monte Carlo modeling in nuclear medical imaging*. Medical physics, vol. 26, no. 4, pages 574–608, 1999.
- [Zaidi 02] H Zaidi. *Monte Carlo techniques in diagnostic and therapeutic nuclear medicine*. Rapport technique, 2002.
- [Zeng 10] Gengsheng Lawrence Zeng. *Medical image reconstruction: a conceptual tutorial*. Springer, 2010.
- [Ziemons 05] Karl Ziemons, E Auffray, R Barbier, G Brandenburg, P Bruyndonckx, Y Choi, D Christ, N Costes, Y Declais, O Devroede *et al.* *The ClearPET<sup>TM</sup> project: development of a 2nd generation high-performance small animal PET scanner*. Nuclear Instruments and Methods in Physics Research Section A: Accelerators, Spectrometers, Detectors and Associated Equipment, vol. 537, no. 1-2, pages 307–311, 2005.

## Resumé en Français

La tomographie par émission de positrons (TEP) est l'une des techniques d'imagerie nucléaire utilisée dans les domaines de l'oncologie [Rohren 04, Hoh 93, Conti 91], de la cardiologie [Ratib 14, Iskandrian 16] et de la neurologie [Kitson 09, Cai 19] en tant que modalité d'imagerie fonctionnelle. Cette technique nécessite des biomolécules marquées uniquement avec des radionucléides émetteurs de positrons (tel que F-18) et un dispositif d'imagerie. Bénéficiant des propriétés appropriées du F-18 [Le Bars 06, Jacobson 14], 2-[18 F] fluoro-2-deoxy-D-glucose (FDG) (un analogue du glucose), est la molécule biologiquement active la plus couramment utilisée pour la détection précoce de tumeurs [Oyen 04, Schmid 03, Hicks 01]. Au cours des trois dernières décennies, les progrès de la modalité TEP et le développement de modèles animaux de maladies humaines ont conduit au développement de la technologie TEP dédiée aux animaux. La motivation était d'étudier les modèles animaux, de manière non destructive, pour pouvoir comprendre le comportement d'une maladie et la réponse au traitement, dans son état biologique naturel. Initialement, tous les scanners TEP dédiés aux animaux ont été développés pour les primates non humains à des fins de recherche en neurosciences et en cardiologie. Pour effectuer l'étude sur les primates non humains, la taille de la région observée était assez similaire à celle étudiée pour le patient. Dans ce contexte, une amélioration de la résolution spatiale n'était pas cruciale. Plus tard, vers le milieu des années 1980, les souris sont devenues le choix approprié pour la modélisation de maladies humaines, en raison de leur cycle de reproduction plus rapide, de leur durée de vie plus courte, de leur similarité avec les gènes humains, de l'évolution de la technologie de la biologie moléculaire, etc. Le rat est également devenu un modèle animal favorable pour la recherche en neurologie, en raison de la taille plus importante du cerveau par rapport à la souris [Kuntner 14, Cherry 01, Vandamme 14]. Cependant, considérer les souris et les rats comme des sujets d'imagerie a conduit à la nécessité de concevoir des scanners plus performants [Chatziioannou 02]. Cela nous permet de visualiser clairement et de quantifier avec précision l'absorption du traceur dans des organes individuels et dans les sous-structures de petits animaux (rats et souris).

Le premier défi fondamental de la technologie TEP pour petits animaux vient de la différence de taille entre les humains et les petits animaux comme les rats et les souris. Pour pouvoir effectuer les mêmes recherches sur l'homme et la souris, les systèmes d'imagerie humaine et petit animal devraient présenter le même rapport entre l'objet observé et la résolution spatiale du système. Ainsi, les scanners pour petits animaux nécessitent une amélioration de la résolution spatiale. Un autre défi important provient du fait que le niveau de rapport signal sur bruit dépend du nombre d'événements détectés par élément de résolution volumétrique. En raison de l'amélioration de la résolution spatiale, la taille



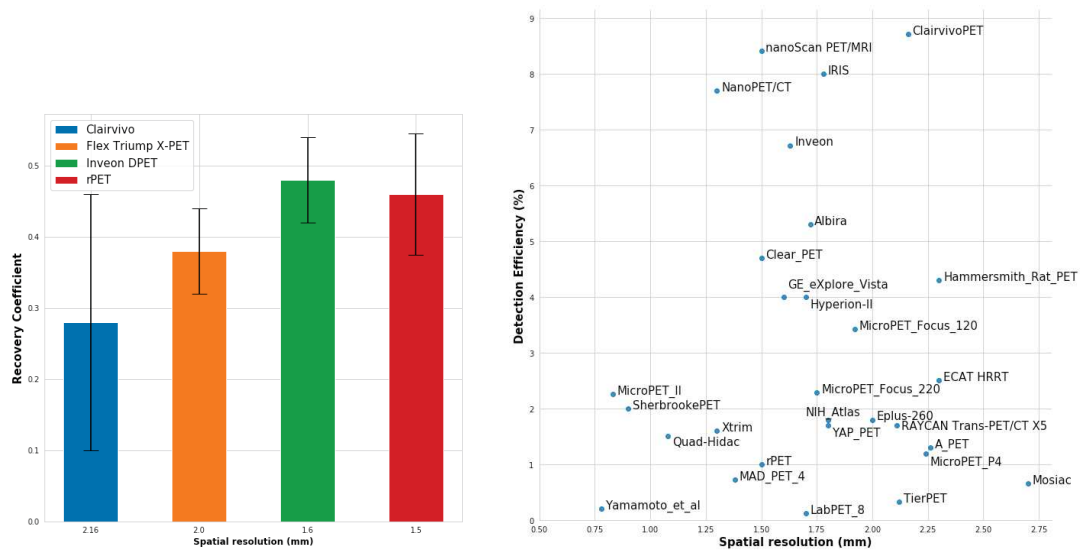
du voxel diminue de manière significative, réduisant ainsi le nombre de signaux d'un voxel. Plus le nombre détecté est élevé, plus le rapport signal sur bruit (SNR) est élevé; ainsi, l'amélioration de l'efficacité de détection joue un rôle important. De plus, afin de maintenir l'état biologique naturel des petits animaux, on leur injecte une radioactivité à une échelle moindre que celle de l'homme [Oehr 03]. Cependant, une radioactivité injectée plus faible entraîne moins de statistiques d'événements et a un impact direct sur le SNR.

Au milieu des années 90, plusieurs groupes de recherche ont commencé à mettre au point des scanners TEP pour petits animaux. Cela a conduit au développement de plusieurs prototypes de recherche et systèmes commerciaux. Afin d'identifier les organes critiques ou les zones cibles chez les petits animaux, l'un des principaux objectifs des groupes de recherche est de développer des scanners à haute résolution spatiale. En 2008, NEMA a publié une directive visant à comparer les performances de différents scanners TEP précliniques en suivant un ensemble commun de normes. Les paramètres de performance rapportés sont la résolution spatiale, l'efficacité de détection, la mesure du taux de comptage (c'est-à-dire la fraction de diffusion, le taux de comptage équivalent au bruit), les coefficients de recouvrement et l'uniformité dans l'image reconstruite. Le coefficient de recouvrement, c'est-à-dire le rapport entre l'activité observée et l'activité réelle dans une image reconstruite, est décrit pour caractériser la résolution spatiale du scanner.

La figure B.1(a) présente une comparaison du coefficient de recouvrement de certains scanners TEP précliniques commerciaux conformes aux normes NEMA. Les scanners sont disposés de gauche à droite avec une résolution spatiale améliorée. On s'attend à ce que, à mesure que la résolution spatiale s'améliore, la valeur du coefficient de recouvrement augmente. On peut observer qu'en améliorant la résolution spatiale de 2,16 mm à 1,5 mm, les valeurs de RC s'améliorent comme prévu. Cependant, l'erreur associée à l'estimation des valeurs de RC est relativement élevée, ce qui rend difficile la quantification correcte de l'amélioration des valeurs de RC. L'erreur est due à plusieurs facteurs tels que la géométrie du scanner, le processus de reconstruction d'image, l'efficacité de détection, les différents processus de correction des phénomènes physique tels que l'atténuation et la diffusion, etc. Si le degré d'amélioration de la valeur de RC n'est pas supérieur à l'erreur dans son estimation, nous ne pouvons pas quantifier correctement l'amélioration de RC due à l'amélioration de la résolution spatiale. Il convient donc de noter que l'amélioration de la résolution spatiale à elle seule peut compromettre d'autres paramètres tels que l'efficacité de détection et n'entraîne pas une amélioration de la qualité de l'image.

La figure B.1(b) présente un graphique montrant divers scanners de recherche commerciaux et prototypes en fonction de leur efficacité de détection et de leur résolution spatiale. On peut observer qu'à mesure que la résolution spatiale s'améliore au niveau inférieur au millimètre, l'efficacité de la détection est compromise. Des scanners tels que Quad-Hidac, scanner de prototypes de Yamamoto et al ont même atteint une résolution spatiale inférieure à et proche de 1 mm avec une efficacité de détection proche de 1%.

La motivation de ce travail de thèse découle des deux observations ci-dessus (figure B.1(a) et figure B.1(b)). Dans cette thèse, l'un des principaux objectifs est d'étudier l'impact de la géométrie du scanner et ses paramètres de performance, tels que la résolution spatiale et l'efficacité de détection,



(a) Comparaison de certains scanners commerciaux (Clairvivo de SHIMADZU, Flex triumph X-PET de Gamma Medica-Ideas, Inveon DPET de Siemens Medical Solutions, rPET-1 de Sedecal, SA, ayant une résolution spatiale de 2,16 mm, 2,0 mm, 1,6 mm, 1,5 mm respectivement au CFOV) en fonction du coefficient de recouvrement (insert chauds de 2 mm) estimé selon les normes NEMA NU-4 2008

(b) Comparaison des performances de plusieurs systèmes commerciaux et prototypes de recherche.

Figure B.1 – Représentation des performances de systèmes TEP en termes de résolution spatiale, efficacité de détection et coefficients de recouvrement.

sur la qualité globale de l'image reconstruite. Afin d'étudier l'impact de la géométrie du scanner, nous simulons quatre scanners développés sur la base de différentes approches géométriques. Pour évaluer les performances des scanners, nous avons utilisé différents outils tels que GATE pour effectuer des simulations Monte-Carlo, une approche d'analyse des données développée dans notre laboratoire, les normes NEMA NU-4 2008 établies pour évaluer les performances des scanner TEP précliniques, et l'algorithme de reconstruction d'image. L'algorithme MLEM est utilisé dans le cadre de mon travail de thèse pour reconstruire toutes les images. Afin de reconstruire les données acquises à l'aide de l'algorithme MLEM, nous générons la matrice système (SM) à l'aide de simulations MC pour tous les scanners. Nous avons également utilisé CASToR, un nouveau logiciel de reconstruction d'images open source, pour reconstruire les images acquises. Castor utilise des projecteurs analytiques pour calculer les éléments SM à la volée. Un autre objectif de la thèse est de comparer le processus de reconstruction d'image et la qualité d'image reconstruite, pour les deux approches lorsque les éléments SM sont calculés à l'aide de simulations MC et de projecteurs analytiques utilisant CASToR.

Le manuscrit de thèse est composé de six chapitres. L'introduction aux chapitres est donnée ci-dessous:

1. **Chapter 1: Basics of PET imaging:** Il fournit une introduction aux concepts de base de l'imagerie TEP, tels que les processus physiques (dégradation du positon, annihilation, etc.) im-



pliqués, l'émission et la détection de photons gamma, les détecteurs gamma, l'approche d'acquisition de données et le processus de reconstruction d'image. Les avantages (résolution spatiale et efficacité de la détection) sont également abordés pour caractériser les performances du scanner TEP.

2. **Chapter 2: Small animal imaging PET scanners:** Il fournit une brève introduction à l'imagerie des petits animaux. Certains des principaux défis dans le domaine de l'imagerie TEP préclinique sont également abordés. Nous fournissons également des exemples de scanners TEP précliniques de prototype et disponibles dans le commerce.
3. **Chapter 3: Scanner geometries:** Dans ce chapitre, nous discutons de quatre géométries de scanner différentes étudiées dans cette thèse. Tous les détails tels que le champ de vision axial, le champ de vision transaxial, le matériau cristallin, la taille du cristal, les photodétecteurs, etc. sont discutés.
4. **Chapter 4: Simulation and Image reconstruction approaches:** Ce chapitre présente la méthodologie générale utilisée pour étudier l'impact des propriétés du scanner sur la qualité de l'image. Nous décrivons principalement la simulation Monte Carlo, la plate-forme de reconstruction, notre approche d'analyse des données et les normes NEMA NU-4 2008. Nous soulignons également la nécessité de corrections de normalisation et de différentes techniques pour effectuer le processus de normalisation.
5. **Chapter 5: Performance measurement of the scanners:** Ce chapitre présente le résultat de toutes les simulations MC effectuées dans la thèse. Les valeurs estimées de résolution spatiale et d'efficacité de détection pour les quatre scanners et pour le scanner IRIS à la pointe de la technologie sont rapportées. Nous rapportons également l'impact des performances des scanners sur la qualité d'image globale à l'aide du fantôme de qualité d'image (IQP). Une comparaison est également étudiée pour les images reconstruites à l'aide de l'algorithme MLEM, où les éléments SM sont calculés selon deux approches différentes.
6. **Chapter 6: Normalization:** Dans ce chapitre, nous soulignons la procédure de normalisation et le rôle de cette correction sur la qualité globale de l'image. Nous discutons des différentes approches de normalisation possibles pour gérer la variation de l'efficacité de la détection LOR dans le champ de vision. Nous rapportons également l'impact des facteurs de correction de normalisation sur la qualité de l'image reconstruite.

## Matériaux et méthodes

Pour atteindre cet objectif, quatre scanners basés sur des conceptions différentes (Scanner A, Scanner B, Scanner C et Scanner D) sont examinés. Le choix de ces différentes approches géométrique sélectionnées pour ce travail de thèse est d'ajouter progressivement une dimension supplémentaire dans la position estimée de l'interaction du photon gamma dans le détecteur. La première conception, Scanner A, consiste en une matrice de cristaux scintillants pixelisée et agencée radialement qui permet la détection 2D de l'interaction gamma (figure B.2a). La deuxième conception, Scanner B, consiste

en deux couches de matrices pixélisées disposées radialement, ce qui nous permet une détection 2D ainsi qu'un échantillonnage binaire dans la dimension radiale (figure B.2b). La troisième conception, Scanner C, consiste en une matrice de cristaux orientée axialement, qui permet une détection 2D dans la direction transversale ainsi qu'un échantillonnage continu dans la dimension axiale (figure B.2c). Enfin, la dernière conception, Scanner D, utilise un cristal monolithique, permettant l'estimation 3D complète de la position de détection (figure B.2D). Ces quatre géométries de scanner discutées sont évaluées pour estimer leurs performances. Les performances mesurées sont également comparées aux performances du scanner de pointe, IRIS TEP, comme indiqué à la figure B.3. Il s'agit d'un scanner TEP préclinique disponible dans le commerce (utilisant une matrice à cristaux pixellisés, permettant ainsi la détection 2D des interactions gamma). installé dans notre établissement. Le tableau 1 présente le résumé des spécifications de tous les scanners étudiés dans la thèse.

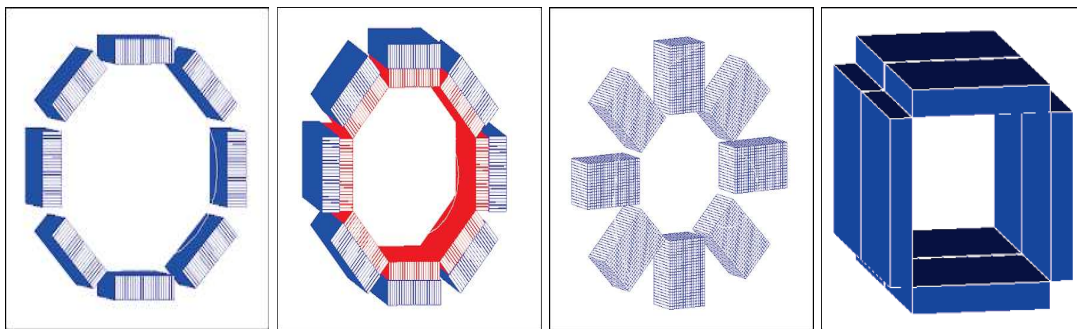


Figure B.2 – Illustration de la disposition cristalline des quatre géométries du scanner (Scanner A, Scanner B, Scanner C et Scanner D) étudiées dans cette thèse, générée à l'aide du logiciel de simulation GATE.

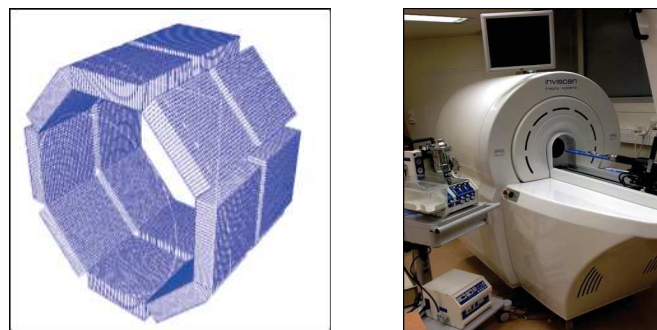


Figure B.3 – Gauche: Disposition des cristaux dans le scanner IRIS générée via la plate-forme de simulation GATE MC. Les cristaux sont radialement allongés et le cristal de 27 x 26 en fait un module. L'image présente deux anneaux composés chacun de 8 modules. Droite: image du scanner IRIS installé dans nos locaux

Les paramètres de performance de tous les scanners sont estimés à l'aide de simulations MC. L'idée de base des simulations MC est de générer un modèle aussi proche que possible du modèle réel d'intérêt. Le modèle est créé pour étudier le comportement d'un processus en fonction

	Scanner A	Scanner B	Scanner C	Scanner D	IRIS
<b>Module</b>					
<b>Crystal material</b>	LYSO:Ce	LYSO:Ce	LYSO:Ce	LYSO:Ce	LYSO:Ce
<b>Crystal pixel size</b> $mm^3$	$0.98 \times 0.98 \times 8$	$0.98 \times 0.98 \times 6$ $+0.98 \times 0.98 \times 8$	$1.45 \times 1.45 \times 20$	$50 \times 50 \times 8$	$1.6 \times 1.6 \times 12$
<b>Crystal pixel pitch</b> $mm^2$	$1.065 \times 1.065$	$1.065 \times 1.065$	$1.5 \times 1.5$	$50 \times 50$	$1.68 \times 1.71$
<b>No. of crystals/module</b> $mm^2$	$23 \times 48$	$22 \times 47$ $+23 \times 48$	$24 \times 16$	$1 \times 1$	$27 \times 26$
<b>Scanner</b>					
<b>No. of modules</b>	$16(8 \times 2)$	$16(8 \times 2)$	$40(8 \times 5)$	$8(4 \times 2)$	$16(8 \times 2)$
<b>No. of crystals</b>	17,664	34,208	15,360	8	11,232
<b>Diameter (mm)</b>	68.60	56.60	66.80	50.50	110.80
<b>Length (mm)</b>	102.24	102.24	110.40	102.00	100.00

Table B.1 – Résumé des spécifications de tous les scanners discutés dans la thèse

de probabilités d'occurrence connues à l'aide d'un échantillonnage aléatoire de fonctions de densité de probabilité (PDF). Afin de réaliser des simulations MC, le logiciel GATE est utilisé dans le cadre de cette thèse. GATE est un logiciel de simulation de code source ouvert largement utilisé basé sur les bibliothèques Geant4. Il est conçu sur la base de l'idée que l'utilisateur ne peut pas être issu du fond de codage, il peut donc être utilisé sans connaissances en programmation. Bénéficiant des bibliothèques de physique Geant4, GATE peut modéliser avec précision les processus physiques sous-jacents des scanners de tomographie à émission complexes. Les simulations GATE ont été validées par plusieurs groupes de recherche à travers des études approfondies en les comparant avec les résultats expérimentaux pour un certain nombre de systèmes TEP commerciaux [Jan 05c, Lamare 04, Lamare 06, Schmidtlein 06] ainsi que des systèmes TEP précliniques pour petits animaux [Jan 05b, Merheb 06, Baghaei 07, Yang 10, Lu 16]. Pour effectuer des simulations dans GATE, nous avons fourni la description des différents composants nécessaires à la modélisation précise d'un scanner TEP, à partir de la configuration de la géométrie, de la source radioactive utilisée, de la géométrie de l'objet, des processus physiques associés, du format de sortie et de la formulation du traitement. chaîne (numériseur) pour les événements détectés.

Une fois les géométries du scanner simulées, les événements acquis sont analysés à l'aide d'un système de détection de lecture développé par notre laboratoire. Ce système de lecture analyse les événements selon l'acquisition réelle du scanner. Le système de détection de lecture développé est décrit ci-dessous:

1. Les fichiers de sortie GATE ("hits" et "singles") sont lus en parallèle. Pour chaque événement contenu dans le fichier .singles, les "hits" correspondants sont recherchés et si l'interaction conduit à une ionisation, ce qui conduira à sa détection par le système (émission de photons optiques), alors l'interaction est considérée. De tels événements sont stockés dans un fichier binaire de sortie avec ses caractéristiques telles que la valeur d'énergie déposée, la position de l'interaction, le type d'interaction, etc.
2. Une fois que les événements sont stockés dans un fichier binaire, ils sont ensuite traités sur la

base de leur énergie déposée (la position de frappe minimum de l'énergie déposée est sélectionnée ou en suivant la logique de la colère dans le cas d'un scanner IRIS) afin de fournir les indices cristallins de la victime. des cristaux. A la fin de cette étape, les événements coïncidents sont stockés dans les fichiers de sortie en mode liste (LM).

3. La dernière étape inclut les caractéristiques du système, telles que la fenêtre d'énergie, la fenêtre de synchronisation, etc. Selon les valeurs obtenues, les événements sont rejetés ou acceptés.

Après analyse des événements, les images sont reconstruites à l'aide de l'algorithme itératif (MLEM). Pour les algorithmes de reconstruction d'image itérative, SM est un élément central et est utilisé dans les opérations de projection avant et arrière pour chaque itération du processus de reconstruction d'image. Ainsi, la qualité de l'image reconstruite dépend fortement de la précision du SM [Li 15, Rahmim 13, Rafecas 04]. Il existe différentes approches pour estimer les éléments SM, telles que l'estimation via des simulations MC, l'estimation des éléments SM via des projecteurs analytiques ou l'estimation expérimentale via une acquisition réelle par scanner. Dans cette thèse, nous avons utilisé deux approches pour obtenir du SM, à savoir, via des simulations de MC et en utilisant des projecteurs analytiques, comme indiqué ci-dessous:

1. **Estimation SM à l'aide de simulations MC:** Les éléments SM estimés via des simulations MC prennent en compte tous les phénomènes physiques et géométriques apparaissant dans le scanner et dans l'objet à balayer, tels que la diffusion intercristalline, la profondeur cristalline, l'atténuation et la diffusion dans l'objet, la plage de positrons, la non colinéarité, etc. En utilisant des simulations MC, nous avons simulé la géométrie du scanner dans GATE avec une source cylindrique uniforme (source de photons gamma 511 keV dos à dos émettant dos à dos) couvrant essentiellement le champ de vue complet du scanner. Une fois l'acquisition effectuée, le champ de vision est voxelisé pour déterminer la probabilité d'émission dans un voxel particulier. Chaque élément  $a_{ij}$  est déterminé en estimant le nombre d'événements de coïncidence provenant de chaque image voxel  $j$ , ainsi qu'en estimant le nombre d'événements détectés le long de la  $i^{th}$  LOR. Ainsi

$$a_{ij} = \frac{N_i^D}{N_j^E} \quad (\text{B.1})$$

où  $N_i^D$  correspond au nombre de photons détectés le long du  $i^{th}$  LOR et  $N_j^E$  correspond au nombre de photons émis par le voxel  $j$ .

2. **Estimation SM à l'aide de projecteurs analytiques:** L'approche analytique pour peupler un SM est basée sur l'utilisation de différents projecteurs géométriques estimant des éléments via un modèle intégral de ligne [Joseph 82] ou un modèle intégral de zone. Dans cette thèse, nous utilisons un logiciel de reconstruction d'image open source, CASToR (Customizable and Advanced Software for Tomographic Reconstruction), qui utilise différents projecteurs pour estimer les éléments SM immédiatement. Le projecteur piloté par la distance (l'un des projecteurs mis en œuvre dans CASToR) a été reconnu comme étant le projecteur le plus exact qui puisse

rendre compte avec précision de la largeur finie des détecteurs. Il a également été signalé que le projecteur contrôlé par la distance n'introduit pas les artefacts dans l'image reconstruite introduite par d'autres projecteurs [De Man 04]. Nous avons utilisé le projecteur piloté par la distance pour estimer les éléments SM à la volée pour toutes les géométries de scanner discutées.

Le logiciel CASToR est écrit en C++. Il est conçu pour utiliser directement les fichiers d'entrée et de sortie GATE. Le processus complet de reconstruction d'image est divisé en différentes parties, telles que l'identification de la géométrie du scanner, la conversion des données de sortie de GATE dans son format lisible, la génération du profil de sensibilité et enfin le processus de reconstruction.

Lors de la comparaison de différentes géométries de scanner, il est important de disposer d'une méthode standard pour évaluer les paramètres de performance du scanner. La National Electrical Manufacturers Association (NEMA) propose une méthodologie standard pour évaluer les performances des scanners TEP précliniques. L'objectif de la norme est d'établir une base de référence pour les performances du scanner mesurées dans des conditions d'imagerie identiques et d'être indépendantes de la géométrie du scanner. La norme NEMA NU-4 2008 stipule que la procédure d'évaluation des performances du scanner est applicable à toutes les géométries de scanner TEP précliniques, à savoir les scanners utilisant des cristaux discrets, des cristaux monolithiques, des scanners rotatifs, des scanners TOF, des scanners à une tranche et à plusieurs tranches. Ainsi, nous estimons les paramètres de performance de tous les scanners selon les normes NEMA NU-4 2008. Dans la section suivante, nous présentons et discutons les paramètres de performance estimés et la qualité d'image reconstruite.

## Résultats et discussion

De l'émission de positrons à la reconstruction d'image, de nombreux facteurs ont un impact significatif sur la résolution spatiale, l'efficacité de la détection et leur compromis. Par exemple, l'amélioration de la résolution spatiale a conduit au développement de scanners à petits cristaux, ce qui permet de réduire le nombre de comptages par cristal, ce qui a un impact sur le rapport signal sur bruit. Plusieurs groupes de recherche ont développé des scanners TEP dédiés aux petits animaux à partir de 1997 et certains de ces scanners sont disponibles dans le commerce. Cependant, comme discuté dans cette thèse, la plupart des scanners TEP dédiés aux petits animaux développent un compromis entre la résolution spatiale et l'efficacité de la détection. La question importante est de savoir comment décider quels scanners offrant une résolution spatiale améliorée ou une efficacité de détection supérieure permettront de quantifier la distribution des radiotraceurs chez les petits animaux. ou est-il possible d'améliorer les deux simultanément? Si oui, dans quelle mesure pourrait-on améliorer la quantification de la distribution des traceurs en améliorant simultanément les deux?

Afin d'examiner les questions mentionnées ci-dessus, nous avons simulé quatre conceptions de scanner différentes et reconstruit les événements simulés. La qualité d'image reconstruite est caractérisée en termes de coefficient de récupération et d'uniformité. Sur la base des questions susmentionnées, des méthodes d'investigation et des conceptions de scanner étudiées, voici les principales conclusions de cette thèse :

### 1. Optimisation simultanée de la résolution spatiale et de l'efficacité de la détection :

Nous avons étudié quatre géométries de scanner (A, B, C et D) basées sur différentes approches géométriques. L'approche géométrique choisie a pour principe d'ajouter progressivement une dimension supplémentaire dans la position d'interaction estimée du photon gamma. La première géométrie, Scanner A, consiste en une matrice cristalline pixelisée disposée radialement qui permet la détection 2D de l'interaction gamma. La deuxième géométrie du scanner, Scanner B, est conçue pour améliorer l'efficacité de la détection du Scanner A sans dégrader la résolution spatiale. Il se compose de deux couches de matrices cristallines pixelisées disposées radialement (même dimension cristalline que celle utilisée pour le scanner A). Deux couches radiales permettent la détection 2D ainsi que l'échantillonnage binaire dans la dimension radiale. La troisième conception, Scanner C, améliore encore le compromis entre la résolution spatiale et l'efficacité de la détection en incorporant un niveau élevé de codage DOI. Il consiste en une matrice cristalline orientée axialement, qui permet une détection 2D dans la direction transversale ainsi qu'un échantillonnage continu dans la dimension axiale. Jusqu'ici, l'optimisation de la résolution spatiale et de l'efficacité de la détection entraîne simultanément une augmentation des coûts, car les conceptions incluent davantage de matrices cristallines (ainsi que les photodétecteurs). Enfin, dernière solution, Scanner D est une solution simplifiée utilisant un cristal monolithique, permettant l'estimation complète en 3D de la position de détection.

En effectuant des simulations MC, en suivant la procédure standard décrite dans NEMA-NU 4, nous estimons la résolution spatiale et l'efficacité de détection des quatre scanners, comme indiqué dans le tableau B.2.

Scanners	Spatial Resolution (mm)	Detection efficiency (%)
A	0.92	5.50
B	0.87	13.87
C	0.88	23.42
D	0.85	9.55

Table B.2 – Les valeurs de résolution spatiale (mm) et d'efficacité de détection (%) estimées via des simulations MC pour une source ponctuelle placée au cFOV pour les quatre géométries de scanner

Selon leur conception, les quatre géométries de scanner fourniraient une résolution spatiale proche de 1 mm au cFOV. De plus, le scanner C, qui nous permet d'utiliser plusieurs couches de cristaux dans la direction radiale (offrant plus de profondeur pour que les photons entrants puissent interagir par rapport aux autres scanners), fournit l'efficacité de détection maximale au niveau du cFOV. Par ailleurs, le scanner A, comme prévu, fournit la plus faible valeur d'efficacité de détection. Ainsi, les valeurs obtenues sont conformes au comportement attendu. Il est également observé et signalé (section 5.3.3) que la résolution spatiale des scanners A et B se dégrade à mesure que nous déplaçons la source radialement vers l'extérieur en raison d'une erreur de parallaxe. Sur la base de la valeur estimée des paramètres de performance, la figure B.4 compare les scanners étudiés aux scanners prototype et commercial.

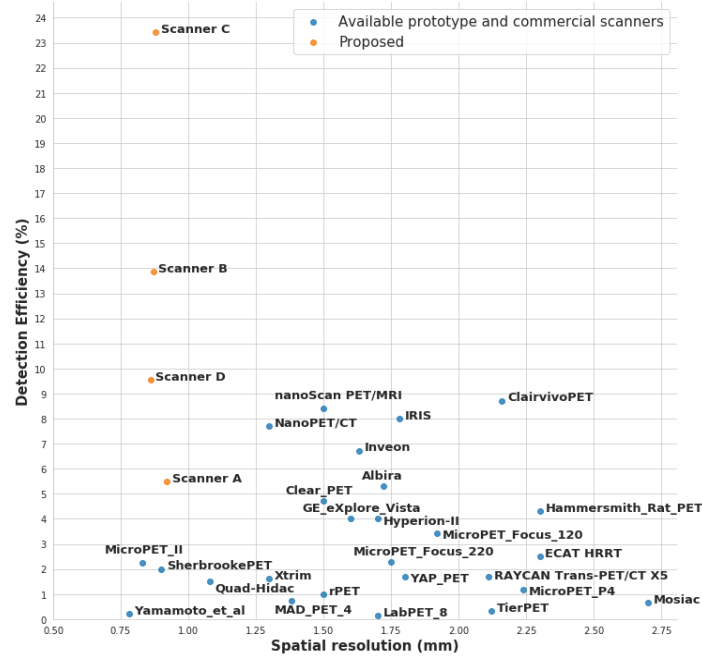


Figure B.4 – Comparaison des scanners étudiés avec d’autres scanners prototypes commerciaux et de recherche en termes de résolution spatiale et d’efficacité de détection.

Ainsi, nous pouvons observer que la résolution spatiale et l’efficacité de la détection sont découplées à mesure que l’on passe de l’estimation 2D à 3D de la position d’interaction du photon gamma. En découplant ces deux paramètres, nous pouvons améliorer simultanément les deux paramètres de performance.

**2. CASToR: Une approche plus rapide pour reconstruire des images pour les scanners nouvellement conçus à des fins de recherche :** Dans cette thèse, l’algorithme MLEM est utilisé pour reconstruire des images pour toutes les géométries de scanner étudiées. SM est un élément central de tous les algorithmes itératifs. Le SM peut être généré en utilisant différentes approches, telles que l’utilisation de projecteurs, la simulation de MC et l’acquisition expérimentale. Nous avons utilisé deux approches a) en effectuant des simulations MC et b) en utilisant des projecteurs analytiques pour générer le SM pour tous les scanners. Les résultats des deux approches sont discutés ci-dessous:

- (a) via des simulations MC: La génération d’éléments SM via des simulations MC présente l’avantage de prendre en compte tous les processus aléatoires associés à l’émission et à la détection de photons gamma. Il en résulte une modélisation précise de la réponse du détecteur à l’espace image. Cependant, cette approche nécessite de pré-calculer le SM pour tous les scanners et de le stocker sur le disque afin de l’utiliser ultérieurement pendant le



processus de reconstruction d'image. L'espace occupé par le SM sur le disque dépend entièrement du nombre d'éléments qu'il contient (c'est-à-dire le produit de  $i$  LOR et de  $j$  voxels d'image). Ainsi, une limitation majeure de cette approche est le stockage des éléments SM.

Un autre inconvénient de la génération de SM via des simulations MC provient du temps de simulation long. Toutes ces simulations sont effectuées à l'aide d'une grille informatique, ce qui nous permet d'utiliser la puissance de plusieurs ordinateurs en parallèle. Si nous utilisons la puissance de calcul d'un seul ordinateur, les simulations MC prendront plusieurs années pour chaque scanner. Le tableau B.3 présente une idée approximative du temps d'exécution de la simulation pour la génération de SM pour les quatre scanners, en supposant que les simulations sont effectuées sur un seul ordinateur. Cependant, il a été rapporté (section 5.2) qu'après plusieurs années de simulations équivalentes, le nombre d'éléments SM non nuls continue d'augmenter alors que de plus en plus de simulations sont lancées. Ainsi, on peut en conclure que nous n'avons pas encore généré le SM complet pour aucune des géométries du scanner. Pour cette raison, l'image reconstruite obtenue ne fournit aucune information quantitative.

Scanner	MC Simulation run time (years)	Castor Sensitivity image time (s)
A	3.84	1466
B	2.67	6182
C	1.01	435606
D	2.16	138066

Table B.3 – Comparaison de la durée des simulations MC pour générer le SM et de CASToR pour générer un profil de sensibilité pour toutes les géométries du scanner.

- (b) via des projecteurs (comme implémenté dans CASToR): CASToR calcule les éléments SM à la volée à l'aide de projecteurs analytiques; aucun stockage d'éléments SM n'est donc nécessaire. Avant l'étape de reconstruction d'image, CASToR calcule un profil de sensibilité dans lequel une étape de projection vers l'arrière est effectuée sur tous les éléments de détection possibles présents dans le scanner. Le profil de sensibilité est un tableau 3D ayant la même taille que la matrice d'images. Chaque élément du profil de sensibilité représente la somme des valeurs de probabilité pour un événement généré par ce voxel d'image et détecté par toute paire de détecteurs ( $\sum_{j=1}^m a_{ij}$ ). Le tableau B.3 présente également le temps pris par CASToR pour générer un profil de sensibilité pour tous les scanners. Alors que les simulations MC prennent des années pour générer le SM et reconstruire ainsi les images, nous avons montré qu'en utilisant CASToR, nous pouvons reconstruire les images pour le même ensemble de données en quelques jours. Nous pouvons donc en conclure que CASToR est une approche plus rapide pour reconstruire des images lorsqu'il étudie plusieurs géométries de scanner différentes.



Cependant, il convient de noter que dans CASToR, les projecteurs estimant les éléments SM ne prennent pas en compte la variation de l'efficacité de détection de différents LOR due à la géométrie du scanner. Ainsi, nous observons des artefacts dans les images reconstruites. Nous devons normaliser les éléments SM pour intégrer la fonction de réponse du détecteur. En outre, au fur et à mesure que la géométrie du scanner devient de plus en plus compliquée (c'est-à-dire constituée de plusieurs couches de cristal), la variation de l'efficacité de détection de différents LOR augmente davantage, entraînant des images plus dégradées. De plus, pour une acquisition réelle d'un scanner, il suffit de calculer le SM une seule fois et celui-ci peut être effectué à l'aide de simulations MC sur une longue période. CASToR est utile lorsque nous étudions plusieurs géométries de scanner.

3. **Effet des performances du scanner sur la qualité d'image reconstruite:** Nous avons simulé l'IQP selon la procédure décrite dans NEMA NU-4 2008. La qualité d'image reconstruite est caractérisée en termes de valeurs RC et SNR. Comme indiqué dans le point précédent, les images reconstruites à l'aide de SM pré-calculées (générées via des simulations MC) ne peuvent pas être utilisées pour fournir des informations quantitatives; les images reconstruites avec CASToR sont donc utilisées à des fins de quantification. Le tableau B.4 fournit les valeurs RC et SNR estimées pour tous les scanners.

Scanner	Recovery Coefficient	Signal-to-Noise Ratio
A	$0.95 \pm 0.21$	7.3
B	$0.77 \pm 0.12$	9.5
C	$0.84 \pm 0.35$	2.1
D	$0.74 \pm 0.17$	3.7

Table B.4 – Estimation des valeurs RC (pour un diamètre de tige chaude de 2 mm) et SNR pour les images reconstituées d'IQP par CASToR pour tous les scanners étudiés

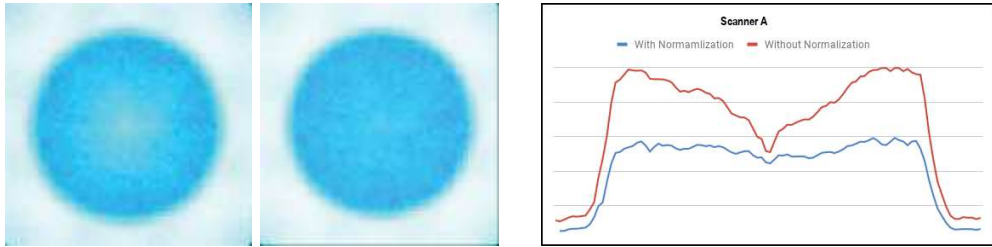
Les scanners ayant une résolution spatiale limitée par rapport à l'objet imageur entraînent une sous-estimation de l'activité en raison de l'effet de volume partiel (PVE). Les valeurs RC indiquent la résolution spatiale. Par conséquent, les scanners à meilleure résolution spatiale devraient fournir des valeurs RC plus élevées pour les hot rod de diamètre beaucoup plus petit. Tous les scanners étudiés, avec une résolution spatiale estimée proche de 1 mm, fournissent des valeurs de RC comparables pour une tige de 2 mm de diamètre. Cependant, les erreurs associées aux valeurs RC respectives ne sont pas négligeables. Les valeurs d'erreur dépendent principalement de la valeur SNR (indiquée pour tous les scanners du tableau B.4), qui dépend en outre de l'efficacité de la détection du scanner. L'efficacité de la détection doit être aussi élevée que possible pour obtenir un bon SNR et donc une quantification plus précise. Comme indiqué précédemment, le scanner C fournit l'efficacité de détection la plus élevée par rapport aux autres scanners. Cependant, la valeur du rapport signal sur bruit signalée est la plus faible du scanner D. Cela est dû au fait que la valeur du rapport SNR et donc l'erreur dépend également de la reconstruction de l'image. processus et les corrections apportées. Comme mentionné précédemment, les images sont reconstruites à l'aide du logiciel CASToR où les corrections pour

la normalisation (ou la variation de l'efficacité de détection de différents LOR) ne sont pas prises en compte et il en résulte une augmentation des valeurs d'erreur. Dans ce cas, les valeurs d'erreur résultant d'images non normalisées l'emportent sur l'impact attendu de l'efficacité de la détection.

Tous ces scanners étudiés présentent un compromis entre résolution spatiale et efficacité de détection dans une mesure différente. Le scanner C fournit une valeur très élevée d'efficacité de détection et une résolution spatiale proche de 1 mm (c'est-à-dire offrant une optimisation maximale). Cependant, l'impact de l'optimisation de ce compromis pour le scanner C sur la qualité globale de l'image n'est pas observé par rapport au scanner A (optimisation minimale entre la résolution spatiale et l'efficacité de la détection). Il est observé que l'approche de reconstruction d'image ainsi que les corrections de normalisation jouent un rôle important. Ainsi, on peut en conclure que la qualité d'image globale est dominée par la correction de normalisation et non par la performance intrinsèque.

#### 4. La normalisation joue un rôle important dans le processus de reconstruction d'image:

Nous avons observé les artefacts dans les images reconstruites par CASToR au centre du IQP pour toutes les géométries du scanner. Pour ce processus de reconstruction, les projecteurs sont utilisés pour estimer à la volée les éléments SM. Cependant, les projecteurs ne peuvent pas modéliser la réponse du détecteur pour les éléments SM calculés. En conséquence, les images reconstruites présentent un manque d'intensité au niveau de la cFOV, comme le montre la figure B.5(a) (left).



(a) Comparaison qualitative dans le profil radial (à gauche: sans normalisation; à droite: avec normalisation)  
(b) Comparison of line profile passing through the center of the radial profile

Figure B.5 – Comparaison du profil radial de la région uniforme du IQP reconstruit en utilisant CASToR sans et avec des facteurs de normalisation.

Ces artefacts sont dus au fait que les images reconstruites ne sont pas normalisées pour la variation de l'efficacité de détection de différents LOR, alors que l'algorithme MLEM suppose que l'efficacité de détection de tous les LOR est la même. Nous avons estimé les facteurs de normalisation axiaux et transaxiaux en utilisant une approche par composant pour le scanner A. Les facteurs de normalisation sont estimés à l'aide de simulations MC, toutefois, les simulations sont effectuées sur une très courte durée en raison de contraintes de temps. Nous avons fourni tous les facteurs de normalisation estimés pour les paires de cristaux respectives à CASToR afin

de calculer les éléments SM normalisés. Nous montrons que les images reconstruites incorporant des facteurs de normalisation (calculés pour une courte simulation d'une heure) montrent une amélioration qualitative significative (figure B.5(a) gauche) entraînant une amélioration de 16 % de la valeur SNR et, par conséquent, la valeur RC est 25 % plus précise (c'est-à-dire une amélioration de 25 % de la valeur d'erreur du RC). Ainsi, nous avons observé que la correction de normalisation joue un rôle important.

L'objectif initial de cette thèse était d'étudier la faisabilité d'optimiser simultanément la résolution spatiale et l'efficacité de détection et d'étudier l'impact de cette optimisation sur la qualité globale de l'image. Nous avons démontré qu'il était possible de découpler la résolution spatiale et l'efficacité de la détection en utilisant différents modèles de scanners. Pour étudier plus avant l'impact de ces géométries sur la quantification de la distribution des radiotraceurs, nous avons utilisé l'algorithme de reconstruction d'image itérative (MLEM). Les SM ont été générés à l'aide de simulations MC, mais il a été observé que la génération de SM est un processus très long et fastidieux. Avec un SM incomplet et inexact, il n'est pas possible de reconstruire et d'étudier les images reconstruites. En outre, pour le scanner C et le scanner D, en raison de l'augmentation significative du nombre d'éléments SM, le stockage a également été signalé comme l'une des principales limitations. Ainsi, un logiciel de reconstruction d'images open source CASToR est utilisé pour effectuer tous les processus de reconstruction. L'un des objectifs de l'algorithme itératif était d'étudier l'utilité de CASToR. CASToR est développé pour reconstruire des images pour une géométrie de scanner utilisant des matrices cristallines pixelisées. Ainsi, nous avons adapté le code CASToR pour prendre en compte les différentes géométries de scanner et reconstruit les données simulées IQP pour obtenir les images. Comme CASToR reconstruit l'image à l'aide de projecteurs analytiques et ne prend pas en compte la variation de l'efficacité de détection de différents LOR, nous avons observé des artefacts dans les images reconstruites. Ces artefacts ont un impact significatif sur la composante de bruit des paramètres de quantification.

L'erreur dans le paramètre de quantification due à notre approche de reconstruction (artefact dans les images reconstruites) l'emporte sur l'impact de l'optimisation de la résolution spatiale du scanner et de l'efficacité de la détection. Nous avons étudié différentes techniques de normalisation afin de prendre en compte la variation de l'efficacité de détection de différents LOR. Sur la base de la méthode basée sur les composants, des facteurs de normalisation sont générés en effectuant des simulations MC pour une géométrie de scanner. Le code CASToR est également modifié pour intégrer les facteurs de normalisation générés au cours du processus de reconstruction d'image. Nous avons observé une amélioration significative de l'image reconstruite ainsi que de la précision de la quantification. Sur la base de l'amélioration, il est possible de conclure qu'avec un processus de reconstruction d'image approprié et les corrections appliquées, nous pouvons améliorer la précision de la quantification de la distribution des radiotraceurs par rapport à l'optimisation en fonction de la résolution spatiale et de l'efficacité de la détection.

Sur la base de nos constatations, conclusions et travaux de recherche réalisés sur quatre géométries de scanner, voici les perspectives des travaux de recherche en cours:

1. **Corriger les images reconstruites pour normalisation pour tous les scanners :** Comme

discuté dans la thèse, les facteurs de normalisation basés sur les composants générés en effectuant une simulation MC améliorent la qualité de l'image reconstruite. Une perspective importante de ce travail de recherche consisterait à estimer les facteurs de normalisation pour tous les scanners restants et à caractériser les facteurs estimés pour leur précision. Une fois que tous les facteurs de normalisation sont estimés et caractérisés pour la précision, il sera utilisé pour reconstruire les images à l'aide de CASToR. Nous pourrions alors quantifier l'impact de l'optimisation de la résolution spatiale et de l'efficacité de la détection sur la qualité de l'image reconstruite.

La version actuelle de CASToR fonctionne en chargeant un fichier de correction en entrée (contenant les facteurs de correction pour tous les LOR) et en le stockant dans la mémoire. Étant donné que le scanner C et le scanner D impliquent un grand nombre de paires de cristaux, il est impossible (avec la version actuelle de CASToR) d'effectuer le processus de reconstruction. Ainsi, une autre perspective pourrait consister à incorporer une solution permettant de résoudre cette limitation et de reconstruire avec succès les images en tenant compte de tous les facteurs de normalisation estimés.

2. **Extraction de paramètres cinétiques pour la quantification :** Une fois les images corrigées pour les artefacts, il serait intéressant d'étudier l'impact de l'optimisation des performances du scanner en effectuant une modélisation cinétique par traceur. La modélisation cinétique du traceur explique mathématiquement le mécanisme de transport et les réactions biochimiques du traceur dans les tissus. Cela nécessite d'imager la dynamique de la distribution du radiotraceur dans le temps dans le tissu local pour extraire les constantes de vitesse de transfert, le volume de distribution ou les potentiels de liaison du radiotraceur à la cible. Une perspective importante de ce travail de recherche consiste à étudier l'impact de l'amélioration des performances intrinsèques du scanner sur l'estimation des paramètres de modélisation cinétique.

## Impact of preclinical PET scanner characteristics on the overall image quality

### Résumé:

La tomographie par émission de positrons (TEP) est l'une des techniques d'imagerie nucléaire utilisées dans les domaines de l'oncologie, de la cardiologie et de la neurologie en tant que modalité d'imagerie fonctionnelle. Au cours des trois dernières décennies, les progrès de la modalité PET et le développement de modèles animaux de maladies humaines ont conduit au développement de la technologie PET dédiée aux petits animaux. En raison de la différence de taille entre l'homme et la souris, les scanners pour petits animaux nécessitent une résolution spatiale améliorée. En raison de l'amélioration de la résolution spatiale, la taille du voxel diminue de manière significative, réduisant ainsi le nombre de signaux d'un voxel. Plus le nombre détecté est élevé, plus le rapport signal sur bruit (SNR) est élevé; l'amélioration de l'efficacité de la détection joue donc également un rôle important.

Notre objectif est d'étudier l'impact des caractéristiques du scanner PET sur la qualité globale de l'image. Pour ce faire, nous avons simulé quatre modèles de scanners différents. L'idée des conceptions de scanner sélectionnées dans cette thèse est d'ajouter progressivement une dimension supplémentaire dans la position estimée de l'interaction du photon gamma, c'est-à-dire en passant de la détection 2D à la détection 3D.

Nous avons démontré qu'il était possible de découpler la résolution spatiale et l'efficacité de la détection, en améliorant les deux simultanément. En outre, nous avons caractérisé le fait que l'amélioration de la résolution spatiale entraîne l'amélioration du coefficient de récupération (RC). L'efficacité de la détection a un impact sur le RSB, ce qui a également un impact sur l'erreur estimée dans les valeurs de RC. Cependant, d'autres facteurs, tels que l'approche de reconstruction d'image et les corrections de normalisation, dégradent ces valeurs d'erreur. Il est donc important non seulement d'améliorer les paramètres de performance des scanners, mais également de mettre en œuvre avec précision le processus de reconstruction d'image, afin de quantifier correctement l'amélioration de la qualité de l'image.

**Mots clés : Scanners TEP précliniques - Résolution spatiale - Efficacité de la détection - Coefficient de récupération - Reconstruction - Normalisation.**

### Abstract:

Positron Emission Tomography (PET) is one of the nuclear imaging techniques, used in the field of oncology, cardiology and neurology as a functional imaging modality. During the last three decades, advancement of PET modality and the development of animal models of human disease have lead to the development of PET technology dedicated to small animals. Due to the size difference between humans and mice, small animal scanners require improved spatial resolution. Due to the improved spatial resolution, the voxel size decreases significantly thereby, reducing the number of signals from a voxel. Higher the detected counts, higher the signal-to-noise ratio (SNR), thus improvement in the detection efficiency also plays an important role.

Our objective is to study the impact of PET scanner characteristics on the overall image quality. To achieve this, we have simulated four different scanner designs. The idea behind the selected scanner designs studied in this thesis is to progressively add an extra dimension in the estimated position of interaction of the gamma photon, i.e., going from 2D detection to 3D detection.

We demonstrated that it is possible to decouple the spatial resolution and detection efficiency, improving both simultaneously. Further, we characterized that improving spatial resolution results in improved Recovery Coefficient (RC). Detection efficiency impacts the SNR, which further impacts the estimated error in the RC values. However, there are other factors such as image reconstruction approach and normalization corrections that degrade these error values. Thus, it is important to not only improve the performance parameters of the scanners but also to accurately implement the image reconstruction process, so as to correctly quantify the improvement in the image quality.

**Keywords: Preclinical PET - Spatial resolution - Detection efficiency - Recovery coefficient - Reconstruction - Normalization.**

